


# A Sonochemical Approach for Sustainable Hydrogen and Syngas Generation

**Cheuk Yin (Cherie) WONG**
**Balliol College**

*A thesis submitted in partial fulfilment of the requirement for the degree of Doctor of Philosophy in Engineering Science at the University of Oxford*

**Supervisor: Professor James Kwan**
**Physical Acoustic Laboratory**

**June 2025**

# Abstract

Achieving global carbon neutrality is one of the most pressing technological challenges of the 21st century. Green chemical processes are central to this transition, particularly those that reduce fossil fuel dependence, improve energy efficiency, and avoid toxic by-products. Among these, sonochemistry, the use of ultrasound to drive chemical reactions, offers unique advantages through the phenomenon of acoustic cavitation, which generates localised zones of extreme temperature and pressure capable of initiating reactions that are otherwise difficult to achieve. This thesis explores the development of a sonochemically efficient reactor and its application to two key green processes: hydrogen production via water splitting and syngas production from biomass.

To address limitations in conventional ultrasonic reactor design including dispersed acoustic fields and slow reaction kinetics, a novel cylindrical sonochemical reactor, SonoCYL, was developed to guide and focus acoustic energy using cylindrically converging waves to a reactor vessel. Hydroxyl radical production and sonochemical efficiency were assessed using a highly sensitive fluorescent probe, Resorufin-3,5-dihydroxybenzyl, alongside terephthalic acid dosimetry. Under optimised conditions (15.1 $MPa_{pkpk}$, pulsed ultrasound at 100 acoustic cycles), SonoCYL produced a hydroxyl radical yield two orders of magnitude higher and achieved at least twice the sonochemical efficiency compared to conventional systems, when normalised to the same reaction volume. These findings highlight the importance of reactor geometry and acoustic parameter optimisation in advancing sonochemical technologies.

Building on the novel sonochemical reactor design, the thesis investigated its application in sustainable technologies. The following study explored sonochemical hydrogen production from water and seawater splitting without relying on noble-metal catalysts or purified water. Using SonoCYL and $TiO_2$ as a sonocatalyst, the system (780 kHz, 5.1 W) was optimised acoustically and chemically with 100 acoustic cycles and 0.3 mg/mL $TiO_2$. The research then investigated the system's cavitation activity using passive cavitation detection and signal processing. It was shown that dissolved salts in seawater reduced hydrogen yield primarily through radical scavenging, as confirmed by electron paramagnetic resonance and bubble dynamics simulations. The system achieved the highest reported normalised hydrogen production efficiencies to date for both pure water (7906 μmol $g^{-1}$ $L^{-1}$ $Whr^{-1}$) and seawater (4398 μmol $g^{-1}$ $L^{-1}$ $Whr^{-1}$), demonstrating the potential of ultrasound-based hydrogen generation.

Recognising that $TiO_2$ may not be the most effective sonocatalyst despite its widespread use, the following chapter investigated less commonly used metal oxides for sonochemical hydrogen production. Among the materials tested, $CeO_2$ showed the highest activity, potentially due to its oxygen-release properties and $Ce^{3+}/Ce^{4+}$ redox cycling capacity. However, doping $CeO_2$ with transition metals (Mn, Zn, Cu, Fe, Ni, Co) appeared to reduce activity, which might be linked to a disruption of its oxygen storage-release mechanisms and loss of active surface sites. No clear correlation was observed between the sonocatalytic performance and parameters such as particle size or cavitation intensity. These preliminary findings suggest that catalyst surface chemistry may significantly influence sonochemical performance, but there is a need for deeper mechanistic understanding in sonocatalyst design.

While water and seawater splitting offer relatively simple and well-controlled systems to demonstrate the green potential of sonochemistry, the study encourages broader exploration of more complex and industrially relevant feedstocks. Building on this foundation, this work further investigates ultrasound-assisted biomass gasification as a sustainable sonochemical application. This approach is motivated by the high energy demands of conventional thermochemical methods, which require high temperatures and pre-dried feedstocks. In contrast, ultrasound enables a room-temperature alternative by harnessing acoustic cavitation to convert liquid-based biomass directly into syngas. Molasses, a readily available by-product of the sugar industry, was selected as a representative liquid biomass for this investigation. Experimental parameters such as dissolved gas type, sugar composition, dilution ratio, and catalyst incorporation were studied. From the results, argon was shown to promote higher $H_2$ and CO yields than air, and an optimal 15x dilution was identified, balancing organic content with favourable physical properties for cavitation. While unmodified zeolites (ZSM5, Y, Beta) showed little improvement, Ni-doped ZSM5 increased total gas yields, particularly $CO_2$, without altering the $H_2$/CO ratio. The integrated cavitation index revealed a linear correlation between $H_2$, CO, and $CH_4$ yields, confirming cavitation as the primary driving mechanism to produce these gases. The $H_2$/CO ratio remained constant at 1.125 under all conditions.

This thesis contributes to the ongoing development of sonochemical reactor designs and sonocatalyst systems, with demonstrated potential to advance green chemical processes and sustainable energy technologies. The insights gained are expected to guide future research in optimising sonochemical systems for real-world applications.

# Contents

**Abstract** 2
**Contents** 4
**Authorship Attribution Statement** 7
**Acknowledgements** 9
**1. Introduction** 11
1.1. Background and motivation 11
1.2. Main objectives of the thesis 13
1.3. Outline of the thesis 14
**2. Literature review** 15
2.1. Sonochemistry and acoustic cavitation 15
2.2. Operando conditions for sonochemistry 16
2.3. Sonochemical reactors 20
2.3.1. Sonochemical reactor design 21
2.4. Characterisation for sonochemical reactors 23
2.4.1. Physical methods 24
2.4.2. Chemical methods 25
2.4.3. Sonochemical efficiency 28
2.5. Sonochemical hydrogen production 29
2.5.1. Conventional green hydrogen production from seawater splitting 29
2.5.2. Mechanisms of sonochemical hydrogen production 30
2.5.3. Existing sonochemical hydrogen production work in the literature 31
2.5.4. Metal oxide sonocatalysts for sonochemical hydrogen production 32
2.5.5. Quantification of hydrogen and gases 33
2.6. Sonochemical biomass gasification for syngas production 34
2.6.1. Thermochemical biomass gasification system 34
2.6.2. Factors influencing biomass gasification efficiency 36
2.6.3. Sonochemical biomass gasification 37
2.6.4. Molasses as a selected biomass for the study 38
2.6.5. Zeolite catalysts and metal doping for biomass gasification 39
**3. Design and characterisation of a novel sonoreactor ('SonoCYL')** 41
3.1. Materials and methods 42
3.1.1. Materials 42
3.1.2. Reactor design and experimental set-up 43
3.1.3. Acoustic pressure characterisation and sonochemical reactions 45
3.1.4. Sonochemical hydroxyl radical production determination 51
3.1.5. Sonochemical efficiency determination 52
3.1.6. Conventional sonochemical reactor 53
3.2. Results and discussion 55
3.2.1. Acoustic characterisation 55
3.2.2. Res-DHB dosimetry for hydroxyl radicals 58
3.2.3. Optimal operational parameters for SonoCYL 60
3.2.4. Comparisons with conventional sonochemical reactors 63
3.2.5. Comparisons with literature 69
3.3. Conclusions 72
**4. Sonocatalytic seawater splitting for hydrogen production** 73
4.1. Materials and methods 74
4.1.1. Materials 74
4.1.2. Sonochemical reactor system and cavitation noise measurements 75
4.1.3. Reaction solution preparation and sonochemical reactions 76

4.1.4. Cavitation noise signal processing 81
4.1.5. Cavitation threshold determination 81
4.1.6. Hydrogen gas analysis 81
4.1.7. Collapse temperature estimation from single bubble simulation 85
4.1.8. EPR spectroscopy 86
4.1.9. SEM images 88
4.2. Results and discussion 88
4.2.1. Sonochemical hydrogen production optimisations 88
4.2.2. Effect of seawater 92
4.2.3. Kinetics of sonocatalytic water splitting 99
4.2.4. Comparison with literature 103
4.3. Conclusions 107
**5. Screening of metal oxides for sonochemical hydrogen production 108**
5.1. Materials and methods 108
5.1.1. Materials 108
5.1.2. Sonochemical reactor system and cavitation noise signal measurements 109
5.1.3. Reaction solution preparation and sonochemical reactions 110
5.1.4. Cavitation noise signal processing 110
5.1.5. Hydrogen gas analysis 110
5.1.6. Preparation of metal-doped $CeO_2$ 110
5.2. Results and discussion 111
5.2.1. Metal oxide screening 111
5.2.2. Incorporation of metal-doped $CeO_2$ 115
5.3. Conclusions 117
**6. Sonocatalytic biomass gasification for syngas production 118**
6.1. Materials and methods 119
6.1.1. Materials 119
6.1.2. Sonochemical reactor system and cavitation noise measurements 120
6.1.3. Cavitation noise signal processing 120
6.1.4. Molasses reaction solution preparation and sonochemical reactions 120
6.1.5. Gas analysis 121
6.1.6. Liquid analysis 124
6.2. Results and discussion 125
6.2.1. Effect of dissolved gas 125
6.2.2. Main contributors to gaseous products 127
6.2.3. Effect of water-to-molasses dilution ratio 129
6.2.4. Effect of zeolite sonocatalyst incorporation 130
6.2.5. Kinetic and cavitation study of sonochemical biomass gasification 134
6.2.6. Selectivity for syngas production 138
6.3. Conclusions 139
**7. Conclusions and future work 140**
7.1. Conclusions 140
7.2. Future work 144
**Appendix 147**
A.1. Calorimetry measurements and fitting 147
A.2. Fenton chemistry 158
A.3. An example calculation of hydrogen production 161
A.4. Sigmoid function fitting for cavitation noise index 162
A.5. Categorised gas production rate data for biomass gasification 163
A.6. MATLAB code 165
A.6.1. EPR data fitting 165
A.6.2. PCD noise collection for cavitation threshold determination 167

A.6.3. Noise signal processing for cavitation index determination 172
A.6.4. PCD noise collection over time 174
A.6.5. Noise signal processing for cavitation noise over time 179
**References** **181**

# Authorship Attribution Statement

This thesis contains material from three papers published in the following peer-reviewed journals.

Chapter 2 and Chapter 3 are published as: Wong, C. C. Y., Sun, L.-L., Liu, M.-J., Stride, E., Raymond, J. L., Han, H.-H., Kwan, J. & Sedgwick, A. C. Fluorescence-based chemical tools for monitoring ultrasound-induced hydroxyl radical production in aqueous solution and in cells. *Chemical Communications* **59**, 4328-4331, doi:https://doi.org/10.1039/D3CC00364G (2023).

The contributions of the co-authors are as follows:

- Cherie C.Y. Wong conducted the experimental work of Umb-DHB and Res-DHB under an ultrasonic environment, data analysis and data visualisation, and wrote the original draft of the paper regarding sonochemistry.
- Lu-Lu Sun performed the fluorescence imaging and quantification of HeLa cells.
- Professor Eleanor Stride supervised the research and acquired the funding for the work.
- Professor Jason L. Raymond developed and implemented the experimental design of the sonochemical reactor used in the study.
- Professor Hai-Hao Han supervised the research and acquired the funding for the work.
- Professor James Kwan conceptualised the research idea with Dr. Adam C. Sedgwick, supervised the research, and acquired the funding for the work.
- Dr. Adam C. Sedgwick conceptualised the research idea with Professor James Kwan, developed and implemented the experimental design and methodology, conducted experimental work, prepared the original draft of the paper, and supervised the research.
- All authors edited and reviewed the manuscript revision.

Chapter 2 and Chapter 3 are published as: Wong, C. C. Y., Raymond, J. L., Usadi, L. N., Zong, Z., Walton, S. C., Sedgwick, A. C. & Kwan, J. Enhancement of sonochemical production of hydroxyl radicals from pulsed cylindrically converging ultrasound waves. *Ultrasonics Sonochemistry* **99**, 106559, doi:https://doi.org/10.1016/j.ultsonch.2023.106559 (2023).

The contributions of the co-authors are as follows:

- Cherie C.Y. Wong conducted the experimental work, visualised the results, and wrote the original draft of the paper.
- Professor Jason L. Raymond conceptualised the research idea with Professor James Kwan, developed and implemented the experimental design of the sonochemical reactor and methodology used in the study.
- Lillian N. Usadi conducted the experimental work and visualised the results.
- Zhiyuan Zong assisted on the experimental work.
- Stephanie C. Walton assisted on the experimental work.
- Dr. Adam C. Sedgwick developed the methodology and synthesised the fluorescence probe Res-DHB used in the study.
- Professor James Kwan conceptualised the research idea with Professor Jason L. Raymond, supervised the research, and acquired the funding for the work.
- All authors edited and reviewed the manuscript revision.

Chapter 2 and Chapter 4 are published as: Wong, C. C. Y., Preso, D. B., Qin, Y., Sinhmar, P. S., Zong, Z. & Kwan, J. Ultrasound-driven seawater splitting catalysed by $TiO_2$ for hydrogen production. *International Journal of Hydrogen Energy* **111**, 723-734, doi:https://doi.org/10.1016/j.ijhydene.2025.02.327 (2025).

The contributions of the co-authors are as follows:

- Cherie C.Y. Wong conceptualised the research idea with Professor James Kwan, developed and implemented the experimental design and methodology, conducted the experimental work and data analysis, visualised the results, and wrote the original draft of the paper.
- Dr. Davide Bernardo Preso conducted the bubble simulations and contributed the original draft of the paper regarding the method and results of the bubble simulations.
- Yi Qin conducted the scanning electron microscopy imaging.
- Dr. Pankaj S. Sinhmar advised on the experimental design.
- Zhiyuan Zong advised on the data analysis.
- Professor James Kwan conceptualised the research idea with Cherie C.Y. Wong, supervised the research, and acquired the funding for the work.
- All authors edited and reviewed the manuscript revision.

In Chapter 5, most of the experimental work in this study was conducted as part of the UNIQ+ internship project by Zoe Fang. In this work, Cherie C.Y. Wong conceptualised the research, developed the methodology, and visualised the results. Cherie C.Y. Wong and Zoe Fang jointly carried out the experimental investigations. The project was jointly supervised by Professor James Kwan and Cherie C.Y. Wong.

In Chapter 6, Dr. Haokun Wang synthesised and provided the Ni-doped ZSM5 used in the study.

Use of graphics obtained from flaticon.com (Eucalyp, Freepik, Good Ware, GOWI, kmg design, Pause08, Smashicons).

# Acknowledgements

This thesis marks the conclusion of my four-year journey as a DPhil student at Oxford. This would not be possible with the support from many, which I am forever grateful for.

First and foremost, I am deeply thankful to Professor James Kwan for entrusting me with the opportunity to be the first PhD student in his group. The early years of my DPhil were at times stressful and filled with challenges, but his guidance consistently offered direction while giving me the space to think and find my own way. It has also been inspiring to witness how he built the group from the ground up, fostering a supportive lab environment where innovative ideas could grow. On a personal level, I am immensely grateful to James for being an exceptional mentor. His willingness to share his experiences and stories has provided great guidance and encouragement during moments when I faced obstacles and doubts. I also appreciate the freedom he gave me to explore beyond my research, which has been an enriching aspect of my DPhil journey. His encouragement and trust have played a significant role in shaping both my academic and personal growth during my DPhil, and for that, I am truly thankful.

I would also like to thank Professor Ronald Roy and Professor Jason Raymond for their support. I am especially grateful to Ron for his invaluable knowledge in acoustics and wisdom, and to Jason for his patience and hands-on guidance in teaching me how to operate the instruments during the early stage of my research. I am also thankful to Professor Edman Tsang for his generosity in allowing me to conduct catalysis work in his laboratory. I would like to thank Dr. Binjian Nie and Professor Aidong Yang for being my transfer and confirmation examiners and for providing many valuable pieces of advice that hugely improved the quality of my research.

Thank you so much to my fellow labmates in PACLAB: Stephanie Walton, Yihao Huang, Lillian Usadi, Chris Zong, Yi Qin, Ying Wei, and Lucia Mullings. A special thanks to Steph for your friendship, our trip to Canada and hiking in Banff remain a highlight of my DPhil journey. To Lillian, thank you for your companionship and all the fun we had when it was just the two of us in the group and during our time in Chicago. And to Yihao, thank you for your always-delicious dinner parties and your fascinating (and sometimes delightfully bizarre) breadth and depth of knowledge you are willing to share, I'm always amazed by the things you know! Thank you so much to the postdocs in PACLAB: Dr. Pankaj Sinhmar, Dr. Davide Bernardo Preso, Dr. Mohamad Salimi, Dr. Xuelei Pan, and Dr. Dong Xia. Special thanks to Pankaj for your countless conversations, guidance, and the help you've generously offered in the lab, you've always been there whenever I needed support! To Davide, thank you for the cheerful chats and support, and your scientific rigour, which continues to inspire me. And to Mo, thank you for consistently showing up in the lab at exactly 12 pm to invite us to have lunch, and for sharing your boxing stories, which I always found very interesting.

I would like to thank the many collaborators and individuals who supported me throughout this DPhil. I sincerely thank Dr. Umesh Jonnalagadda for his invaluable guidance in acoustics and for sharing his experience in sonochemistry during the early stages of my DPhil. I am also grateful to Dr. Roong Jien Wong for his valuable advice on reactor design and for introducing me to the Harwell campus during the early years of my research. Dr. Adam Sedgwick, thank you for collaborating on the Res-DHB project, your passion for scientific research has inspired me. I am grateful to Dr. Haokun Wang

for the stimulating conversations and for providing the catalyst that allowed me to explore novel ideas, even though it did not yield meaningful conclusions in the end. I thank Zhangyue (Jennifer) Xie for her assistance with my EPR experiments. I also deeply appreciate Dr. Nicholas Tenci and Dr. Laura Martin for their generosity in lending instruments and taking the time to teach us how to use them in their lab. A special thanks to Nick for the many helpful conversations, support, and suggestions you provided whenever I was stuck or confused.

I thank the exceptional research support I received from many. Jon, Andy, and Sofia from Shimadzu, thank you for patiently answering emails and always being willing to address my many (sometimes silly) questions about the GCMS. Dr. William Myers from CAESR, I appreciate your help in setting up our experiments and hands-on guidance in operating the EPR. A special thanks to the incredible admin team at Begbroke, Helen Banks, Helen Crockford, Karen, Louise, and Rachel, for managing countless purchase orders and handling every detail of lab operations with efficiency and care.

Completing the DPhil would not be possible without the generous funding I have received from the DTP Scholarship from Department of Engineering Science, University of Oxford, and the Dervorguilla Scholarship from Balliol College, University of Oxford.

I am grateful for the friendships that have brought joy, support, and unforgettable memories throughout my DPhil journey and beyond. To my Begbroke-mates, Sean, Kin, Govind, and Simrin, thank you for your friendship, and a special thanks to Sean for your delightful conversations and so much more. I'm also thankful to my dear friends Vivian and Chris for the countless BBQs, board games, and late-night chats. To Matthew, Angel, Beryl, and Mandy, thank you for your lifelong friendship, even as our paths diverge.

I thank Terence for the shared laughter, companionship, and support throughout the DPhil and beyond.

I thank the Shum family and Wong family for their unwavering support and comfort food whenever I return. Finally, I extend my deepest gratitude to my parents in Hong Kong for their unconditional love, support, and encouragement. The shelter you provided, which I call home, has given me the strength to pursue my aspirations anywhere, and knowing I can always return, is truly the greatest blessing I could ever ask for.

# 1. Introduction

## 1.1. Background and motivation

Achieving global carbon neutrality by 2050 stands as one of the most critical challenges of our time[1]. Chemical processes play a critical role in this transition by reducing reliance on fossil fuels, enhancing energy efficiency, and eliminating toxic intermediates and by-products. Among these, sonochemistry, the use of ultrasound to drive a physical or chemical process, has attracted interest. The chemical effects of ultrasound were first observed in 1927 by Richards and Loomis[2]. Since then, interest has grown substantially in recent decades due to its broad applications. Examples include extraction processes, wastewater treatment, and both organic and nanoparticle synthesis, particularly in sectors such as pharmaceuticals, food processing, and industrial cleaning[3]. Beyond these, ultrasound holds significant promise for green chemistry, as it often leads to shorter reaction times, higher yields, and improved selectivity compared to conventional thermal methods[4,5].

The effects of ultrasound arise primarily from acoustic cavitation, broadly defined as the formation, growth, and collapse of bubbles within a liquid. When these bubbles collapse, they generate highly localised hotspots characterised by extreme temperatures and pressures. This phenomenon creates extreme physical and chemical conditions within an otherwise ambient bulk liquid, effectively forming transient microreactors at the sites of bubble collapse. These extreme conditions facilitate the formation of reactive species, such as hydrogen and hydroxyl radicals, which are produced within the hotspots. These radicals may recombine or react with species in the surrounding liquid, thereby driving a range of chemical transformations.

As acoustic cavitation underpins sonochemistry, precise control of the acoustic field within the liquid medium is essential for optimising sonochemical reactions. The reactor design and the operating acoustic parameters are therefore critical factors that must be carefully selected and controlled. However, most conventional ultrasonic reactor designs suffer from dispersed acoustic energy, requiring continuous and high-power ultrasound over extended durations to achieve meaningful chemical yields. Furthermore, these designs typically struggle to deliver consistent acoustic energy across the reaction volume, making it difficult to reproduce sonochemical results reliably. This research presents a novel cylindrical sonochemical reactor design, termed SonoCYL, which is engineered to guide and concentrate acoustic waves within the reactor vessel. Based on its geometry, it is hypothesised that the reactor reflects and converges radially spreading waves to create intense, localised acoustic pressure fields at the reaction vessel. To evaluate the chemical effects, the hydroxyl

radical production and sonochemical efficiency of SonoCYL was quantified, which were then compared against those of conventional reactor designs.

To assess the chemical effects of SonoCYL and compare its sonochemical reactor efficiencies with other designs, accurate quantification of hydroxyl radical production is essential. Traditionally, chemical dosimetry methods such as the Weissler reaction, Fricke dosimetry, and terephthalic acid assays have been used for this purpose[6]. However, these methods often suffer from limited selectivity, sensitivity, or stability under sonochemical conditions, making them unsuitable for precise measurement of hydroxyl radical. This study explored and measured the response of Resorufin-3,5-dihydroxybenzyl (Res-DHB), a highly sensitive and selective fluorescent probe for hydroxyl radical detection. This approach enabled accurate quantification of hydroxyl radical production in the sonochemical environment and facilitated a robust comparison of sonochemical efficiency between the SonoCYL reactor and conventional reactor designs.

Following the establishment of the enhanced sonochemically efficient sonoreactor, the following chapters explored innovative green applications for this technology. Hydrogen, as a zero-emission fuel, is widely recognised for its potential to facilitate the transition to a low-carbon economy. However, water electrolysis, which is the standard green hydrogen production technology, often requires the use of expensive and scarce noble metals as catalysts, as well as ultra-pure water as reactant, which further escalates the cost and availability of hydrogen production. In this context, seawater, an abundant and virtually inexhaustible resource, presents a promising feedstock for hydrogen generation. Sonolysis from seawater, the generation of hydrogen driven by ultrasound hydrolysis, offers an alternative and sustainable pathway for clean hydrogen production due to its potential for volumetric scaling and prevention of instrumental corrosion when seawater is used as feedstock. To date, this research area is still in its nascent stage with a limited number of works exploring the most effective acoustic and sonocatalytic conditions. This research explores an effective, optimised, and sustainable system to convert water and seawater into hydrogen with SonoCYL and cheap, corrosion-resistant titanium dioxide ($TiO_2$) under sonochemical conditions.

While $TiO_2$ is one of the most commonly used sonocatalysts, it is not necessarily the most effective. To broaden the scope of investigation that constrains the optimisation and further development of sonocatalytic processes, the sonochemical hydrogen production performance of a range of less commonly used metal oxides were evaluated. Additionally, the effects of metal doping on catalytic activity were examined to determine whether such modifications enhance hydrogen yield. This study aims to provide insight into how catalyst composition and structural modifications influence

sonochemical hydrogen generation, and to provide a basis for future research focused on expanding the range of sonocatalysts used in system optimisation.

Splitting water into hydrogen represents just one of the promising green applications of sonochemistry. This research continues to explore additional avenues for applying sonochemical techniques to sustainable practices. Current biomass gasification methods for syngas production, which typically rely on pyrolysis, require high temperatures ranging from 800 to 1200 °C and energy-intensive pre-drying of the biomass, this results in a less efficient overall process[7]. Ultrasound-assisted gasification offers an alternative approach by utilising acoustic cavitation at room temperature, thereby eliminating the need for high-temperature conditions and enabling the direct use of wet, dissolved biomass. In this project, molasses, a by-product of the sugar extraction and refining process, is used as a proof-of-concept liquid biomass to demonstrate the feasibility of ultrasound-driven gasification, an application not previously reported in the literature to the best of current knowledge. The effects of various conditions on gas production rate and $CO/H_2$ production ratios are explored, with the aim of advancing the current state of biomass gasification technology.

## 1.2. Main objectives of the thesis

This thesis presents the development of an improved sonochemically efficient sonoreactor and its potential applications in green chemistry. The initial phase of the research focuses on the sonochemical and acoustic characterisation of the reactor, which demonstrates its enhanced sonochemical efficiency. Then, the second phase of the research explores two potential green applications of the sonoreactor. The first application focuses on ultrasound-driven hydrogen production from sonochemical water splitting. The second application investigates ultrasound-driven liquid-based biomass gasification for syngas production.

## 1.3. Outline of the thesis

This thesis is structured into seven chapters.

- **Chapter 1:** This chapter introduces the background and motivation, objectives, and outline of the thesis.
- **Chapter 2:** This chapter explores the fundamentals of sonochemistry, reviewing recent advances and challenges in the field. It specifically focuses on the characterisation methods of sonochemical systems and sonochemical reactor designs, as well as recent developments in sonochemical hydrogen production and biomass gasification processes.
- **Chapter 3:** This chapter focuses on the acoustic and sonochemical characterisation of the bespoke sonoreactor, 'SonoCYL', and evaluates its performance in this study.
- **Chapter 4:** This chapter explores a green application of sonochemistry using the sonoreactor, specifically focusing on sonocatalytic water and seawater splitting for hydrogen production.
- **Chapter 5:** This chapter presents a systematic screening of metal oxides and metal-doped catalysts for sonochemical hydrogen production.
- **Chapter 6:** This chapter explores an alternative green application of sonochemistry, focusing on sonocatalytic biomass gasification for syngas production with molasses as feedstock.
- **Chapter 7:** This chapter offers the conclusion and outlook for future research.

# 2. Literature review

## 2.1. Sonochemistry and acoustic cavitation

Sonochemistry is a branch of science studying the intersection of sound and chemistry. The chemical effects of ultrasound irradiation were observed by Richards and Loomis nearly a century ago, but the field remained stagnant for nearly 60 years after their discovery[8]. With the advance of inexpensive and reliable laboratory ultrasound devices, there was a renaissance of sonochemistry in the 1980s for its use in organic chemistry. Sonochemistry provides a way to bypass tedious and dangerous organometallic reactions such as Grignard reactions and metal activation[9]. More recently, scientists have shown that the chemical effects of ultrasound are useful in other chemical reactions including hydrogen production, chemical synthesis, and pollutant degradation[10,11].

Cavitation in the broadest definition is the formation of gas and/or vapour cavities (i.e., a bubble) in response to the decrease in local liquid pressure. When these pressure variations are acoustically driven, the phenomenon is termed acoustic cavitation[12,13]. In most cases of acoustic cavitation, the local liquid pressure decreases to a negative value, generating tensile stress that expands the liquid volume and enables bubble nucleation. Generation of cavitation in ultra-pure liquids using ultrasound alone is theoretically possible; however, achieving this under typical laboratory conditions is extremely challenging. In practice, impurities or 'weak points' in liquids reduce the cavitation threshold under ambient conditions, facilitating cavity formation[14,15]. These impurities are usually in the form of pre-existing microbubbles or gas-filled crevices in suspended particles. For example, more than 1000 atm of negative acoustic pressure is required to nucleate cavitation in pure water. However, cavitation may be detected at less than 1 atm of negative acoustic pressure for a liquid containing microbubbles[16].

Following nucleation, bubbles in an acoustic field undergo volumetric oscillations in response to alternating compression and rarefaction cycles. Bubbles expand during low-pressure rarefaction phases and contract during high-pressure compression phases. Under the effect of ultrasound, bubbles may grow through coalescence and rectified diffusion – the net preferential inward diffusion of gas into oscillating bubbles over each acoustic cycle, driven by differences in surface area between expansion and contraction phases. As a bubble grows to a certain resonance size, it couples strongly with the driving acoustic field and undergoes rapid expansion. Once the bubble reaches a critical expansion ratio, where its maximum radius is at least twice its equilibrium radius (i.e., the radius of

the bubble in the absence of an acoustic field), the dynamics are no longer dominated by the acoustic field but by the inertia of the surrounding fluid[13]. As such, cavitation is governed by inertia and is termed 'inertial cavitation' or 'transient cavitation'. Subsequently, the bubble implodes and collapses during the compression phase of ultrasound, achieving wall velocities exceeding the speed of sound in water.

The inertial collapse of a bubble involves two key phases: the expansion phase and the inertial collapse phase. During the expansion phase, heat exchange between the bubble interior and the surrounding liquid is nearly unrestricted, as the slow expansion in an ultrasonically irradiated liquid involves compression of the surrounding fluid and may be approximated as isothermal[17]. Yet, during the inertial collapse of the bubble, the bubble wall velocity is too fast for heat transfer between the liquid medium and the bubble, leading to quasi-adiabatic heating inside the bubble[18]. This creates extremely high temperature and pressure conditions inside the bubble at the moment of collapse[19,20]. The extreme environment in the hotspot during acoustic cavitation leads to physical effects, such as shock waves, and chemical effects, such as the formation of radical species and light, known as sonoluminescence. In general, the radicals generated during inertial cavitation are necessary for sonochemistry. Therefore, unlike using thermal or light energy, sonochemical reactions are triggered by these extreme and transient phenomena whilst maintaining ambient conditions in the bulk liquid[21]. This highly energetic and transient environment effectively creates temporary 'microreactors' that enable unique reaction paths useful for many chemical processes.

## 2.2. Operando conditions for sonochemistry

Though spatially and temporally stochastic, the dynamics of the acoustic bubble – nucleation, oscillation, and potential inertial collapse – are broadly dependent on the operando conditions of the ultrasonic field. Therefore, controlling the behaviour of the acoustic bubble by tuning the ultrasound frequency, pressure amplitude, pulse sequence, presence of exogenous cavitation nuclei and so on enables control over sonochemical processes. Here, several conditions most relevant to this research are discussed.

**Acoustic frequency**

The natural resonance frequency of a gas bubble in a liquid, also referred to as the Minnaert frequency, represents the characteristic frequency at which the bubble oscillates in size when disturbed by an external force such as ultrasound. This resonance frequency is size-dependent and inversely

proportional to the bubble's equilibrium radius, as expressed by the Minnaert formula. For example, under ambient pressure in water, a bubble with a radius of 3.3 μm resonates at approximately 1 MHz, while a bubble with a radius of 4.2 μm resonates at about 780 kHz. This resonance is critical for cavitation effects, as the bubble oscillates with the largest pulsation amplitude when the ultrasound driving frequency matches or approaches its resonance frequency.

In practical applications, the driving ultrasound frequency is generally the most accessible parameter to control. An optimum frequency often exists for sonochemical reactions, arising from two opposing effects. At lower frequencies, the range of bubble sizes capable of nucleating inertial cavitation is broader, and the extended rarefaction phase promotes larger bubble growth. Larger bubbles attain higher maximum collapse temperatures, leading to more radical formation. In contrast, at higher frequencies, the number of acoustic antinodes increases, resulting in a greater bubble population and, thus, a higher overall radical yield. Therefore, while radical generation per collapsing bubble is greater at lower frequencies, total radical production often increases at higher frequencies due to larger bubble populations. These opposing trends indicate that each reaction has an optimal operating frequency, which depends on both the chemical system and the reactor design.

Acoustic frequency also influences whether physical or chemical effects dominate during the ultrasound irradiation. Low-frequency ultrasound (typically <100 kHz) produces fewer but larger bubbles, favouring physical effects such as cleaning, emulsification, liquid extraction, and mechanical degradation. At higher frequencies (several hundred kilohertz to around 1 MHz), sonochemical effects dominate due to greater yield of radical generation. Applications in this frequency range include chemical synthesis, pollutant degradation, and other sonochemical processes. Many studies have reported optimal frequencies for sonochemistry in the range of 200–500 kHz. However, this typically serves only as a general guideline, as each reaction system operates at a different optimal frequency[22]. At even higher frequencies (2–15 MHz), cavitation activity is significantly reduced, and applications are almost exclusively limited to medical imaging and diagnostics.

**Acoustic pressure**

Acoustic pressure amplitude is proportional to the power driving the ultrasound transducer. For a given frequency, it is often the determining factor for the bubble nucleation threshold. At low acoustic pressure amplitudes below the inertial cavitation threshold, the ultrasonic waves dominate the bubble dynamics; the bubbles simply oscillate in radius around the initial radius. This cavitation activity is

often termed ‘non-inertial cavitation’ or ‘stable cavitation’. At acoustic pressure over the cavitation threshold, increasing acoustic pressure leads to a higher bubble population and larger maximum bubble sizes during expansion. This enhances the intensity of inertial cavitation, resulting in more production of reactive radicals. This effect is often observed in sonochemiluminescence experiments, whereby increasing acoustic power correlates with increased light intensity, irrespective of the type of dosimeter[23].

Acoustic power enhances cavitation activity only up to a certain threshold. Beyond this point, excessive bubble nucleation leads to competition for space, limiting bubble growth and reducing cavitation intensity. Moreover, a high concentration of bubbles scatters incoming acoustic waves and alters the acoustic impedance of the liquid. This scattering effect diminishes the effective propagation of ultrasound, resulting in a lower acoustic pressure amplitude. In severe cases, bubble accumulation on the surface of the transducer may form a barrier layer, decoupling it from the liquid. This separation weakens acoustic coupling and significantly reduces energy transfer from the transducer to the medium.

**Pulse sequence**

Ultrasound may be transmitted either as a continuous wave (CW) or with a pulse sequence. CW is commonly used in sonochemistry because it delivers the maximum acoustic energy output, with the intent to maximise radical production to drive chemical reactions. However, this rather simple interpretation ignores the fact that persisting bubbles in an ultrasound field undergo rectified diffusion. These steadily growing gassy bubbles tend to resist inertial collapse. Larger bubbles are prone to agglomeration and coalescence, subsequently becoming buoyant and rising to the liquid’s surface. This degassing effect reduces the likelihood of further bubble nucleation. These larger bubbles also significantly attenuate the soundwave. Combining these effects, CW ultrasound may not be the optimal strategy for maximum radical generation.

Pulsed ultrasound may overcome the issues with CW ultrasound. By providing time between ultrasound bursts, persisting bubbles may dissolve back into the liquid, allowing reuse of seed bubble for nucleation in the next cycles[24]. Thus, pulsed ultrasound likely reduces bubble coalescence, bubble degassing, and wavefield attenuation, ensuring the unshielded transmission of ultrasound compared to CW mode[25]. Pulsed ultrasound may also slow down the liquid temperature increase by allowing heat to transfer from the vessel between pulses[26]. Furthermore, previous literature suggests that the

intervals between the pulses also give time for chemicals in the reaction solution to diffuse to bubbles. The proximity of the chemical species and inertial cavitation leads to higher sonochemical activity[27,28].

**Temperature**

Temperature plays a crucial role in sonochemistry. Increasing the solution temperature above the ambient temperature counter-intuitively decreases the rate of sonochemical reactions, unlike virtually all other chemical reactions. An increase in bulk solution temperature raises the vapour pressure inside the bubble, cushioning the implosion of the cavity and lowering the temperature of the implosion. Additionally, increasing temperature decreases the gas solubility in the liquid. As a result, this limits the number of available cavitation nuclei. Nevertheless, lower temperatures are not always favourable for higher reaction rates: higher temperature may promote the reaction kinetics by conventional mechanisms. This results in an optimum temperature for sonochemical reactions.

**Dissolved gas**

The presence of pre-dissolved gas bubbles in the liquid medium facilitates cavitation by promoting the nucleation of cavitation bubbles, while degassing the liquid suppresses nucleation and significantly reduces the sonochemical yield. Continuously bubbling gas into the medium helps sustain cavitation by maintaining a consistent supply of nucleation sites[29].

The composition of the dissolved gas strongly influences sonochemical activity and radical production. Among various gases, argon has been reported to generate higher temperatures during bubble collapse compared to gases such as $CO_2$, $N_2$, or air, resulting in more intense implosions and enhanced radical formation[29]. This enhanced performance is attributed to two key physical properties of argon. Firstly, monatomic gases such as argon typically have a higher adiabatic ratio ($\gamma = C_p/C_v$) than polyatomic gases. A higher $\gamma$ indicates that during compression (such as the collapse of cavitation bubbles), a greater proportion of energy is converted into temperature rather than stored as internal energy, which in gases refers to molecular motions including rotation and vibration. For example, argon has a $\gamma$ of 1.7, whereas nitrogen, air, and oxygen have values of 1.4, assuming the same initial temperature and bubble radius[30]. This leads to argon having a higher maximum temperature during bubble collapse than other gases, enhancing the sonochemical activity. Secondly, argon has a lower thermal conductivity ($\lambda$), which reduces heat dissipation from the collapsing bubble to the surrounding liquid. This allows thermal energy to be retained more effectively inside the bubble,

further increasing the implosion temperature. For instance, argon's thermal conductivity is 0.018 $Wm^{-1}K^{-1}$, compared to 0.026 $Wm^{-1}K^{-1}$ for oxygen, nitrogen, and air[31].

Notably, some polyatomic gases, such as oxygen, may also enhance radical generation through pyrolytic dissociation within the collapsing bubble. This mechanism partially compensates for the lower hotspot temperature caused by their lower $\gamma$ and higher $\lambda$. However, this effect becomes significant only at ultrasonic frequencies below 515 kHz[31]. At such frequencies, oxygen may outperform argon in promoting sonochemical activity. Since the frequencies used in this research are all above 515 kHz, this mechanism is not applicable, and argon remains the most effective dissolved gas for enhancing sonochemical reactions in this study.

**Presence of cavitation nuclei**

Exogenous cavitation nuclei, such as dispersed solid particles like powders and nanoparticles, enhance the rate of sonochemical reactions. For this effect to occur, the surface of these particles requires cavities or roughness that trap gas nuclei. These surface bubbles lower the nucleation threshold for inertial cavitation as the trapped gas nuclei act as pre-existing weak points within the liquid, requiring less energy input (lower acoustic pressure) to initiate bubble formation and subsequent inertial collapse, compared to homogeneous nucleation in a pure liquid. Furthermore, the inertial cavitation events usually occur near the solid particles. If these solids function as a heterogeneous catalyst, the inertial collapse may induce the activation or generation of catalytic sites, thereby facilitating chemical reactions[32]. The sonocatalytic reaction is sensitive to the type (particle size and surface area) and the quantity of the catalyst used. On the other hand, an over-concentration of solid particle suspensions may lead to attenuation of the wave field via wave scattering. Therefore, there is a fine balance in the concentration of sonocatalysts used in sonochemical reactions.

## 2.3. Sonochemical reactors

Acoustic cavitation has numerous applications, resulting in diverse ultrasonic reactor designs. This review briefly covers transducers, followed by a discussion of the three main conventional reactor designs employed in sonochemistry.

**Ultrasonic transducers**

A transducer is a device that converts electric energy into mechanical displacement or vice versa. In general, transducers are constructed from piezoelectric materials driven by a signal generator and a power amplifier. Piezoelectric materials respond to an alternating electric field by changing their shape: a transducer expands or contracts as the applied voltage polarity changes (i.e., switches between positive and negative voltage relative to the reference potential), leading to the mechanical pressure waves being transmitted to the surrounding liquid medium. The piezoelectric effect also results in the generation of small electric potentials across the transducer when its shape is distorted by external forces. Ultrasound transducer design is therefore crucial in the effective generation and transmission of ultrasound waves.

### 2.3.1. Sonochemical reactor design

Generally, there are two main types of reactor designs: (1) direct sonication from the transducer to the reaction solution, such as horn and plate reactors and (2) indirect sonication where the reaction vessel is immersed in the liquid medium under unfocused or focused ultrasonic irradiation, such as ultrasonic bath and plate reactors. A schematic of these reactor types is shown in Figure 2.1. Furthermore, it is common to have a temperature regulation system such as jacketed reactors or Rosett cells, since a high liquid temperature has a negative impact on cavitation intensity.

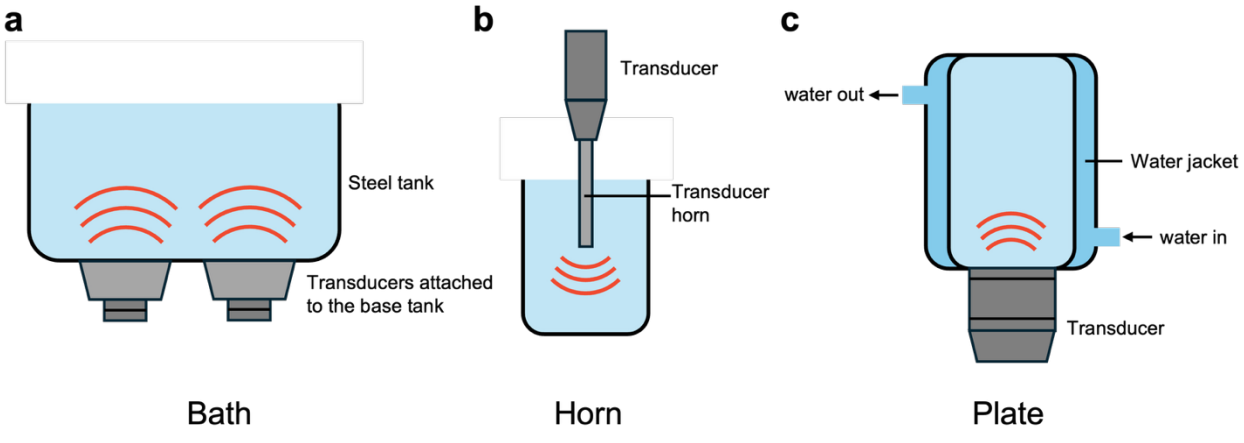



**Figure 2.1.** Diagram of ultrasonic **(a)** bath reactor, **(b)** horn reactor, and **(c)** plate reactor.

### Ultrasonic bath reactor

Ultrasonic baths are stainless-steel tanks, generally equipped with ultrasonic transducers at the bottom or on the wall of the tank. The reactors usually have a temperature control system to maintain the liquid temperature during extended operation over several hours. The operation of ultrasonic baths typically has only a limited number of adjustable settings. For most ultrasonic baths, the frequency of the transducers is fixed by the manufacturer in a low frequency range between 20–40 kHz. At these frequencies, physical effects tend to dominate. Therefore, ultrasonic baths are mostly used for cleaning purposes or breaking up aggregated particles in liquids. The chemical effects of ultrasonic baths are often overlooked by most chemists, and they are generally not regarded as sonochemical reactors.

### Horn reactor

Immersed ultrasound horn reactors are used for direct sonication of a liquid. An ultrasound horn consists of a metal rod attached to the end of a transducer, typically operated at 20–60 kHz. As a sonochemical reactor, the metal rod is immersed in the reaction solution to deliver ultrasonic pressure directly, while the transducer is kept clean from the reaction medium. The metal horn (or horn tip) is often replaceable when contamination or erosion occurs. Horn reactors are operated at high intensities of ultrasonic power and are used widely in sonochemical studies. Typical applications of ultrasonic horn systems include food processing, nanomaterial synthesis, and degradation of organic contaminations.

### Plate reactor

An ultrasonic plate reactor consists of a planar transducer flanged or clamped directly at the bottom of a reaction vessel. Ultrasonic waves propagate through the medium from the transducer at the bottom to the top of the reactor. When mounted to a reaction vessel, the system may incorporate a cooling jacket to control reaction temperature. This reactor may be used as a direct or indirect sonochemical reactor, and the energy intensity is often much higher compared to ultrasonic baths. It has been reported to be used for the extraction of trace metals from complex matrices and in harsh environments such as concentrated acids or hydrofluoric acid, which easily degrade an immersed horn[33,34].

On the other hand, a cup-horn reactor, although it may appear similar to a plate reactor, consists of a high-intensity, wide-base horn transducer immersed in an inverted position within a coupling vessel. Sample vials are usually placed indirectly in the liquid medium, which serves as an acoustic coupling and cooling medium. This configuration enables the transmission of localised and high-intensity acoustic energy up to 50 times greater than a conventional ultrasonic bath system[35]. The key distinction between a cup-horn reactor and plate reactor is that a cup-horn reactor concentrates acoustic energy through a localised resonant horn geometry, while a plate reactor utilises a flat planar transducer to generate a spatially distributed acoustic field across the base of the vessel[35,36].

**Drawbacks of the conventional sonochemical reactors**

In most direct sonication sonochemical reactors, the acoustic wavefields are dispersed throughout the reaction solution, resulting in low acoustic pressure. This limits the bubble population and consequently reduces sonochemical activity. Additionally, the direct coupling between the ultrasonic source and the reaction liquid often constrains the amount of power transmitted. This limitation is designed to prevent excessive input ultrasonic power, which may generate a high density of bubbles, leading to acoustic shielding and eventual decoupling of the transducer from the liquid. In horn-type reactors, the metallic horn is immersed directly into reactive media and is prone to chemical degradation over time, leading to recurring maintenance costs. In contrast, indirect sonochemical reactors typically deliver lower acoustic intensity to the reaction mixture, as most of the energy is attenuated by the coupling liquid. Furthermore, the acoustic pressure experienced by the reaction solution depends strongly on the precise positioning of the reaction vessel. Small deviations in vessel placement significantly affect power transmission and sonochemical efficiency. However, achieving consistent and precise positioning across multiple experiments is often challenging and non-trivial.

## 2.4. Characterisation for sonochemical reactors

Acoustic fields are generally easily determined, yet acoustic cavitation is a dynamic process that is heterogeneous in nature and difficult to define. Quantifying cavitation in a sonochemical reactor is crucial for optimising operating parameters and improving reactor design. Here is a brief overview of various physical and chemical characterisation methods for sonochemical reactors.

### 2.4.1. Physical methods

#### Hydrophone measurements

Hydrophones are commonly used to measure the distribution of acoustic pressure fields by converting pressure fluctuations in a fluid into electric signals. There are two main types of hydrophones: piezoelectric needle hydrophones and fibre-optic hydrophones[37]. Piezoelectric needle hydrophones contain a pressure-sensitive material (commonly piezo-ceramic or piezo-polymer) on the top of the probe that deforms in response to acoustic pressure waves. This deformation generates an electric signal proportional to the pressure fluctuation, which is then transmitted for analysis. Although piezoelectric hydrophones offer high sensitivity, they are susceptible to damage under the intense pressures generated during bubble implosions. As a result, measurements are typically performed under low acoustic power settings, and the voltage-pressure relationship is extrapolated linearly.

On the other hand, fibre-optic hydrophones are more robust and may better withstand the mechanical effects of cavitation at lower acoustic pressures. These devices detect acoustic pressure fluctuations by measuring light modulation, such as its phase, intensity, polarisation, or wavelength[38,39]. However, they are generally more expensive than piezoelectric hydrophones and exhibit lower sensitivity to acoustic pressure fields. In practice, neither type is commonly used for direct cavitation measurements, due to the need for immersion in the liquid phase and the high cost of replacing these sensitive instruments.

#### Input electric energy

The input electrical energy is the energy required to drive a sonochemical reactor. The electrical power supplied to the transducer is calculated from the input voltage, current, and phase angle, as shown in Eq. 2.1. In pulsed operation, the maximum power ($P_{max}$) is defined as the peak electrical power output delivered during the 'on' state (the pulse time), determined before any duty cycle is applied. The nominal power ($P_{nom}$) is the time-averaged power delivered over the entire burst period, as shown in Eq. 2.2. The pulse time, which is defined as the duration of the 'on' signal, is calculated based on the number of cycles and the operating frequency in Eq. 2.3. The number of cycles is defined as the number of complete oscillations contained within a single ‘on’ pulse. The total duration of one complete cycle, including both the 'on' and 'off' intervals, is defined as the burst period. The duty cycle (DC) represents the fraction of the burst period during which the signal is active, expressed as a percentage of the pulse time to burst period ratio, as given in Eq. 2.4.

$$P = I_{rms} V_{rms} \cos(\theta) \quad \text{(Eq. 2.1)}$$

$$P_{nom} = (P_{max})(DC) \quad \text{(Eq. 2.2)}$$

$$\text{Pulse time (s)} = \frac{\text{Number of cycles}}{\text{frequency (Hz)}} \quad \text{(Eq. 2.3)}$$

$$\text{Duty cycle (DC)(\%)} = \frac{\text{Pulse time (s)}}{\text{Burst period (s)}} \quad \text{(Eq. 2.4)}$$

where P is the power, $I_{rms}$ is the root mean square (RMS) current, $V_{rms}$ is the RMS voltage, θ is the phase angle, $P_{nom}$ is the nominal power, $P_{max}$ is the maximum power, and DC is the duty cycle. Here, this electric power represents the total energy supplied to the reactor including the 'useful' ultrasonic energy triggering cavitation implosion as well as the 'wasted' heat energy from the attenuation of the ultrasonic waves into the liquid medium and power losses during transmission.

**Calorimetry**

Calorimetry is a conventional way to define the input ultrasonic power[40,41]. As ultrasonic waves propagate through a liquid, part of the energy is absorbed by the liquid as heat. Measuring the change in the bulk temperature of the liquid medium provides information about the total amount of heat entering the reactor due to attenuation. The equation to calculate the calorimetric power is shown in Eq. 2.5:

$$P = \left(\frac{dT}{dt}\right)(c_p)(M) \quad \text{(Eq. 2.5)}$$

where $\left(\frac{dT}{dt}\right)$ is the temperature change per unit time, $c_p$ is the heat capacity of solvent (4200 J $kg^{-1}$ for water), and M is the mass of solvent used. It assumes that all ultrasonic energy is converted to heat and absorbed by the reaction solution without accounting for the heat loss to the surroundings. As such, Eq. 2.5 likely underestimates the energy used in the reactor.

### 2.4.2. Chemical methods

Chemical dosimetry is used to quantify highly reactive free radicals generated from water sonolysis during inertial collapse of cavitation bubbles. In particular, this collapse splits water vapour into hydrogen atoms (H•) and hydroxyl radicals (•OH), as shown in Eq. 2.6. It has been demonstrated that •OH radicals dominate over H• due to a secondary reaction with water vapour in the gas phase (Eq. 2.7). Although this reaction is endothermic, because of the extremely high temperatures reached

during cavitation implosion combined with the excess water molecules relative to H• radicals inside the bubble, a considerable portion of H• may convert to •OH[42]. Moreover, hydroxyl radicals are strong oxidising agents and play a key role in initiating subsequent, targeted chemical reactions. As a result, most dosimetry methods focus on quantifying •OH radicals. When •OH reacts with a chemical dosimeter, the resulting product may be detected using spectroscopic techniques such as UV-vis spectrometry or fluorometry, allowing the determination of •OH concentration. Conventionally, •OH generation is linearly correlated with sonochemical efficiency, and is commonly assessed using one of three standard dosimetry methods: the Weissler reaction, Fricke dosimetry, and terephthalic acid assay[6].

$$H_2O \xrightarrow{)))} H\cdot + \cdot OH \qquad \text{(Eq. 2.6)}$$

$$H\cdot + H_2O \rightarrow H_2 + \cdot OH \qquad \text{(Eq. 2.7)}$$

**Weissler reaction**

The oxidation of iodine has been used to test the sonochemical effect since its discovery by Weissler et al. in 1950[43]. In Weissler dosimetry, the oxidation of potassium iodide (KI) is used to estimate the hydroxyl radical yield by quantifying the amount of $H_2O_2$ produced during the sonication of water (Eq. 2.6). This method assumes that all •OH radicals recombine to form $H_2O_2$ (Eq. 2.8). The $H_2O_2$ then oxidises iodide ion ($I^-$) to form molecular iodine ($I_2$) (Eq. 2.9), which subsequently reacts with an excess of $I^-$ to form triiodide complex anion* ($I_3^-$), which is detectable by UV-vis spectrometry (Eq. 2.10). However, the Weissler reaction has its limitations. The assumption that all chemically active •OH radicals recombine to form $H_2O_2$ may not be accurate[44]. Merouani et al. have proposed 12 possible chemical pathways involving •OH within a collapsing cavitation bubble[45]. Additionally, $H_2O_2$ may be generated via other reactive oxygen species (ROS) such as singlet oxygen ($^1O_2$) and superoxide ($O_2^-$).

$$2\cdot OH \rightarrow H_2O_2 \qquad \text{(Eq. 2.8)}$$

$$H_2O_2 + 2I^- \rightarrow I_2 + 2OH^- \qquad \text{(Eq. 2.9)}$$

$$I_2 + I^- \rightarrow I_3^- \qquad \text{(Eq. 2.10)}$$

* $I_3^-$ is measured by UV-vis spectroscopy at 350 nm ($\varepsilon = 26400\ M^{-1}\ cm^{-1}$).

**Fricke reaction**

Fricke reaction is based on the oxidation reaction of $Fe^{2+}$ to $Fe^{3+}$ activated by hydroxyl radicals. The concentration of $Fe^{3+}$ ions is measured by UV-vis spectrometry[†]. The Fricke reaction depends on the oxidation of ferrous ($Fe^{2+}$) to UV-vis active ferric ($Fe^{3+}$) by the •OH (Eq. 2.11) generated in the sonolysis of water. Sulphuric acid ($H_2SO_4$) is added to supply the protons and prevent the oxidation of ferrous by oxygen in air. However, the Fricke reaction has its limitation. $Fe^{2+}$ is not selective to •OH and may also react with $H_2O_2$ (Eq. 2.12).

While this reaction may decompose $H_2O_2$ and regenerate •OH, enabling continued oxidation of $Fe^{2+}$, it does not exclusively reflect the concentration of free •OH radicals generated originally from water sonolysis. Again, $H_2O_2$ may be generated via other ROS as mentioned, reducing the specificity of the Fricke method for •OH quantification. Furthermore, the H• may be scavenged by dissolved oxygen ($O_2$) (Eq. 2.13). At lower pH, $Fe^{2+}$ may also be oxidised by hydroperoxyl radicals ($HO_2$•), forming $H_2O_2$ which then reacts with $Fe^{2+}$ to regenerate •OH radical (Eq. 2.14)[6]. These side reactions complicate the interpretation of results and limit Fricke dosimetry's reliability as a selective measure of chemically active •OH.

$$\cdot OH + Fe^{2+} + H^+ \rightarrow Fe^{3+} + H_2O \quad \text{(Eq. 2.11)}$$

$$H_2O_2 + Fe^{2+} + H^+ \rightarrow Fe^{3+} + H_2O + \cdot OH \quad \text{(Eq. 2.12)}$$

$$H\cdot + O_2 \rightarrow HO_2\cdot \quad \text{(Eq. 2.13)}$$

$$HO_2\cdot + Fe^{2+} + H^+ \rightarrow H_2O_2 + Fe^{3+} \quad \text{(Eq. 2.14)}$$

**Terephthalic acid assay**

In terephthalic acid assays, non-fluorescent terephthalic acid (TA) reacts with •OH to form fluorescent 2-hydroxylterephthalic acid (HTA) as illustrated in Figure 2.2. Although the TA assay offers good selectivity for •OH detection, it suffers from several limitations. TA has low solubility in aqueous media and is highly sensitive to pH, which may affect the assay performance[46]. Additionally, intermediates formed during the reaction may further react with dissolved oxygen, leading to the formation of undesired side products[42].

[†] $Fe^{3+}$ is measured by UV-vis spectroscopy at 304 nm ($\varepsilon = 2197\ M^{-1}\ cm^{-1}$).

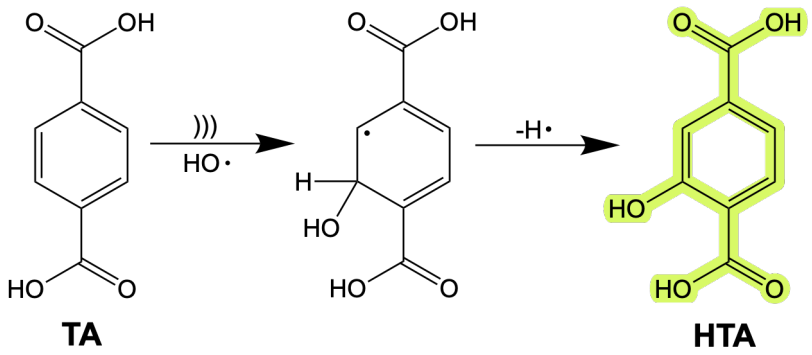



**Figure 2.2.** Reaction of non-fluorescent TA with hydroxyl radicals yielding fluorescent HTA.

In general, chemical dosimetry is a simple, effective way to measure the sonochemical effect of cavitation activity. However, dosimetry only provides a global quantification of the hydroxyl radical production in the reaction vial and is not sensitive to the contribution of individual bubbles collapse. Furthermore, it has been reported that only approximately 20% of the generated radical species diffuse into the surrounding bulk liquid, where they contribute to measurable sonochemical reactions. The remaining 80% of these reactive radicals undergo rapid recombination within the collapsing bubbles, forming stable molecules and therefore are not detected by standard dosimetric methods[6].

### 2.4.3. Sonochemical efficiency

A definition for sonochemical efficiency (SE) is based on the generated •OH concentration per unit input energy of the reactor, as shown in Eq. 2.15.

$$SE = \frac{c}{E} = \frac{c}{(P)(t)(DC)} \qquad \text{(Eq. 2.15)}$$

where c is the concentration of •OH in the reaction vessels, E is the input energy in the sonochemical reactor, P is the input power, t is the reaction time and DC is the duty cycle calculated from Eq. 2.4. There is another way to interpret sonochemical efficiency based on the mole of •OH generated per unit input energy in the reactor. This equation is shown in Eq. 2.16.

$$SE = \frac{n}{E} = \frac{(c)(V)}{(P)(t)(DC)} \qquad \text{(Eq. 2.16)}$$

where n is the number of moles of •OH and V is the total reaction volume in the reaction vessel.

Here sonochemical efficiency is defined as the number of reacted molecules or the concentration of reacted molecules in the reaction solution per unit of input energy. Koda et al.[47], Mark et al.[42], and

Kojima et al.[48] have employed similar SE definitions in their studies. As discussed, the input energy may be determined in two ways: (1) input electric energy and (2) the calorimetric energy. The input electric energy represents the total energy supplied for the system. This representation compares the efficiency of different devices for a desired reaction and is unrestricted by the reactor configuration or the position of the reaction vessels[49]. On the other hand, the calorimetric energy is a common way to represent the acoustic energy absorbed into the system. However, as supported by Koda et al., heat generated in the calorimetric measurement is a 'wasted energy' rather than the effective acoustic energy driving sonochemical reactions[47]. However, it remains the most widely used parameter for estimating acoustic energy provided in the field.

## 2.5. Sonochemical hydrogen production

Hydrogen is a pivotal energy vector in the transition towards a net-zero world by 2050. As a versatile chemical, it is used as fuel and feedstock directly in transportation and industrial sectors, or indirectly as an energy vector for electricity generation. Additionally, when hydrogen is combusted, it releases heat and may be supplied for residential or commercial purposes, yielding only water as a by-product. By developing technologies for water splitting using renewable energy to produce hydrogen, the implementation of a circular hydrogen economy becomes feasible[50,51]. As illustrated in Figure 2.3, this process involves the sustainable production of hydrogen and its integration into various applications, forming a circular economy that supports green energy transition.

### 2.5.1. Conventional green hydrogen production from seawater splitting

**Seawater electrolysis**

Direct seawater electrolysis has attracted significant interest as a technology for hydrogen evolution because of the abundant availability of seawater[52,53]. Seawater electrolysis works by splitting water molecules in seawater into hydrogen and oxygen gases using an electric current. At the cathode, hydrogen ions are reduced to form hydrogen gas, while at the anode, water molecules are oxidised to produce oxygen gas. However, several major technological challenges are hindering the full adoption of the technology. First, the electrode surface of conventional electrolysers is composed of noble-based materials, including platinum and iridium[54,55], which act as catalyst. These noble metals are scarce and expensive, making the infrastructure of industrial-scale electrolysers economically unsustainable. Moreover, the complex composition of seawater leads to unwanted side reactions at the electrode surfaces. Organic compounds naturally present in seawater facilitate the growth of

biofilms and biofouling layers. These biological deposits act as insulating barriers that physically hinder electron transfer between the electrode and the electrolyte. Simultaneously, dissolved inorganic metal ions in seawater precipitate on the electrode surfaces as insoluble salts, adding an additional layer of physical blockage. Together, biofouling and inorganic scaling significantly reduce the number of active catalytic sites on the electrodes, decreasing the overall electrolysis efficiency and accelerating the rate of electrode corrosion. This ultimately leads to more frequent and costly electrode replacement and system maintenance. Furthermore, the high chloride ion concentration in seawater promotes the formation of toxic chlorine gas and contributes to catalyst poisoning[56]. This further shortens the electrolyser lifespan.

**Photocatalytic seawater splitting**

As an alternative water splitting technique, photocatalytic seawater splitting has also attracted widespread attention as a sustainable method for hydrogen production. Photocatalytic seawater splitting uses solar energy and a photocatalyst to break down seawater into hydrogen and oxygen gases. When light with energy greater than the photocatalyst's bandgap irradiates its surface, it generates electron-hole pairs; these charge carriers migrate to the catalyst's surface, where electrons reduce water to hydrogen, and holes oxidize water to oxygen. Advanced catalysts and elevated temperatures are often used to overcome challenges like ionic interference in seawater environments. However, the current process still suffers from poor quantum efficiency and stability of photocatalysts in a salty environment[57].

### 2.5.2. Mechanisms of sonochemical hydrogen production

The mechanism of sonochemical hydrogen production is not yet fully understood. As previously discussed, acoustic cavitation generates extreme conditions during bubble collapse, leading to the decomposition of water molecules by ultrasonic energy, or sonolysis. The water molecules undergo dissociation to form reactive radical species such as H•, •OH, and $HO_2$•. A fraction of these radicals recombines to produce molecular hydrogen.

A kinetic model involving 25 reversible reactions has been proposed to study the complex chemistry occurring inside a collapsing bubble[58]. The number of possible chemical reactions inside a collapsing bubble and the short lifetime of these reactive radicals show that bubble chemistry is highly intricate and complex. To date, no experimental technique has definitively identified the exact mechanism of hydrogen formation within the bubble. Some studies have suggested that hydrogen is primarily

formed at the bubble-liquid interface, where hydrogen radicals diffuse out of the bubble and recombine to form hydrogen (Eq. 2.17)[59,60]. In contrast, Merouani et al. proposed that over 99% of hydrogen is generated within the gas phase of the bubble through reactions between hydrogen and hydroxyl radicals (Eq. 2.18), followed by diffusion of molecular hydrogen into the surrounding liquid[58]. This pathway, supported by numerical simulations, indicates that hydrogen radical recombination at the interface plays only a minor role in sonochemical hydrogen production. While experimental validation remains limited, the model of Merouani et al. is currently regarded as the more plausible mechanism until improved simulations or direct measurements become available.

$$H\cdot + H\cdot \leftrightarrow H_2 \qquad \text{(Eq. 2.17)}$$

$$H\cdot + \cdot OH \leftrightarrow H_2{+}O \qquad \text{(Eq. 2.18)}$$

Furthermore, hydroxyl radicals may also recombine to form hydrogen peroxide, which accumulates in the solution as inertial cavitation proceeds (Eq. 2.19)[61,62]. While hydrogen peroxide formation is an important reaction in some sonochemical systems, it is not a focus in this literature review as this research focuses specifically on hydrogen production rather than peroxide chemistry.

$$\cdot OH + \cdot OH \leftrightarrow H_2O_2 \qquad \text{(Eq. 2.19)}$$

### 2.5.3. Existing sonochemical hydrogen production work in the literature

Sonolysis offers numerous advantages compared to electrolysis and photocatalysis. First, sonolysis is not a surface-driven reaction as compared to electrolysis, allowing for volumetric scaling. This further prevents instrumental corrosion such as biofouling and deposition[34]. Sonolysis also operates at room temperature, providing a more energy- and cost-effective approach as compared to some thermal-assisted photocatalytic hydrogen production, which typically operates at 100–300 °C[63,64]. Moreover, sonolysis has been shown to achieve higher hydrogen production rates than some other emerging technologies. For example, Gentili et al. and Penconi et al. demonstrated that sonolysis of water/ethanol solutions yielded hydrogen production rates 100 to 200 times higher than those of photocatalysis, in terms of μmol/h[65,66].

Sonochemical hydrogen production has the potential to serve as a green hydrogen production pathway if integrated with renewable energy sources such as solar or wind power. Despite the potential, this research area is still at its nascent stage with a limited number of works demonstrating the concept. Rashwan et al. conducted a comprehensive review discussing the challenges and opportunities of

sonohydrogen production ahead[67]. However, little has been done to explore the most effective acoustic and catalytic conditions[10,68-70]. To the best of current knowledge, only two works have reported sonochemical hydrogen production from seawater with an efficiency of 10.3 $g_{cat}^{-1}$ $L^{-1}$ $Whr^{-1}$ (Qi et al.[68]) and 3.0 µmol $g_{cat}^{-1}$ $L^{-1}$ $Whr^{-1}$ (Harada et al.[69]), respectively. Furthermore, most of the reported sonochemical catalysts involve complex, costly, and energy intensive synthesis processes, which are difficult to scale in industrial processes. A few examples include $Au/TiO_2$, $La_{2x}Ga_{2y}In_{2(1-x-y)}O_3$, and $Co_4N$ nanowires with N-defects[65,71,72]. A summary of previous studies on sonochemical hydrogen production, including acoustic parameters, chemical conditions, catalysts used, and sonochemical efficiencies, is presented in Chapter 4. The summary is presented alongside the results of this study for direct and meaningful comparison.

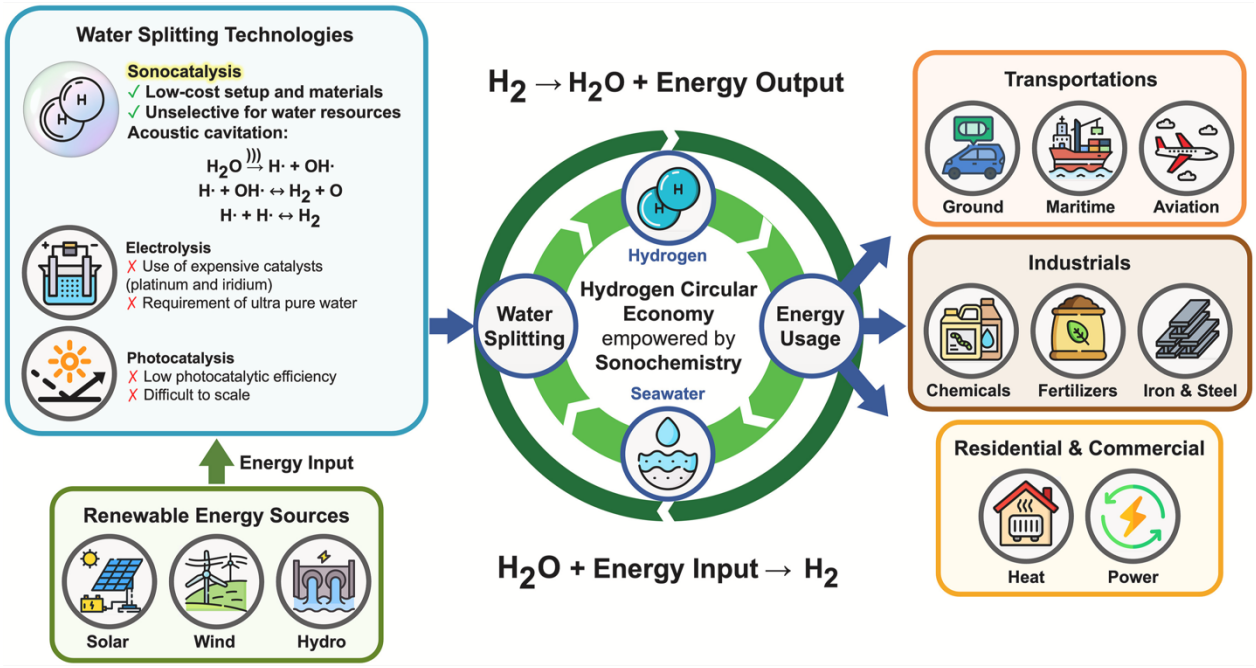



**Figure 2.3.** Hydrogen circular economy enabled by sonochemistry, presented as an alternative hydrogen production technology. The technology is compared with water electrolysis and photocatalysis, which are widely studied technologies for clean hydrogen production.

### 2.5.4. Metal oxide sonocatalysts for sonochemical hydrogen production

Sonocatalysts are often introduced into a sonochemical system to enhance sonochemical activities[73]. Metal oxides have emerged as particularly promising catalysts for sonochemical hydrogen production because they offer high activity, relatively low cost, and robust stability under extreme local conditions such as high temperature and pressure[74-76]. Previous studies have shown that metal oxides such as $TiO_2$, $ThO_2$, and $ZrO_2$ enhance sonochemical hydrogen production by promoting microbubble nucleation and facilitating the transfer of reactive radicals into the liquid bulk during bubble

collapse[71,77,78]. However, current research has largely focused on a narrow set of metal oxides, leaving the potential of many less conventional oxides underexplored. This limited scope constrains the optimisation and further development of sonocatalytic processes for hydrogen production. To address this knowledge gap, the study in Chapter 5 examined a broader range of metal oxides and the influence of metal doping on hydrogen production under ultrasound irradiation.

### 2.5.5. Quantification of hydrogen and gases

It is essential to employ a reliable method for quantifying hydrogen production from sonochemical reactions. Gas chromatography (GC) is a widely used analytical technique for identifying and quantifying components in gas mixtures. It works by injecting a sample into a carrier gas, which transports the sample through a column containing a stationary phase. As the sample moves through the column, its components interact differently with the stationary phase based on their physical and chemical properties, leading to separation. As a result, each compound exits the column at a different retention time, which is recorded as peaks on a chromatogram. The concentration of each compound is then determined by comparing the integrated area of its peak to that of calibration standards. Ideally, seven calibration standards have been recommended to achieve reliable linear regression, but due to the high cost of calibration gases, using three points is generally considered acceptable in most cases.

Detectors play a crucial role in GC by identifying and quantifying the separated compounds as they elute from the column. There are various types of detectors, broadly categorised into destructive and non-destructive types. Destructive detectors, such as flame ionisation detectors (FID), combust the sample in a hydrogen-air flame to measure ionised particles, making them highly sensitive for organic compounds but unsuitable for inorganic gases like hydrogen. Non-destructive detectors, such as thermal conductivity detectors (TCD), measure changes in thermal conductivity and are universal but less sensitive than FID. Among all detectors, the dielectric-barrier discharge ionisation detector (BID), as a proprietary technology of Shimadzu, stands out as one of the most advanced options in the market. BID uses helium plasma to generate high-energy photons that ionise nearly all compounds except helium and neon. This universal detection capability makes BID ideal for hydrogen analysis and other gases. BID offers exceptional sensitivity with detection limits below 0.1 ppm, far surpassing TCD in performance, which is only in the 10-ppm range. As a universal detector, BID was a superior option to detect and quantify hydrogen and other gases at low concentrations in this research.

## 2.6. Sonochemical biomass gasification for syngas production

The previous section examined sonochemical hydrogen production from water and seawater splitting, demonstrating the potential of sonochemistry for green hydrogen generation using relatively simple feedstocks and well-controlled systems. This research extends the application of sonochemistry with more complex feedstocks. Biomass, a renewable, carbon-neutral, and abundant natural feedstock, has attracted increasing attention for its effective utilisation as the global community continues to seek methods for reducing carbon emission. Among the various conversion technologies, biomass gasification is an established method for converting biomass into valuable chemicals. Building on the previous findings from the studies on sonochemical hydrogen production, Section 2.6.1 to Section 2.6.5 explore the potential of ultrasound-assisted biomass gasification as a sustainable alternative to conventional thermochemical processes.

### 2.6.1. Thermochemical biomass gasification system

Syngas is a highly versatile industrial feedstock used directly as a fuel or as an intermediate to produce synthetic fuels and value-added chemicals. It is a mixture mainly composed of CO, $H_2$, $CO_2$, and $CH_4$. While combustion primarily generates heat and pyrolysis yields liquid bio-oil and solid biochar, gasification offers a highly efficient thermochemical pathway for producing syngas from biomass[79,80]. This performance is characterised by its high cold gas efficiency, defined as the percentage of the chemical energy contained in the product syngas to the chemical energy of the feedstock biomass[81]. Depending on the biomass feedstock, reactor design, and operating conditions, gasification typically achieves cold gas efficiencies of 63-66%, with syngas being the primary product[79,82].

The gasification process involves the partial oxidisation of biomass components, such as carbohydrates, proteins, and lipids, to produce syngas[83]. The gasification process comprises several key stages: drying, pyrolysis, combustion (oxidation), and reduction[84,85]. In the drying stage, moisture is removed through the endothermic evaporation of water and other low-boiling-point compounds, typically occurring between 100 and 150 °C. This step prepares the biomass for subsequent thermal decomposition. During pyrolysis, the biomass undergoes thermochemical breakdown in an oxygen-deficient environment at temperatures ranging from 200 to 500 °C[86]. This produces volatile gases such as $H_2$, CO, $CO_2$, and light hydrocarbons, along with condensable liquids like tar and oil, and solid residues including char. The gasification stage, also referred to as the oxidation zone, involves the introduction of a gasifying agent (e.g. air, oxygen, or steam) to react with the pyrolysis products at elevated temperatures, typically above 650 °C and up to 1200 °C[83]. This exothermic process

supplies the heat necessary for endothermic reactions occurring simultaneously, and its primary purpose is to convert the low-calorific-value compounds from pyrolysis into useful gaseous products. In the final stage, reduction, the remaining solid carbon (or char) reacts with the hot gasifying agents to generate additional gaseous products, including syngas (a mixture primarily of $H_2$ and CO). A summary of the biomass gasification stages is shown in Figure 2.4[83,87].

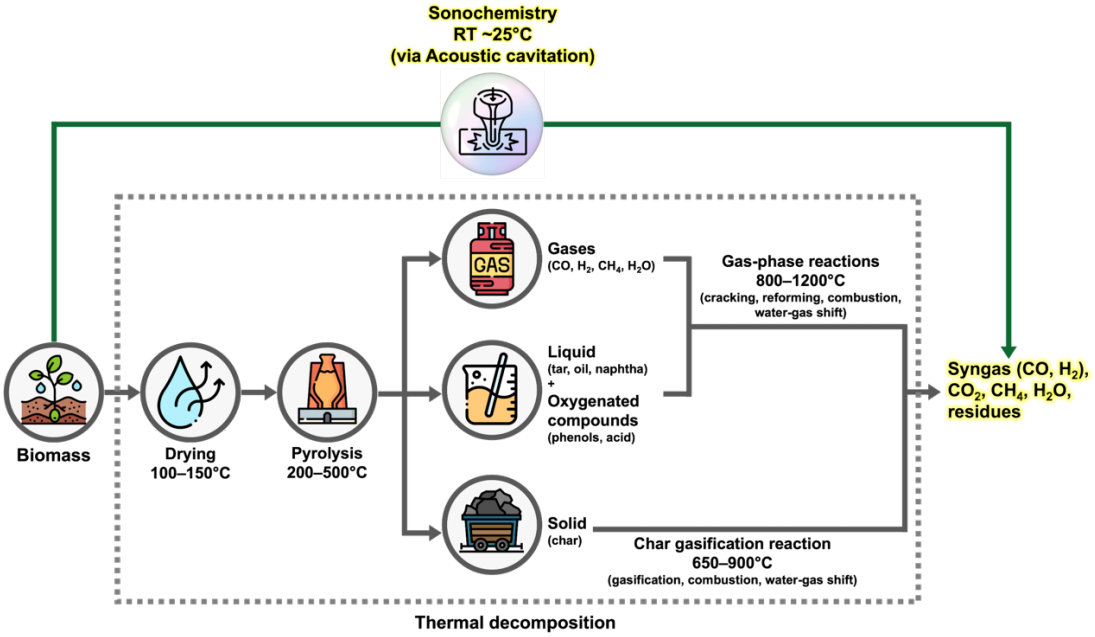



**Figure 2.4.** Schematic comparison of thermochemical biomass gasification stages and the conceptual framework of sonochemical biomass gasification.

Multiple chemical reactions occur simultaneously throughout the process, varying with the stage. These reactions are generally categorised into heterogeneous reactions, in which solid carbon reacts with gaseous reactants to form gases, and homogeneous reactions, where gaseous species react with each other to form syngas. A summary of the biomass gasification mechanisms is provided in Table 2.1.

**Table 2.1.** Main reactions during biomass gasification[88,89].

| Reactions | | $\Delta H^{0}_{298K}$ [kJ mol$^{-1}$] |
|---|---|---|
| **Heterogeneous reactions** | | |
| Water gas | $C(s) + H_2O \rightarrow H_2 + CO$ | +131 |
| Char-steam | $C(s) + 2H_2O \rightarrow CO_2 + 2H_2$ | +90 |
| | $C(s) + H_2O \rightarrow \frac{1}{2}CH_4 + \frac{1}{2}CO_2$ | +8 |
| Boudouard | $C(s) + CO_2 \rightarrow 2CO$ | +173 |
| Methanation | $C(s) + 2H_2 \rightarrow CH_4$ | –75 |
| Partial oxidation | $C(s) + \frac{1}{2}O_2 \rightarrow CO$ | –111 |
| Complete oxidation | $C(s) + O_2 \rightarrow CO_2$ | –394 |
| **Homogenous reactions** | | |
| Water gas shift | $CO + H_2O \rightleftharpoons H_2 + CO_2$ | –41 |
| Steam reforming | $CH_4 + H_2O \rightleftharpoons CO + 3H_2$ | +206 |
| | $CH_4 + 2H_2O \rightleftharpoons CO_2 + 4H_2$ | +165 |
| | $C_nH_m + nH_2O \rightleftharpoons n\,CO + \left(n + \frac{m}{2}\right)H_2$ | Endothermic |
| Dry $CO_2$ reforming | $CH_4 + CO_2 \rightleftharpoons 2CO + 2H_2$ | +247 |
| | $C_nH_m + n\,CO_2 \rightleftharpoons 2n\,CO + \left(\frac{m}{2}\right)H_2$ | Endothermic |
| CO oxidation | $CO + \frac{1}{2}O_2 \rightarrow CO_2$ | –283 |
| $H_2$ oxidation | $H_2 + \frac{1}{2}O_2 \rightarrow H_2O$ | –242 |

### 2.6.2. Factors influencing biomass gasification efficiency

One of the most critical factors influencing biomass gasification is the selection and distribution of gasifying agents, such as air, steam, oxygen, or their combinations. It significantly affects the composition and yield of the product gas. In conventional packed-bed gasifiers, the use of oxygen as a gasifying agent has been shown to enhance the production of hydrogen and carbon monoxide[89,90]. Oxygen supports exothermic oxidation reactions that raise the reactor temperature, which in turn promotes endothermic reforming and cracking reactions. These thermal reactions break down hydrocarbons and tars present in the biomass, resulting in increased syngas yield. Oxygen is also fed with steam as a gasifying agent to overcome the nitrogen dilution of syngas, which occurs when only air is used as the gasifying agent[10].

Temperature is also a key parameter. It determines the extent of gasification reactions and influences the quality of the product gas. Higher temperatures tend to favour thermal cracking of tar and facilitate the yield of endothermic gasification reactions according to Le Chatelier's principle, increasing the syngas and total gas yield[91]. However, increasing the operating temperature also increases energy

consumption and operational costs[92]. Thus, the type of gasifying medium and its associated thermal effects must be carefully balanced to optimise the process efficiency and economic viability.

Additional influencing factors include the reactor type, steam-to-biomass ratio (S/B), and the air equivalence ratio (ER), which is defined as the ratio of actual oxygen supply to the amount required for stoichiometric combustion of the biomass. These parameters directly affect the feed rate of biomass relative to the gasifier's oxidant supply and indirectly influence reactor temperature, pressure, and product gas composition[88]. Biomass properties also play an important role. The relative proportions of cellulose, hemicellulose, and lignin, the primary components of biomass, are particularly relevant, as they decompose at different temperatures and exhibit distinct reaction behaviours[93]. Particle size and biomass structure further influence the gasification process by affecting residence time, reaction kinetics, and the likelihood of entrainment within the reactor.

### 2.6.3. Sonochemical biomass gasification

As discussed in the previous section, conventional thermochemical biomass gasification processes typically require high operating temperatures, reaching up to 1200 °C. These processes also involve energy-intensive pre-drying of the biomass to ensure proper gasifier operation and to improve the quality of the product gas. In contrast, ultrasound-assisted gasification presents a promising alternative. By harnessing acoustic cavitation at room temperature and ambient pressure, this approach eliminates the need for high-temperature processing and enables the direct use of wet or dissolved biomass without prior drying. Moreover, water plays a beneficial role in the sonochemical process, serving as both the transmission medium for ultrasound and a reactant in the gasification reaction. However, this requirement also represents a limitation of sonochemical biomass gasification. The process is currently limited to liquid-phase or highly soluble biomass feedstocks. While most biomass resources are available in solid forms such as wood chips, agricultural residues, and animal manure, water-soluble feedstocks only represent a small fraction of the available biomass[94]. Therefore, although the elimination of thermal drying is a unique advantage of the sonochemical approach, its application is limited by the requirement for a liquid feedstock, an important consideration when comparing it with conventional thermochemical technologies.

Most research on ultrasound-assisted biomass processing has focused on biomass valorisation. Applications include biomass pretreatment, lignin degradation, cellulose conversion, and enhancement of sugar production through biochemical pathways[95-98]. In these studies, ultrasound is

primarily used to improve the efficiency of biomass conversion into biofuels, bioethanol, fine chemicals, and chemical building blocks[99,100].

However, to date, no study has reported the direct production of syngas from liquid biomass using ultrasound, despite an extensive review of the literature. The closest related work is by Chen et al., who demonstrated syngas generation from $CO_2$-saturated water using a sonocatalytic system involving Cu nanoparticles supported on Zn–Al layered double oxides[101]. While related in concept, this approach does not involve liquid biomass as the carbon source. The present study proposes a one-step, ultrasound-driven conversion of liquid biomass directly into syngas. To the best of current knowledge, this represents a novel and original contribution to the literature, aimed at demonstrating the feasibility of this process as an exploratory work for future development.

### 2.6.4. Molasses as a selected biomass for the study

In this project, molasses was used as a proof-of-concept liquid biomass to demonstrate the feasibility of ultrasound-driven gasification for syngas production. Molasses is a by-product of the sugarcane or sugar beets extraction process and is characterised by a high content of sugars and other organic compounds[102,103]. It is a viscous, water-soluble liquid, which makes it particularly suitable for sonochemical studies. The composition of molasses varies depending on the extraction method, age and maturity of the sugar plants, and the geographical origin of the crop. However, it is generally characterised by a total sugar content of approximately 45–55%, typically consisting of 30–35% sucrose and 10–25% glucose and fructose[104].

Given its high sugar content, molasses provides a rich source of carbon-based molecules for gasification. Previous work by Xie et al. demonstrated the sonochemical oxidation of glucose to glucuronic acid under ambient conditions, indicating that sugars such as glucose may undergo chemical reaction under ultrasound[105]. This study may also serve as a reference point for identifying potential reactions occurring in the liquid phase during ultrasound exposure.

As discussed, there is currently limited literature on ultrasound-driven liquid biomass gasification, and even fewer studies have explored the sonochemical gasification of molasses. It is hypothesised that during inertial cavitation, carbon-based molecules in molasses, located either within or near the cavitating bubbles, undergo pyrolysis or gasification due to the extreme temperatures and pressures generated by bubble collapse. These conditions may initiate thermal decomposition of the organic molecules or facilitate reactions with other species, such as water vapour and reactive radicals,

leading to the formation of gaseous products. Despite the extreme localised temperatures during cavitation, the bulk temperature of the solution remains at room temperature and exhibits minimal change throughout the reaction. This operating condition is characteristic of sonochemical processes and contrasts with thermochemical biomass gasification, which requires sustained high temperatures throughout the bulk medium. The concept of sonochemical biomass gasification is illustrated in Figure 2.4.

### 2.6.5. Zeolite catalysts and metal doping for biomass gasification

Catalysts play a critical role in the liquid-phase biomass gasification process. Among them, zeolites are widely used due to their ability to selectively crack large dissolved, biomass-derived molecules and tars into smaller gaseous and liquid products. This is achieved through the physical properties of zeolites, such as their well-defined pore channels and chemical activation by acidic sites[106,107]. Zeolites also offer several advantages, including low cost, excellent thermal stability, resistance to nitrogen- and sulphur-containing compounds, and good regenerability, all of which are beneficial under the high temperature conditions typical of liquid-based biomass gasification. Furthermore, their catalytic properties may be tailored by incorporating various metals or metal oxides[108]. Commonly used microporous zeolites in biomass gasification and catalytic cracking include ZSM5, Y, Beta, and USY, each offering different pore structures, acidities, and surface characteristics that influence reaction selectivity and kinetics[91,108-110].

The acidity of zeolites is closely correlated with their catalytic activity in liquid-phase biomass gasification, particularly in the cracking of large, dissolved biomass-derived molecules and tars. This relationship is explained by the reaction mechanisms involved in catalytic cracking. Acid sites on the zeolite surface facilitate the formation of reactive intermediates, most notably the carbenium ion. There are two types of acidic sites in zeolites: Brønsted acid sites, which are protons attached to bridging hydroxyl groups Si-O(H)-Al and act as proton donors, and Lewis acid sites, which are coordinatively unsaturated metal centres like $Al^{3+}$ that function as electron pair acceptors. Brønsted acid sites on the zeolite surface protonate biomass-derived hydrocarbons to form a carbonium ion intermediate, which is characterised by a three-centre, two-electron bond. This intermediate subsequently undergoes dehydrogenation to generate a carbenium ion[111,112]. Alternatively, Lewis acid sites on zeolite accept a hydride ion directly from the hydrocarbon, also producing a carbenium ion through C-H bond cleavage. Once formed, the carbenium ion may undergo cracking through different reaction pathways. One pathway involves β-scission, in which C-C and C-O bond cleavage yields alkenes[113,114]. In another, the carbenium ion undergoes further hydride shift, followed by protonation

and fragmentation, forming shorter and lighter hydrocarbons (branched or straight-chain)[115]. A higher density of acid sites (or a low Si/Al ratio) on the zeolite enables more frequent activation of these pathways, thereby enhancing cracking activity and increasing the yield of cracked products.

Metal loading on zeolites is a widely employed strategy to enhance the activity and selectivity of catalysts in liquid-phase biomass gasification. Among various metals, nickel-doped zeolites have been extensively studied due to their high catalytic activity in breaking C-H, C-C, and C-O bonds[116]. Buchireddy et al. reported that nickel exhibits strong activity in steam and dry reforming reactions, contributing to the complete removal of tar, if present, and increasing the yields of $H_2$ and CO[108]. There is also a synergistic effect between the nickel metal sites and the zeolite support that promotes more efficient biomass conversion. The effect results from its bifunctional catalytic properties: zeolite provides acidic sites necessary for cracking large molecules into smaller fragments, while nickel facilitates steam reforming reactions and gasifies carbon deposits via reaction with steam to generate syngas. Nickel also suppresses coke formation through hydrogenation to prevent blockage of active sites in zeolite[114,117,118].

However, there are certain limitations with the nickel-zeolite catalyst. At the high temperatures typically encountered during biomass processing, zeolite frameworks may undergo structural collapse, and nickel particles may sinter, both of which reduce active surface area and overall catalytic performance[117]. Moreover, excessive metal loading may block the active sites within the pore structure of zeolites, hindering the catalytic activity in liquid biomass gasification. Therefore, careful selection of zeolite type and optimisation of metal loading are critical for tuning catalyst acidity, hydrogen transfer ability, and thermal stability, thereby achieving effective catalytic performance in biomass gasification[119].

# 3. Design and characterisation of a novel sonoreactor ('SonoCYL')

Sonochemistry has emerged as a promising green chemical approach for the synthesis of a wide range of chemical products, including high-value chemicals, hydrogen, and reactive oxygen species[9,10,120]. These sonochemical reactions are driven by acoustic cavitation, a phenomenon in which ultrasound waves, typically operating between 16 kHz and 3000 kHz, induce the nucleation and oscillation of gas-vapour bubbles within a liquid medium[121]. Under sufficiently intense acoustic power, these bubbles undergo rapid volumetric oscillations that are governed by the inertia of the surrounding liquid that may result in an inertial collapse. The collapse process is often described as quasi-adiabatic and generates highly localised transient hotspots characterised by temperatures exceeding 5000 K and pressures greater than 1000 bar[13]. These extreme conditions promote the thermal pyrolysis of molecules present within the bubble interior. In aqueous systems, this leads to the dissociation of water vapour into hydrogen radicals and hydroxyl radicals. Hydroxyl radicals may diffuse into the surrounding liquid, where they initiate advanced oxidation processes and other chemical reactions, including pollutant degradation, chemical synthesis, and targeted drug delivery[11,122,123].

Since acoustic cavitation directly governs sonochemical activity and chemical reactions, precise control of the acoustic field is essential. As a result, significant research efforts have focused on optimizing operating parameters, such as ultrasonic frequency, acoustic amplitude, acoustic duty cycle, as well as reactor design and geometry[124-126]. Conventional sonochemical reactors commonly reported in the literature include ultrasonic baths, immersed horn reactors, and plate reactors[34]. A detailed overview of these conventional reactor configurations is provided in Section 2.3.1. Despite their widespread use, these reactor configurations suffer from several limitations[35,127]. A major drawback of conventional designs is their inefficient utilization of acoustic energy. The acoustic field is often highly dispersed and subject to significant attenuation, resulting in poor energy concentration within the reaction volume. Consequently, achieving meaningful chemical yields typically requires prolonged operation at substantial acoustic power. In addition, the acoustic pressure distribution within these reactors is often unevenly distributed. This spatial heterogeneity results in uneven cavitation activity and energy delivery throughout the reactor volume, leading to variations in sonochemical activity. Consequently, optimizing and scaling up conventional sonochemical reactors remains challenging.

This chapter presents a novel sonochemical cylindrical reactor design that guides acoustic waves to a reactor vessel. These converging waves cause intense localised acoustic pressure fields. The novel reactor design is analogous to a high intensity focused ultrasound (HIFU) transducer. Yet most HIFU transducers use spherical lensing to create a point-like focus[128]. In contrast, the cylindrical acoustic field from this reactor, termed 'SonoCYL', is produced by reflecting a spreading wave to create a converging wave. Under this focused acoustic field, spontaneous bubble nucleation (also known as homogeneous bubble nucleation) where vapour bubbles form within a homogeneous liquid free of solid impurities, is observed[129]. To measure a chemical effect resulting from this cavitation, this study employed a highly sensitive and •OH selective molecular fluorescence probe, Res-DHB, to dosimetrically quantify the yield of •OH generated in PBS at various operating conditions for SonoCYL. Furthermore, SonoCYL showed a higher •OH production rate and sonochemical efficiency compared to conventional sonochemical reactors. Ultimately, this design strategy may lead to scalable industrially relevant sonochemical reactors.

## 3.1. Materials and methods

### 3.1.1. Materials

The chemicals used were as follows: ethylenediaminetetraacetic acid (ACS reagent, 99.4–100.6%, powder, Merck), hydrogen peroxide (30% (w/w) in water, Merck), iron(II) chloride tetrahydrate (ReagentPlus, 98%, Merck), n,n-Dimethylformamide (DMF, anhydrous, 99.8%, Merck), phosphate buffered saline (PBS, tablet, Merck), and terephthalic acid (analytical standard, Merck). All chemicals were used without further processing unless otherwise stated.

Deionised filtered Type 1 water (DI water) was obtained from a water purification system (Millipore Direct Q5-UV). Degassed DI water was prepared using a bespoke degas unit. The unit consisted of a membrane contactor (3M Liqui-Cel™ G541), a water pump (Flojet LFP, 24V RLFP222202D), and a vacuum pump (Welch MPC 090 E, type 412021). DI water was considered degassed until the oxygen concentration reached <20%, which was measured by Duo pH/Ion/DO meter SG98, Mettler Toledo.

Austenitic stainless steel (316 alloy, Taybroh Alloys) was used for the construction of SonoCYL. The ultrasound transducer used in the reactor was a cylindrical tube piezoelectric ceramic (Type I lead zirconate titanate (PZT), APC International, Ltd) with a dimension of 38 mm outer diameter, 34 mm inner diameter and 25 mm length. All materials were used without further processing unless otherwise

stated. All sonochemical reactions were performed in 5 mL polypropylene (PP) test tubes (Scientific Laboratory Supplies).

### 3.1.2. Reactor design and experimental set-up

**Contribution statement:** Professor James Kwan and Professor Jason L. Raymond conceptualised the reactor design, implemented the experimental design of the sonochemical reactor, and developed the methodology used in the study. Dr. Adam Sedgwick conducted the design and synthesis of Res-DHB.

**Reactor design**

Figure 3.1 shows (a) a schematic of the reactor, (b) an external view of the reactor, and (c) the internal structure of the SonoCYL reactor. SonoCYL was constructed of stainless steel and was designed to have two conical reflectors with a 45° bevel. The reflectors were placed adjacent to the top and bottom plate to reflect the acoustic wave, where each reflection changes the direction of propagation by 90°. These 45° reflectors were spaced approximately 30 mm apart with a spacer (a cylindrical stainless-steel tube) and capped with a top and bottom plate. The top plate consisted of an opening for placing a vessel for reagents and samples. Centred on the 16 cm diameter bottom plate was the tube ultrasound transducer, which consisted of a cylindrical tube PZT mounted onto a Delrin plastic holder to ensure central alignment with the bottom plate.

To emit a radially spreading acoustic pulse, the transducer was driven in its thickness mode. The radially spreading pulse was reflected by the bottom 45° reflector, then transmitted through the spacer, and finally reflected again by the top 45° reflector, the acoustic wave was effectively rotated 180°, creating a cylindrically converging wave with a focus along the longitudinal axis of the reactor vessel.

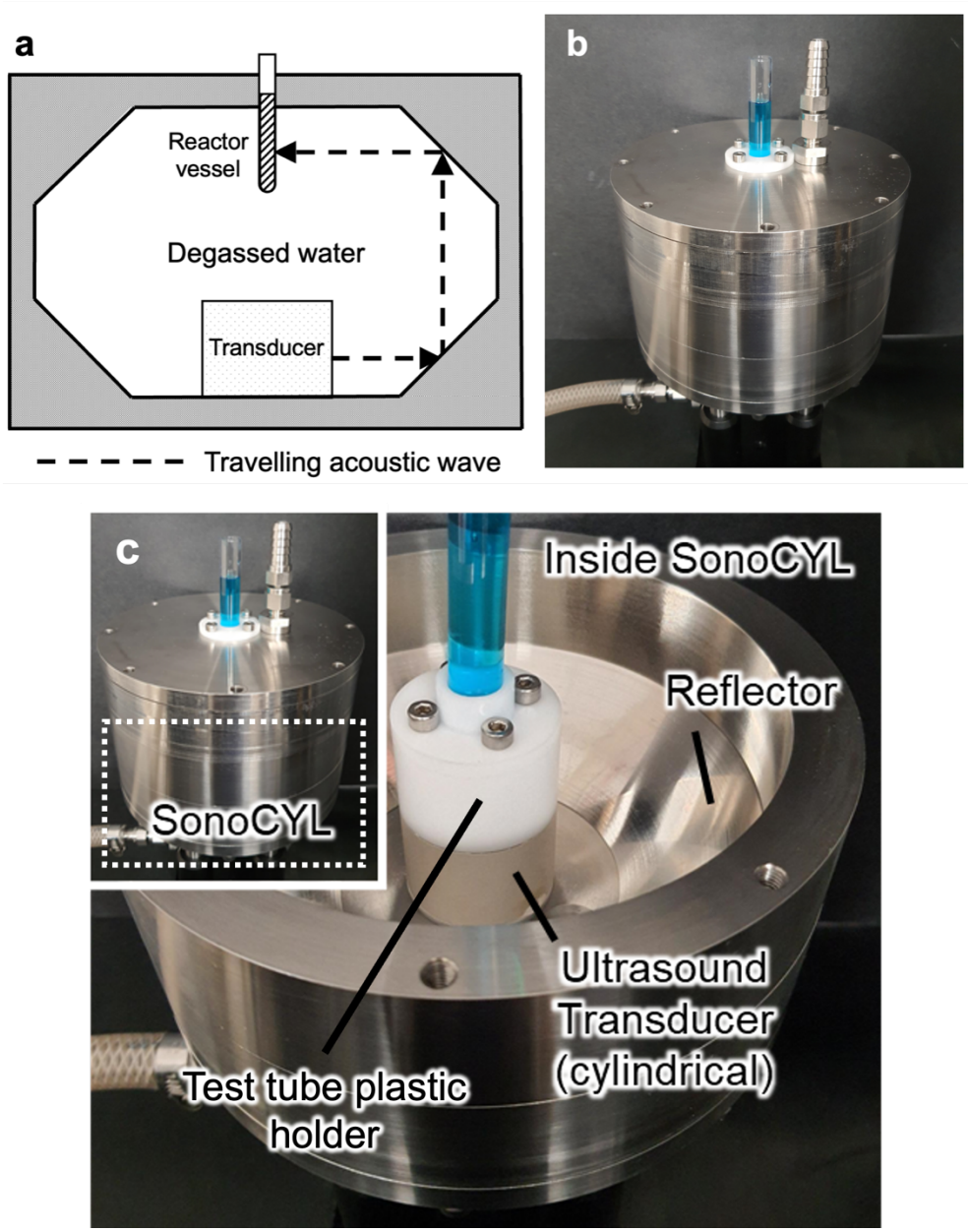



**Figure 3.1. (a)** Schematic of the SonoCYL reactor design. **(b)** External view of the SonoCYL reactor. **(c)** Internal structure of the SonoCYL reactor. The height of the cylindrical reactor is 11 cm with a diameter of 16 cm.

**Experimental set-up**

Prior to any acoustic experiments, the SonoCYL was slowly filled with degassed DI water to couple the transducer to the reaction vessel and minimise the chances of unwanted acoustic cavitation from dissolved bubbles in the coupling medium. During any acoustic measurements and sonochemical reactions, the cylindrical tube transducer at the bottom of the reactor was operated at the measured resonance frequency of 1 MHz. The transducer had an impedance of ~50 Ω when submerged in the degassed DI water, omitting the need for an impedance matching network.

Figure 3.2 shows the experimental set-up for acoustic pressure characterisation and sonochemical reactions. To drive the transducer, a sinusoidal wave signal was generated from a function generator (Keysight Waveform Generator, 33400A). The signal from the function generator was first attenuated using a −20 dB attenuator before being amplified by a 55 dB radiofrequency (RF) amplifier (Electronics & Innovation 1040L RF Amplifier) and transmitted to the ultrasound transducer. In line with the high-voltage signal was a current probe and voltage probe, which were connected to an oscilloscope (LeCroy, LT264). The static capacitance and resonance of the PZT were measured using an inductance, capacitance, and resistance (LCR) meter (BK879B, BK Precision) and an impedance analyser (Digilent Analog Discovery Impedance Analyser and Digilent Analog discovery 2), respectively.

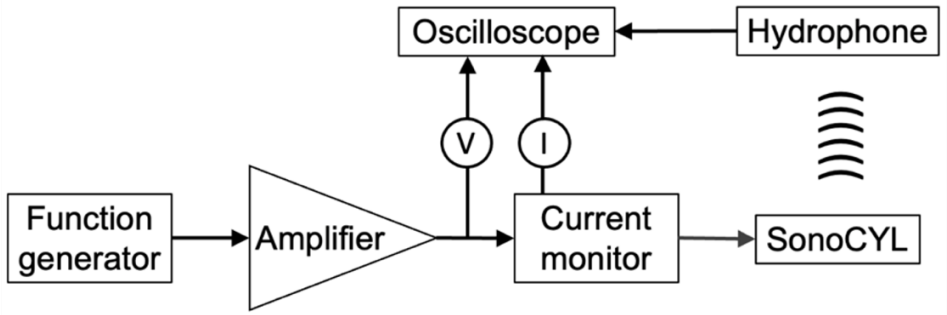



**Figure 3.2.** Schematic experimental set-up for the acoustic pressure characterisation and sonochemistry. Note that for sonochemical reactions, the hydrophone was removed to avoid damage.

### 3.1.3. Acoustic pressure characterisation and sonochemical reactions

**Acoustic field measurements**

A needle hydrophone (Precision Acoustics, SN 3222) with a diameter of 0.2 mm was used to measure the acoustic pressure in the reaction vessel. For pressure field measurements, the hydrophone was placed on a 3D positioning system (3-Stepping Motor Controller, Velmex VXM) operated using a custom MATLAB script. The hydrophone was connected to an oscilloscope (LeCroy, LT264) to record hydrophone signals and determine the maximum, minimum, peak-to-peak amplitudes, and phase angle. The input voltage, current (Pearson model 6027 1.0V/A), and phase were also recorded by the oscilloscope to calculate the input electrical power to the transducer. A point scan relating drive voltage and power to acoustic pressure amplitude was measured at the focal point. For the acoustic measurement with the needle hydrophone, the number of cycles and the burst period were

set to 50 and 10 ms, respectively. All reported acoustic pressure field values were expressed as peak-to-peak pressure.

**Sonochemical reactions**

For driving sonochemical reactions with SonoCYL, the hydrophone was removed. The operating parameters for the sonochemical reactions are described in Table 3.1 to Table 3.4. The number of cycles is defined as the number of complete oscillations contained within a single ‘on’ pulse. The burst period is defined as the total duration of one complete cycle, including both the 'on' and 'off' intervals. The duty cycle represents the fraction of the burst period during which the signal is active, expressed as a percentage of the pulse time to burst period ratio, as given previously in Eq. 2.4. Acoustic pressure is quantified in peak-to-peak megapascals ($MPa_{pkpk}$). This value represents the total pressure amplitude of an ultrasonic waveform, calculated as the difference between the maximum positive pressure and the maximum negative pressure within a single oscillation.

**Table 3.1.** Acoustic parameters and power measurements of Res-DHB dosimetry under different acoustic pressures. The electric maximum power is calculated by Eq. 2.1. The nominal electric power was calculated as the product of the maximum power and the duty cycle (Eq. 2.2).

| | Set up | | | | | |
|---|---|---|---|---|---|---|
| **Parameters** | **SonoCYL** | | | | | |
| **Time [min]** | 2 | 2 | 2 | 2 | 2 | 2 |
| **Frequency [kHz]** | 1083 | 1083 | 1083 | 1083 | 1083 | 1083 |
| **Number of cycles** | 100 | 100 | 100 | 100 | 100 | 100 |
| **Burst time [ms]** | 1 | 1 | 1 | 1 | 1 | 1 |
| **Duty cycle [%]** | 9.23 | 9.23 | 9.23 | 9.23 | 9.23 | 9.23 |
| | | | | | | |
| **Voltage [$V_{rms}$]** | **14.39** | **32.10** | **52.71** | **74.74** | **95.74** | **118.51** |
| **Current [$A_{rms}$]** | 0.40 | 0.92 | 1.51 | 2.11 | 2.72 | 3.32 |
| **Phase angle [degree]** | 159.48 | 160.48 | 161.48 | 162.48 | 163.48 | 164.48 |
| **Electric maximum power [W]** | 5.37 | 27.79 | 75.28 | 150.44 | 249.24 | 378.69 |
| **Nominal electric power [W]** | 0.50 | 2.57 | 6.95 | 13.89 | 23.01 | 34.97 |
| | | | | | | |
| **Electric energy [Whr]** | 0.02 | 0.09 | 0.23 | 0.46 | 0.77 | 1.17 |
| | | | | | | |
| **Acoustic pressure [$MPa_{pkpk}$]** | **2.51** | **5.03** | **7.54** | **10.06** | **12.57** | **15.09** |

**Table 3.2.** Acoustic parameters and power measurements of Res-DHB dosimetry under different number of cycles and burst time at a fixed duty cycle. The electric maximum power is calculated by Eq. 2.1. The nominal electric power was calculated as the product of the maximum power and the duty cycle (Eq. 2.2).

| | Set up | | | | |
|---|---|---|---|---|---|
| **Parameters** | **SonoCYL** | | | | |
| **Time [min]** | 2 | 2 | 2 | 2 | 2 |
| **Frequency [kHz]** | 1083 | 1083 | 1083 | 1083 | 1083 |
| **Number of cycles** | **10** | **30** | **100** | **1000** | **10000** |
| **Burst time [ms]** | **0.1** | **0.3** | **1** | **10** | **100** |
| **Duty cycle [%]** | 9.23 | 9.23 | 9.23 | 9.23 | 9.23 |
| | | | | | |
| **Voltage [$V_{rms}$]** | 118.51 | 118.51 | 118.51 | 118.51 | 118.51 |
| **Current [$A_{rms}$]** | 3.32 | 3.32 | 3.32 | 3.32 | 3.32 |
| **Phase angle [degree]** | 164.48 | 164.48 | 164.48 | 164.48 | 164.48 |
| **Electric maximum power [W]** | 378.69 | 378.69 | 378.69 | 378.69 | 378.69 |
| **Nominal electric power [W]** | 34.97 | 34.97 | 34.97 | 34.97 | 34.97 |
| | | | | | |
| **Electric energy [Whr]** | 1.17 | 1.17 | 1.17 | 1.17 | 1.17 |
| | | | | | |
| **Acoustic pressure [$MPa_{pkpk}$]** | 15.09 | 15.09 | 15.09 | 15.09 | 15.09 |

**Table 3.3.** Acoustic parameters and power measurements of Res-DHB dosimetry with different sonochemical reactors. The duty cycle is kept as a constant for the four setups. The number of cycles is set to a constant after the steady-state acoustic pressure amplitude of the transducer was reached. The electric maximum power is calculated by Eq. 2.1. The nominal electric power was calculated as the product of the maximum power and the duty cycle (Eq. 2.2).

| | Set up (Res-DHB) | | | |
|---|---|---|---|---|
| **Parameters** | **SonoCYL** | **Ultrasonic Bath‡** | **Immersed horn** | **Plate** |
| **Frequency§ [kHz]** | 1083 | 35 | 40 | 583 |
| **Number of cycles** | 100 | N/A | 200 | 150 |
| **Burst time [ms]** | 1 | N/A | 54.2 | 2.79 |
| **Duty cycle [%]** | 9.23 | 9.23 | 9.23 | 9.23 |
| | | | | |
| **Voltage [$V_{rms}$]** | 118.51 | - | 67.18 | 45.43 |
| **Current [$A_{rms}$]** | 3.32 | - | 0.11 | 1.08 |
| **Phase angle [degree]** | 164.48 | - | 113.00 | 152.83 |
| **Electric maximum power [W]** | 378.69 | 160.00 | 2.78 | 43.63 |
| **Nominal electric power** [**] **[W]** | 34.97 | 14.77 | 0.26 | 4.03 |

‡ The ultrasonic bath reactor was operated in continuous, factory-default mode. Therefore, the acoustic number of cycles and burst time were not adjusted externally. Consequently, a duty cycle was established by adjusting the reaction time relative to the continuous sonication period within the total experimental duration, resulting in a reduced effective exposure time under continuous operation. This approach was necessary due to hardware limitations of the ultrasonic bath system, which did not allow external control of acoustic cycles or burst time.

§ The driving frequency of SonoCYL was determined by the resonance frequency of the piezoelectric ceramic vibrating in its thickness mode. At the resonance frequency, the transducer translates most of the electrical energy to mechanical energy (as opposed to heat). This is because operation at the resonant frequency results in the highest sonochemical activity. The resonance frequency for each transducer in the other sonochemical reactors was used to maximise sonochemical yield, thereby ensuring a fair comparison between systems.

** The nominal electric power for the four compared sonochemical reactors were different. The instantaneous electric power (and the operating voltage and current) of SonoCYL was significantly higher than the three conventional reactors (ultrasonic bath, immersed horn, and plate reactor). It is noted that the three conventional reactors were operated at their maximum drive voltages and further increasing the drive voltages may damage their transducers. Therefore, it was impossible to exactly match the nominal electric power for the four compared reactors. Thus, the maximum drive voltage of the reactors is selected for a fair comparison. The SE of the reactors are also compared, which effectively normalised the hydroxyl radical concentration by the nominal electric power of the reactors.

**Table 3.4.** Acoustic parameters and power measurements of TA assay with different sonochemical reactors. The duty cycle is kept as a constant for the four setups. The number of cycles is set to a constant after the steady-state acoustic pressure amplitude of the transducer was reached. The electric maximum power is calculated by Eq. 2.1. The nominal electric power was calculated as the product of the maximum power and the duty cycle (Eq. 2.2).

| | Set up (TA assay) | | | |
|---|---|---|---|---|
| **Parameters** | **SonoCYL** | **Ultrasonic Bath** | **Immersed horn** | **Plate** |
| **Frequency [kHz]** | 1055 | 35 | 40 | 583 |
| **Number of cycles** | 100 | N/A | 200 | 150 |
| **Burst time [ms]** | 1 | N/A | 54.2 | 2.79 |
| **Duty cycle [%]** | 9.23 | 9.23 | 9.23 | 9.23 |
| | | | | |
| **Voltage [$V_{rms}$]** | 66.11 | - | 67.18 | 45.43 |
| **Current [$A_{rms}$]** | 3.89 | - | 0.11 | 1.08 |
| **Phase angle [degree]** | 36.00 | - | 113.00 | 152.83 |
| **Electric maximum power [W]** | 208.02 | 160.00 | 2.78 | 43.63 |
| **Nominal electric power [W]** | 19.21 | 14.77 | 0.26 | 4.03 |

### 3.1.4. Sonochemical hydroxyl radical production determination

**Res-DHB reaction solution preparation**

A stock phosphate buffer saline (PBS) was prepared by dissolving one PBS tablet into 200 mL of deionised water (pH 7.4 at 25 °C). The Res-DHB compound was synthesised following the schematics in Figure 3.3 and Figure 3.4 with the method described in Wong et al.[130]. The design and synthesis of Res-DHB used in this research were conducted by Dr. Adam Sedgwick. Res-DHB was pre-dissolved in DMF (5 mM) and added to PBS to make a 3 mL reaction solution with Res-DHB concentration at 5 µM. Before every sonochemical reaction, the reaction vessel was saturated with dissolved gas by vigorously shaking every two minutes. All reactions were performed at ambient temperature and pressure.

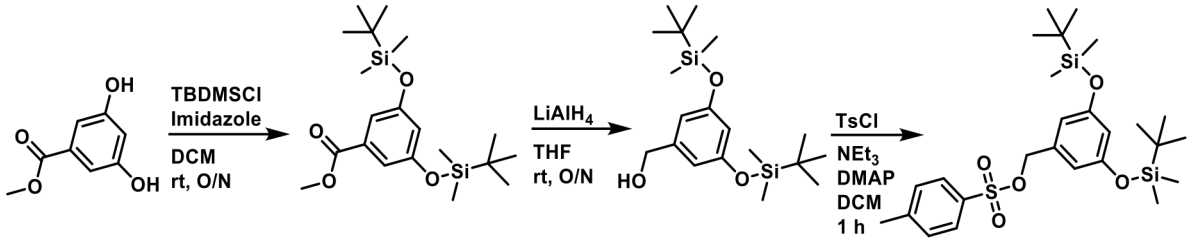



**Figure 3.3.** Synthetic scheme for the synthesis of tosyl-based alkylating agent. The design and synthesis were conducted by Dr. Adam Sedgwick.

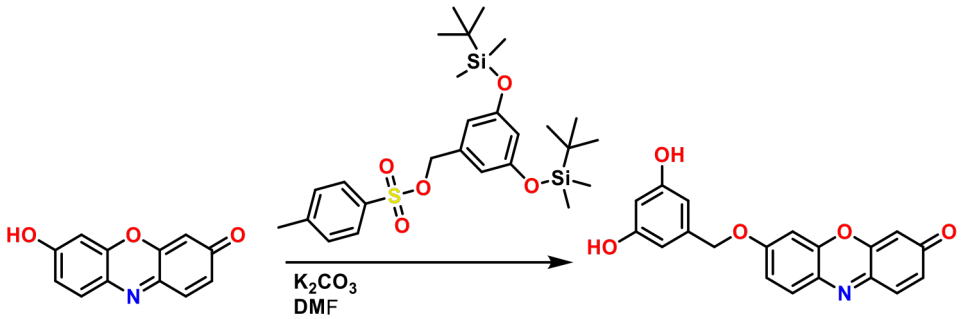



**Figure 3.4.** Synthetic scheme for the synthesis of Res-DHB. The design and synthesis of Res-DHB were conducted by Dr. Adam Sedgwick.

**Reaction solution preparation for TA assay**

The TA assay was adopted from the methodology of Villeneuve et al.[131]. A fresh reactant solution was prepared prior to each set of experiments. A stock phosphate buffer saline (PBS) solution was prepared by dissolving one PBS tablet in 200 mL of deionised water (pH 7.4 at 25 °C). Terephthalic

acid was then dissolved in 1x PBS to prepare a 1 mM reaction solution. A volume of 3 mL of TA reaction solution was used for each experiment. Prior to each sonochemical reaction, the reaction vessel was saturated with dissolved gas by vigorous shaking every two minutes. All reactions were performed at ambient temperature and pressure.

**Fluorescence measurements**

A fluorometer (Perkin Elmer LS 55, $\lambda_{excitation}$ = 500 nm, $\lambda_{emission}$ = 585 nm, slit widths: excitation = 10 nm and emission = 3.5 nm) was used to detect the fluorescence response from resorufin (Res). The excitation wavelength, emission wavelength, and slit widths were selected based on preliminary optimisation experiments to maximise the fluorescence response of Res. From the fluorescence measurement of Res, the •OH yield was quantified using a calibration curve relating fluorescent emission intensity and •OH concentrations.

For the measurement of HTA, a fluorometer (Perkin Elmer LS 55, $\lambda_{excitation}$ = 310 nm, $\lambda_{emission}$ = 425 nm, slit widths: excitation = 10 nm and emission = 3.5 nm) was used to detect the fluorescence response. The measurement parameters were selected based on preliminary optimisation experiments to maximise the fluorescence signal of HTA. The excitation and emission wavelengths (310 and 425 nm, respectively) were adopted from the method reported by Chen et al.[132]. The fluorescence reading was taken directly for the measurement.

### 3.1.5. Sonochemical efficiency determination

The sonochemical efficiency was determined from Eq. 2.15. The input power was calculated based on the input electric power (Eq. 2.1). The calorimetric method was alternatively used to determine the power generated from acoustic transducer. It was determined by measuring the temperature change in the reaction vessel. To measure the reaction solution temperature, a thermocouple (Type N thermocouple) was inserted into the sample solution and the temperature was recorded with a thermometer (Fluke 54 II B). The derivation of the heat transfer equations used to fit the temperature data is described in Appendix Section A.1.

### 3.1.6. Conventional sonochemical reactor

Three conventional sonochemical reactors were used in this study to compare the sonochemical performance of the SonoCYL reactor. They were an ultrasonic bath reactor (35 kHz, Bandelin Electronic Ultrasonic Bath RK 100, internal dimensions of 240 x 140 x 100 mm), an immersed horn reactor (40 kHz, Sonic Systems 021940A), and a plate reactor (583 kHz, Meinhardt Ultrasonics, E/805/T/solo, diaphragm diameters of 75 mm). Their pictures are presented in Figure 3.5.

The operating parameters used in the Res-DHB dosimetry experiments for the comparison of the sonochemical reactors are summarised in Table 3.3. For each conventional sonochemical reactor, the driving frequency was selected to match the resonance frequency of its transducer in order to maximise acoustic energy transfer. Due to differences in reactor geometry in the immersed horn, plate reactor, and SonoCYL, the number of cycles required to reach a steady-state acoustic pressure amplitude varied between systems. To ensure a fair comparison between different sonochemical reactors, the duty cycle (9%) and the number of cycles (after the steady-state pressure amplitude was reached) were kept constant for all reactor types. The duty cycle of 9% was maintained by adjusting the burst period for each system, as the time required to deliver a fixed number of acoustic cycles varied depending on the specific driving frequency of the reactor. In addition, differences in reaction volume (3 mL for the SonoCYL, ultrasonic bath, and plate transducer systems, and 12 mL for the immersed horn system) were addressed by normalising the amount of hydroxyl radicals to the reaction volume, hence obtaining the product concentration.

The operating parameters used in the TA assay for the comparison of the sonochemical reactors are summarised in Table 3.4. The operating parameters used for the ultrasonic bath, horn, and plate reactors were identical to those employed in the Res-DHB dosimetry experiments. The SonoCYL reactor design and experimental setup, including the number of cycles and duty cycle, were also maintained under the same conditions as those used for Res-DHB dosimetry. However, the frequency and electrical power (calculated from the voltage and current) used in the TA assay differed from those used in the Res-DHB dosimetry experiments. This difference arose because the 1083 kHz transducer used in the Res-DHB dosimetry experiments was damaged and cracked during the TA assay experiments. A 1055 kHz transducer was therefore used for the TA assay as the closest available alternative, with a different permitted driving power (i.e., the safe operating limit without damaging the device or causing non-linear behaviour). Although this transducer had a lower maximum power output, its dimensions were identical and the reactor configuration remained unchanged. Therefore,

it was considered suitable for comparison with the TA assay results across different sonochemical reactors.

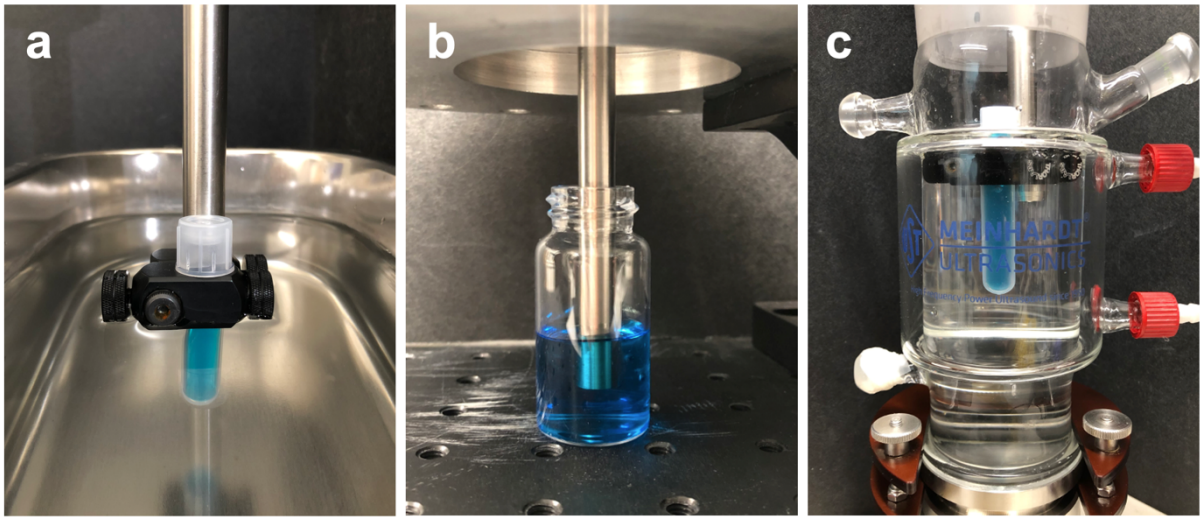



**Figure 3.5.** The experimental set-ups of **(a)** ultrasonic bath reactor, **(b)** immersed horn reactor, and **(c)** plate reactor.

**Ultrasonic bath reactor**

For each experimental trial, a single 5 mL PP test tube was filled with 3 mL of the reactant solution and positioned vertically in the centre of the bath. The ultrasonic bath was freshly filled with 3 L of deionised water prior to each run to serve as an acoustic coupling medium. The submersion depth was carefully adjusted so that the water level of reactant solution inside the test tube aligned with the water level of the surrounding bath. The equipment operated on a factory-default power setting, no external acoustic modulation was applied, and operations were governed by the exposure runtime. Due to the short duration of each experiment, the bath water temperature remained relatively stable during sonication. However, repeated experimental runs resulted in gradual heat accumulation within the bath. To minimise thermal effects, the bath water temperature was monitored and replaced with fresh, cool DI water between runs.

**Horn reactor**

Due to the dimensions of the ultrasonic horn tip, a standard 5 mL PP tube was incompatible with the setup. Instead, experiments were conducted with a 25 mL glass vial containing 12 mL of reactant solution. The horn tip was positioned at the midpoint of the reactant solution's liquid level. The immersed horn reactor utilised the same electrical drive system shown in Figure 3.2, omitting the

hydrophone setup. A continuous sinusoidal waveform was generated using a Keysight 33400A function generator and passed through a −20 dB attenuator before amplification by a 55 dB RF power amplifier (Electronics & Innovation 1040L). The amplified signal was then supplied to the ultrasonic horn transducer. Voltage and current probes were connected to a LeCroy LT264 digital oscilloscope to enable real-time monitoring of the electrical input parameters.

**Plate reactor**

The plate transducer was mounted under a glass vessel using a clamping assembly and sealed with vacuum grease to prevent leakage. The vessel was filled with 500 mL of water to serve as an acoustic coupling medium. A 5 mL PP test tube containing 3 mL of reactant solution was centrally positioned within the vessel. The vertical position of the tube was adjusted so that the water level inside the tube matched the surrounding coupling medium water level. The electrical driving configuration was identical to that used for the immersed horn reactor. A sinusoidal signal generated by the Keysight 33400A function generator was attenuated by −20 dB, then amplified using the E&I 1040L RF amplifier, and transmitted to the transducer. Input voltage and current were monitored using the LeCroy LT264 oscilloscope. Due to the short duration of each experiment, the temperature of the coupling medium remained relatively stable during sonication. However, repeated experimental runs resulted in gradual heat accumulation within the water jacket. To minimise thermal effects and maintain consistent operating conditions, the temperature of the coupling medium was monitored and the water was replaced with fresh, cool water between runs.

## 3.2. Results and discussion

### 3.2.1. Acoustic characterisation

Figure 3.6 shows the spatial distribution of the acoustic pressure amplitude across two planes. For (a), the bottom of the top plate was defined as 0 mm in the z-axis. For (b), the position of peak acoustic pressure amplitude was defined as 0 mm in the x- and y-axis. The full-width half maximum (FWHM) for the x- and y-axis was ~0.5 mm and for the z-axis was ~5.9 mm as shown in Figure 3.7. Based on these measurements, the acoustic focal volume was calculated to be ~1.16 μL. These measurements agreed with the expectations; the measured x- and y-axis FWHM was similar to the FWHM of the primary peak of the cylindrical Bessel function of the first kind (~0.7 mm assuming that the speed of sound of water is 1.481 mm/μs at 20 °C). It suggested that the converging waves constructively interfered at the centre of the reaction vessel.

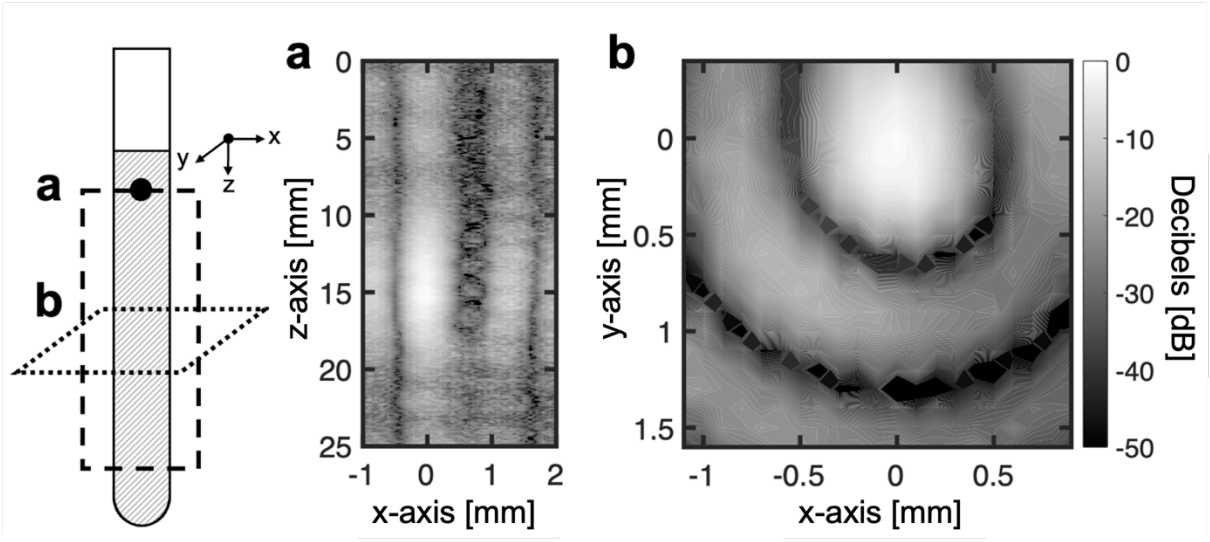



**Figure 3.6. (a)** xz- and **(b)** xy- pressure scan in the reaction vessel.

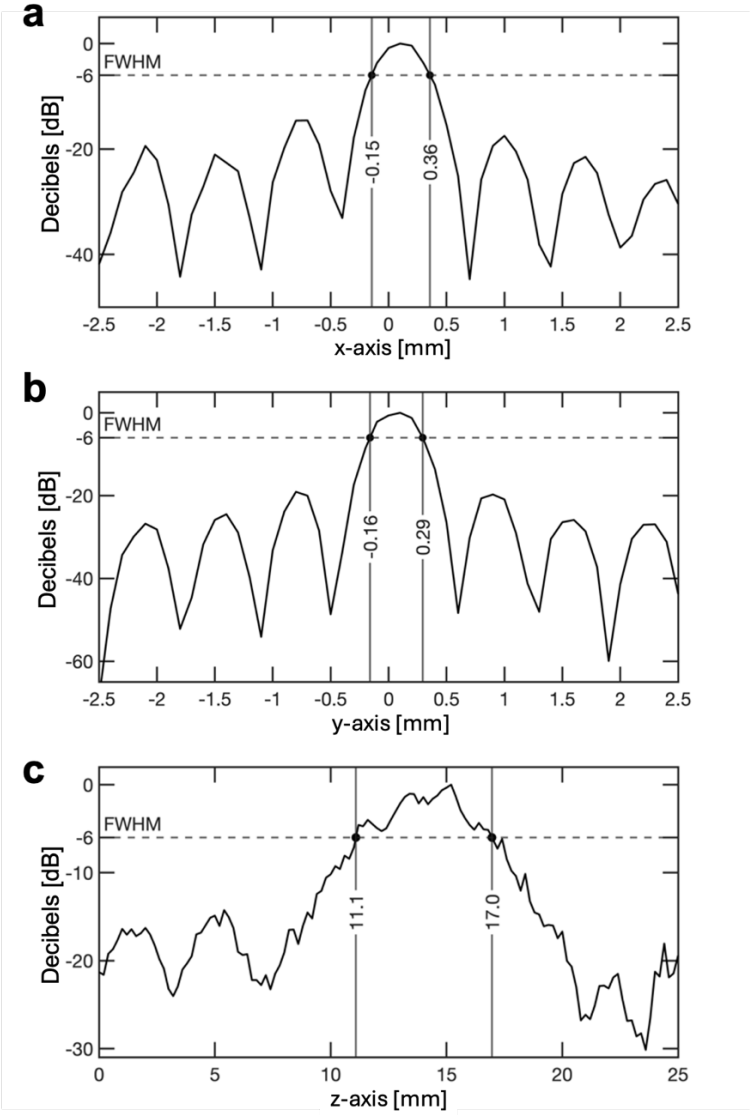



**Figure 3.7.** 1D-pressure scan at the x-, y-, and z-axis in the reaction vessel. The x-axis FWHM (–6 dB) was 0.51 mm. The y-axis FWHM (–6 dB) was 0.45 mm. The z-axis FWHM (–6 dB) was ~5.9 mm. It is noted that the x- and y-axis measurements were slightly off centre due to the space

limitations to fit the hydrophone inside the reaction vessel. 0 dB was set to be the maximum voltage of the hydrophone signal.

In addition to the acoustic pressure distribution, the range of pressure amplitudes achievable by the transducer was measured since acoustic cavitation is in part governed by the acoustic pressure amplitude. Hydrophone measurements of the acoustic pressure amplitude at the spatial peak for different input electrical powers were conducted at low drive powers to avoid damaging the hydrophone, as shown in Figure 3.8.

Figure 3.8 illustrates both the relationship between RMS voltage and acoustic pressure (Figure 3.8 (a)), and the relationship between RMS voltage and input electrical power (Figure 3.8 (b)). While voltage is used as the direct control parameter of the system, acoustic pressure fundamentally scales with input electrical power.

Higher acoustic pressure amplitudes were then estimated by extrapolation from linear fit in Figure 3.8 (a). By substituting the maximum operating voltage (118.51 $V_{rms}$) into the regression equation, the corresponding maximum pressure amplitude was estimated to be 15 $MPa_{pkpk}$. However, the extrapolated acoustic pressure amplitudes outside the measured values may not be accurate due to the wave becoming increasingly non-linear with increasing power.

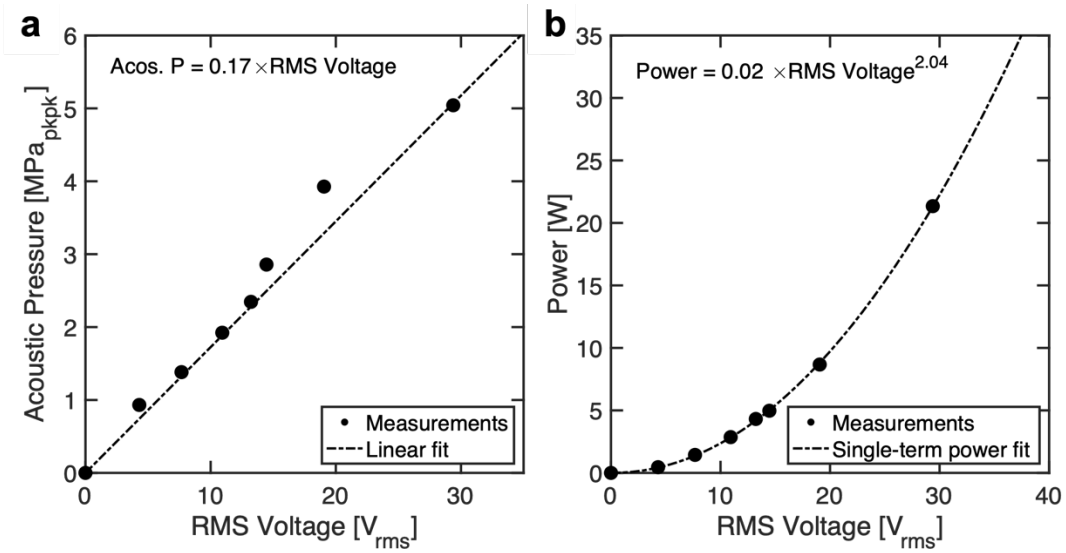



**Figure 3.8. (a)** RMS acoustic pressure vs RMS voltage relationship and **(b)** RMS power vs RMS voltage at the reaction vessel focused pressure point. While voltage is the experimentally controlled input parameter, it is noted that acoustic pressure is fundamentally governed by input electrical power rather than voltage.

### 3.2.2. Res-DHB dosimetry for hydroxyl radicals

Chemical probes are commonly used to quantify •OH yield[6]. As discussed, •OH dosimetry is performed by Weissler reaction, Fricke reaction, and terephthalic acid assay. However, the former two dosimetry methods assume •OH goes through specific reaction pathways to form $H_2O_2$ without any side reactions and the probes detect the concentration of $H_2O_2$. Yet, side reactions are present in practice, leading to inaccurate values of •OH yield[6,44]. Additionally, the Weissler reaction relies on the temperature-dependent equilibrium between iodide ($I^-$) and triiodide ($I_3^-$). Since sonochemical reactors generate heat at varying rates depending on reactor design and operating conditions, this temperature sensitivity may shift the equilibrium and compromise the accuracy of •OH measurements in systems with temperature fluctuations[44,133]. On the other hand, even though TA assay is selective to •OH by reacting with the radicals via an arene hydroxylation reaction mechanism, its solubility is low in aqueous media and is highly pH sensitive[46]. TA intermediate may also react with oxygen in air and undergo double OH-radical-induced hydroxylation to form side products[6,42]. These factors make TA assays sensitive to experimental conditions and setups, hindering direct comparisons across literature. Moreover, the three dosimetry assays require the chemical concentration in the range of milli-molar, which is not ideal in the detection of very low concentrations of •OH[6].

This research quantified the •OH yield by chemical dosimetry with Res-DHB, a highly sensitive, non-temperature dependent, and selective probe for •OH[130]. Similar to TA, Res-DHB proceeds with •OH via an arene hydroxylation reaction mechanism, which is selective to •OH. Other radicals produced from inertial cavitation do not have this capability.

The reaction mechanism between Res-DHB and •OH is illustrated in Figure 3.9. A low concentration of Res-DHB was added to the solution, where it selectively reacted with •OH to release Res, generating a fluorescent emission signal at 585 nm. As shown in Figure 3.10, fluorescence emission increased with sonication time using the SonoCYL reactor (0–6 min). The peak fluorescence intensity in the emission spectra was used to quantify •OH concentration, allowing the determination of •OH yield from the sonochemical reaction.

The reported •OH values are derived from a calibration curve based on the reference Fenton chemistry system and represent the equivalent •OH concentration generated by the Fenton chemistry required to produce the measured fluorescence response. The Fenton chemistry methodology is described in Appendix Section A.2.

The reported Fenton-equivalent •OH concentrations are derived from a kinetic calibration of the Fenton reaction at a fixed measurement timepoint rather than from direct stoichiometric quantification of •OH. Due to the slow kinetics of the Fenton chemistry reaction, fluorescence measurements were conducted 60 minutes after preparation of the Fenton solution[130]. Under this fixed measurement period, an increase in •OH generation increases the probability of reaction between •OH and Res-DHB, resulting in a higher rate of fluorescent Res-OH formation and consequently a higher fluorescence intensity. The reported •OH values in the hundreds of µM represent Fenton-equivalent •OH activity derived from the calibration curve rather than stoichiometric conversion of the 5 µM Res-DHB probe. The calibration therefore provides a measure of relative •OH production and not the absolute concentration of •OH present in the system.

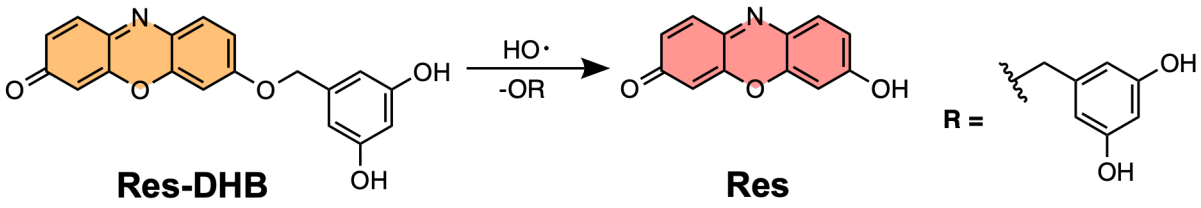



**Figure 3.9.** Reaction of Res-DHB with •OH yielding fluorescent Res probe. Res-DHB is orange in colour and Res is pink in colour.

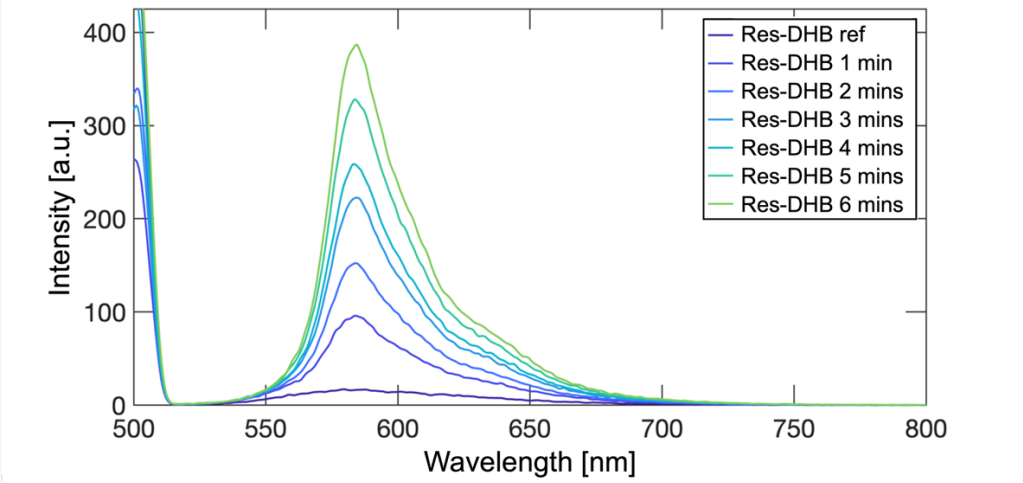



**Figure 3.10.** Representative fluorescence spectra of the Res-DHB reaction obtained using SonoCYL over reaction times ranging from 0 to 6 minutes. The spectra shown are consistent with those observed in other experimental trials.

During the preparation of the Res-DHB samples, PBS was used to maintain the pH of the reactants throughout the reaction. Res-DHB was shown to be stable in PBS and temperature insensitive up to 60 °C, which is below the temperature rise under the ultrasonic irradiation with SonoCYL at the maximum power output (Figure 3.11)[130].

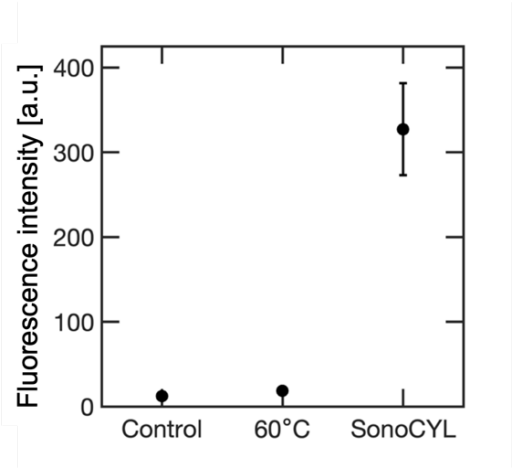



**Figure 3.11.** The Res-DHB temperature stability study by evaluating the fluorescence intensity of a control sample, a reaction solution immersed in a water bath at 60 °C for 6 mins, and a reaction solution irradiated by irradiation using SonoCYL for 6 mins.

### 3.2.3. Optimal operational parameters for SonoCYL

**Dependence on acoustic pressure**

Figure 3.12 shows the concentration of •OH yield resulting from different acoustic pressure amplitudes. No •OH was detected for reactions at pressure amplitudes below 7.5 $MPa_{pkpk}$. At 10.1 $MPa_{pkpk}$, •OH was detected. This apparent threshold for •OH detection suggested there was a cavitation threshold between 7.5 $MPa_{pkpk}$ and 10.1 $MPa_{pkpk}$, which confirms that acoustic inertial cavitation is the source of •OH and agrees with previous research[12]. Higher acoustic pressure amplitudes likely lead to the nucleation of a larger population of bubbles that underwent inertial collapse and or forced bubbles to grow to a larger maximum radius just before the moment of implosion. Larger bubble radii before implosion generally increase the maximum temperature within the bubble[134]. Thus, both more nucleation sites and larger bubble radii likely contributed to the increase in radicals produced in the reaction.

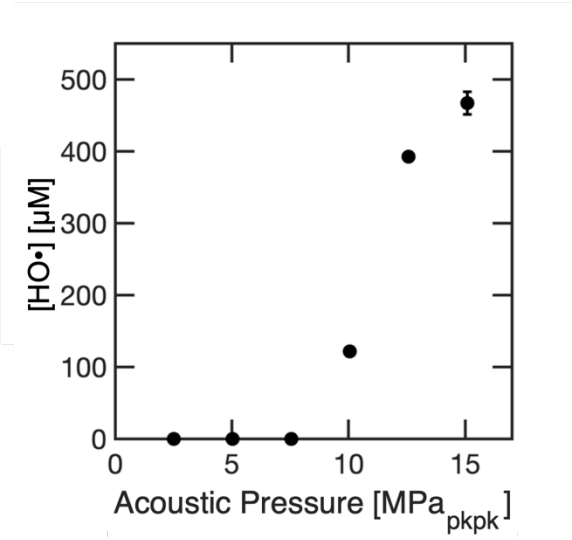



**Figure 3.12.** The •OH concentration obtained from the Res-DHB reaction at different acoustic pressures. Each data point represents the average of three trials, and the error bars indicate the standard deviation.

Cavitation thresholds in water vary widely depending on multiple factors and have been reported to range from 0.3 MPa to more than 12MPa[135-137]. In this study, the cavitation threshold at 1 MHz was estimated to be between 7.5 MPa and 10.1 MPa. Although these values are higher than some reported in the literature, they are consistent with other studies[138-140]. This discrepancy is likely due to inherent differences in the sources of ultrasound used and the operating conditions. The reported cavitation thresholds between 0.3 and 0.4 MPa at 1 MHz were measured in a standing wave field from a plate transducer likely operated in a continuous wave mode. However, SonoCYL delivers pulsed focused ultrasound and may be better compared to HIFU. Previous work determining cavitation thresholds in water using 1.1 MHz HIFU transducers reported that 5 MPa peak rarefactional pressure amplitude was not able to nucleate cavitation[138]. Other work indicated that cavitation thresholds of ~12 MPa peak rarefactional pressure amplitude were required to achieve cavitation ~50% of the time[140]. In addition, Lafon et al. showed a 10 MPa acoustic pressure cavitation threshold measured with hydroxyl radical dosimetry[139]. This threshold was around twice higher than thresholds under continuous sonication.

These findings reinforce that pulsed, acoustically focused systems such as SonoCYL require higher pressure amplitudes to initiate cavitation, consistent with thresholds observed in HIFU-based measurements. Importantly, cavitation thresholds cannot be attributed solely to the frequency of the sonoreactor, as other factors such as wave propagation characteristics, pulse duration, acoustic field geometry, and transducer design also play critical roles.

**Dependence on number of acoustic cycles**

Sonochemical reactions are typically carried out using CW ultrasound. However, some studies have reported the use of pulsed ultrasound and demonstrated that it yielded better sonochemical effects. They typically used pulse lengths exceeding $10^5$ acoustic cycles at moderate duty cycles (≥10%)[24,141-143]. In this study, the •OH radical yield under different acoustic cycle lengths (or burst durations) was investigated while maintaining a fixed duty cycle of 9%. This ensured the consistent total energy input across all conditions for a given reaction time. Additionally, the low duty cycle prevented thermal effects and allowed nucleated bubbles to re-dissolve into the liquid between bursts, thereby reducing bubble accumulation and maintaining reproducibility. The results are shown in Figure 3.13. It is observed that 100 acoustic cycles produced the largest yield of •OH. It is noted that the concentration of •OH radicals was higher at $10^4$ cycles than at $10^3$ cycles. Yet, the difference between the two concentrations was less than 10%. Both data points were notably lower than the concentration of hydroxyl radicals at 100 cycles.

This effect is explained by segmenting the response into two regimes: when the number of cycles is below the optimal range and when it exceeds it. When the number of cycles is below 100 cycles, the pulse was too short to nucleate enough cavitation events to yield radicals. There were not enough acoustic cycles to cause the transducer to ring up and reach the sufficient acoustic pressure amplitude for inertial cavitation. This was expected as the piezoelectric ceramic of the transducer had a large (>100) Q-factor, indicating the material stores energy relatively slowly. In contrast, when the number of cycles exceeds 100 cycles, most of the nucleated bubbles may undergo inertial collapse in the initial 100's of cycles. However after these collapses, these bubbles may become much larger due to rectified diffusion, bubble agglomeration, and coalescence, owing to the extended burst duration[24]. These large bubbles tend not to inertially collapse and instead float to the surface of the liquid medium, thereby degassing the liquid. These degassing bubbles also prevent the sound propagation by absorption and scattering of the sound, which leads to a decrease in the sound pressure amplitude and hence a spatial reduction of the active sonochemical reaction region[24].

Furthermore, there are simply fewer number of pulses at $10^3$ and $10^4$ cycles under a fixed period of reaction time compared to 100 cycles. If most •OH production occurred within the initial few hundred cycles, the reduced numbers of pulses at higher cycle counts may contribute to a lower net •OH yield. Some studies have suggested that the intervals between ultrasonic pulses slow down bubble growth, allowing more time for the diffusion and accumulation of chemical species at the bubble interface. As a result, a greater number of reactant molecules are brought into proximity with the bubble

interface, increasing the likelihood of chemical reactions[27,28]. However, it remains unclear whether this mechanism was relevant in the system, as it was uncertain whether Res-DHB accumulates at the bubble interface and whether its diffusion rate is fast enough to affect the reaction significantly.

In conclusion, using 100 acoustic cycles achieves an effective balance for this sonochemical system: the burst duration is sufficient to generate the necessary acoustic pressure amplitude for inertial cavitation, while remaining short enough to avoid excessive bubble growth and degassing the liquid. Additionally, the ultrasound off time may allow smaller bubbles to dissolve back into the liquid, effectively resetting the solution back to an initial state and preventing the possibility of forming larger bubbles that cause the shielding effect[24].

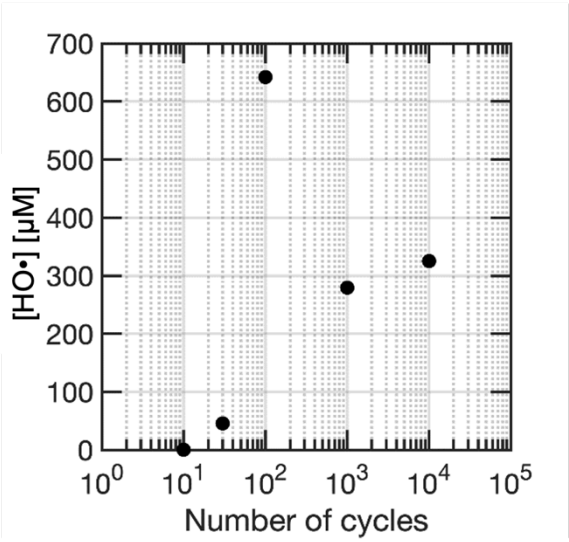



**Figure 3.13.** The •OH concentration from the Res-DHB reaction at different number of cycles. Each value is the average of three trials, and the error bars (overlap with the markers) indicate the standard deviation.

### 3.2.4. Comparisons with conventional sonochemical reactors

Once the optimal operating conditions were established, the kinetics and SE of sonochemical •OH production were evaluated by exposing the reaction solution to ultrasound (15.1 $MPa_{pkpk}$, 100 cycles, and 9% duty cycle) over varying durations. Due to the different geometry of the transducers in the immersed horn, plate reactor, and SonoCYL, the number of cycles required to reach the acoustic pressure amplitude steady state were different. To ensure a fair comparison between different sonochemical reactors, the duty cycle (9%) and the number of cycles (after the steady-state pressure amplitude was reached) were kept constant for all reactor types.

The •OH production rate was assessed by monitoring the •OH concentration as a function of ultrasound exposure time. The resulting data were fitted using a linear regression model (Figure 3.14 (a)), with the slope of the regression line representing the •OH production rate measured by Res-DHB dosimetry. The linear regression fitting results for •OH production rate of the four sonochemical reactors using Res-DHB are shown in Table 3.5. SonoCYL exhibited a production rate at least three orders of magnitude higher than the immersed horn reactor and five orders of magnitude higher than the plate reactor. There was no detectable production of •OH for the bath reactor given the reaction timescale (the negative slope value in Table 3.5 was attributed to experimental noise and was therefore considered not detectable).

**Table 3.5.** Linear regression fitting results for •OH production rate of the four sonochemical reactors using Res-DHB dosimetry.

| Reactor | Regression fit equation | Slope (m) | y-intercept (c) | $R^2$ |
|---|---|---|---|---|
| SonoCYL | y = mx + c | 159 | 41 | 0.98 |
| Horn | y = mx + c | 0.46 | -6.44 | 0.96 |
| Plate | y = mx + c | 0.0058 | 0.097 | 0.05 |
| Bath | y = mx + c | -0.11 | 5.81 | 0.07 |

The linear regression analysis showed notable differences in the fit quality among the reactor configurations. SonoCYL exhibited the highest $R^2$ value ($R^2 = 0.98$) among the reactors, indicating that the measured •OH concentration increased linearly with ultrasound exposure time. The immersed horn reactor also showed a high $R^2$ value ($R^2 = 0.96$), suggesting a consistent relationship between •OH concentration and exposure time. In contrast, the plate reactor and bath reactor exhibited substantially lower $R^2$ values, indicating a less consistent relationship between •OH concentration and ultrasound exposure time. The lower $R^2$ values ($R^2 = 0.05$ for plate reactor and $R^2 = 0.07$ for bath reactor) observed for the plate and bath reactors are likely attributable to their sensitivity to reaction vessel positioning. In these reactor configurations, the acoustic pressure experienced by the reaction solution depends strongly on the precise location of the vessel within the acoustic field. Consequently, small shifts in the position of the reactor vial between experiments may lead to high variations in ultrasonic power transmission and sonochemical activity. Although efforts were made to maintain consistent reactor vial positioning throughout the experiments, achieving identical placement across repeated measurements is inherently challenging. The lower $R^2$ values therefore suggest that the sonochemical performance of the plate and bath reactors is more sensitive to vessel positioning, resulting in greater experimental variability than that observed for SonoCYL and the immersed horn reactor.

Figure 3.14 (b) presents the •OH production concentration as a function of input electrical energy for different reactor types. Here, electric energy input (in the unit of Whr) was used as the metric for SE calculation, allowing comparison independent of reactor configuration[49]. The •OH production concentration of each reactor was plotted against the input electrical energy and fitted using a linear regression model. The slope of the resulting regression line was defined as the SE. The linear regression results for the SE of the four sonochemical reactors, determined using Res-DHB dosimetry, are summarised in Table 3.6. The results showed that the horn reactor used here had a relatively low maximum drive power (see inset of Figure 3.14 (b)), limiting energy input over time.

The •OH production rate and SE values of the four sonochemical reactors are summarised in Table 3.7. The SonoCYL achieved an SE twice that of the immersed horn reactor and nearly four orders of magnitude higher than the plate reactor. The bath reactor did not produce an observable •OH yield (the negative slope value in Table 3.6 was attributed to experimental noise and was therefore considered not detectable). The lower sonochemical efficiency observed for the plate and bath reactors highlights the structural efficiency trade-offs associated with indirect sonication reactor configurations. In these setups, a liquid coupling medium is required to transmit acoustic energy from the transducer to the reaction vessel. However, this medium also contributes to energy dissipation, attenuating a portion of the acoustic energy before it reaches the reaction vial. This effect becomes more significant at mid-to-high operating frequencies, such as the 583 kHz frequency used in the plate reactor[144].

**Table 3.6.** Linear regression fitting results for sonochemical efficiency of the four sonochemical reactors using Res-DHB dosimetry.

| Reactor | Regression fit equation | Slope (m) | y-intercept (c) | $R^2$ |
|---|---|---|---|---|
| SonoCYL | y = mx + c | 273 | 41 | 0.98 |
| Horn | y = mx + c | 107 | -6 | 0.96 |
| Plate | y = mx + c | 0.086 | 0.097 | 0.05 |
| Bath | y = mx + c | -0.44 | 5.81 | 0.07 |

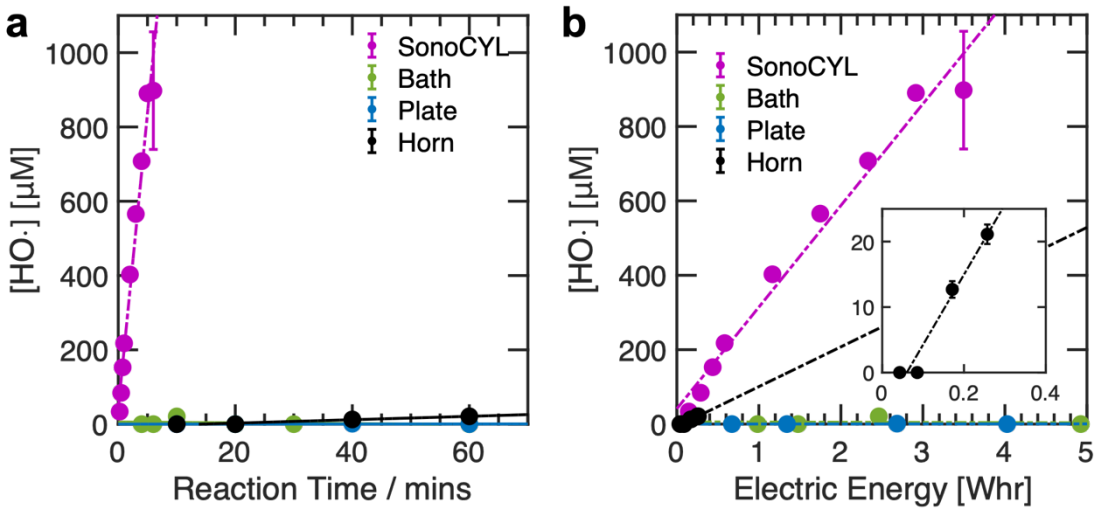



**Figure 3.14. (a)** The •OH concentration vs reaction time for the four sonochemical reactors using Res-DHB: SonoCYL (1 MHz), immersed horn reactor (40 kHz), plate reactor (583 kHz), and bath reactor (35 kHz) at 9% duty cycle. The slope of the linear regression represents the •OH production rate in the reaction. **(b)** The •OH concentration vs the input electrical energy for the four sonochemical reactors using Res-DHB. The slope of the linear regression represents the SE (•OH production per unit energy). Each value is the average of three trials, and the error bars indicate the standard deviations.

**Table 3.7.** The table shows the •OH production rate and SE for the four sonochemical reactors using Res-DHB. The •OH production rate and the SE were determined from the slope of the linear regression. The rate may also be converted directly into SE by dividing the rate by the nominal electrical power and converting the time unit from minutes to hours. The nominal electric power is presented from Table 3.3.

| Reactor | Nominal electric power [W] | Rate [$\mu M_{\cdot OH}$ $min^{-1}$] | SE [$\mu M_{\cdot OH}$ $Whr^{-1}$] |
|---|---|---|---|
| SonoCYL | 34.97 | 159 | 273 |
| Horn | 0.26 | 0.46 | 107 |
| Plate | 4.03 | 0.0058 | 0.086 |
| Bath | 14.77 | Not detected | Not detected |

To relate these energy losses to the sonochemical efficiency used in this study, sonochemical efficiency is defined based on the concentration of hydroxyl radicals generated per unit of input electrical energy (Eq. 2.15). Since the input electrical energy represents the total electrical energy supplied to the system, the calculated sonochemical efficiency accounts for all device-level, transmission, and coupling-medium losses. Any energy dissipated within the coupling medium is ultimately converted into heat and does not contribute to the desired sonochemical reactions. Therefore, evaluating reactor performance based on total electrical energy consumption provides a

comparable measure of sonochemical efficiency regardless of reactor designs, aligning with established methodologies used by Koda et al., Mark et al., and Kojima et al[42,47,48].

Importantly, a similar coupling arrangement was also present in the SonoCYL, where the same reaction vial and reaction volume were used, and acoustic transmission relied on water as an intermediate coupling medium. The SonoCYL also operated at a higher frequency (1.083 MHz) while still demonstrating higher sonochemical efficiency, suggesting that SE is influenced not only by the presence of a coupling medium or the operating frequency, but also by the reactor configuration itself.

These findings were independently corroborated by TA assay. Although the TA method is subject to certain uncertainties, as discussed in Section 3.2.2, it remains one of the most widely used •OH dosimetry techniques in the literature compared to Res-DHB, which is still a relatively novel probe despite offering greater selectivity and sensitivity. The linear regression fitting results for the •OH production rate and SE determined using TA assay are presented in Tables 3.8 and 3.9, respectively. As shown in Figure 3.15 and summarised in Table 3.10, the SonoCYL demonstrated the highest •OH production rate and SE across the four reactors when evaluated using TA assay. This confirms that the superior sonochemical performance of the SonoCYL was independent of the •OH probe used.

Since the primary objective was to assess the relative sonochemical performance of different sonochemical reactor types, full quantification of •OH using TA assay (which served as a secondary dosimetry method in this study) was not pursued. Some discrepancies were observed between the relative •OH production rates and SE obtained from the Res-DHB and TA assays. These variations may be attributed to the different chemical mechanisms with •OH and the different kinetics of the two chemical dosimetry methods.

**Table 3.8.** Linear regression fitting results for •OH production rate of the four sonochemical reactors using TA assay.

| Reactor | Regression fit equation | Slope (m) | y-intercept (c) | $R^2$ |
|---|---|---|---|---|
| SonoCYL | y = mx + c | 395 | 80 | 0.99 |
| Horn | y = mx + c | 2.79 | 55.87 | 0.99 |
| Plate | y = mx + c | 2.85 | 53.01 | 0.94 |
| Bath | y = mx + c | 2.39 | 49.43 | 0.95 |

**Table 3.9.** Linear regression fitting results for sonochemical efficiency of the four sonochemical reactors using TA assay.

| Reactor | Regression fit equation | Slope (m) | y-intercept (c) | $R^2$ |
|---|---|---|---|---|
| SonoCYL | y = mx + c | 1200 | 80 | 0.99 |
| Horn | y = mx + c | 651.4 | 55.9 | 0.99 |
| Plate | y = mx + c | 42.51 | 53.01 | 0.94 |
| Bath | y = mx + c | 9.96 | 49.43 | 0.95 |

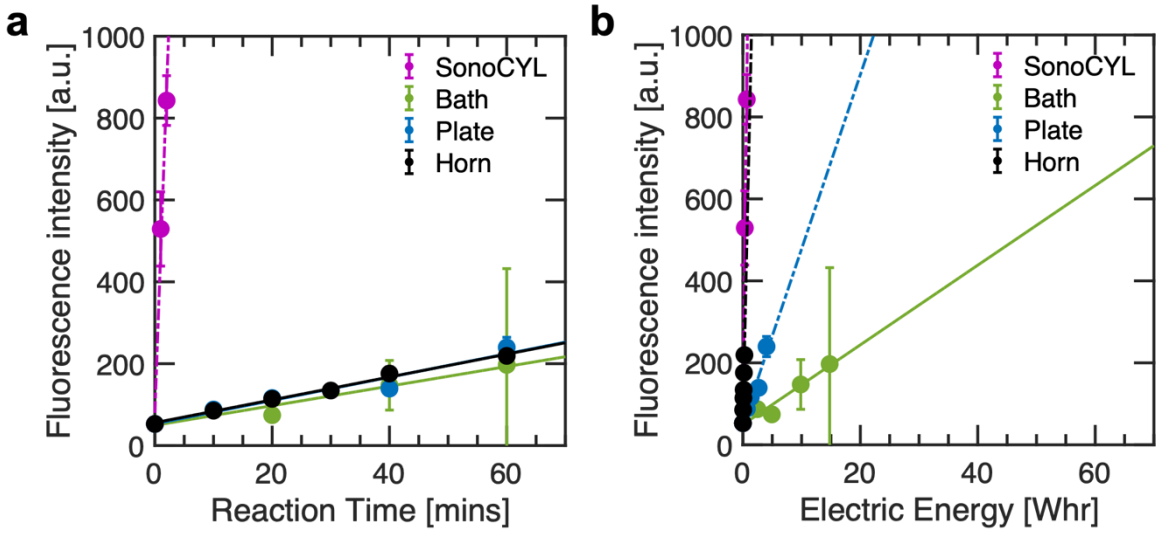



**Figure 3.15. (a)** The fluorescence intensity of HTA ($\lambda_{ex}$ = 310 nm; $\lambda_{em}$ = 425 nm) vs reaction time for the four sonochemical reactors using TA assay (1mM): SonoCYL (1 MPa), immersed horn reactor (40 kHz), plate reactor (583 kHz), and bath reactor (35 kHz) at 9% DC. **(b)** The fluorescence intensity of HTA vs the input electric energy for the four sonochemical reactors. The slope of the linear regression represents the •OH production rate in the reaction. Each value is the average of three trials, and the error bars indicate the standard deviations.

**Table 3.10.** The table shows the •OH production rate and SE for the four sonochemical reactors using TA assay. The •OH production rate and the SE were determined from the slope of the linear regression. The rate may also be converted directly into SE by dividing the rate by the nominal electrical power and converting the time unit from minutes to hours. The nominal electric power is presented from Table 3.4. Note that the nominal electrical power used for SonoCYL in the TA assay differed from that reported for SonoCYL in the Res-DHB dosimetry, as explained in Section 3.1.6.

| Reactor | Nominal electric power [W] | Rate [intensity $min^{-1}$] | SE [intensity $Whr^{-1}$] |
|---|---|---|---|
| SonoCYL | 19.21 | 395 | 1200 |
| Horn | 0.26 | 2.79 | 651.4 |
| Plate | 4.03 | 2.85 | 42.51 |
| Bath | 14.77 | 2.39 | 9.96 |

Our results suggest that reactor design plays a critical role in enhancing both •OH production rate and efficiency. While much of the literature identifies the optimal frequency range for sonochemistry as 300–500 kHz[47], the results demonstrate that reactor geometry may significantly influence performance. For instance, the 1 MHz SonoCYL outperformed the 583 kHz plate, and the 40 kHz immersed horn produced detectable •OH while the 35 kHz bath did not, despite their similar driving frequencies. These results highlight that focused acoustic energy and reactor design are key elements for an efficient sonochemical reactor. The SonoCYL effectively overcomes the limitations of dispersed acoustic energy in conventional reactor design and enables faster reaction and more efficient •OH production.

Additionally, the SonoCYL exhibited highly reproducible experimental results. Acoustic inertial cavitation is inherently stochastic, making it difficult to control and limiting the industrial scale up of sonochemical reactions. Moreover, the acoustic pressure is spatially dependent, making it crucial to control the position of the reaction vessel relative to the liquid medium (volume and height) and transducer location[145,146]. For example, Rochebrochard et al. reported a nine-fold difference in SE depending on the liquid height in a plate system. Similarly, Asakura et al. showed a seven-fold variation in SE values with different liquid heights in another plate system. Consequently, precise positioning of the reactor vessel is essential to obtain reproducible data, but this is difficult to achieve in practice with conventional sonochemical reactors. The design of SonoCYL allows accurate control of the acoustic field within the reaction vessel, resulting in highly reproducible experimental results.

### 3.2.5. Comparisons with literature

The SE of the SonoCYL reactor was compared with various sonochemical reactors reported in the literature across different operating frequencies (Table 3.11). The data were categorised by different sonochemical reactors (border colours), power determination methods (face colours), and dosimetry methods (marker shapes) in Figure 3.16.

There was no obvious trend for the SE shown in Figure 3.16. It demonstrated that SE were affected by various factors including the input energy determination, the type of •OH probe, and the sonochemical reactor design. For example, the horn at 40 kHz using Res-DHB (black, circle) had a higher SE than other reactors. This is likely attributed to the high sensitivity of Res-DHB compared to other dosimetry methods. Moreover, the input electric energy and calorimetric energy were used to compare the SonoCYL performance to other literature. The results showed that the SonoCYL (in purple) had a larger SE compared to other reactors at the same frequency (1 MHz) and reactors that

operate at all other reported frequencies, regardless of whether the input energy calculation was based on electrical energy (filled, purple) or calorimetric energy (unfilled, purple). These findings suggest that SonoCYL is more efficient than conventional reactors in the literature.

This highlights the lack of standardisation in SE determination. It is important that the sonochemistry community reaches a standard protocol to determine the SE, as well as clear reporting of the method used. This will enable more reliable comparisons across studies and support the advancement of reactor design and the general field of sonochemistry in the future.

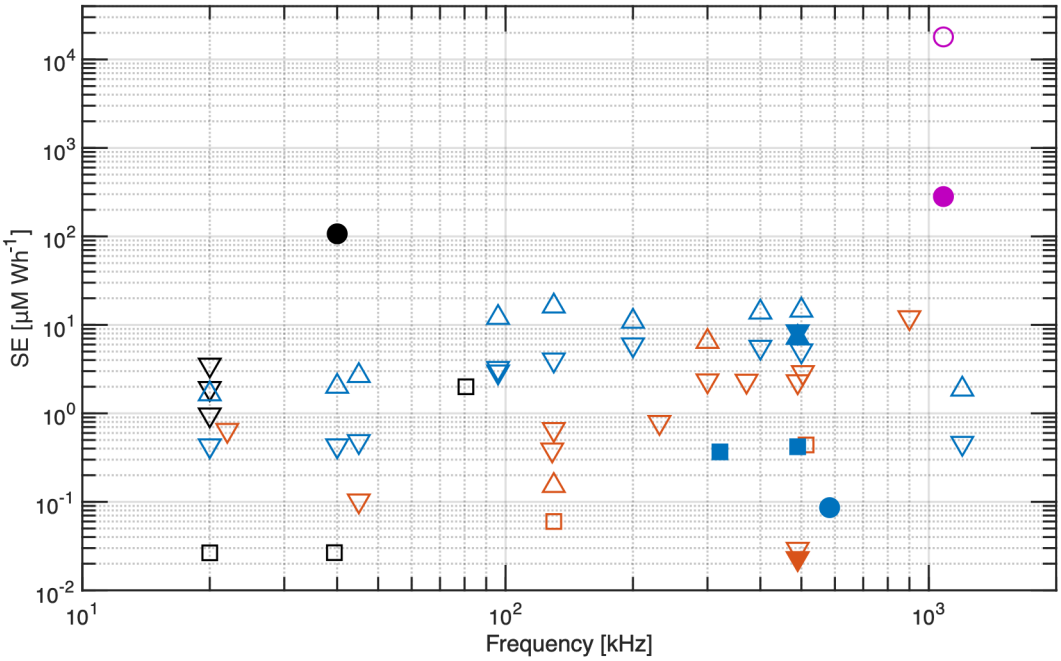



**Figure 3.16.** SE (•OH concentration production per unit energy) vs the operating frequency of the sonochemical reactor. **Colours**: Purple: SonoCYL; Orange: Plate (direct ultrasonic irradiation from the transducer to the reaction solution); Blue: Plate (indirect ultrasonic irradiation from the transducer to the reaction solution); Black: Horn. **Face colours**: Filled: Drive electrical power; Unfilled: Calorimetry. **Marker shapes**: Circle (●): Res-DHB; Upside down triangle (▼): Weissler reaction; Triangle (▲): Fricke reaction; Square (■): terephthalic acid.

**Table 3.11.** Selected reports on sonochemical efficiency results (Weissler reaction, Fricke reaction and terephthalic acid assay) obtained from the literature. This is reported in concentration of hydroxyl radicals produced per unit energy (Whr).

| | | | | | Method (μM $Whr^{-1}$) | | | |
|---|---|---|---|---|---|---|---|---|
| **Reactor design** | **Frequency (kHz)** | **Load power (W)** | **Reaction volume ($dm^3$)** | **Ultrasonic power measurement** | **Weissler reaction** | **Fricke reaction** | **Terephthalic acid** | **Ref.** |
| Plate (Direct) | 45.0 | 50 | 1.92 | Drive electric power | 1.03 | - | - | [146] |
| Plate (Direct) | 128.9 | 50 | 0.58 | Drive electric power | 3.97 | - | - | [146] |
| Plate (Direct) | 130.0 | 100 | 0.30 | Calorimetry | 13.20 | 15.24 | 0.60 | [147] |
| Plate (Direct) | 231.0 | 50 | 0.30 | Drive electric power | 8.04 | - | - | [146] |
| Plate (Direct) | 300.0 | 60 | 0.30 | Calorimetry | 14.40 | 21.60 | - | [148] |
| Plate (Direct) | 371.0 | 14.9 | 0.53 | Calorimetry | 13.45 | - | - | [145] |
| Plate (Direct) | 490.0 | 5–50 | 4.00 | Drive electric power | 0.33 | - | - | [48] |
| Plate (Direct) | 490.0 | 30 | 0.11 | Drive electric power | 23.24 | - | - | [48] |
| Plate (Direct) | 513.0 | 39 | 0.60 | Calorimetry | - | - | 4.12 | [149] |
| Plate (Direct) | 900.0 | 76 | 0.10 | Calorimetry | 12.11 | - | - | [150] |
| Plate (Indirect) | 20.0 | 40–200 | 0.05 | Calorimetry | 8.64 | 16.56 | - | [47] |
| Plate (Indirect) | 40.0 | 35 | 0.05 | Calorimetry | 8.64 | 20.16 | - | [47] |
| Plate (Indirect) | 45.0 | 110–220 | 0.05 | Calorimetry | 9.65 | 26.64 | - | [47] |
| Plate (Indirect) | 96.0 | 50–100 | 0.05 | Calorimetry | 59.04 | 120.96 | - | [47] |
| Plate (Indirect) | 96.0 | 50–150 | 0.05 | Calorimetry | 64.80 | - | - | [47] |
| Plate (Indirect) | 130.0 | 50–200 | 0.05 | Calorimetry | 80.64 | 162.72 | - | [47] |
| Plate (Indirect) | 200.0 | 140–200 | 0.05 | Calorimetry | 119.52 | 109.44 | - | [47] |
| Plate (Indirect) | 321.0 | 100 | 0.50 | Drive electric power | - | 23.54 | 4.75 | [42] |
| Plate (Indirect) | 400.0 | 120 | 0.05 | Calorimetry | 112.32 | 138.96 | - | [47] |
| Plate (Indirect) | 490.0 | 40 | 0.01 | Drive electric power | 84.00 | 72.00 | 4.20 | [6] |
| Plate (Indirect) | 500.0 | 10–40 | 0.05 | Calorimetry | 102.24 | 146.16 | - | [47] |
| Plate (Indirect) | 1200.0 | 120 | 0.05 | Calorimetry | 9.22 | 18.72 | - | [47] |
| Horn | 20.0 | 70 | 0.10 | Calorimetry | 2.00 | - | - | [150] |
| Horn | 20.0 | 106 | 0.05 | Drive electric power | 1.66 | 0.25 | - | [151] |
| Horn | 20.0 | 15.8 | 0.20 | Calorimetry | - | - | 26.54 | [149] |
| Horn | 39.4 | 13.5 | 0.20 | Calorimetry | - | - | 26.09 | [149] |
| Horn | 80.6 | 1.05 | 0.10 | Calorimetry | - | - | 20.00 | [149] |

## 3.3. Conclusions

This research chapter introduced the design and characterisation of a novel sonochemical reactor, SonoCYL, which employs cylindrically converging acoustic waves to focus energy within a focal reaction volume of approximately 1.16 μL. The reactor was evaluated through both acoustic and chemical characterisation. Hydroxyl radical generation was quantified using a highly sensitive and selective fluorescent probe Res-DHB, while sonochemical efficiency was assessed under various operating conditions, including acoustic pressure and the number of acoustic input cycles.

Sonochemical efficiency increased with acoustic pressure, with optimal performance observed at 15.1 $MPa_{pkpk}$ and 100 acoustic cycles. Under these optimised conditions, Res-DHB dosimetry showed that SonoCYL achieved a •OH production rate of 159 $\mu M_{\bullet OH}$ $min^{-1}$, which is at least two orders of magnitude higher than conventional sonochemical reactors, including ultrasonic baths, immersed horns, and plate reactors. The corresponding sonochemical efficiency was 273 $\mu M_{\bullet OH}$ $Whr^{-1}$, representing at least a twofold improvement over other conventional reactor designs. Similar trends in enhanced •OH production rate and sonochemical efficiency were also observed using the TA assay method, confirming the improved sonochemical performance of SonoCYL. These findings highlight the important role of reactor geometry and acoustic operating conditions in enhancing sonochemical performance, and this design may inform future developments for industrial scale sonochemical systems.

# 4. Sonocatalytic seawater splitting for hydrogen production

Hydrogen is widely recognised as a key energy vector for achieving the global transition towards net-zero carbon emissions. When used as a clean fuel or industrial feedstock, its utilisation produces only water as a by-product, making hydrogen a key pillar of a green energy economy[152]. Among the various production pathways, direct seawater splitting is particularly attractive because seawater is an abundant and virtually inexhaustible resource for hydrogen generation. However, conventional seawater electrolysis faces several significant technological challenges that limit its deployment[53,153]. Most commercial electrolysers depend on scarce and costly noble-metal catalysts, such as platinum and iridium, making widespread implementation economically challenging[154]. In addition, the complex chemical composition of natural seawater promotes severe electrode biofouling by organic matter[153]. It also leads to the deposition of insoluble inorganic precipitates that block active reaction sites and the formation of toxic chlorine gas, which accelerates catalyst degradation and deactivation. Alternative solar-driven approaches, including photocatalytic seawater splitting, also suffer from low quantum efficiencies and poor photocatalyst stability under highly saline conditions[155,156].

Sonochemical hydrogen production, commonly referred to as sonohydrogen, has emerged as a promising alternative based on ultrasound-driven water splitting (sonolysis)[10,68]. This process is driven by acoustic cavitation, in which gas-vapour bubbles within the liquid undergo rapid growth followed by violent inertial collapse. The implosion of these microbubbles generates highly localised transient hotspots with extreme temperatures and pressures. Under such conditions, water molecules trapped within the collapsing bubbles undergo thermal pyrolysis, producing highly reactive radical species, including hydrogen, hydroxyl, and hydroperoxyl radicals[42]. Subsequent radical recombination reactions lead to the formation of molecular hydrogen[157]. The sonochemical hydrogen production mechanism is described in detail in Section 2.5.2. Unlike electrochemical systems, sonolysis occurs throughout the bulk liquid phase rather than at a solid-liquid interface, avoiding operational challenges associated with electrode-based technologies, including biofouling and scale deposition[34]. This also offers greater scalability by decoupling hydrogen production from the available surface area of an electrode. Furthermore, sonochemical water splitting is performed under ambient conditions, offering potential energy and cost advantages over thermally assisted photocatalytic systems, which often require operating temperatures between 100 and 300 °C[63,64].

Sonochemical hydrogen production may serve as a green hydrogen pathway when coupled with renewable energy sources, including solar and wind power. Despite these advantages, sonohydrogen technology remains at an early stage of development. A comprehensive understanding of the optimal

acoustic and catalytic parameters governing sonohydrogen production is still lacking[67]. A detailed review of current sonochemical hydrogen production research is presented in Section 2.5.3. Most reported sonocatalysts require complex and energy-intensive synthesis procedures that hinder their practical scalability[65,71,72]. Moreover, only a limited number of studies have successfully demonstrated sustained hydrogen production from natural, untreated seawater without significant catalyst degradation[72]. Consequently, developing efficient sonochemical hydrogen production using low-cost and chemically robust sonocatalysts remains essential.

This chapter presents an effective and sustainable strategy for converting seawater into hydrogen using a low-cost, corrosion-resistant titanium dioxide ($TiO_2$) catalyst under high-frequency ultrasound (780 kHz) at room temperature[158]. This study investigates the optimal acoustic and catalytic conditions for hydrogen production, focusing on parameters such as pulsed ultrasound cycle number and catalyst concentration, and examines their relationship to the cavitation noise index. In addition, single-bubble dynamics simulations and Electron Paramagnetic Resonance (EPR) spectroscopy are used to study the effects of a seawater environment on sonochemical hydrogen production. These analyses provide insights into the physical and chemical mechanisms influencing hydrogen generation. Finally, the sonochemical efficiency of the system is evaluated and compared with values reported in other studies.

## 4.1. Materials and methods

This section details the materials, experimental setup, and methodologies used in this study. It includes the preparation of reaction solutions and reagents, measurement and processing of cavitation noise signals, and the analytical techniques used to assess hydrogen production. Additionally, catalyst characterisation techniques and investigations into the effect of salt on sonochemical hydrogen production are presented, including single bubble simulations and EPR spectroscopy.

### 4.1.1. Materials

The following chemicals were used: Calcium chloride (anhydrous, granular, ≤7.0 mm, ≥93.0%, Sigma-Aldrich), Magnesium chloride (anhydrous for synthesis, Sigma-Aldrich), Potassium chloride (ACS reagent, 99.0–100.5%, Sigma-Aldrich), Sodium bicarbonate (ACS reagent, ≥99.7%, Sigma-Aldrich), Sodium chloride (ACS reagent, ≥99.0%, Sigma-Aldrich), Sodium sulfate (ACS reagent, ≥99.0%, Sigma-Aldrich), Titanium(IV) oxide (anatase, 99.6% metals basis, Thermo Scientific Chemicals). The gases used were as follows: Argon (Zero grade Ar, BOC), Helium (A Grade,

99.996%, BOC). Deionised filtered Type 1 water was obtained from a water purification system (Millipore Direct Q5-UV). The natural seawater was sourced from the Atlantic coast of Cornwall, United Kingdom, provided by Natural Seawater Supplier. The high purity spin trap agent 5,5-dimethyl-1-pyrroline-N-oxide (DMPO) (> 99%) was purchased from Dojindo Molecular Technology Co., Ltd. All chemicals were used without further processing unless otherwise stated.

### 4.1.2. Sonochemical reactor system and cavitation noise measurements

The experimental setup is shown schematically in Figure 4.1. It was based on the reactor design described in Chapter 3 but included key modifications. Specifically, a transducer with a resonance frequency of 780 kHz was used because the transducer with a resonance frequency of 1083 kHz used in Chapter 3 was broken and cracked. The replacement transducer has the same dimensions as the one used in Chapter 3 and was the closest available frequency that could be sourced at the time the experiments were conducted. Within this chapter, the operational frequency was kept constant for all experiments to ensure fair comparison of results under consistent conditions. Additionally, an acoustic cavitation noise measurement system was added, which was not present in the previous chapter. In this study, the system was composed of a sonochemical reactor with a maximum input power of 5.1 W (the maximum operating power). In the system, the configuration of the reactor cylindrically focused the acoustic waves generated from the transducer into a reactor vessel, creating a localised, intense acoustic pressure field that triggered sonochemical reactions. The transducer's operating voltage and current were measured. Cavitation noise was recorded by a passive cavitation detector (PCD) and further analysed to determine the cavitation threshold and cavitation noise index. Hydrogen production was analysed via gas chromatography. The catalysts used in this study were untreated, commercially available $TiO_2$ particles. Using economical catalysts eliminated the need for expensive noble metals or energy-intensive complex catalyst synthesis.

The materials used for the construction of the reactor are described in Chapter 3[159]. The ultrasound transducer used was a cylindrical tube piezoelectric ceramic (Navy Type III (PKI802), PZT, Precision Acoustics Ltd) with dimensions of 38 mm outer diameter, 34 mm inner diameter, 25 mm length, and a resonance frequency of 780 kHz.

The signal generation and acoustic measurement system also differed slightly from the setup in Chapter 3, particularly in the choice of oscilloscope. The general experimental setup for sonochemical reaction and noise acquisition was as follows: a waveform generator (Keysight Waveform Generator, 33600A) generated a pulsed sinusoidal wave. The wave was fed through a –20 dB attenuator before

being amplified by a 55 dB radiofrequency amplifier (Electronics & Innovation 1040L RF Amplifier), and finally transmitted to the ultrasound transducer to drive the sonochemical reaction. The driving voltage and current were measured and recorded using an oscilloscope with a sampling frequency of 100 MHz (TiePie Handyscope HS5 USB oscilloscope).

To detect cavitation noise, a PCD (Evident 384V-SU, 3.5 MHz, 0.25", 1304373) was inserted into the cylindrical tube spacer through a hole. This spacer was used to position the PCD directly beneath the PP reaction vial. The noise signal received by the PCD passed through a 1.8 MHz high-pass filter (Thor Labs High-Pass Filter 1.8 MHz, EF509), then into a 5 dB gain preamplifier (EG&G Instruments, Model 5185 Wideband Preamplifier) and a 50 Ω feed-through terminator (Tetratronix 011-0049-01 BNC feed-through termination), and eventually to the oscilloscope. The oscilloscope was interfaced with a computer to record the noise data for subsequent data processing. A high-pass filter was employed to prevent the drive signal from overpowering the PCD signal, which enabled the acquisition of frequencies higher than the drive signal. A terminator was used to match a 50 Ω impedance with the digital oscilloscope.

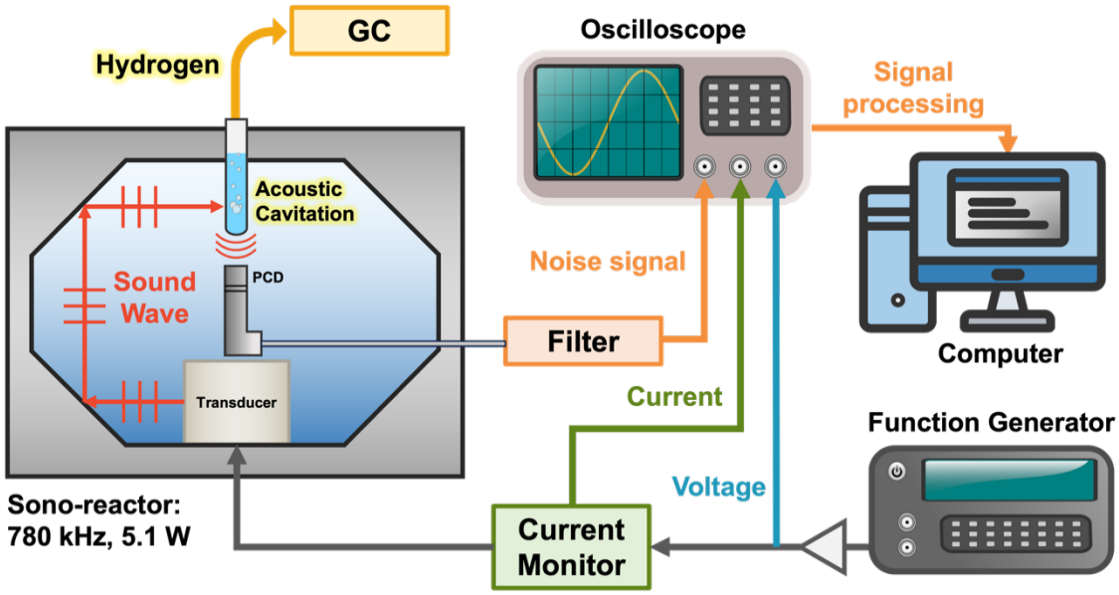



**Figure 4.1.** Schematic of the reactor design and the experimental setup for the sonochemical hydrogen production, alongside an acoustic cavitation noise measurement system.

### 4.1.3. Reaction solution preparation and sonochemical reactions

2.5 mL of reaction solution was used for every reaction using a 5 mL PP reaction vessel (round bottom test tube, Scientific Laboratory Supplies). The reaction solution for the sonochemical acoustic and chemical optimisation tests was DI water with $TiO_2$ (0.3 mg/mL) unless otherwise specified.

Simulated seawater was prepared by dissolving NaCl, $Na_2SO_4$, KCl, and $NaHCO_3$ into DI water. The detailed composition of the simulated seawater is described in Table 4.1. The test parameters of the natural seawater were: salinity 34–36 ppt, nitrates 0–0.9, calcium 400–450 ppm, alkalinity 7.5–8.6 dKH, pH 8.0–8.3, magnesium 1250–1350 ppm, phosphate 0–0.05 ppm [160], and silicate 0–0.1.

**Table 4.1.** Composition of the simulated seawater used in this work. The protocol of preparing the simulated seawater was adapted from Kester et al.[161].

| **Gravimetric salts** | | |
|---|---|---|
| **Salt** | **Molecular weight [g mol$^{-1}$]** | **Mass of salt [g L$^{-1}$]** |
| NaCl | 58.44 | 23.926 |
| $Na_2SO_4$ | 142.04 | 4.008 |
| KCl | 74.56 | 0.677 |
| $NaHCO_3$ | 84.00 | 0.196 |

Before every sonochemical reaction, the reaction solution and headspace were saturated with argon gas by purging the gas into the reaction solution for five minutes. All reactions were performed at ambient temperature and pressure. The standard operating frequency for the ultrasonic reaction was 780 kHz, reaction time was 20 minutes, duty cycle was 4.5% with 100 acoustic cycles and 2.849 ms burst period unless otherwise specified. The operating parameters for the sonochemical reactions are described in Table 4.2 to Table 4.4.

**Table 4.2.** Acoustic parameters and power measurements of the sonochemical hydrogen production under different number of cycles and burst time at a fixed duty cycle.

| | Set up | | | | |
|---|---|---|---|---|---|
| **Parameters** | **The reactor used in this work (SonoCYL)** | | | | |
| **Time [min]** | 20 | 20 | 20 | 20 | 20 |
| **Frequency [kHz]** | 780 | 780 | 780 | 780 | 780 |
| **Number of cycles** | **10** | **30** | **100** | **1000** | **10000** |
| **Burst time [ms]** | **0.2849** | **0.8547** | **2.849** | **28.49** | **284.9** |
| **Duty cycle [%]** | 4.5 | 4.5 | 4.5 | 4.5 | 4.5 |
| | | | | | |
| **Voltage [$V_{rms}$]** | 74.44 | 74.44 | 74.44 | 74.44 | 74.44 |
| **Current [$A_{rms}$]** | 1.51 | 1.51 | 1.51 | 1.51 | 1.51 |
| **Phase angle [degree]** | 3.00 | 3.00 | 3.00 | 3.00 | 3.00 |
| **Electric maximum power [W]** | 114.1 | 114.1 | 114.1 | 114.1 | 114.1 |
| **Nominal electric power [W]** | 5.13 | 5.13 | 5.13 | 5.13 | 5.13 |
| | | | | | |
| **Electric energy [Whr]** | 1.71 | 1.71 | 1.71 | 1.71 | 1.71 |

**Table 4.3.** Acoustic parameters and power measurements of the sonochemical hydrogen production under different power.

| | Set up | | | | |
|---|---|---|---|---|---|
| **Parameters** | **The reactor used in this work (SonoCYL)** | | | | |
| **Time [min]** | 20 | 20 | 20 | 20 | 20 |
| **Frequency [kHz]** | 780 | 780 | 780 | 780 | 780 |
| **Number of cycles** | 100 | 100 | 100 | 100 | 100 |
| **Burst time [ms]** | 2.849 | 2.849 | 2.849 | 2.849 | 2.849 |
| **Duty cycle [%]** | 4.5 | 4.5 | 4.5 | 4.5 | 4.5 |
| | | | | | |
| **Voltage [$V_{rms}$]** | **55.83** | **65.13** | **68.86** | **71.65** | **74.44** |
| **Current [$A_{rms}$]** | 1.10 | 1.31 | 1.39 | 1.45 | 1.51 |
| **Phase angle [degree]** | 3.00 | 3.00 | 3.00 | 3.00 | 3.00 |
| **Electric maximum power [W]** | 60.87 | 85.23 | 96.23 | 104.96 | 114.1 |
| **Nominal electric power [W]** | 2.74 | 3.84 | 4.33 | 4.72 | 5.13 |

**Table 4.4.** Acoustic parameters and power measurements of the sonochemical hydrogen production under different reaction time.

| | Set up | | | | |
|---|---|---|---|---|---|
| **Parameters** | **The reactor used in this work (SonoCYL)** | | | | |
| **Time [min]** | **20** | **40** | **60** | **120** | **180** |
| **Frequency [kHz]** | 780 | 780 | 780 | 780 | 780 |
| **Number of cycles** | 100 | 100 | 100 | 100 | 100 |
| **Burst time [ms]** | 2.849 | 2.849 | 2.849 | 2.849 | 2.849 |
| **Duty cycle [%]** | 4.5 | 4.5 | 4.5 | 4.5 | 4.5 |
| | | | | | |
| **Voltage [$V_{rms}$]** | 74.44 | 74.44 | 74.44 | 74.44 | 74.44 |
| **Current [$A_{rms}$]** | 1.51 | 1.51 | 1.51 | 1.51 | 1.51 |
| **Phase angle [degree]** | 3.00 | 3.00 | 3.00 | 3.00 | 3.00 |
| **Electric maximum power [W]** | 114.1 | 114.1 | 114.1 | 114.1 | 114.1 |
| **Nominal electric power [W]** | 5.13 | 5.13 | 5.13 | 5.13 | 5.13 |
| | | | | | |
| **Electric energy [Whr]** | **1.71** | **3.42** | **5.13** | **10.26** | **15.39** |

### 4.1.4. Cavitation noise signal processing

The cavitation noise signal was segmented within the cavitating time window and transformed by Fast Fourier Transform (FFT) using the MATLAB function. The FFT spectrum was then integrated by the MATLAB trapezoidal numerical method to yield an integrated voltage value, $V_{sample}$. This operation was repeated for 100 bursts within the same trial; the 100 voltage values were averaged out, then further averaged by at least two independent trials to obtain the sample average voltage value, $V_{avg\ sample}$. The same method was used to determine the average voltage value of the sonication of degassed water, $V_{avg\ degassed}$. Finally, the normalised cavitation noise index was calculated using Eq. 4.1.

$$\text{Normalised cavitation noise index (dB)} = 20 \log \left( \frac{V_{avg\ sample}}{V_{avg\ degassed}} \right) \qquad \text{(Eq. 4.1)}$$

### 4.1.5. Cavitation threshold determination

The cavitation threshold is defined as the smallest power at which cavitation is detected in the long-duration and constant exposure of acoustic cycles[162]. The cavitation noise index was measured and plotted against the average operating power. The cavitation threshold power was identified from the rise of the fitted sigmoid curve, adapted from the method of Jonnalagadda et al.[163]. The data were fitted using a sigmoid function according to Eq. 4.2 with MATLAB Curve fitting Toolbox.

$$\text{Cavitation noise index} = f(x) = (a–d) \left[ e^{\left(-e^{(-b(x-c))}\right)} \right] \qquad \text{(Eq. 4.2)}$$

where f(x) is the normalised cavitation noise index, x is the power, and a, b, c, and d are the fitting parameters.

### 4.1.6. Hydrogen gas analysis

The amount of hydrogen was quantified using a GC (Shimadzu Nexis GC-2030) equipped with a dielectric-barrier discharge ionisation detector and helium as carrier gas. A Carboxen®-1010 PLOT Capillary GC Column (Supelco, L × I.D. 30 m × 0.32 mm, average thickness 15 μm) was used as the analytical column. The oven temperature was set at a constant 40 °C for 10 minutes, corresponding to the total run time, with hydrogen eluting at a retention time of 2.52 minutes. The injection temperature was set at 160 °C under 5:1 split ratio. The column flow was set at 2.81 mL/min, and the

purge flow was set at 6.0 mL/min, making a total flow of 22.8 mL/min with a pressure of 130 kPa and a linear velocity of 45.0 cm/s. The BID was kept at 260 °C with a sampling rate of 40 ms and a discharge gas flow of 50 mL/min.

The GC method was co-developed by the author, Dr. Pankaj Sinhmar, and the Shimadzu GC team, as this was a newly established system in the laboratory. Initial parameters were set according to recommendations from Shimadzu engineers based on their experience with hydrogen gas analysis. The author and Dr. Pankaj Sinhmar subsequently refined several parameters, including oven temperature, column flow rate, purge flow, and split ratio, to optimise peak sharpness in the chromatogram. The guiding criteria were run efficiency in terms of time and helium consumption, and the absence of ghost peaks, ensuring complete column purging between runs.

At the start of each experimental day, a blank run was performed prior to sample analysis using the same method described above, with the exception that 30 mL of argon was injected in place of a sample. This served to purge and condition the column. The reduced accuracy typically observed in the first run of the day is likely attributed to moisture adsorption in the system overnight, which is cleared by this blank run.

Before every GC measurement, 30 mL of argon gas was purged through the injector to ensure there was minimal leftover gas sample or air at the injector port. For the analysis, 2.5 mL of headspace gas in the reaction vessel was extracted and injected into the GC for analysis with a gas-tight syringe. The hydrogen retention time was observed at 2.52 minutes. Figure 4.2 presents a representative GC chromatogram of the hydrogen produced from sonochemical water splitting from DI water and natural seawater.

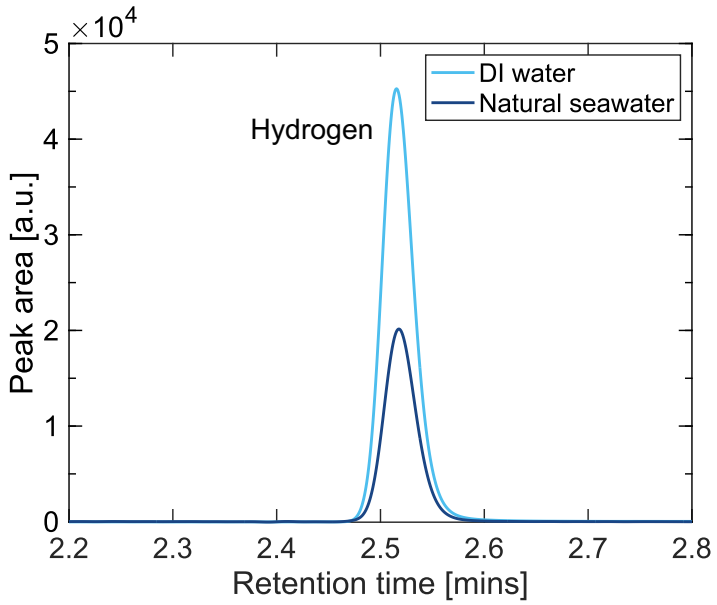



**Figure 4.2.** A representative GC chromatogram of hydrogen produced from sonochemical water splitting from DI water and natural seawater.

The GC-BID system was calibrated by an external standard method using 50 ppm, 525 ppm, and 1000 ppm of hydrogen gas with He as the balance gas. The peak area of the GC signal was converted to the concentration of gas (ppm) using the calibration curve. The calibration curve of hydrogen in gas chromatography is shown in Figure 4.3. The calibration curve exhibited strong linearity across the evaluated concentration range between 50 to 1000 ppm, with an $R^2$ value of 0.9991, indicating low calibration error. While the highest experimental concentrations reached approximately 4200 ppm, exceeding the upper limit of the standard gas range, this extrapolation is validated by manufacturer specifications. According to the Shimadzu GC-BID operating specifications, the detector maintains a wide linear dynamic range up to 4.81% for hydrogen gas (corresponding to 48,100 ppm), which is well above the maximum concentration measured in these experiments[164]. Therefore, the extrapolated values up to 4200 ppm are considered analytically reliable, though they may carry a slightly higher margin of uncertainty than those within the bounded calibration window.

The instrumental Limit of Detection (LOD) of the GC-BID system is 0.05 ppm (or 50 ppb), as specified in the Shimadzu Nexis GC-2030 technical specifications[165]. Following IUPAC guidelines, the limit of quantification (LOQ) was determined as three times the LOD (LOQ = 3 × LOD), corresponding to 0.15 ppm[160]. Based on the calibration curve presented in Figure 4.3, the LOD and LOQ correspond to peak areas of approximately 2 and 6, respectively. Therefore, hydrogen production values corresponding to peak areas below the LOQ (peak area < 6) were considered unquantifiable, while values below the LOD (peak area < 2) were considered undetectable. The

hydrogen production rate reported in this study exceed this quantification limit, ensuring the analytical reliability of the low-value data points.

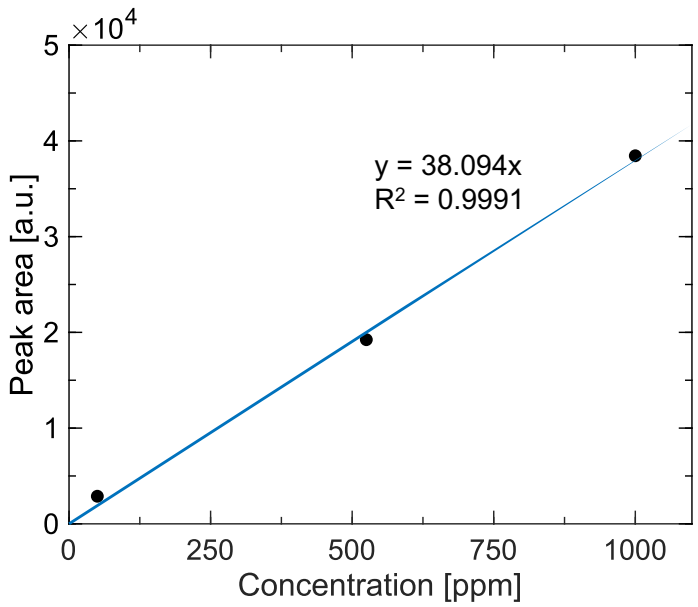



**Figure 4.3.** The calibration curve of hydrogen gas in gas chromatography. The best fit line has an equation y = 38.094x, $R^2$ = 0.9991. Each value is the average of three trials, and the error bars (overlap with the markers) indicate the standard deviation.

The volume and number of moles of the hydrogen produced is estimated with the ideal gas law.

The volume of gas is calculated by Eq. 4.3.

$$V_{Hydrogen}(mL) = (c)(V_{total})(10^{-6}) \qquad \text{(Eq. 4.3)}$$

c is the hydrogen concentration (ppm).

$V_{total}$ is the total volume of gas injected into the gas chromatography. 2.5 mL of gas product was injected to the instrument for every experiment.

The number of moles of hydrogen is estimated by Ideal Gas Law Eq. 4.4.

$$n_{hydrogen} = \frac{(p)\,(V_{hydrogen})}{(R)(T)} \qquad \text{(Eq. 4.4)}$$

n is the number of moles of hydrogen.

p is the pressure of the gas. The atmospheric pressure value was used here (101.325 kPa).

$V_{hydrogen}$ is the volume of hydrogen gas.

R is the ideal gas constant (8.314 J $K^{-1}$ $mol^{-1}$).

T is the absolute temperature of the gas. The room temperature was used here (293.15 K).

An example calculation of hydrogen production is shown in Appendix Section A.3.

### 4.1.7. Collapse temperature estimation from single bubble simulation

**Contribution statement:** Dr. Davide Bernardo Preso developed the bubble simulation methodology and conducted the simulations.

Single spherical bubbles in water at different salinity were numerically investigated with the Keller-Miksis model with Eq. 4.5[166].

$$(1 - \mathrm{Ma})R\ddot{R} + \frac{3}{2}\left(1 - \frac{\mathrm{Ma}}{3}\right)\dot{R}^2 = \frac{1}{\rho}(1 + \mathrm{Ma})\left(p_I - p_\infty\right) + \frac{R}{\rho c}\frac{\partial p_I}{\partial t} \qquad \text{(Eq. 4.5)}$$

where R is the bubble radius, $\mathrm{Ma} = \dot{R}c^{-1}$ is the Mach number, ρ is the liquid density, c is the speed of sound in the liquid, $p_I$ is the liquid pressure at the bubble-liquid interface, and $p_\infty$ is the liquid pressure in the far field. The overdot notation indicates differentiation with respect to time. The interface pressure is given by Eq. 4.6.

$$p_I = p_{b0}\left(\frac{R_0}{R}\right)^{3\gamma} - \frac{2S}{R} - \frac{4\mu\dot{R}}{R} \qquad \text{(Eq. 4.6)}$$

where γ is the heat capacity ratio, which was set to 1.4, S is the surface tension, μ is the liquid viscosity. This model assumed adiabatic compression of the bubble contents with pressure $p_{b0}$ at maximum expansion, consisting of non-condensable gas $p_{g0}$ and water vapour $p_v$, the latter arbitrarily taken as 30% of the liquid vapour pressure at ambient temperature. The Keller-Miksis equation was solved with a fourth-order Runge-Kutta method. The collapse temperature was estimated with adiabatic assumption from a bubble of initial diameter of 25 μm, with $p_{g0}$ of 10 Pa and an initial temperature of 25 °C[167]. The parameters used for the simulations are listed in Table 4.5.

**Table 4.5.** The parameters used for the single bubble simulations.

| NaCl [M] | Vapour pressure†† [Pa] | Density [kg m$^{-3}$][168] | Viscosity ×10$^4$ [Pa s$^{-1}$][169] | Surface tension [N m$^{-1}$][170] | Speed of sound [m s$^{-1}$][171] |
|---|---|---|---|---|---|
| 0.10 | 2295.87 | 1001.16 | 8.94 | 0.7279 | 1506.33 |
| 0.25 | 2289.70 | 1007.21 | 9.08 | 0.7289 | 1515.83 |
| 0.48 | 2280.30 | 1017.09 | 9.29 | 0.7326 | 1530.39 |
| 0.75 | 2269.36 | 1026.75 | 9.54 | 0.7352 | 1547.48 |
| 1.00 | 2259.33 | 1036.21 | 9.72 | 0.7377 | 1563.31 |

### 4.1.8. EPR spectroscopy

EPR spectroscopy is an analytical technique used to detect and characterise species containing unpaired electrons, such as radicals, and to investigate their local chemical environments[172,173]. The technique is based on the interaction between the magnetic moment of an unpaired electron and an externally applied magnetic field ($B_0$). When a paramagnetic species is exposed to a magnetic field, the electron spin states split into two energy levels through a phenomenon known as Zeeman splitting[172,173]. These levels correspond to a lower-energy state aligned parallel to the magnetic field ($M_s = -1/2$) and a higher-energy state aligned antiparallel to the field ($M_s = +1/2$). When microwave radiation of a specific frequency is applied, resonance absorption occurs if the microwave energy matches the energy difference between the two spin states, as described by Eq. 4.7.

$$\Delta E = h\nu = g\mu_B B_0 \qquad \text{(Eq. 4.7)}$$

where ΔE is the energy difference between the spin states, h is Planck's constant, ν is the microwave frequency, g is the electron g-factor, and μB is the Bohr magneton.

The absorbed energy induces transitions between the spin states, generating an absorption signal that is processed to produce an EPR spectrum. The g-factor is an important spectroscopic parameter because it determines the magnetic field strength at which resonance occurs and provides information about the electronic environment of the unpaired electron.

In addition to Zeeman splitting, unpaired electrons may interact with nearby magnetic nuclei, giving rise to hyperfine interactions[172,173]. These interactions cause further splitting of the EPR signal and provide information regarding the local structure and chemical environment of paramagnetic species.

†† The vapour pressure is calculated by applying Raoult's Law.

Analysis of the hyperfine splitting patterns may reveal the identity and number of neighbouring nuclei, such as hydrogen or nitrogen atoms, that interact with the unpaired electron.

In the present study, EPR spectroscopy was used to identify radical species generated during sonochemical reactions. As these radicals are highly reactive and have extremely short lifetimes, a spin-trapping agent, 5,5-dimethyl-1-pyrroline N-oxide (DMPO), was added to the reaction solution[174]. DMPO reacts with the generated radicals to form more stable radical adducts such as DMPO-H and DMPO-OH, enabling their detection and characterisation by EPR spectroscopy.

The EPR spectroscopy methodology employed in this study was developed collaboratively by the author, Dr. William Myers, and Zhangyue (Jennifer) Xie based on their collective experience in conducting EPR experiments. EPR spectra were measured at room temperature on a continuous-wave Bruker EMX micro spectrometer with an X-band frequency of 9.864 GHz. The detailed spectrometer parameters were as follows: central field of 3515 G; scanning width of 100 G; sweep time of 40 seconds with a total of 16 scans; receiver gain of 64 dB; modulation amplitude of 1 G; microwave attenuation of 16 dB; microwave power of 5.024 mW. Sample solutions with 25 mM DMPO were transferred to 50 µl quartz capillary tubes and then placed in the EPR cavity.

EPR simulations were performed using the EasySpin package in MATLAB. EasySpin is a computational toolbox designed for the visualisation, simulation, and fitting of EPR spectra[175]. By generating theoretical spectra and comparing them with experimental spectra, it enables the determination of key spectroscopic parameters, including g-values and hyperfine coupling constants, to identify paramagnetic species and characterise their local chemical environments.

The theoretical spectra in the study were generated using the *garlic* simulation function, which is designed for isotropic, fast-motion continuous-wave (CW) EPR spectra of solution-phase radicals with an electron spin of ($S = 1/2$) coupled to one or more nuclear spins ($I \geq 1/2$) with relatively small hyperfine interactions[175]. As the radical species investigated in this study were the DMPO-OH and DMPO-H spin adducts, the *garlic* function was well-suited for modelling their spectra[176].

Initial spin system parameters were defined based on the expected radical adducts and included the electron spin ($S = 1/2$), the coupled nuclei and the number of interacting nuclei, isotropic g-values, hyperfine coupling constants (A), linewidths, and the relative weighting of each radical component. The garlic algorithm calculates resonance fields using the analytical Breit-Rabi expression and incorporates line-broadening effects associated with rapid molecular tumbling by using the Kivelson

formula[175,177,178]. Further details of the simulation principle are described in Stoll and Schweiger (2006)[175].

The simulated spectra were iteratively fitted to the experimental data using the EasySpin *esfit* function, which utilises least-squares optimisation[175]. This fitting procedure enabled the determination of spectroscopic parameters, including g-values and hyperfine coupling constants, identifying the presence of radical species and their local chemical environments through comparison with the experimental spectra. The scripts used for data processing and EPR spectral fitting are provided in Appendix A.6.1.

### 4.1.9. SEM images

The scanning electron microscope (SEM) images were obtained using a field emission gun scanning electron microscope (FEG-SEM, Zeiss Sigma 300) at an electron high tension voltage of 3.0 kV and a working distance of 4.6–4.7 mm.

## 4.2. Results and discussion

This section first investigates the optimisation of sonochemical hydrogen production using $TiO_2$ catalysis, focusing on the effects of acoustic conditions and catalyst concentration. After identifying the optimal conditions, this research extends the analysis to salty environments, including seawater, to examine how salt influences hydrogen production in the presence of $TiO_2$. The observed discrepancy between hydrogen production in pure and seawater is explored by evaluating both physical and chemical effects through single bubble simulations and radical analysis through EPR, respectively. Finally, the results from this study are compared with previous studies in the literature to assess the relative performance and efficiency of this system.

### 4.2.1. Sonochemical hydrogen production optimisations

The reactor was operated under a constant duty cycle at 4.5%. This was to ensure that the ultrasound energy input remained constant at fixed reaction times across different exposure conditions. Additionally, the low duty cycle prevented the transducer from overheating and avoided thermal damage. At this constant duty cycle, the impact of catalyst concentration, ultrasound pulse width, and ultrasound drive power were first investigated.

Figure 4.4 (a) compares the hydrogen production rates obtained in deionised water with and without the presence of the $TiO_2$ catalyst. The mean hydrogen production rate was approximately 25% higher when the $TiO_2$ catalyst was present than in the catalyst-free DI water control. However, a Welsh's t-test yielded a p-value of 0.25, indicating that the observed increase was not statistically significant. A similar trend was observed for the cavitation noise index, where a higher mean value was recorded in the presence of $TiO_2$ compared with DI water alone. However, this difference was also statistically non-significant ($p = 0.06$). In line with previous studies, the solid-liquid phase boundaries between $TiO_2$ and water likely provide preferential sites for cavitation bubble formation due to the decreased bubble nucleation energy barrier[179,180]. This heterogeneous nucleation mechanism may therefore contribute to the observed increases in both the average cavitation noise index and hence the hydrogen production rate. However, the lack of statistical significance ($p > 0.05$) for both parameters likely results from the limited number of experimental replicates ($n = 3$ per condition) and the inherently stochastic nature of acoustic cavitation[127]. The random behaviour of cavitation events may introduce considerable experimental variability, resulting in relatively large standard deviations. Consequently, a greater number of experimental replicates are required in future work to reduce uncertainty and determine whether the observed trends are statistically significant.

In addition to cavitation-induced reaction, $TiO_2$ photocatalytic and thermocatalytic processes may also enhance the rate by generating reaction species under light and heat, respectively[73,181]. As a semiconductor, $TiO_2$ generates electron-hole pairs (excitons), and consequently creates intermediate radicals such as •OH for hydrogen production when it absorbs sonoluminescent light (with energy higher than the $TiO_2$ bandgap 3.2 eV) or under the extreme localised temperature in collapsing bubbles[163,182,183]. In this case, it remains unclear how much each process contributes to the total hydrogen production, especially since photocatalytic and thermocatalytic processes involve the formation of electron-hole pairs in the semiconductor, albeit triggered by different energy sources.

Having established that the presence of $TiO_2$ improves sonochemical hydrogen production rates, the study next explored the effect of acoustic cycles on reaction performance to acoustically optimise the sonochemical process. Figure 4.4 (b) presents the hydrogen production rates measured at acoustic cycles ranging from 10 to 10000. The maximum rate was achieved at 100 acoustic cycles under the tested conditions, consistent with earlier findings reported in Chapter 3 using the same setup[159,184]. To reiterate and summarise the explanation, 100 cycles reached an effective balance: the transducer was given enough time to "ring up" and reach maximum displacement to generate sufficient acoustic pressure and initiate inertial cavitation, while the duration remained short enough to prevent excessive

bubble growth via coalescence or rectified diffusion, which may otherwise degas the liquid and suppress cavitation activity[24].

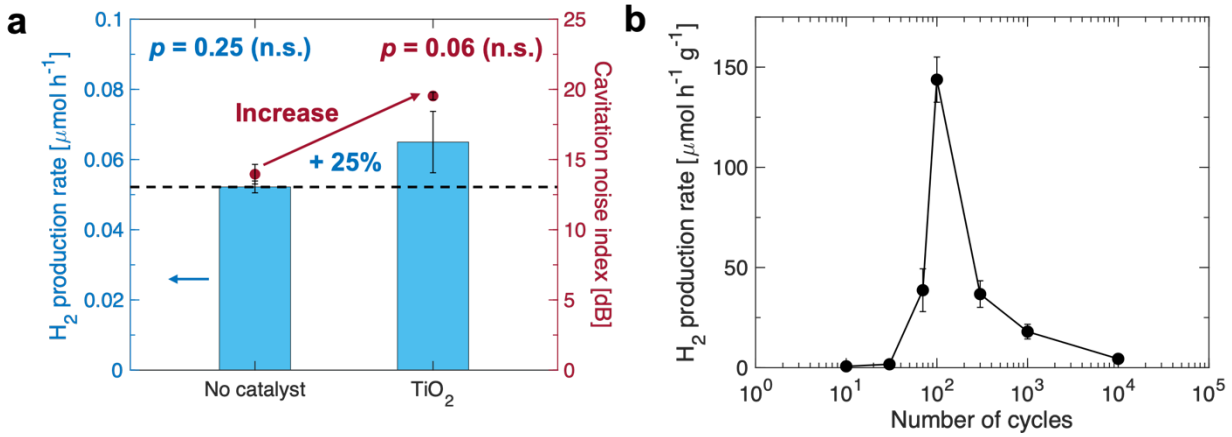



**Figure 4.4. (a)** Comparison of hydrogen production rate (blue bar chart, left) and the cavitation noise index (red points, right) with and without the presence of $TiO_2$ (0.5 mg/mL) (n.s. indicates no statistically significant difference at $p > 0.05$). **(b)** Hydrogen production rate as a function of the number of acoustic cycles.

The acoustic cavitation response of the sonocatalyst $TiO_2$ at different concentrations and reactor powers was investigated further. The normalised cavitation noise index was a proxy for the acoustic cavitation activity at the reaction solution. Here, Figure 4.5 presents the normalised cavitation noise index at varying input power across five different $TiO_2$ concentrations. Specifically, Figure 4.5 (a) shows the sigmoid function fitting for the normalised average cavitation noise index as a function of electrical drive power for five different $TiO_2$ concentrations. Consistent with literature, the cavitation noise index showed a sigmoidal shape over the range of electrical power[163,185]. For all $TiO_2$ concentrations investigated, the cavitation threshold was found in the range of 2.0–2.7 W (Figure 4.5 (b–f)). Details about the sigmoid fit formula and fitting parameters are shown in Appendix Section A.4. Interestingly, comparing the upper plateau region of the curve, $TiO_2$ with a concentration of 0.3 mg/mL exhibited the highest cavitation noise index. This suggested that 0.3 mg/mL provided optimal sonochemical performance compared to other concentrations.

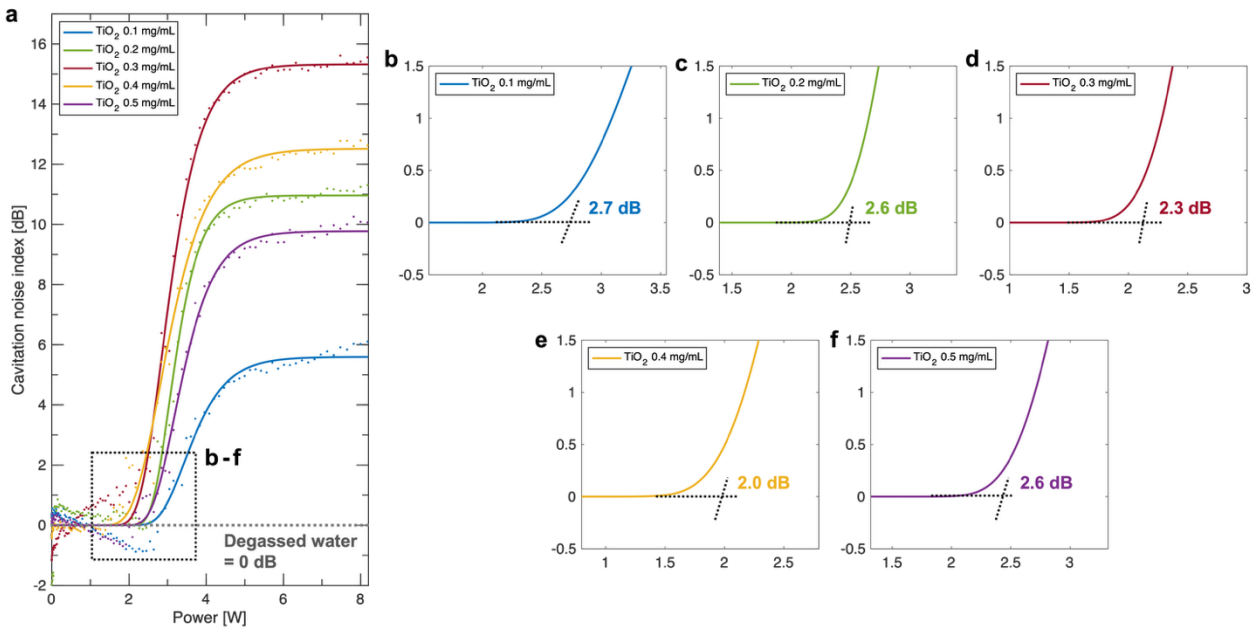



**Figure 4.5.** (**a)** The sigmoid function fitting for the normalised average cavitation noise index as a function of power across five $TiO_2$ concentrations. The cavitation noise index at 0 W was corrected to baseline at 0 dB. The enlarged signal of the thresholds is shown on their individual plot in Figure (b–f). **(b–f)** The cavitation thresholds for the five $TiO_2$ concentrations are indicated on Figure 4.5 (b–f), respectively.

This observation aligns with the result in Figure 4.6 (a), which shows that hydrogen production rate reached its maximum at a $TiO_2$ concentration of 0.3 mg/mL. The observed trend is attributed to the effect of bubble populations. At a sub-optimal $TiO_2$ concentration (below 0.3 mg/mL), the results suggest that there are fewer bubble nucleation sites for bubble formation, causing a lower sonochemical rate. When the concentration of $TiO_2$ exceeds the optimal level, too many particles may scatter the sound waves, subsequently shielding the acoustic field reaching the focus area of the reactor. Furthermore, there may also be decoupling loss: the high concentration of sonocatalysts may alter the acoustic impedance of the medium and consequently cause the energy transfer efficiency from the transducer to the water to decrease[186].

Figure 4.6 (b) shows the sonochemical hydrogen production rate at different power inputs. The production rate increases particularly at the upper plateau region (changes in the cavitation noise index are nearly minimal beyond 4.3 W), indicating the cavitation probability ($P_{cav}$) is nearly unity[185]. Although the cavitation probability at 4.3 W or higher is nearly unity, higher reactor power results in a greater acoustic pressure amplitude. This may cause larger bubble size just before implosion, which further causes higher cavitation temperature within the hotspots, and increases in the bubble

population, further enhancing radical production[134]. It is expected that the hydrogen production rate will continue to increase beyond 5.1 W until the shielding and decoupling effect from the overcrowded bubble population becomes significant[186]. This was not tested because 5.1 W is the maximum safe operating power input for the transducer.

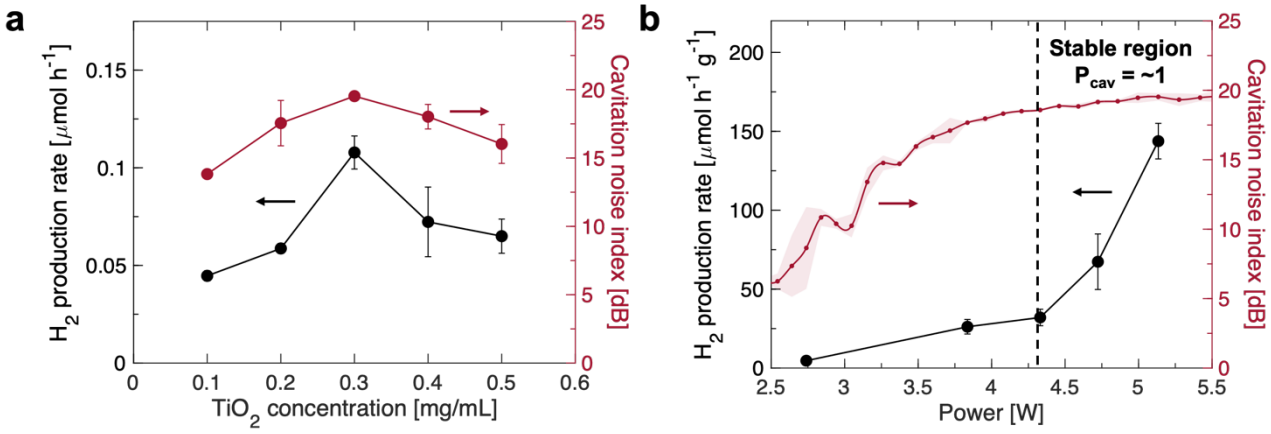



**Figure 4.6. (a)** The hydrogen production rate (black points, left) and cavitation noise index (red points, right) as a function of $TiO_2$ concentration in the solution. The lines are linear interpolations of the points for better illustration of the trend. **(b)** Hydrogen production rate (black points, left) and cavitation noise index (red points, right) as a function of power input.

### 4.2.2. Effect of seawater

Next, the effect of salts and different water sources on sonochemical hydrogen production was examined using the optimised parameters identified earlier, focusing on how seawater composition and NaCl concentration influence the reaction. The results are presented in Figure 4.7. Figure 4.7 (a) shows the sonochemical hydrogen production in the presence of $TiO_2$ catalyst at the maximum concentration (0.3 mg/mL as determined above) from DI water, natural seawater, simulated seawater, and 0.48 M NaCl solution. A one-way ANOVA showed that the choice of water resource had a statistically significant effect on the hydrogen production rate ($F_{3,8} = 9.95$, $p < 0.005$). The superior hydrogen yield from DI water may be attributed to the lack of ions and salts, which may interfere with the sonochemical reactions by altering the chemical environment[187]. Seawater had approximately half the yield of DI water ($p < 0.01$). The presumed presence of organic microorganisms in these natural waters is deemed negligible in the cavitation generation process, evidenced by the similar hydrogen production rates between natural and simulated seawater. However, reactive oxygen species generated from water sonolysis with high oxidation potentials may degrade microorganisms in advanced oxidation processes, reducing microorganism-related effects[188]. Additionally, this exploration included hydrogen production from a 0.48 M NaCl solution, replicating

the NaCl molarity of natural seawater[161]. Simulated seawater, composed of a 0.48 M NaCl solution along with other salts such as KCl, $Na_2SO_4$, and $NaHCO_3$, yielded hydrogen at rates nearly identical to those from a solution containing only 0.48 M NaCl. This suggests that NaCl is the predominant salt influencing the sonochemical reactions due to its high concentration.

To elucidate why seawater yielded less hydrogen production, the effect of NaCl concentration on sonolysis was explored. Figure 4.7 (b) shows the hydrogen production rate of water at different NaCl concentrations, revealing a decreasing trend with increasing concentration. This decrease is attributed to a complex interplay of physical alterations and chemical reactions influenced by the NaCl concentration. Physically, NaCl modifies several properties of the solution, such as density, vapour pressure, viscosity, surface tension, and speed of sound[189,190]. These parameters were incorporated into a simulation of single spherical bubble dynamics to explore the bubble temperature during collapse at different NaCl concentrations.

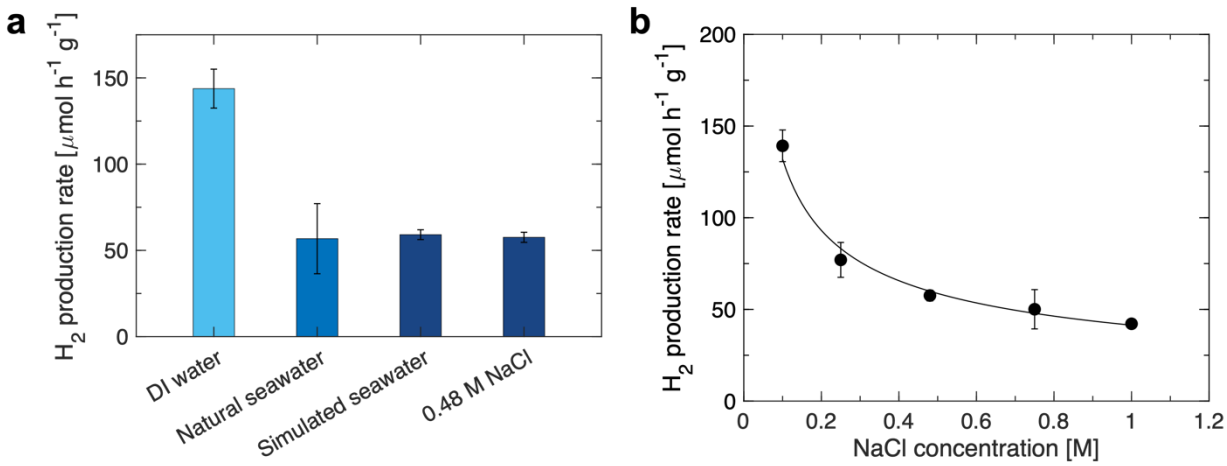



**Figure 4.7.** Sonochemical hydrogen production under the effect of salts and different water sources. **(a)** Hydrogen production rate during sonication with water, natural seawater, simulated seawater, and 0.48 M NaCl solution. **(b)** Sonochemical hydrogen production rate as a function of NaCl solution with different concentrations.

Figure 4.8 shows the temporal evolution of a bubble's internal temperature at the final stage of the collapse. Simulations were performed with the Keller-Miksis model for a single spherical bubble under the assumption of adiabatic collapse. The results revealed that a higher NaCl concentration increased the maximum temperature during bubble collapse. Although higher temperatures typically promote radical generation and hydrogen production, the experimental results paradoxically showed a reduction in hydrogen yield[191,192], in contrast with the simulations. It is noted that the temperature variation is relatively modest, with only a 400 K temperature difference between the 0.1 M and the 1

M solutions. However, the model does not account for mass transfer effects, which may be exacerbated by the presence of salt. Specifically, the evaporation at the bubble-liquid interface may increase the local salt concentration. Since the mass transfer of salt from the interface to the bulk liquid does not occur spontaneously, and vapour pressure inversely relates to salt concentration, this may slow down the rate of further vapour evaporating into the bubble, causing less vapour to react within the bubble at each cycle. Furthermore, increasing the salt concentration decreases the concentration of dissolved gas, i.e. argon, leading to fewer microbubble nuclei in the solutions, hence fewer sonochemically active bubbles[187]. Previous studies have demonstrated a positive correlation between the concentration of dissolved gases and bubble number[191].

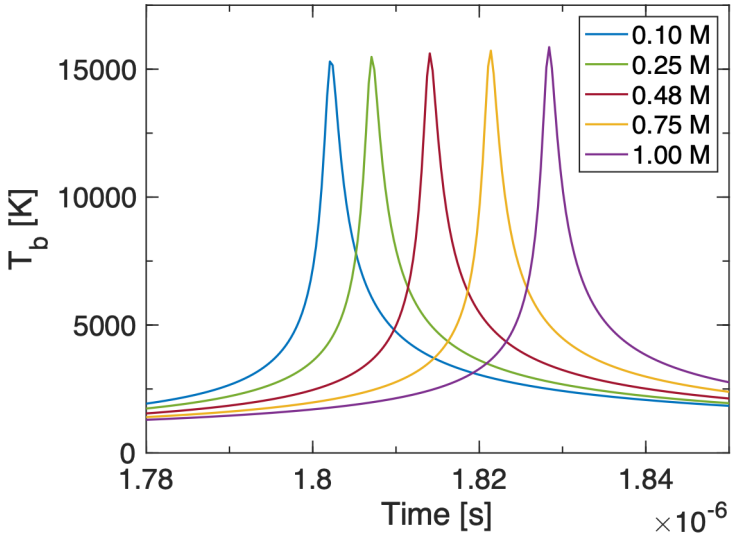



**Figure 4.8.** Simulations of bubble temperature at final collapse stage of a single cavitation bubble collapsing in the solution with different NaCl concentrations. This simulation was conducted by Dr. Davide Bernardo Preso.

Chemical effects also contribute to the decreased hydrogen production in NaCl solution. The reactions are represented as follows[193]:

$$NaCl\ (g) \overset{)))}{\rightarrow} Na\cdot + Cl\cdot \qquad \text{(Eq. 4.8)}$$

$$Na\cdot + H_2O \rightarrow NaOH + H \qquad \text{(Eq. 4.9)}$$

$$Cl\cdot + H_2O \rightarrow HCl + \cdot OH \qquad \text{(Eq. 4.10)}$$

$$Na\cdot + \cdot OH \rightarrow NaOH \qquad \text{(Eq. 4.11)}$$

$$Na\cdot + H + M \rightarrow NaH + M \qquad \text{(Eq. 4.12)}$$

$$Cl\cdot + \cdot OH \rightarrow HOCl \qquad \text{(Eq. 4.13)}$$

$$Cl\cdot + H\cdot \rightarrow HCl \qquad \text{(Eq. 4.14)}$$

$$Cl\cdot + H_2 \rightarrow HCl + H \qquad \text{(Eq. 4.15)}$$

$$Na\cdot + Cl\cdot + M \rightarrow NaCl + M \qquad \text{(Eq. 4.16)}$$

While NaCl exists as dissociated and solvated ions ($Na^+$(aq) and $Cl^-$(aq)) under ambient aqueous conditions, the extreme temperatures and pressures generated during acoustic cavitation may change the state in which these ions exist. Lepoint-Mullie et al. suggested that the introduction of dissolved salts into the highly compressed and hot gas phase of a cavitation bubble closely resembles the projection of metal species from salt solutions into a flame[193]. During bubble collapse, water evaporates from the NaCl solution at the bubble-liquid interface due to the extreme temperatures generated within the hotspot of the cavitating bubble. The rapid evaporation of water causes the dissolved salt to crystallise and dry into fine salt microscopic salt particles, which subsequently vaporise under the high-temperature conditions of the collapsing bubble to form gaseous NaCl[193]. Reported cavitation bubble temperatures range from approximately 2000 to as high as 20,000 K, depending on the technique used to estimate the bubble temperature[194-197]. These temperatures are substantially higher than the boiling point of NaCl (1686 K)[198]. As a result, the vapourised NaCl species present within or near the hotspot may undergo homolytic cleavage, producing sodium and chlorine radicals (Na• and Cl•) in their plasma state, as shown in Eq. 4.8[193]. These plasma species may subsequently react with water molecules and other water-based radicals, in turn impacting the overall yield of sonolysis. Possible reactions between these species are listed in Eq. 4.9 to Eq. 4.16, where M denotes a third body in the reactions. A higher concentration of NaCl may increase the amount of Na• and Cl•, resulting in more H• and •OH radicals being scavenged and limiting the hydrogen production. This may explain the observed decrease in hydrogen production rate with increasing salt concentration.

EPR was also employed to investigate the NaCl scavenging effect in sonochemical hydrogen production. As H• and •OH radicals in the solution have an extremely short half-life and are generally not directly detectable by EPR, indirect detection was performed at room temperature using spin-trapping with DMPO. After sonication of DI water, natural seawater, and simulated seawater with the addition of 25 mM DMPO, the formation of H• and •OH radicals (Figure 4.9 (a)) was observed. This is consistent with findings in the literature, where the radicals are generated from water sonolysis during inertial cavitation[199]. The spectrum matches well with the EPR simulation, which is the sum of DMPO-OH ($a_N$ = 14.9 G and $a_H$ = 14.9 G) and DMPO-H ($a_N$ = 16.4 G and $a_H$ = 22.6 G), giving $a_N$ and $a_H$ values in line with the DMPO-radical adduct. Details of the EPR simulation with each component spectrum are shown in Figure 4.9 (b–d). It was also observed that the EPR spectra of natural and simulated seawater had much lower amplitude DMPO-OH signals and nearly no DMPO-

H signal. This confirms that salts scavenge H• and •OH radicals, decreasing the hydrogen production compared to the case of DI water. It is noted that the EPR signal from natural seawater is slightly higher than the simulated solution. This is likely due to the trace concentration of Fe ions present in natural seawater, reacting with hydrogen peroxide as generated from water sonolysis and causing the generation of •OH radicals by Fenton chemistry. However, as the amount of Fe in seawater is negligible (0.1–10 nM), the small amount of •OH radicals formed from Fenton chemistry may be ignored. This supports the conclusion that NaCl quenches H• and •OH radicals[200]. Considering this along with the physical effect, which demonstrated contrasting results by the above bubble simulation, the chemical effect is likely the dominant effect for the decreased hydrogen yield under salty water.

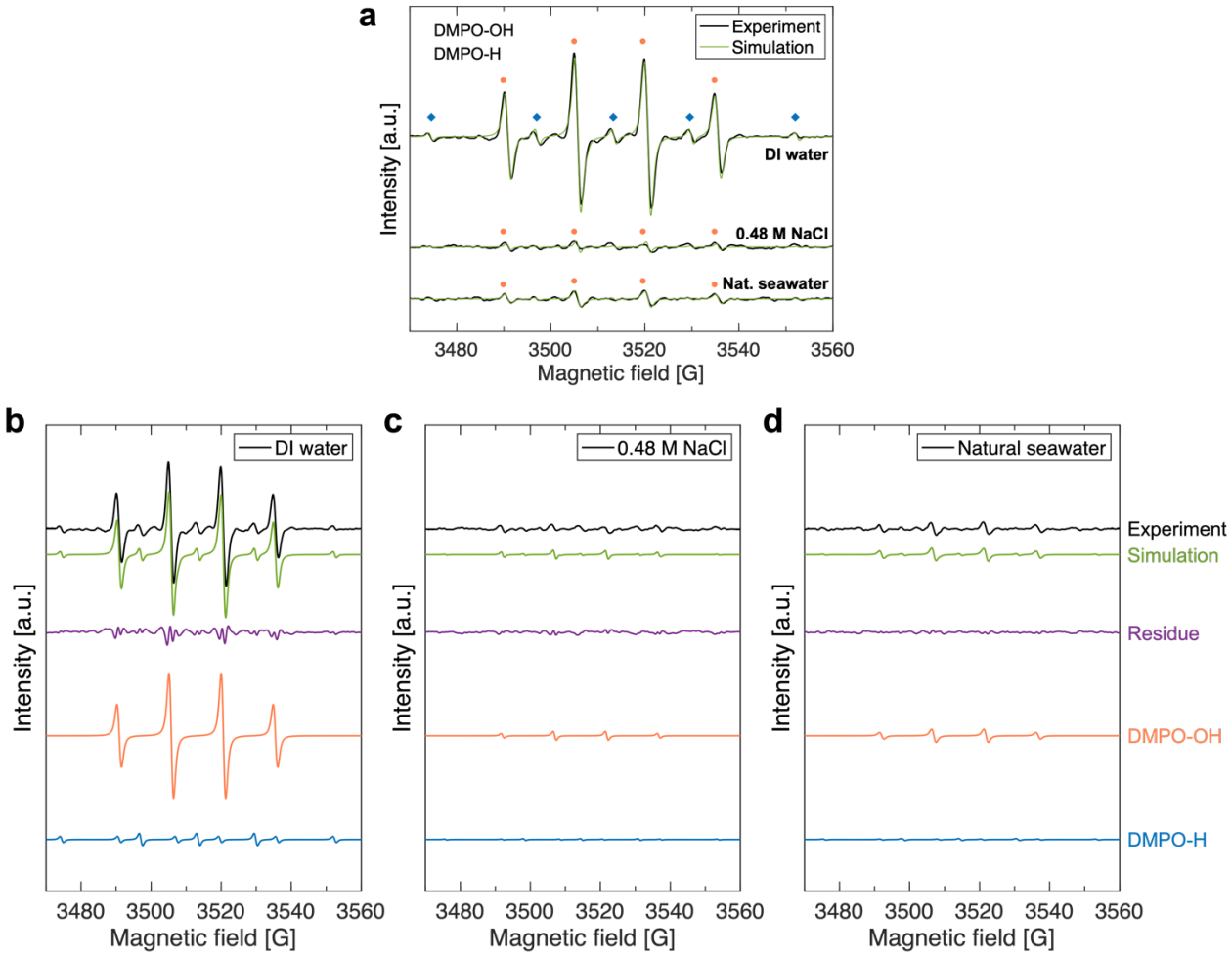



**Figure 4.9. (a)** The experimental and simulated EPR spectra obtained after the sonochemical reaction of DI water, 0.48 M NaCl solution, and natural seawater in the presence of 25 mM DMPO spin trap. **(b–d)** The details of the simulated EPR spectra of the sonochemical reaction with **(b)** DI water, **(c)** 0.48 M NaCl solution, and **(d)** natural seawater. The reaction time was 20 minutes. Experimental spectra were simulated. The simulated spectrum, residue, and each of the two radical components (DMPO-OH and DMPO-H) are presented as separate spectra.

Out of curiosity, the effect of different salt solutions, varying in salt composition, on the sonochemical hydrogen production rate was explored. The results are presented in Figure 4.10. The addition of salts had a highly significant effect on hydrogen production (one-way ANOVA, $F_{5,12} = 23.70$, $p < 0.001$). DI water exhibited the highest average $H_2$ production rate, likely due to the absence of ions that might interfere with radical generation or bubble dynamics. Among the 0.1 M salt solutions tested, the hydrogen production rate followed the general trend: NaCl > KCl ≈ $MgCl_2$ ≈ $CaCl_2$ > $Na_2SO_4$. Post hoc analysis using Tukey's HSD test showed that the hydrogen production rates of KCl, $MgCl_2$, and $CaCl_2$ were not significantly different from one another ($p_{KCl,MgCl_2} = 0.999$, $p_{KCl,CaCl_2} = 0.955$, and $p_{MgCl_2,CaCl_2} = 0.995$). Therefore, these three salts are considered to exhibit comparable sonochemical performance rather than being interpreted as having decreasing hydrogen production rates.

This trend reveals several key observations. First, salts that dissociate into fewer ions tend to favour higher hydrogen production rates. For instance, NaCl, which dissociates into two ions, had a higher hydrogen production rate than $MgCl_2$ and $CaCl_2$, which dissociates into three ions in water. This suggests that increasing the total number of ions in the solution may hinder cavitation efficiency or radical activity. However, the lack of significant differences among KCl, $MgCl_2$, and $CaCl_2$ suggests that the number of ions present in solution is unlikely to be the only factor governing hydrogen production. Second, the size of the cation may play a role. Smaller cations, such as $Na^+$, yielded higher hydrogen production than larger cations like $K^+$. A similar trend was observed between $Mg^{2+}$ and $Ca^{2+}$, with $Mg^{2+}$ being the smaller of the two ions achieved a slightly higher hydrogen production rate. However, the difference between $MgCl_2$ and $CaCl_2$ was not statistically significant, and further experimental validation is required to confirm this relationship. Finally, the type of anion had an impact on the sonochemical efficiency. The presence of a divalent anion, such as $SO_4^{2-}$ in $Na_2SO_4$, resulted in the lowest hydrogen production rate among the salts tested. This suggests that anions with higher charge density may suppress sonochemical activity more effectively than monovalent anions like $Cl^-$, even when the total ionic strength is comparable, as seen in the examples of $MgCl_2$ and $CaCl_2$.

Previous studies have investigated the effects of salts on sonochemical reactions, though results remain inconsistent. For instance, Mahamuni et al. and Gole et al. reported that the addition of NaCl enhanced the sonochemical degradation rates of phenol and chlorobenzene, indicating a positive effect of salt addition[201,202]. In contrast, Chen and Smirniotis observed a decrease in the sonochemical degradation rate of phenol upon the addition of NaCl or $Na_2SO_4$[203]. The negative effect of salt addition is attributed to a reduction in gas solubility in the presence of salts, which in turn decreases cavitation

activity. However, there is currently no consensus in the literature on the mechanisms or trends associated with the effect of salt addition on sonochemical efficiency.

To date, there is no direct literature explaining how specific salt compositions influence sonochemical hydrogen production. Based on the present findings, the observed negative effects are likely related to a combination of factors, including the total number of ions in the solution, ionic radius, and ionic density. A higher number of ions may lead to increased formation of plasma species during bubble collapse, which could quench •OH radicals and reduce hydrogen yields. However, the roles of ionic radius and charge density remain unclear. It is possible that charged intermediates are formed during the reaction, or local electrostatic forces induced by salt ions influence the diffusion and interaction of reactive species. Nevertheless, sonochemical reactions are generally considered to be driven by neutral yet highly reactive species such as hydroxyl radicals, rather than by electrostatic interactions. Further studies are required to understand the effect of salt compositions on sonochemical hydrogen production.

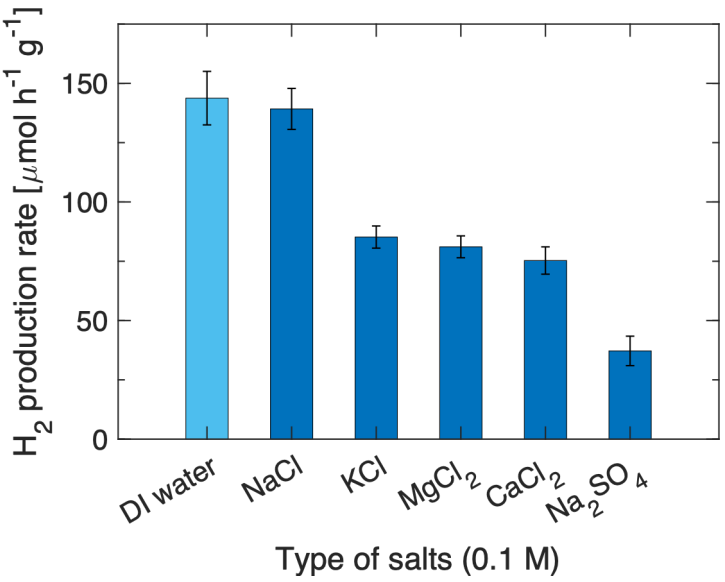



**Figure 4.10.** Sonochemical hydrogen production rate with different salt compositions (0.1 M solution).

### 4.2.3. Kinetics of sonocatalytic water splitting

The reaction kinetics of sonocatalytic water splitting over $TiO_2$ in DI water and natural seawater were explored. To investigate the kinetic profile, the experimental data were fitted using two kinetic models: a zero-order linear model ($y = mx + c$) and a pseudo-first-order kinetic model[‡‡] ($y = y_{max}(1 - e^{-kx})$)[204]. The corresponding model fits are shown in Figures 4.11 (a) and 4.11 (b), respectively. The fit equations, fitting parameters, root-mean-square error (RMSE) values, and $R^2$ values (for the zero-order fittings) for both water systems are summarised in Table 4.6. RMSE was chosen as the primary metric for model comparison because it calculates the residual distance between the data points and the fitting line in units of the system (μmol $g^{-1}$)[205].

Under the zero-order model, which assumes a constant reaction rate, the slope of the linear regression represents the hydrogen production rate. The fitted slopes corresponded to hydrogen production rates of 1.69 μmol $g^{-1}$ $min^{-1}$ (101.4 μmol $g^{-1}$ $h^{-1}$) for DI water and 0.94 μmol $g^{-1}$ $min^{-1}$ (56.4 μmol $g^{-1}$ $h^{-1}$) for natural seawater. Both linear fits exhibited strong agreement with the experimental data, with $R^2$ values exceeding 0.95. A pseudo-first-order kinetic model was also used to assess whether hydrogen production approached a plateau during the reaction period, which may indicate catalyst deactivation, reactant depletion, or mass-transfer limitations[206,207]. Comparison of the fitting statistics showed that the pseudo-first-order model provided limited improvement over the zero-order model. Specifically, the RMSE merely decreased from 34.12 to 28.69 μmol $g^{-1}$ for the DI water system and from 14.52 to 12.98 μmol $g^{-1}$ for the natural seawater system.

Furthermore, the fitted pseudo-first-order rate constants (k) were very small, with values of 0.0015 $min^{-1}$ for DI water and 0.00002 $min^{-1}$ for natural seawater. These near-zero rate constants indicate that the pseudo-first-order model remains close to its linear approximation ($1 - e^{-kx} \approx kx$) over the timescale studied. Consequently, the pseudo-first-order model closely approximates the zero-order linear model within the experimental time range, resulting in only a marginal improvement in the quality of fit. As a result, the sonochemical hydrogen production rate remained approximately linear throughout the experimental period. This likely indicated that the catalyst retained its activity and that the catalytic sites on the $TiO_2$ surface were fully utilised throughout the reaction period, with no clear

[‡‡] Sonocatalytic water splitting is hypothesised to follow a pseudo-first-order kinetic model. Since water serves as both the reactant and the solvent, its concentration is in excess and remains effectively constant throughout the reaction. As a result, the reaction rate is unlikely to be limited by the availability of water molecules. Instead, it is expected to be governed primarily by other physical and catalytic factors, such as the number of available active sites on the $TiO_2$ surface. Therefore, the observed reaction behaviour may be approximated as first-order kinetics, with the rate determined by these surface and catalytic constraints rather than by the fundamental reaction kinetics of water dissociation.

evidence of catalyst deactivation or reaction-rate saturation. Therefore, the reaction kinetics were characterised using the zero-order linear model, with the slope of the linear regression representing the production rate[208,209].

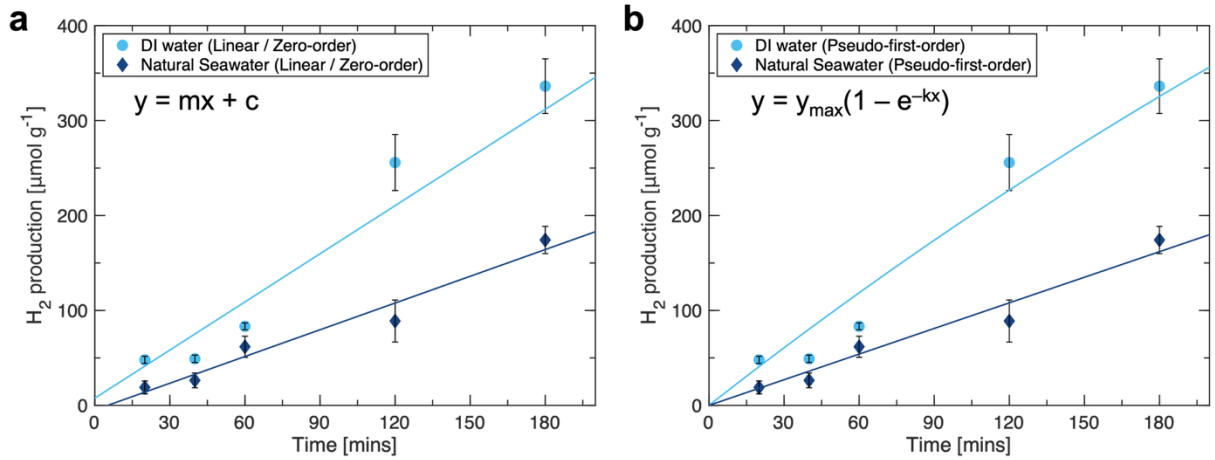



**Figure 4.11.** Sonocatalytic hydrogen production kinetics fitting of DI water and natural seawater. **(a)** Steady-state fitting with a linear model representing zero-order kinetics. **(b)** Pseudo-first-order kinetic model fitting. The error bars represent the standard deviation of three experimental trials for each reaction time. The hydrogen production rate was quantified by a linear fitting of hydrogen production over reaction time.

**Table 4.6.** Comparison of steady-state fitting (zero-order) and pseudo-first-order kinetic models and their respective fitting parameters, RMSE, and $R^2$ values (for the zero-order fittings) for sonocatalytic hydrogen production in DI water and natural seawater systems.

| Water system | Kinetic model | Fit equation | Fitting parameters | RMSE [µmol $g^{-1}$] | $R^2$ |
|---|---|---|---|---|---|
| DI water | Zero-order (linear) | $y = mx + c$ | $m = 1.69$<br>$c = 7.55$ | 34.12 | 0.97 |
| | Pseudo-first-order | $y = y_{max}(1 - e^{-kx})$ | $y_{max} = 1359$<br>$k = 0.0015$ | 28.69 | - |
| Natural seawater | Zero-order (linear) | $y = mx + c$ | $m = 0.94$<br>$c = -4.84$ | 14.52 | 0.96 |
| | Pseudo-first-order | $y = y_{max}(1 - e^{-kx})$ | $y_{max} = 39555$<br>$k = 0.00002$ | 12.98 | - |

The pH variation during the sonication of DI water over time was also monitored (Figure 4.12). The results showed that during the reaction, the pH value gradually decreased from around 8 to 7. This trend suggests two simultaneous effects during the reaction. Initially, the pH immediately following the sonochemical reaction consistently exceeded the initial pH=7 of DI water, indicating a shift

toward basicity[210]. This increase in basicity is attributed to the continuous consumption of hydrogen species from water molecules due to the formation of hydrogen gas. This process releases hydrogen into the gas phase, leaving behind oxygen species into the water, which increases the basicity of the solution. The term species is used deliberately because the underlying reaction mechanism is not yet fully understood. Sonolysis of water generates H• and •OH radicals, with H• radicals undergoing recombination reactions to form molecular hydrogen, which subsequently leaves the solution and enters the gas phase. On the other hand, pH is determined by the concentrations of protons ($H^+$) and hydroxide ions ($OH^-$) in solution. Although the observed increase in pH indicates an accumulation of hydroxide ions relative to protons, the electron-transfer processes by which •OH radicals contribute to the formation of $OH^-$ ions remain unclear. Furthermore, due to the current lack of mechanistic understanding, it remains unclear how electroneutrality is maintained during the accumulation of $OH^-$ species in the solution.

At the same time, despite the initial increase in $OH^-$ concentration in the liquid phase, as demonstrated by the initial rise in pH, there was a decrease in pH over time. This may be explained by the simultaneous production of a small amount of hydrogen peroxide during the cavitation process, which introduces acidic properties (increases the pH) to the solution[61]. Hydrogen peroxide, being a weak acid with a pH range of 3–6, counteracts the increase in basicity from the residual OH species, contributing to the gradual decrease in pH. The initial increase in basicity may also indicate that hydrogen peroxide is kinetically slower than the consumption of hydrogen species during the sonochemical reactions.

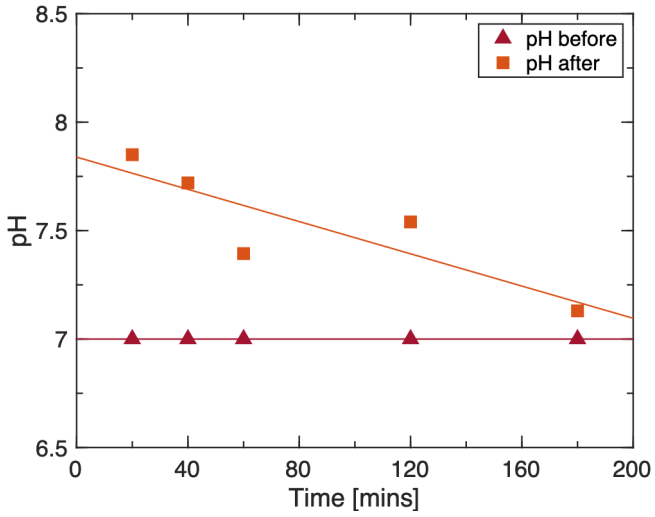



**Figure 4.12.** The pH changes over time for DI water with and without sonication.

After establishing the kinetics of sonocatalytic water splitting and examining the pH changes in DI water over time, the focus shifted to the physical changes experienced by the sonocatalyst throughout the reaction. Understanding whether the catalyst had any structural transformation under prolonged sonication is essential for evaluating its long-term performance, such as the catalyst's recyclability and durability.

As shown in Figure 4.13, the $TiO_2$ catalyst experienced a notable reduction in particle size during the initial phase of sonication (0 to 20 minutes), which effectively increased its surface area. This initial size reduction was expected to enhance catalytic activity, as smaller particles provide more surface area and offer a greater number of nucleation sites for cavitation bubbles, thereby improving sonochemical efficiency[211,212]. The observed reduction in size was likely caused by the mechanical effects of inertial cavitation, including microjets and shock waves[213]. Following this initial ultrasonic fragmentation and surface modification, the $TiO_2$ particles maintained a consistent ball-like rough nanostructure throughout the reaction time. This stability suggested that the catalyst structure remained largely intact under cavitating conditions for the duration studied, supporting the constant hydrogen production rate discussed earlier. Moreover, this emphasised the potential recyclability and corrosion resistance of $TiO_2$ in different types of water source.

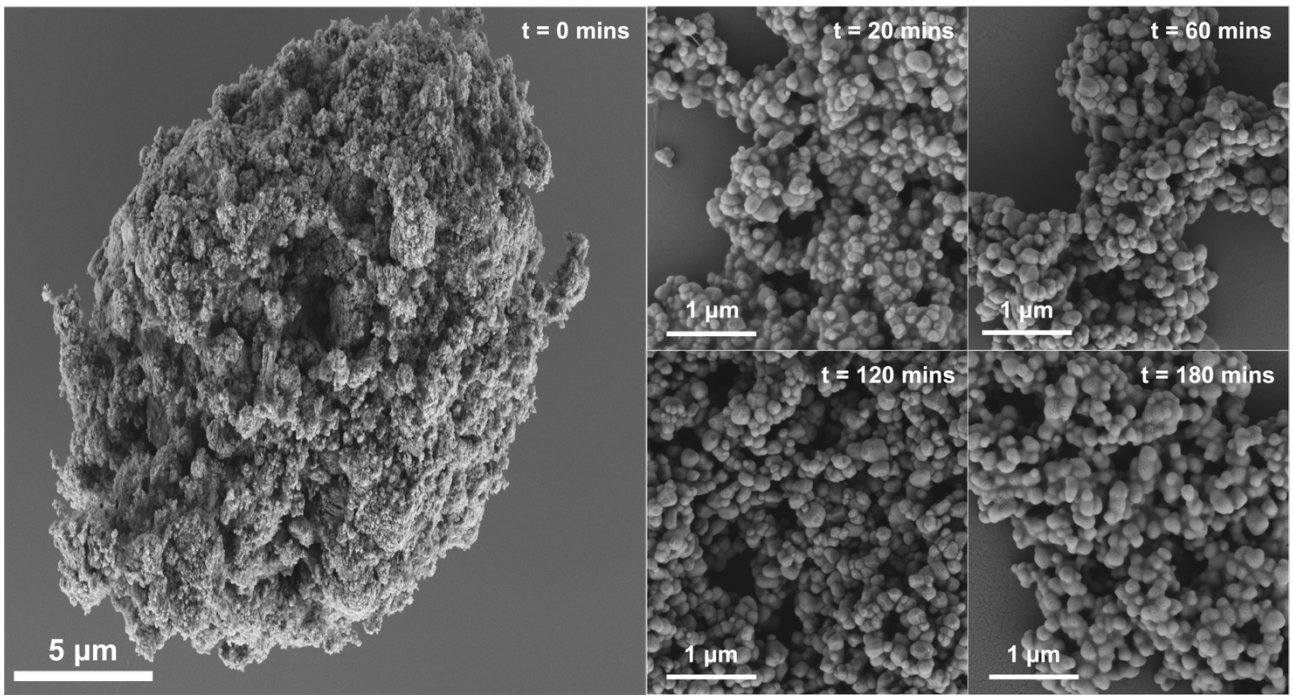



**Figure 4.13.** SEM images of $TiO_2$ sonocatalysts at 0 min, 20 mins, 60 mins, 120 mins, and 180 mins for sonochemical seawater splitting. The SEM imaging was conducted by Yi Qin.

### 4.2.4. Comparison with literature

Our system's sonocatalytic hydrogen production rate and sonochemical efficiency are compared with those reported in existing literature across various operating frequencies, as detailed in Table 4.7 and illustrated in Figure 4.14. The systems are categorised by the type of reaction solution used, including DI water and seawater. For a comprehensive comparison, other reaction solutions used in sonochemical hydrogen production, such as 10% and 20% ethanol/water mixtures, are also included. As depicted in Figure 4.14, there are only four ultrasound frequencies available in the literature, no consistent trend in hydrogen production is observed with respect to frequency and solvent type with the limited information available. This variability may indicate that factors like sonochemical reactor design, power input, catalyst type, and reactant volume significantly influence hydrogen production.

Figure 4.14 (a) shows that this system had a relatively low hydrogen production rate compared to the existing literature. However, direct comparison between sonochemical systems is not straightforward, as each system employs different reactor volumes, power inputs, and experimental conditions. To enable a fair comparison, the hydrogen production rate was normalised by both the reaction volume (in the unit of L) and energy input (in the unit of Whr), incorporating these varying parameters into a single normalised metric termed the normalised sonochemical efficiency (in the unit of μmol $g^{-1}$ $L^{-1}$ $Whr^{-1}$). This normalisation accounts for the differences in reactor scale and power delivery across studies, allowing a more representative comparison of the sonochemical efficiency of each system regardless of its specific setup. After normalising for these factors, this system displayed the highest sonochemical hydrogen production efficiency ever reported, as shown in Figure 4.14 (b), representing an improvement by a factor of 10 to 100 over existing literature. This superior performance of this system is attributed to the combination of an optimised $TiO_2$ catalyst concentration and acoustic parameter selection, and a reactor design that enhances cavitation activity through cylindrical converging ultrasound waves. Moreover, the results from this study highlight the crucial role of scaling up reactant volumes for achieving large-scale sonochemical hydrogen production.

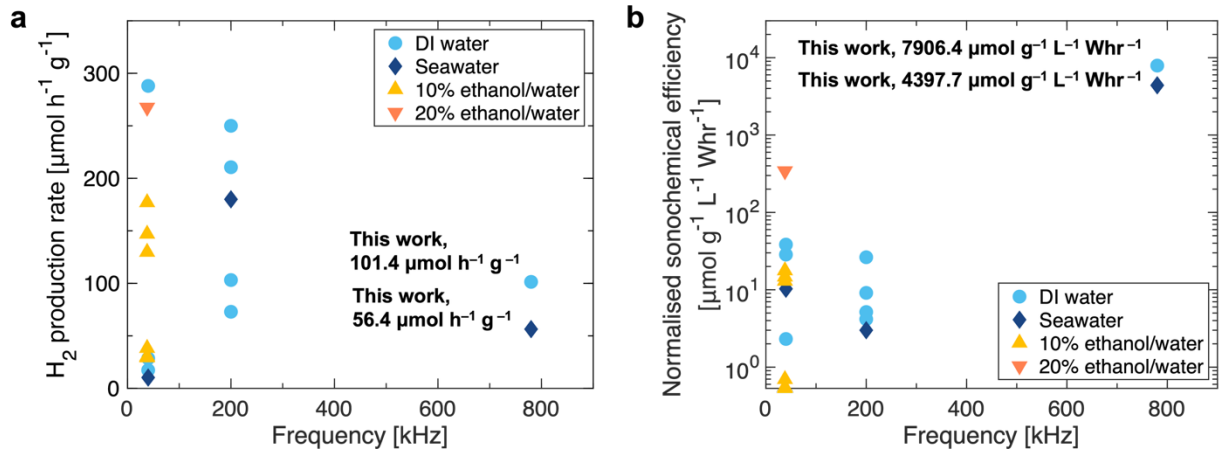



**Figure 4.14.** Sonochemical hydrogen production rate and the type of reaction solutions in comparison to the existing literature. **(a)** Sonochemical hydrogen production rate (μmol $h^{-1}$ $g^{-1}$) vs the operating frequency of the sonochemical reactor. The production rate is categorised by the type of reaction solutions. (**b)** Sonochemical efficiency after being normalised by the mass of catalyst used and input energy (μmol $g^{-1}$ $L^{-1}$ $Whr^{-1}$) vs the operating frequency.

**Current challenges and technology readiness**

It is important to acknowledge that the current system exhibits very low energy efficiency. The overall conversion efficiency remains well below 1%, with measured values around 0.0001% (calculated as the ratio of the chemical energy of the produced hydrogen to the input electrical energy). This is substantially lower than the established green hydrogen production methods: electrolysis typically achieves 40-80% efficiency depending on the electrolyser technology, while state-of-the-art photocatalytic water splitting has reached a solar-to-hydrogen (STH) efficiency of approximately 9.2%[214,215]. Moreover, recent advances in seawater electrolysis are addressing key challenges through innovative approaches, such as proton-selective membranes, negatively charged electrode coatings that repel chloride ions and suppress chlorine gas evolution, and membrane systems capable of self-purifying seawater by extracting freshwater[88,216,217]. In parallel, photocatalytic seawater splitting is progressing through the development of more robust and selective photocatalysts[156].

Several factors likely contribute to the poor energy conversion observed in the current sonochemical system. First, the system was not yet fully optimised: energy losses arose from imperfect electrical connections (i.e., impedance mismatch), as indicated by a non-zero phase angle despite an impedance close to 50 Ω. Additional losses resulted from acoustic attenuation during sound transmission through the liquid medium and from heat dissipation, even with the improved SonoCYL reactor design compared to the conventional systems. Moreover, most of the generated radicals likely did not follow

the desired pathways to recombine into hydrogen gas. Progress in sonocatalyst development to selectively promote hydrogen generation remains in its early stages and is an active area of research. Section 7.2 will further discuss strategies to improve overall energy conversion efficiency in sonochemistry.

Although the current sonochemical efficiency is far from that of incumbent technologies and not yet viable for deployment, it is still important to recognise the value of exploratory research. The intrinsic advantages of the use of non-purified water and the elimination of noble-metal catalysts remain compelling from a conceptual and sustainability standpoint. This work represents an early-stage study aimed at expanding the scope of sonochemistry in sustainable applications, rather than a fully developed technological solution. As sonochemistry continues to gain interest, it is hoped that this study provides insights to encourage future research and ultimately leads to major improvements in energy efficiency as the technology evolves.

**Table 4.7.** Sonochemical hydrogen production results obtained from the literature.

| Reaction solution | Frequency | Power [W] | Gas | Reaction volume [L] | Catalysts | Concentration of catalysts [g/L] | Hydrogen production rate [µmol $h^{-1}$ $g^{-1}$] | Normalised sonochemical efficiency [µmol $g^{-1}$ $L^{-1}$ $Whr^{-1}$] | Reference |
|---|---|---|---|---|---|---|---|---|---|
| DI water | 40 | 50 | Not stated | 0.15 | $TiO_2$ | 0.5 | 17.3 | 2.3 | Wang, 2010, [71] |
| DI water | 40 | 50 | Not stated | 0.15 | Au/$TiO_2$ | 0.5 | 288.0 | 38.4 | Wang, 2010, [71] |
| DI water | 40 | 100 | Argon | 0.01 | $Co_4N$ nanowires with N-defect | 0.5 | 28.5 | 28.5 | Qi, 2023, [72] |
| DI water | 200 | 200 | Argon | 0.3 | $TiO_2$ rutile | 0.7 | 250.0 | 4.2 | Harada, 2001, [218] |
| DI water | 200 | 200 | Argon | 0.1 | Commercial $TiO_2$ powders | 2.0 | 103.1 | 5.2 | Harada, 2003, [219] |
| DI water | 200 | 200 | Argon | 0.04 | $TiO_2$ (Nippon Aerosil P-25) | 5.0 | 210.6 | 26.3 | Harada, 2001, [218] |
| DI water | 200 | 200 | Argon | 0.04 | $MnO_2$ | 5.0 | 72.9 | 9.1 | Harada, 2001, [218] |
| **DI water** | **780** | **5.13** | **Argon** | **0.0025** | **$TiO_2$ anatase** | **0.3** | **101.4** | **7906.4** | **Current study, 2024** |
| Seawater | 40 | 100 | Argon | 0.01 | $Co_4N$ nanowires with N-defect | 0.5 | 10.3 | 10.3 | Qi, 2023, [72] |
| Seawater (4% NaCl solution) | 200 | 200 | Argon | 0.3 | $TiO_2$ rutile | 0.7 | 180.0 | 3.0 | Harada, 2001, [218] |
| **Seawater** | **780** | **5.13** | **Argon** | **0.0025** | **$TiO_2$ anatase** | **0.3** | **56.4** | **4397.7** | **Current study, 2024** |
| 10% ethanol/water | 38 | 50 | Argon | 0.2 | $LaGa_{0.5}In_{0.5}O_3$ | 2.0 | 129.8 | 13.0 | Gentili, 2009, [65] |
| 10% ethanol/water | 38 | 50 | Argon | 1.1 | $LaGa_{0.5}In_{0.5}O_3$ | 0.4 | 29.3 | 0.5 | Gentili, 2009, [65] |
| 10% ethanol/water | 38 | 50 | Argon | 0.2 | $La_{0.8}Ga_{0.2}InO_3$ | 2.0 | 147.0 | 14.7 | Gentili, 2009, [65] |
| 10% ethanol/water | 38 | 50 | Argon | 1.1 | $La_{0.8}Ga_{0.2}InO_3$ | 0.4 | 30.3 | 0.6 | Gentili, 2009, [65] |
| 10% ethanol/water | 38 | 50 | Argon | 0.2 | $S:La_{0.8}Ga_{0.2}InO_3$ | 2.0 | 177.0 | 17.7 | Gentili, 2009, [65] |
| 10% ethanol/water | 38 | 50 | Argon | 1.1 | $S:La_{0.8}Ga_{0.2}InO_3$ | 0.4 | 38.3 | 0.7 | Gentili, 2009, [65] |
| 20% ethanol/water | 38 | 2.6 | Argon | 0.3 | $S:Y_{0.8}Ga_{0.2}InO_3$ | 1.3 | 267.5 | 342.9 | Penconi, 2015, [66] |

## 4.3. Conclusions

This research chapter explores sonochemical hydrogen production using SonoCYL (780 kHz, 5.1 W) as the sonochemical reactor and $TiO_2$ as the sonocatalyst in both pure water and seawater. Acoustic and chemical operating parameters were systematically optimised, with an optimal $TiO_2$ concentration of 0.3 mg $mL^{-1}$ and 100 acoustic number of cycles identified for maximising hydrogen production. The optimum catalyst concentration was determined experimentally and validated through PCD and the acoustic signal processing method.

Following optimisation, the influence of dissolved salts on hydrogen production was investigated. Results from bubble dynamics simulations and EPR measurements suggest that the reduction in hydrogen yield in seawater may be attributed to both physical and chemical effects, with radical scavenging by dissolved salts likely being the primary factor. Under optimised conditions, the system achieved the highest reported normalised sonochemical hydrogen production efficiencies in the literature for both pure water and natural seawater, reaching 7906 and 4398 μmol $g^{-1}$ $L^{-1}$ $Whr^{-1}$, respectively. These correspond to hydrogen production rates of 101.4 μmol $h^{-1}$ $g^{-1}$ in pure water and 56.4 μmol $h^{-1}$ $g^{-1}$ in seawater.

Together, these findings demonstrate the viability of ultrasound-driven water and seawater splitting for hydrogen generation. Furthermore, the findings may provide insights for the future development of sonochemical hydrogen production technologies as a complementary approach to conventional hydrogen generation methods.

# 5. Screening of metal oxides for sonochemical hydrogen production

Building on the findings of Chapter 4, which demonstrated an effective approach for sonochemical hydrogen production from water and seawater using a low-cost, corrosion-resistant $TiO_2$ catalyst under high-frequency ultrasound (780 kHz) at room temperature, $TiO_2$ remains the only studied sonocatalyst. However, alternative materials may offer improved efficiency.

In general, metal oxides have emerged as promising heterogeneous sonocatalysts for enhancing sonochemical activity due to their low cost, strong catalytic performance, and structural stability under the extreme temperature and pressure conditions generated during inertial cavitation[74-76]. These materials may improve hydrogen production by increasing the number of nucleation sites for microbubble formation and facilitating the transport of reactive radicals into the bulk liquid phase during bubble collapse. However, the existing literature remains very limited and is largely limited to a narrow range of oxides, such as $TiO_2$, $ThO_2$, and $ZrO_2$, this limits broader progress in the optimisation of sonocatalytic systems[71,77,78]. Addressing this gap requires exploration of a wider range of materials to understand how material composition influences catalytic performance for sonochemical hydrogen generation.

This chapter investigates the selection of materials for sonocatalysts under ultrasound irradiation for hydrogen production. A range of commercially available metal oxide powders, many of which are less studied in the context of sonochemistry, as well as synthesised metal-doped $CeO_2$ (Mn, Zn, Cu, Fe, Ni, and Co) catalysts, are screened to evaluate their sonocatalytic performance. The investigation also explores potential relationships between catalyst particle size, cavitation intensity, and hydrogen production rates. This early-stage study provides insights into the complex effects of physical and chemical factors in sonocatalysis, highlighting opportunities in selecting and modifying materials to optimise sonocatalyst performance for efficient hydrogen generation.

## 5.1. Materials and methods

### 5.1.1. Materials

The chemicals used were as follows: Aluminium oxide ($Al_2O_3$) (nanopowder, 13 nm primary particle size, 99.8% trace metals basis, Sigma-Aldrich), Cerium(IV) oxide ($CeO_2$) (nanopowder, <5 nm,

>=99.0%, Alfa Chemistry), Cobalt(II) nitrate hexahydrate (≥99.9% trace metals basis, Sigma-Aldrich), Cobalt(II,III) oxide ($Co_3O_4$) (catalogue number A16121.18, Thermo Fisher Scientific), Copper(II) nitrate trihydrate (≥99.9% trace metals basis, Sigma-Aldrich), Copper(II) oxide (CuO) (ACS reagent, ≥99.0%, Sigma-Aldrich), Erbium(III) oxide ($Er_2O_3$) (99.9% trace metals basis, Sigma-Aldrich), Europium(III) oxide ($Eu_2O_3$) (nanopowder, <150 nm particle size, 99.5% trace metals basis, Sigma-Aldrich), Indium tin oxide (ITO) (nanopowder, <50 nm particle size, Sigma-Aldrich), Iron(III) nitrate nonahydrate (≥99.95% trace metals basis, Sigma-Aldrich), Manganese(II) acetate tetrahydrate (99.99% trace metals basis, Sigma-Aldrich), Molybdenum disulfide ($MoS_2$) (~6 μm, Sigma-Aldrich), Nickel(II) nitrate hexahydrate (99.999% trace metals basis, Sigma-Aldrich), Tantalum(V) oxide ($Ta_2O_5$) (99.99%, (trace metal basis), Thermo Scientific Chemicals), Talc (10 μm particle size, Sigma-Aldrich), Titanium dioxide anatase ($TiO_2$ anatase) (99.6% (metals basis), Thermo Scientific Chemicals), Titanium dioxide ($TiO_2$ mixed phase) (nanopowder, 21 nm primary particle size, ≥99.5% trace metals basis, Sigma-Aldrich), Zinc nitrate hexahydrate (reagent grade, 98%, Sigma-Aldrich), Zinc oxide (ZnO) (nanopowder, <100 nm particle size, Sigma-Aldrich), and Zirconium dioxide ($ZrO_2$) (powder, 5 μm, 99% trace metals basis, Sigma-Aldrich). The gases used were as follows: Argon (Zero grade Ar, BOC), Helium (A Grade, 99.996%, BOC). All chemicals were used without further processing unless otherwise stated. Deionised filtered Type 1 water was obtained from a water purification system (Millipore Direct Q5-UV).

### 5.1.2. Sonochemical reactor system and cavitation noise signal measurements

In this study, a transducer operating at a frequency of 1.109 MHz (Type I PZT, Piezo Kinetics Incorporated) with a maximum power input of 5.4 W was used. Except for the transducer specifications, the sonochemical reactor setup and cavitation noise measurement configuration were identical to those described in Section 4.1.2. Note that the transducer used in Chapter 5 has a different resonance frequency compared to those used in Chapters 3 and 4. At the time the Chapter 5 experiments were conducted, the transducer with a resonance frequency of 1 MHz used in Chapter 3 was broken and cracked, and the transducer with a resonance frequency of 780 kHz used in Chapter 4 was occupied for other uses. All transducers share the same dimensions throughout the study, and within each chapter the operational frequency was kept constant to ensure fair comparison of results within the same set of experiments.

### 5.1.3. Reaction solution preparation and sonochemical reactions

2.5 mL of reaction solution was tested for every experiment. The reaction solution for the sonochemical reactions was a mixture of DI water and sonocatalyst with a concentration of 0.3 mg/mL unless otherwise specified. Each experiment was conducted with 100 cycles, a burst period of 2.038 ms, 4.5% duty cycle, and a reaction time of 20 minutes, with a power input of 5.4 W unless otherwise specified. Prior to the sonochemical reactions, the reaction solution and headspace were saturated with argon gas. All reactions were performed at ambient temperature and pressure.

### 5.1.4. Cavitation noise signal processing

Cavitation noise signal processing and the calculation of the normalised cavitation noise index were performed as described in Section 4.1.4.

### 5.1.5. Hydrogen gas analysis

Hydrogen gas analysis was conducted using the same methodology and GC setup as described in Section 4.1.6. As detailed in Section 4.1.6, the GC-BID instrumental LOD and LOQ for hydrogen are 0.05 ppm and 0.15 ppm, respectively. Based on the hydrogen calibration curve, these corresponded to peak areas of approximately 2 and 6 for the LOD and LOQ, respectively. The hydrogen production rates reported in this study exceed this quantification limit, ensuring the analytical reliability of the low-value data points.

### 5.1.6. Preparation of metal-doped $CeO_2$

Six transition-metal-doped $CeO_2$ catalysts (Mn-, Fe-, Co-, Ni-, Cu-, and Zn-$CeO_2$) were prepared by wet impregnation method[220,221]. $Mn(OAc)_2 \cdot 4H_2O$, $Fe(NO_3)_3 \cdot 9H_2O$, $Co(NO_3)_2 \cdot 6H_2O$, $Ni(NO_3)_2 \cdot 6H_2O$, $Cu(NO_3)_2 \cdot 3H_2O$, and $Zn(NO_3)_2 \cdot 6H_2O$ were used as precursors, which were pre-dissolved in deionised water to form 0.1 M metal ion solutions. $CeO_2$ was first suspended in 10 mL of water, and metal precursor solutions were added dropwise to the slurry at a 5 wt% loading. This process was conducted under continuous stirring for three hours at room temperature to ensure thorough mixing. An ultrasound horn (78 W output, VCX 130, Sonic Vibracell) was applied for 30 minutes to further promote uniform impregnation. Following the impregnation, the mixture was evaporated at 80 °C under constant stirring to remove excess water. The resulting powder was then calcined in a furnace

at 500 °C for five hours in air, with a ramp rate of 5 °C per minute. Finally, the calcined powder was ground with a pestle and mortar to achieve a fine, uniform particle size.

## 5.2. Results and discussion

### 5.2.1. Metal oxide screening

The sonochemical hydrogen production rate was investigated across various metal oxides. The results are shown in Table 5.1. Initially, it was hypothesised that particle size strongly influenced hydrogen production because it governed the number of nucleation sites[222]. Under the initial assumption that the physical effects might have a greater influence than chemical composition, Figure 5.1 (a) plots hydrogen production against particle size for the tested metal oxides. No clear correlation between particle size and hydrogen production rate was observed under this assumption. This finding contrasts with previous findings that suggested a simple inverse relationship between sonocatalytic activity and particle size[212]. However, the previous study examined the effect of particle size within a single chemical system, while this study compares a range of chemically distinct materials. This discrepancy may also arise from differences in reaction mechanisms: while the earlier study focused on the sonocatalytic degradation of methyl orange, this research targeted hydrogen production under sonochemical conditions.

**Table 5.1.** The sonochemical hydrogen production rate of screened sonocatalysts and their respective particle size and normalised cavitation index. The error in the hydrogen production rate represents the standard deviation of at least three experimental trials for each reaction condition.

| Chemicals | Particle size[§§] [nm] | Normalised cavitation index [dB] | $H_2$ production rate [μmol $h^{-1}$ $g^{-1}$] |
|---|---|---|---|
| $Al_2O_3$ | 13 | 19.2 | 84.8 ± 11.2 |
| $CeO_2$ | 5 | 14.3 | 277.1 ± 12.1 |
| $Co_3O_4$ | No data available | 16.9 | 21.0 ± 2.7 |
| CuO | No data available | 14.8 | 7.8 ± 4.4 |
| $Er_2O_3$ | No data available | 8.4 | 4.1 ± 1.1 |
| $Eu_2O_3$ | 150 | 15.1 | 5.2 ± 0.7 |
| ITO | 50 | 18.7 | 11.2 ± 2.0 |
| $MoS_2$ | 6000 | 12.9 | 2.2 ± 0.9 |
| $Ta_2O_5$ | No data available | 10.6 | 4.9 ± 0.8 |
| Talc | 10000 | 13.4 | 197.6 ± 34.2 |
| $TiO_2$ anatase | 25 | 8.7 | 64.2 ± 10.9 |
| $TiO_2$ mixed phase | 21 | 18.9 | 3.3 ± 1.0 |
| ZnO | 100 | 15.2 | 3.7 ± 1.2 |
| $ZrO_2$ | 5000 | 14.8 | 14.4 ± 4.9 |

These results suggest that the initial assumption regarding the dominant influence of particle size needs to be reconsidered, as chemical composition appears to be a key factor governing hydrogen production performance. Material dependent properties, including oxygen-vacancy density and radical-generation capabilities, may have a stronger influence on sonochemical hydrogen production than particle size, hence masking the underlying size-dependent trends[223]. For example, $TiO_2$ anatase and mixed-phase $TiO_2$ (anatase and rutile) have similar particle sizes yet exhibit a 20-fold difference in hydrogen production. Moreover, 5 nm $CeO_2$ yields the highest hydrogen production, followed by talc despite being much larger at 10 μm. A one-way ANOVA confirmed that the choice of catalyst material had a highly significant influence on the hydrogen production rate ($F_{13,30} = 44.17$, $p < 0.0001$), with a post hoc Tukey's HSD test confirming that $CeO_2$ statistically outperformed all other tested materials ($p < 0.005$ for all pairwise comparisons). It is surprising that talc, despite not being a metal oxide and acting as a reference cavitation agent, achieves the second-highest hydrogen yield. Talc is primarily known for its role as a cavitation agent due to its resistance to cavitation erosion and its ability to trap air bubbles, serving as effective cavitation nuclei[224]. However, it is not traditionally recognised for its sonocatalytic properties. In contrast, more common catalysts such as $TiO_2$ and ZnO show relatively low activity under these conditions. The photocatalytic properties of these metal

[§§] The manufacturers have not provided the particle size information for $Co_3O_4$, CuO, $Er_2O_3$, and $Ta_2O_5$.

oxides, arising from their band gap characteristics, are assumed to have a negligible effect. Choi et al. previously reported that the intensity of sonoluminescence in the ultraviolet range, where most metal oxides are photochemically excited, was very low in the absence of external light sources, and insufficient to effectively excite photocatalysts[225]. As a result, the photocatalytic contribution from the metal oxides is likely minimal. Therefore, in this study, the metal oxides are considered to function solely as sonocatalysts rather than sonophotocatalysts.

Figure 5.1 (b) compares the normalised cavitation index with the hydrogen production rate. Cavitation noise index is used as a proxy for acoustic bubble-cavitation intensity[226]. Unexpectedly, $CeO_2$ and talc occupy a mid-level noise index yet deliver relatively high hydrogen yields across the tested metal oxides. This may indicate that once a threshold in inertial cavitation activity is reached, the chemical nature of the catalyst surface becomes the dominating factor. A higher noise index or cavitation intensity alone does not necessarily translate into higher hydrogen production.

Another consideration is the role of product selectivity, which may not be fully captured in the current analysis. Although this study focuses on hydrogen production, it is plausible that other products, such as hydrogen peroxide, are being generated simultaneously in unknown amounts. In that case, the total product yield may be comparable across different metal oxides, but the specific distribution between hydrogen and other species may vary.

These findings indicate that no single factor, including particle size, cavitation intensity, and catalyst composition, shows a clear, direct correlation with the hydrogen production rate across all materials tested. This suggests that the effects of these variables are interdependent and cannot be considered in isolation. Further research is required to better understand the role of catalyst surface chemistry in sonocatalysis and to identify materials with high sonocatalytic efficiency for hydrogen generation. It is also important to recognise that each material may exhibit an optimal particle size based on its specific chemical properties. Therefore, particle size and morphology need to be optimised depending on the nature of each catalyst.

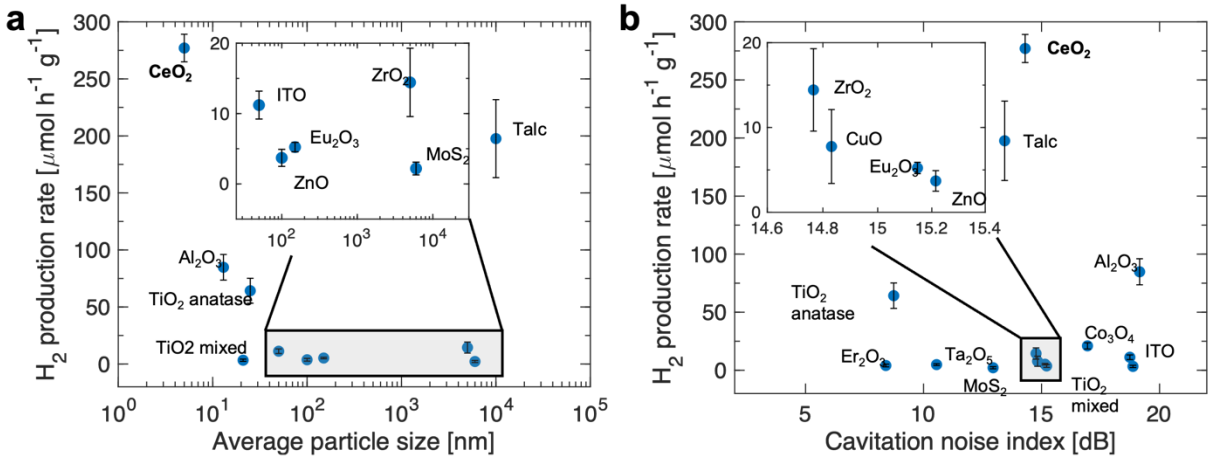



**Figure 5.1. (a)** Effect of average particle size on hydrogen production rate for various metal oxide sonocatalysts. **(b)** Effect of normalised cavitation index on hydrogen production rate for various metal oxide sonocatalysts. The error bars represent the standard deviation of at least three experimental trials for each reaction condition.

$CeO_2$ exhibited the highest hydrogen production rate among the tested metal oxides. Several factors may explain its superior performance. Cerium cations' ability to readily switch between different oxidation states ($Ce^{3+}$ and $Ce^{4+}$) enables the material to release and store oxygen without destabilising its overall structure[227]. The oxygen buffering capacity of $CeO_2$ is crucial in reactions where the supply of oxygen is rate-limiting, such as the generation of ROS like hydroxyl radicals during sonochemical reactions. Merouani et al. reported that over 99% of sonohydrogen is formed within the bubble's gas phase via the reaction $H\bullet + \bullet OH \rightarrow H_2 + O\bullet$[58]. Hence, catalysing the supply of hydroxyl radicals is likely to increase the hydrogen production rate. As $CeO_2$ is believed to facilitate the formation of hydroxyl radicals, it acts as an effective sonocatalyst in the reaction. Moreover, $CeO_2$ is known to be thermally stable, a critical property for high-temperature catalytic applications, especially under the extreme temperatures generated during cavitation implosions in sonochemical reactions[228].

However, these explanations do not fully account for the high hydrogen production rate observed with talc (a hydrous magnesium silicate), which lacks redox-active metal centres. While the exceptional sonocatalytic activity of $CeO_2$ is attributed to the presence of $Ce^{3+}/Ce^{4+}$ redox sites at the surface, talc achieves a comparable hydrogen production rate without any redox couples. In contrast, $Co_3O_4$, which contains both $Co^{2+}$ and $Co^{3+}$ oxidation states that may undergo redox processes, exhibited relatively low activity[229]. This comparison suggests that redox cycling alone does not determine sonocatalytic performance. Instead, other physical factors, such as surface morphology, bubble nucleation behaviour, or cavitation resistance, may also play a crucial role. These observations

highlight the need for further studies to better understand the underlying mechanisms and to explain why $CeO_2$ and talc are highly effective while other materials are not.

### 5.2.2. Incorporation of metal-doped $CeO_2$

Previous studies have shown that metal doping may improve sonocatalytic activity[229,230]. In theory, doping transition metals on $CeO_2$ enhances catalytic properties by promoting the partial reduction of $Ce^{4+}$ to $Ce^{3+}$ through a redox cycle and creating additional oxygen vacancies, which serve as active sites that boost ROS generation[231,232]. Doping may also improve surface reactivity by introducing defects, which often leads to higher reaction rates[233]. Therefore, transition-metal-doped $CeO_2$ catalysts (doped with Mn, Zn, Cu, Fe, Ni, and Co) were investigated to determine whether catalytic modification further enhances sonochemical hydrogen production.

Surprisingly, the results presented in Figure 5.2 indicate that doping $CeO_2$ with transition metals including Mn, Zn, Cu, Fe, Ni, and Co significantly reduces its catalytic performance. A one-way ANOVA indicated that the transition metal modifications had a highly significant effect on the hydrogen production rates ($F_{6,15} = 239.46$, $p < 0.0001$). Undoped $CeO_2$ achieved hydrogen production rates of about 300 $\mu mol\ h^{-1}\ g^{-1}$, all doped variants examined exhibit notably lower activity. This decrease may arise from disrupting the rapid oxygen release-storage mechanism, which breaks the $Ce^{3+}/Ce^{4+}$ equilibrium and suppresses key pathways for the hydrogen generation[234]. Beyond these intrinsic electronic disruptions, the effectiveness of the doping process is dictated by the material preparation procedure adopted in this work. The observed suppression of catalytic activity may reflect a sub-optimised synthesis method that did not yield the expected increase in hydrogen production. For instance, the specific calcination temperature or mixing method may have resulted in the incomplete incorporation of the transition metals into the $CeO_2$ support lattice. As a result, these un-incorporated metals may have segregated to the surface, blocking the active sites needed to form the hydroxyl radicals required for hydrogen production. A similar detrimental effect has been reported previously in the literature, where the introduction of transition metal dopants was shown to deactivate catalytic surface active sites through unfavourable dopant-vacancy combinations[235]. The dopant concentration may also exceed the optimal level, diminishing the catalytic efficiency, an observation reported previously for $TiO_2$ systems[236].

These findings suggest that under the specific synthesis conditions utilised in this study, metal doping did not invariably enhance catalytic performance, highlighting that sonocatalytic efficiency depends heavily on the preparation pathway of the sonocatalyst. Sonocatalysts play a complex role in

sonochemical reactions, and detailed investigation of catalyst properties and mechanisms is needed to improve efficiency. It is usually overly simplistic to assume that catalyst modifications lead to better sonochemical activity, careful optimisation of these modifications is essential to achieve catalytic enhancement.

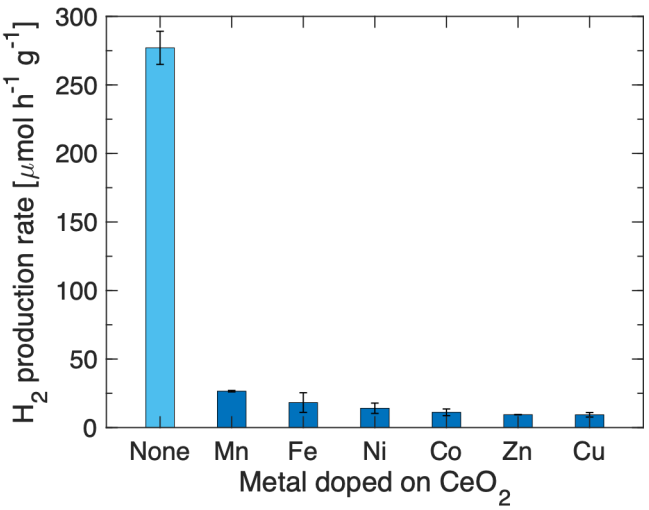



**Figure 5.2.** Hydrogen production rate for various transition-metal-doped $CeO_2$. The error bars represent the standard deviation of the experimental trials for each reaction condition.

In this research, it is acknowledged that the underlying mechanisms responsible for the observed variations in catalytic activity remain unclear, particularly regarding the performance trends among metal oxides and the decrease in activity of metal-doped $CeO_2$. Moreover, despite materials such as $CeO_2$ and talc exhibiting high hydrogen production rates, the fundamental factors responsible for their effectiveness are not yet fully understood. The metal oxides tested in this study differ in several key aspects, such as crystal structure, surface area, electronic properties, defect chemistry, and interaction with ultrasound and cavitation bubbles, which make direct comparison difficult. To identify the key factors influencing sonocatalytic performance, each parameter needs to be isolated to determine its relative importance and better interpret the results of the study.

It is also important to note that several conclusions drawn in this study are based on preliminary observations and have not been substantiated by detailed material characterisations or mechanistic analysis. While literature is used to propose plausible explanations for the observed trends, these postulations remain unverified. Rigorous experimental validations are required to confirm or challenge these interpretations. Consequently, this study represents an initial investigation. Further research is essential to understand the underlying reaction pathways, identify the key catalytic properties influencing the sonocatalytic performance, and develop a deeper understanding to inform future sonocatalyst design and optimisation.

## 5.3. Conclusions

This research chapter expanded upon the findings of the previous Chapter 4, which focused primarily on $TiO_2$ as a sonocatalyst, by investigating a range of less commonly studied metal oxides for sonochemical hydrogen production using SonoCYL. Among the materials evaluated, $CeO_2$ exhibited the highest catalytic activity. The results suggest that the chemical composition of the sonocatalyst is a key factor governing hydrogen production performance. In particular, material-dependent properties, such as oxygen-vacancy density and radical-generation capability, may have a great influence on sonochemical hydrogen production.

Furthermore, the effect of transition-metal doping on the sonochemical performance of $CeO_2$ was investigated. Under the synthesis conditions employed in this study, doping $CeO_2$ with Mn, Zn, Cu, Fe, Ni, and Co resulted in reduced hydrogen production rates. This reduction may be attributed to disruption of the oxygen storage-release properties of $CeO_2$, reduced active site availability, or sub-optimised dopant synthesis conditions. Overall, these findings highlight the importance of catalyst composition and surface chemistry in sonochemical hydrogen production. The findings also highlight the need for further investigation into sonocatalyst design and reaction mechanisms to enable more effective sonochemical processes.

# 6. Sonocatalytic biomass gasification for syngas production

While previous chapters have demonstrated sonochemical hydrogen production via water splitting using $TiO_2$ and alternative catalysts using the novel sonochemical reactor SonoCYL, hydrogen production represents only one of the promising green applications of sonochemistry. To broaden the scope of sonochemical approaches in green chemistry, this research extends its focus to biomass gasification for syngas production. Conventional thermochemical biomass gasification is highly energy-intensive, typically requiring sustained high bulk temperatures of up to 1200 °C, as well as extensive and costly pre-drying of the biomass feedstock to ensure efficient reactor operation[83,84]. In contrast, sonochemical gasification offers a different approach by utilising the extreme, localised conditions generated during acoustic cavitation. These transient hot spots may enable decomposition processes to proceed at ambient bulk temperature and atmospheric pressure, hence eliminating the need for thermal drying and allowing the direct processing of wet or dissolved feedstocks. However, this approach is limited to biomass in liquid form or highly water-soluble substrates, in contrast with conventional solid-fuel gasification technologies.

To date, research on ultrasound-assisted biomass processing has largely been limited to upstream valorisation strategies, including biomass pretreatment, lignin degradation, and cellulose conversion to improve subsequent extraction yields[95-98]. By contrast, the direct, one-step generation of syngas from liquid biomass under ultrasound remains largely unexplored. To establish a proof-of-concept for this pathway, water-soluble, carbon-rich industrial by-products such as molasses are used as feedstocks for the study. Molasses contains a high concentration of dissolved sugars (typically 45-55%), providing an abundant source of readily available carbon[104]. Under ultrasonic irradiation, these dissolved organic compounds may undergo intense, localised pyrolysis and gasification within or near collapsing cavitation bubbles. These transient microreactors may then drive thermal decomposition and radical reactions, producing gaseous products while the surrounding bulk liquid remains at near-ambient conditions.

To enhance gas yields and control syngas selectivity, heterogeneous catalysts are incorporated. Zeolites are widely employed in liquid-phase cracking due to their well-defined pore structures and high densities of Brønsted and Lewis acid sites, which may promote the fragmentation of large organic molecules via carbenium-ion mechanisms[91,106-110]. Section 2.6.5 provides a more detailed discussion of the potential reaction pathways. The incorporation of transition metals such as nickel onto zeolitic frameworks may further introduce bifunctional catalytic activity, combining acid-driven cracking on the support with steam reforming or gasification reaction at the metal sites[116]. Although

conventional thermal gasification often leads to zeolite framework collapse and nickel particle sintering under prolonged high-temperature conditions, the low bulk temperatures characteristic of sonochemical systems may provide a more favourable environment to maintain catalyst structure while enabling these catalytic pathways[117].

This chapter presents a novel ultrasound-driven sonochemical approach for syngas production from molasses, a by-product from the sugar industry, as a proof-of-concept feedstock. In this research, the term sonochemical biomass gasification refers specifically to the ultrasound-assisted conversion of aqueous molasses solutions into syngas via cavitation-driven reactions. Unlike most conventional thermal gasification processes, this study utilises high-frequency ultrasound (780 kHz) to induce cavitation-driven reactions in aqueous molasses solutions under mild conditions, specifically at room temperature and atmospheric pressure, without the need for pre-drying the biomass feedstock. The investigation explores the effects of dissolved gases, sugar composition, water-to-molasses dilution ratio, and the incorporation of zeolite-based catalysts on gas yield and composition. A combination of kinetic analysis and cavitation noise measurements was used to study the reaction mechanisms of the gas formation. The selectivity of hydrogen and carbon monoxide in the resulting syngas is discussed. This study presents syngas production from a liquid-based biomass feedstock, molasses, by a sonochemical process, providing insights into both fundamental mechanisms and practical considerations for future development of the system.

## 6.1. Materials and methods

### 6.1.1. Materials

The following chemicals were used: Glucose (D-(+)-Glucose, ≥99.5% (GC), Sigma-Aldrich), Molasses (El Bawadi), Sucrose (ACS reagent, Sigma-Aldrich), Zeolite Beta (Thermo Scientific Chemicals), Zeolite HY (Si/Al ratio: 15, Thermo Scientific Chemicals), Zeolite ZSM5 (Si/Al ratio: 38, SCG Chemicals), Zeolite Ni-ZSM5 (Ni-doped ZSM5 based on Zeolite ZSM5 (SCG Chemicals), synthesised and provided by Dr. Haokun Wang using impregnation method). The gases used were as follows: Air (Industrial grade, BOC), Argon (Zero grade Ar, BOC), Helium (A Grade, 99.996%, BOC). Deionised filtered Type 1 water was obtained from a water purification system (Millipore Direct Q5-UV). All chemicals were used without further processing unless otherwise stated.

### 6.1.2. Sonochemical reactor system and cavitation noise measurements

The sonochemical reactor setup (780 kHz, 5.1 W) was identical to that described in Section 4.1.2.

### 6.1.3. Cavitation noise signal processing

The cavitation noise measurement setup was identical to that described in Section 4.1.2. However, in this study, the PCD signal was sampled continuously at a rate of three data points per minute (every 20 seconds) over the duration of each experiment, rather than at a single time point for cavitation threshold determination. The recorded signals were processed in MATLAB to calculate the integrated cavitation index, defined as the time-integrated sum of the cavitation signal. Following the method outlined in Section 4.1.4, the cavitation noise was first transformed to extract the total sample voltage value at each time point. These total sample voltage values were then divided by the total degassed water voltage value to normalise the effect of background noise, then summed over time to compute the integrated cavitation index. The MATLAB scripts used for the time-resolved PCD data acquisition and signal processing are provided in the Appendix A.6.4 and A.6.5.

### 6.1.4. Molasses reaction solution preparation and sonochemical reactions

It is necessary to dilute pure molasses prior to the reaction because its high viscosity hinders cavitation bubble evolution and the cavitation activity essential for effective sonochemical reactions[237]. To prepare the molasses reaction solution, pure molasses was freshly diluted with deionised water to create a series of mixtures. Five different dilution ratios were used in the experiments: 6x, 10x, 15x, 20x, and 30x. For example, a 6x dilution refers to a mixture in which six parts by weight of water were added to one part by weight of molasses. This convention was applied to all dilutions.

For each experiment, 2.5 mL of the molasses reaction solution was used. Reactions were carried out under acoustic parameters of 100 cycles, with a burst period of 2.849 ms, a 4.5% duty cycle, and an input power of 5.1 W. When a sonocatalyst was incorporated, its concentration was 0.3 mg/mL unless otherwise stated, based on the optimum sonocatalyst concentration determined in Chapter 5. The reaction time and water-to-molasses dilution ratio for each set of experiments are specified below. Prior to the sonochemical reaction, the reaction solution and headspace were saturated with argon gas, unless otherwise specified. All reactions were conducted at ambient temperature and pressure.

### 6.1.5. Gas analysis

Gas analysis was conducted using a GC (Shimadzu Nexis GC-2030) equipped with a dielectric-barrier discharge ionisation detector and helium as carrier gas. A Carboxen®-1010 PLOT Capillary GC Column (Supelco, L × I.D. 30 m × 0.32 mm, average thickness 15 μm) was used as the analytical column.

The GC setup was identical to that described in Section 4.1.6, but the analytical method was modified to detect additional gases beyond hydrogen including carbon monoxide, carbon dioxide, and methane, as the method in Section 4.1.6 was designed solely for hydrogen detection. Specifically, the oven temperature was initially set to 40 °C and held for 1 minute. It was then increased at a rate of 10 °C per minute until reaching 60 °C and held for 2 minutes. The oven temperature further increased at a rate of 20 °C per minute until reaching 200 °C and held for another 6 minutes. The total analysis time was 18 minutes. The temperature programme was designed to accelerate the elution of carbon monoxide, methane, and carbon dioxide from the column, thereby reducing their retention times and improving the overall time and helium efficiency of the method.

The injection settings, carrier gas flow settings, and detector settings were consistent with those described in Section 4.1.6. To reiterate, the injection temperature was set at 160 °C with a 5:1 split ratio. Column flow was set at 2.81 mL/min and purge flow at 6.0 mL/min, giving a total flow of 22.8 mL/min at a pressure of 130 kPa and a linear velocity of 45.0 cm/s. The BID was maintained at 260 °C with a sampling rate of 40 ms and a discharge gas flow of 50 mL/min.

The GC method was co-developed by the author, Dr. Pankaj Sinhmar, and the Shimadzu GC team, as this was a newly established system in the laboratory. Initial parameters were set according to recommendations from Shimadzu engineers based on their experience analysing small gas molecules, namely hydrogen, carbon monoxide, carbon dioxide, and methane. The author and Dr. Pankaj Sinhmar subsequently refined the parameters to maximise peak separation and sharpness. Oven temperature optimisation was particularly critical for the detection of carbon monoxide, carbon dioxide, and methane, as these gases tend to elute close to atmospheric nitrogen and oxygen and therefore require sufficient peak resolution from one another. The guiding criteria were run efficiency in terms of time and helium consumption, and the absence of ghost peaks, ensuring complete column purging between runs.

At the start of each experimental day, a blank run was performed prior to sample analysis using the same method described above, with the exception that 30 mL of argon was injected in place of a sample. This served to purge and condition the column. The reduced accuracy typically observed in the first run of the day is likely attributed to moisture adsorption in the system overnight, which is cleared by this blank run.

Before every GC measurement, 30 mL of argon gas was purged through the injector to minimise residual sample gas or air at the injector port. For the analysis, 2.5 mL of headspace gas in the reaction vessel was extracted and injected into the GC for analysis with a gas-tight syringe. The retention times for hydrogen, carbon monoxide, methane, and carbon dioxide were 2.52, 4.23, 7.30, and 9.97 minutes, respectively.

These gases were calibrated using a single-point external standard method with 525 ppm calibration gas standards for hydrogen, carbon monoxide, and methane, each balanced in helium. Carbon dioxide was calibrated using the ambient atmospheric concentration of 412 ppm[238]. For each gas, three measurements were collected at the calibration concentration, and the mean peak area was used to calculate a relative response factor (RRF), defined as the peak area per unit concentration (area/ppm). The peak area of the experimental GC signal was converted to the concentration of gas (ppm) using the derived RRF. The use of a single-point RRF calibration is supported by the operating specifications of the Shimadzu GC-BID detector, which exhibits high linearity ($R^2 > 0.995$) over the concentration ranges relevant to the gas measurements reported in this study. Specifically, the detector remains linear without signal saturation for hydrogen concentrations up to 4.81% (48,100 ppm), carbon monoxide up to 2.02% (20,200 ppm), methane up to 10.4% (104,000 ppm), and carbon dioxide up to 2.06% (20,600 ppm)[164]. The corresponding gas volumes and moles were estimated using the ideal gas law, as described in Section 4.1.6. The single-point calibration plots for each gas are provided in Figure 6.1 and Table 6.1. $R^2$ values are omitted for the single-point calibration plots as forcing a single standard through the origin yields an $R^2$ of 1.000 without reflecting actual experimental variance.

The detection limit of the GC-BID system is 0.05 ppm (50 ppb), as specified in the Shimadzu Nexis GC-2030 technical specifications[165]. Following IUPAC guidelines, the limit of quantification (LOQ) was determined as three times the LOD (LOQ = 3 × LOD), corresponding to 0.15 ppm[160]. Based on the respective calibration plots, the LOD peak areas for hydrogen, carbon monoxide, methane, and carbon dioxide were approximately 2, 8, 17, and 15, respectively. The corresponding LOQ peak areas were approximately 6, 24, 51, and 45, respectively. Therefore, chromatographic peaks with areas

below the LOQ were considered unquantifiable, while those below the LOD were considered undetectable. All gas production rates reported in this study, unless labelled as 'not detected', exceeded the quantification limit and were considered analytically reliable.

The calibration was performed assuming a zero-intercept model. This approach is not ideal, as a robust calibration typically employs at least three independently prepared concentration standards for each gas to ensure greater accuracy and reliability, and to avoid constraining the calibration to pass through zero unless this is experimentally justified. However, due to practical constraints during the experimental period, including long procurement lead times for calibration gas standards, it was not feasible to obtain additional calibration gases within the timeframe of this study. Future work needs to prioritise a more comprehensive calibration methodology to improve measurement accuracy and reduce associated uncertainty in gas quantification.

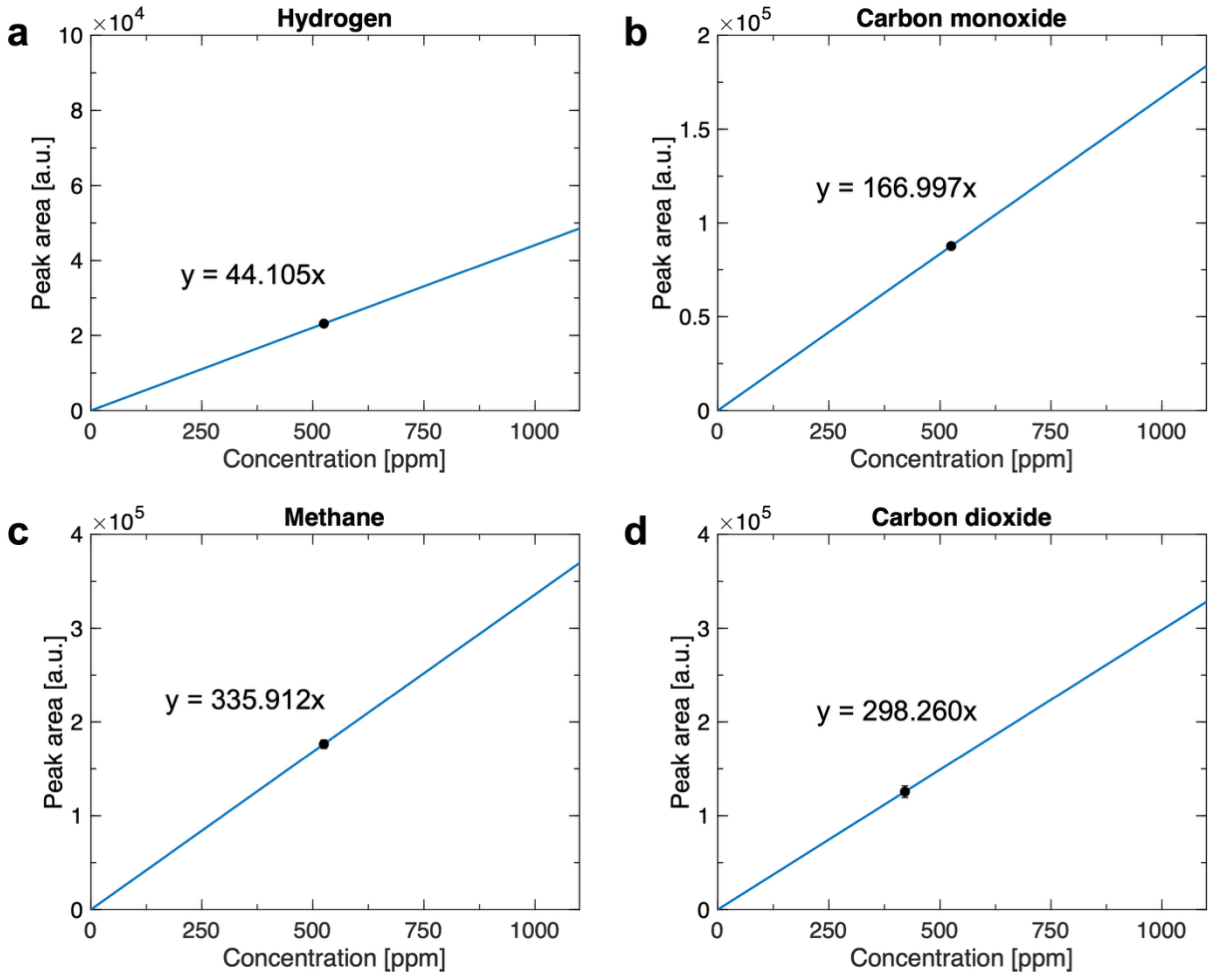



**Figure 6.1.** The calibration plots of hydrogen, carbon monoxide, methane, and carbon dioxide in gas chromatography. Each value is the average of three trials, and the error bars (some overlap with the markers) indicate the standard deviation.

**Table 6.1.** Calibration plots for hydrogen, carbon monoxide, methane, and carbon dioxide.

| Gas | Calibration equation | Slope (a) |
|---|---|---|
| Hydrogen | y = ax | 44.105 |
| Carbon monoxide | y = ax | 166.997 |
| Methane | y = ax | 335.912 |
| Carbon dioxide | y = ax | 298.260 |

### 6.1.6. Liquid analysis

Chemical Oxygen Demand (COD) analysis was performed using pre-dosed dichromate reagents (LCI400 COD cuvette test, Hach), with a measurement range of 0–1000 mg/L $O_2$ following the protocol provided by the manufacturer. Prior to the analysis, samples were diluted 40-fold (1:39 v/v, 1 part sample and 39 parts deionised water by volume) to ensure that COD values fell within the measurement range of the test kit. A 2 mL aliquot of each diluted sample was transferred into a COD digestion cuvette. Deionised water was used as a blank reference for each analytical batch. The cuvettes were then digested in a preheated digestion reactor (DRB200, Hach) at 148 °C for 2 hours. After digestion, the cuvettes were cooled to approximately 60 °C, inverted several times to ensure homogeneity, and then allowed to cool to room temperature. The digested samples were analysed using a spectrophotometer (DR2800, Hach), and COD concentrations were reported as mg/L $O_2$. The COD analysis was performed according to the manufacturer's instructions for the Hach LCI400 COD cuvette test.

High-performance liquid chromatography (HPLC) analysis was performed using a Shimadzu LC-2030C 3D Plus system equipped with an Aminex HPX-87H carbohydrate analysis column (300 x 7.8 mm, hydrogen form, 9 µm particle size, 8% cross-linkage; Bio-Rad, catalog no. 1250140) and a photodiode array (PDA) detector. The column temperature was maintained at 65 °C throughout the analysis. Isocratic elution was carried out using 5 mM $H_2SO_4$ as the mobile phase at a flow rate of 0.5 mL/min. Samples were analyzed directly without further dilution, as they had been diluted during the experimental preparation stage. The injection volume was 20 µL, and detection was performed at 190 nm using the PDA detector. The total analysis run time was 22 min, which was selected to ensure complete elution of all detectable compounds. The molasses compound peaks were observed from 3 to 17 minutes. Data acquisition and processing were conducted using LabSolutions software (version 5.110). The analytical method was adapted from the Bio-Rad Aminex application guide[239].

## 6.2. Results and discussion

This section investigates the effect of dissolved gases in the reaction solution to identify the most suitable dissolved gas for subsequent experiments. Following this, the primary contributors to gas production are examined by studying the sonochemical response of the two most abundant sugars in molasses, glucose and sucrose. The effect of water-to-molasses dilution ratio and incorporation of various zeolite-based sonocatalysts is explored on the gas production. Kinetic and cavitation activity studies are then conducted to understand the underlying reaction mechanisms and to propose the formation pathways of $H_2$, CO, $CH_4$, and $CO_2$. Finally, the selectivity towards $H_2$ and CO in syngas production is explored and discussed.

In addition, liquid-phase analysis was performed on the resultant reaction solutions, including measurements of chemical oxygen demand and high-performance liquid chromatography. However, no conclusive results were obtained. The COD measurements showed negligible changes after the reaction, which may indicate that only a small amount of organic material was consumed during gas production. It is also possible that the COD method lacked the sensitivity to detect minor changes in the concentration of oxidisable organic compounds present in the molasses solution. Similarly, HPLC analysis did not reveal clear differences in organic composition before and after the sonochemical reaction. The chromatograms exhibited significant overlap between the baseline and samples after sonochemical reactions, likely due to either the minimal extent of conversion or limitations in compound separation or detection. Given these uncertainties, the study focuses primarily on the analysis of gaseous products in the subsequent sections.

### 6.2.1. Effect of dissolved gas

The effect of different dissolved gases (or gasifying media) in the reaction solution on gas production is investigated. Figure 6.2 and Table 6.2 present the results obtained when argon and air were used as the dissolved gases in the sonochemical reaction. As expected, air produced a higher total gas yield due to its oxygen content, which likely promoted endothermic reactions and facilitated oxidation processes. However, over 95% of the gaseous product was carbon dioxide, rather than the predicted hydrogen and carbon monoxide. This unexpected outcome is likely due to the presence of oxygen in air, which promotes the complete oxidation of carbon compounds in molasses, favouring $CO_2$ formation rather than partial oxidation, thereby suppressing the generation of $H_2$ and CO. The $CO_2$ contribution from air was subtracted from the results via chromatogram background subtraction, whereby the result chromatogram is subtracted by a background run with air injected into the GC

using the same method, using Shimadzu LabSolutions. The results presented in Figure 6.2 therefore do not include the $CO_2$ originating from air.

In contrast, the use of argon resulted in significantly less $CO_2$ production and generated a $H_2$/CO ratio of approximately 0.78. The lower oxidation observed under argon is attributed to the absence of oxygen, reducing the formation of excess oxidative species (or ROS) and minimising over-oxidation of carbon in the molasses solution. While previous studies suggest that oxygen-rich environments enhance gasification, this discrepancy may be explained by the difference in reactor configuration. Unlike conventional packed bed reactors used in most literature reports, this study employed a sonochemical reactor, which operates through fundamentally different mechanisms. Notably, argon is reported to enhance bubble implosion temperature due to its high isotropic ratio and low specific heat capacity. These properties are predicted to increase the formation of reactive radicals and, therefore, products during cavitation.

Given that $CO_2$ is an undesirable by-product in this context, argon was selected as the dissolved gas for subsequent experiments. The use of argon favours the generation of $H_2$ and CO, which are the targeted products for syngas production.

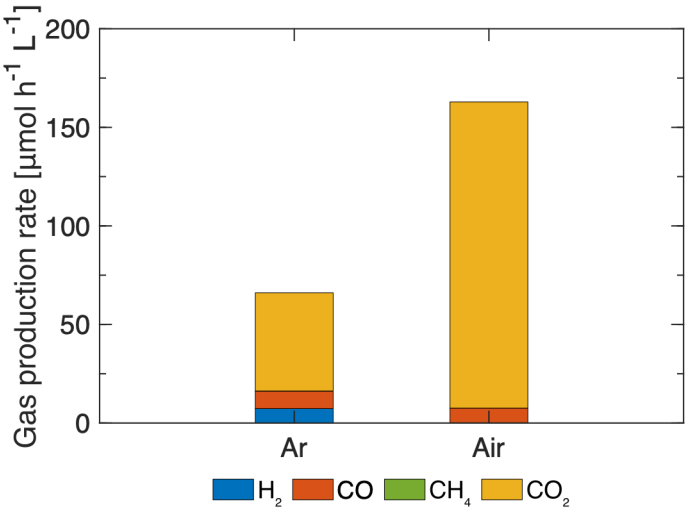



**Figure 6.2.** Gaseous products generated using different dissolved gases during sonochemical biomass gasification. Acoustic parameters: 780 kHz, 100 cycles, 2.849 ms pulse duration, 4.5% duty cycle, 5.1 W power. Reaction time: 2 hours. Chemical parameters: 6x dilution molasses. Results are background-corrected for $CO_2$ originating from air via chromatogram background subtraction using Shimadzu LabSolutions.

**Table 6.2.** Numerical data of gaseous products generated from sonochemical biomass gasification using different dissolved gases. The values represent the average of trials, with the errors indicating the standard deviation. Percentages represent the relative contribution of each gas to the total gas yield.

| Dissolved gas | Gas production rate [μmol $h^{-1}$ $L^{-1}$] | | | | | $H_2$/CO ratio |
|---|---|---|---|---|---|---|
| | $H_2$ | CO | $CH_4$ | $CO_2$ | Total gas production | |
| Ar | 7.3 ± 6.8 (11%) | 9.0 ± 7.9 (13.6%) | Not detected | 49.8 ± 15 (75.4%) | 66.0 ± 29.7 (100%) | 0.78 |
| Air | 0.1 ± 0 (0.1%) | 7.4 ± 2.6 (4.6%) | Not detected | 155.3 ± 24.1 (95.4%) | 162.9 ± 26.7 (100%) | 0.02 |

### 6.2.2. Main contributors to gaseous products

The initial hypothesis postulated that glucose and sucrose, the two most abundant sugar components in molasses, were the primary contributors to the observed gas production. To identify specific reaction pathways, the response of glucose and sucrose was studied separately under ultrasonic irradiation and the results were compared to those obtained from molasses. 6x dilution was chosen initially in the experiment because it aligned with the glucose content of a 0.1 M glucose solution, a commonly used concentration for studies investigating the breakdown of glucose[240,241].

However, as shown in Figure 6.3 and Table 6.3, the $H_2$/CO ratios for glucose and sucrose were nearly 6 and 4, respectively, with measurement errors reported in Table 6.3 and omitted from the figure for clarity. This contrasts sharply with the results from molasses, which exhibited a $H_2$/CO ratio of approximately 1. The difference in these results indicates that glucose and sucrose alone do not account for the gas production observed with molasses. This discrepancy highlights the complexity of molasses as a feedstock, suggesting that numerous carbon-containing compounds in molasses contribute to the gaseous products in sonocatalytic biomass gasification. Furthermore, the gaseous products from sonochemical biomass gasification might originate not only from different organic compounds but also from the catalytic effects of minerals (e.g., calcium, magnesium, iron, potassium, and sodium) and trace elements (e.g., zinc, copper, and manganese) dissolved in the solution, which may facilitate side reactions. Consequently, the chemical composition of molasses cannot be easily deconstructed into single components for isolated study.

Given the multitude of unknowns, it becomes clear that rather than focusing on the precise mechanisms of gaseous product formation from specific components, it is more critical to understand

the overall interaction of molasses with ultrasound. This broader perspective enables a more comprehensive understanding of the sonocatalytic biomass gasification system as a whole.

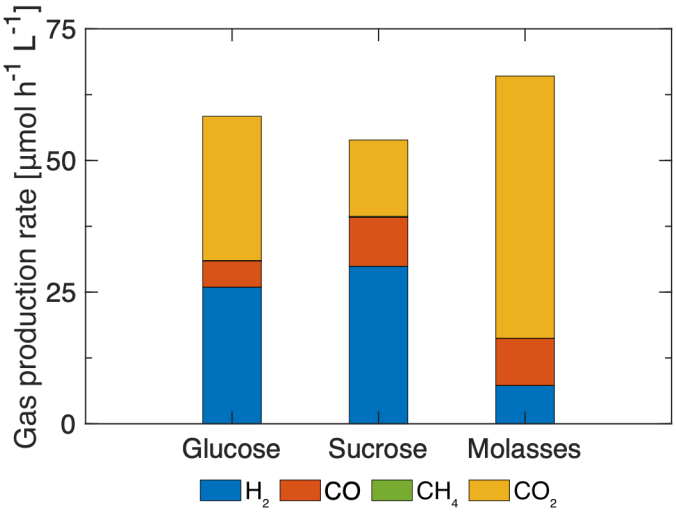



**Figure 6.3.** Gaseous products generated with different reaction solutions (0.1 M glucose solution, 0.1 M sucrose solution, and 6x dilution molasses) during sonochemical biomass gasification. Acoustic parameters: 780 kHz, 100 cycles, 2.849 ms pulse duration, 4.5% duty cycle, 5.1 W power. Reaction time: 2 hours. Chemical parameters: 6x dilution molasses. Errors are reported in Table 6.3. They are not included in the figure for clarity.

**Table 6.3.** Numerical data of gaseous products generated from different reaction solution (0.1M glucose solution, 0.1 M sucrose solution, and 6x dilution molasses) during sonochemical biomass gasification. The values represent the average of trials, with the errors indicating the standard deviation. Percentages represent the relative contribution of each gas to the total gas yield.

| | **Gas production rate [µmol $h^{-1}$ $L^{-1}$]** | | | | | |
|---|---|---|---|---|---|---|
| **Sugar type** | **$H_2$** | **CO** | **$CH_4$** | **$CO_2$** | **Total gas production** | **$H_2$/CO ratio** |
| Glucose | 25.9 ± 19.8 (44.4%) | 4.9 ± 4.1 (8.5%) | 0.1 ± 0.1 (0.2%) | 27.4 ± 16.3 (46.9%) | 58.4 ± 30.3 (100%) | 5.93 |
| Sucrose | 29.9 ± 1.1 (55.5%) | 9.3 ± 4.3 (17.2%) | 0.2 ± 0 (0.4%) | 14.5 ± 6.6 (26.9%) | 53.9 ± 11.9 (100%) | 3.57 |
| Molasses | 7.3 ± 6.8 (11%) | 9.0 ± 7.9 (13.6%) | Not detected | 49.8 ± 15 (75.4%) | 66.0 ± 29.7 (100%) | 0.78 |

### 6.2.3. Effect of water-to-molasses dilution ratio

In the preliminary study, a single water-to-molasses ratio (6x dilution) was initially explored. However, recognising the limitations of studying individual component reactions under ultrasound irradiation, the focus was shifted to investigate the broader interaction between ultrasound and molasses.

Figure 6.4 and Table 6.4 present the gas production rates at different molasses dilutions. Notably, the 15x dilution yielded the highest average total gas production, with the greatest yields of hydrogen and carbon monoxide. A one-way ANOVA indicated that the dilution factor had a significant effect on both hydrogen ($F_{4,14} = 15.56$, $p < 0.001$) and carbon monoxide yields ($F_{4,14} = 11.05$, $p < 0.001$), but the observed differences in total gas production rates were not statistically significant ($F_{4,14} = 1.68$, $p = 0.21$). This outcome likely reflects an optimal balance between the carbon content of the feedstock and the physical properties of the solution. At lower dilutions (i.e., more concentrated molasses), the system receives more organic compounds, leading to increased yields of carbon-based gases such as CO, $CH_4$, and $CO_2$. However, molasses is a highly viscous fluid. When the solution becomes too concentrated, the increased viscosity attenuates sound propagation, reducing cavitation activity, and consequently reducing sonochemical efficiency[242]. Additionally, molasses has a higher surface tension than water, making bubble nucleation and growth more energetically demanding by a higher acoustic pressure threshold[243]. Therefore, the 15x dilution appears to represent an optimal trade-off between the two effects: it supplies sufficient organic content while maintaining favourable physical conditions for cavitation and gas formation.

The trend also suggests that hydrogen production is not solely due to water sonolysis but also involves hydrogen atoms abstracted from the organic components of molasses. This is supported by the absence of a consistent increase in hydrogen yield with higher dilution. Moreover, the hydrogen produced may participate in secondary reactions with molasses-derived hydrocarbons, forming methane via methanation and/or carbon monoxide via the reverse water-gas shift reaction. This may explain why the CO yield at 20x dilution remained similar to that at 10x, despite the lower concentration of organic content.

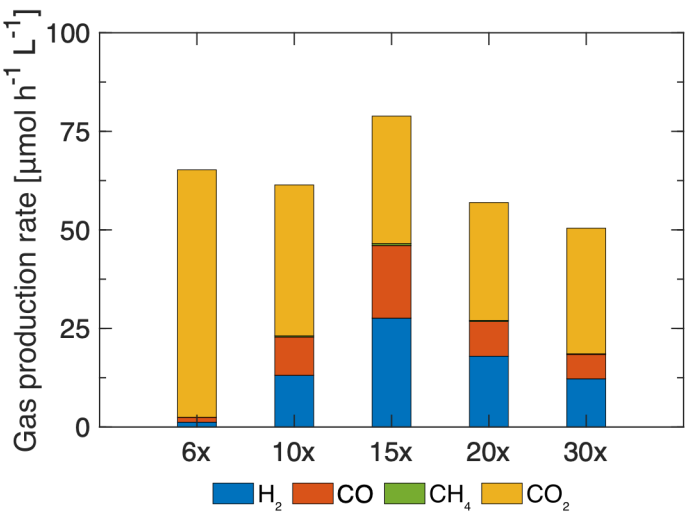



**Figure 6.4.** Gaseous products generated with different water-to-molasses ratios during sonochemical biomass gasification. Acoustic parameters: 780 kHz, 100 cycles, 2.849 ms pulse duration, 4.5% duty cycle, 5.1 W power. Reaction time: 30 minutes. Chemical parameters: 6x, 10x, 15x, 20x, and 30x dilution molasses.

**Table 6.4.** Numerical data of gaseous products generated from different water-to-molasses ratios during sonochemical biomass gasification. The values represent the average of trials, with the errors indicating the standard deviation. Percentages represent the relative contribution of each gas to the total gas yield.

| | Gas production rate [µmol $h^{-1}$ $L^{-1}$] | | | | | |
|---|---|---|---|---|---|---|
| **Dilution** | **$H_2$** | **CO** | **$CH_4$** | **$CO_2$** | **Total gas production** | **$H_2$/CO ratio** |
| 6x | 1.2 ± 0.7 (1.9%) | 1.2 ± 0.8 (1.9%) | Not detected | 62.8 ± 17.4 (96.2%) | 65.2 ± 17.8 (100%) | 1.01 |
| 10x | 13.1 ± 4 (21.3%) | 9.7 ± 4.5 (15.8%) | 0.3 ± 0.1 (0.5%) | 38.3 ± 10.9 (62.4%) | 61.4 ± 15.9 (100%) | 1.44 |
| 15x | 27.6 ± 2.6 (35%) | 18.4 ± 2.3 (23.4%) | 0.5 ± 0.0 (0.6%) | 32.3 ± 5 (41%) | 78.9 ± 9.5 (100%) | 1.50 |
| 20x | 18 ± 4.5 (31.5%) | 8.8 ± 2.7 (15.5%) | 0.3 ± 0.1 (0.5%) | 29.9 ± 8.7 (52.5%) | 56.9 ± 13.9 (100%) | 2.08 |
| 30x | 12.2 ± 6.2 (24.2%) | 6.2 ± 3.5 (12.3%) | 0.1 ± 0.1 (0.3%) | 31.9 ± 6.7 (63.2%) | 50.4 ± 15.9 (100%) | 1.99 |

### 6.2.4. Effect of zeolite sonocatalyst incorporation

It is well-established that the incorporation of heterogeneous catalysts enhances sonochemical activity. This enhancement is attributed to the ability of solid particles to provide preferential sites for cavitation bubble nucleation, while also offering surface active sites for catalytic reactions. This study investigated the effect of introducing zeolite into the sonochemical biomass gasification system.

Zeolites were selected as sonocatalysts due to their widespread use in catalytic biomass conversion, as discussed in Section 2.6.5. They are favoured for their strong acidic sites, which effectively cleave C-C and C-O bonds during cracking reactions. In addition, zeolites possess a uniform microporous structure with shape-selective two-dimensional channels, thermal stability, resistance to nitrogen and sulphur compounds commonly found in biomass, and ease of regeneration[106,244].

Zeolite ZSM5, Zeolite Y, and Zeolite Beta were chosen in the study, as they are several widely recognised catalysts in the literature with proven efficiency in biomass conversion[245-248]. For each type, the variant with the lowest Si/Al ratio was selected, as increased acidity has been shown to enhance catalytic activity. This enhancement is linked to a higher density of Brønsted acid sites (proton-donating Si-OH-Al groups), which promote hydrocracking and facilitate biomass gasification[108].

Figure 6.5 and Table 6.5 present the results of zeolite incorporation in the sonochemical liquid-based biomass gasification system. Surprisingly, the impact of unmodified zeolite was limited: the total gas production rate and the $H_2$/CO ratio remained largely unchanged across all three zeolite types. A one-way ANOVA indicated that the incorporation of unmodified zeolites had no statistically significant effect on either the total gas production rate ($F_{3,10} = 1.31$, $p = 0.32$) or the $H_2$/CO ratio ($F_{3,10} = 0.78$, $p = 0.53$). The maximum increase in total gas yield was only around 6% (comparing 1.50 for no catalyst and 1.60 for using Zeolite Beta), which contradicts the original hypothesis that catalyst addition might significantly improve gasification efficiency.

Several factors may account for this outcome. First, the zeolites may not have been catalytically active under the specific sonochemical conditions used in this study. In many reports, effective biomass conversion occurs only under particular conditions such as temperatures or catalyst concentrations. Previous studies have indicated that an optimal temperature exists for maximising $H_2$ and CO production during biomass gasification[249,250]. However, the exact temperature achieved at the surface of the sonocatalyst during bubble collapse remains unclear to date. Furthermore, the catalyst concentration of 0.3 mg/mL used here was based on previous optimisation in Chapter 4, but this may not be universally suitable given differences in feedstock and sonocatalyst properties. Second, the 15x dilution used in this experiment may have resulted in insufficient concentrations of organic compounds to enable effective interaction with the microporous framework of the zeolites. Finally, unmodified zeolites without metal promoters have been reported to exhibit limited activity in gasification due to coke deposition, which significantly reduces the catalytic lifetime of catalysts.

Literature suggests that doping metal on zeolites is an effective strategy to enhance the catalytic activity by hydrogenation mechanism and stability improvement[251].

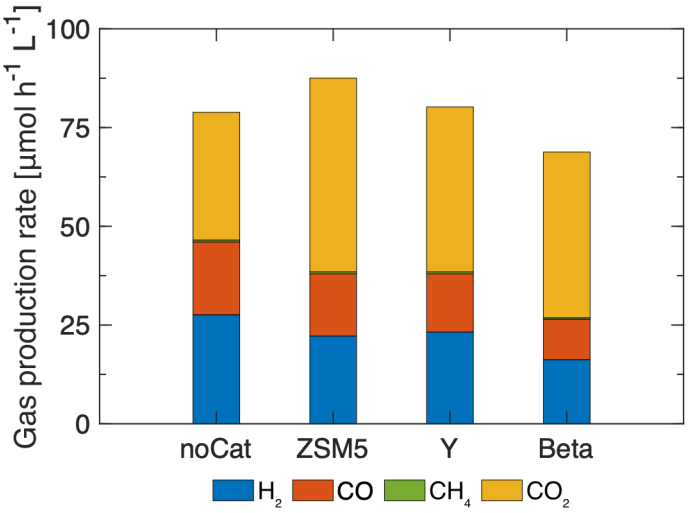



**Figure 6.5.** Gaseous products generated with different zeolites added during sonochemical biomass gasification. Acoustic parameters: 780 kHz, 100 cycles, 2.849 ms pulse duration, 4.5% duty cycle, 5.1 W power, 0.3 mg/mL catalyst concentration. Reaction time: 30 minutes. Chemical parameters: 0.3 mg/mL catalyst concentration, 15x dilution molasses.

**Table 6.5.** Numerical data of gaseous products generated with different zeolites added during sonochemical biomass gasification. The values represent the average of trials, with the errors indicating the standard deviation. Percentages represent the relative contribution of each gas to the total gas yield.

| | Gas production rate [µmol $h^{-1}$ $L^{-1}$] | | | | | |
|---|---|---|---|---|---|---|
| **Zeolite type** | **$H_2$** | **CO** | **$CH_4$** | **$CO_2$** | **Total gas production** | **$H_2$/CO ratio** |
| No catalyst | 27.6 ± 2.6 (35%) | 18.4 ± 2.3 (23.4%) | 0.5 ± 0.1 (0.6%) | 32.3 ± 5 (41%) | 78.9 ± 9.5 (100%) | 1.50 |
| ZSM5 | 22.2 ± 8.3 (25.4%) | 15.7 ± 4.4 (17.9%) | 0.5 ± 0.2 (0.6%) | 49.1 ± 18.3 (56%) | 87.5 ± 13.4 (100%) | 1.42 |
| Y | 23.2 ± 7.9 (29%) | 14.7 ± 5.2 (18.3%) | 0.5 ± 0.2 (0.7%) | 41.8 ± 3.6 (52.1%) | 80.2 ± 15.3 (100%) | 1.59 |
| Beta | 16.2 ± 2.3 (23.6%) | 10.2 ± 1.7 (14.8%) | 0.4 ± 0.1 (0.5%) | 42 ± 10.3 (61%) | 68.8 ± 7.5 (100%) | 1.60 |

Given the limited effectiveness of unsupported zeolites, the investigation was extended to examine the role of catalyst design by evaluating the performance of nickel-loaded ZSM5. It is known that generally metal-loaded acidic zeolite-based catalysts, also known as bifunctional catalysts, enable more efficient catalytic reactions[114]. Nickel was selected as a zeolite promoter based on its promising performance in thermal processing of biomass[116,252,253], particularly in steam reforming and dry

reforming reactions, which enhances $H_2$ and CO production[108]. Nickel-containing catalysts are also favoured for their high efficiency in breaking C-H, C-C, and C-O bonds, relatively low cost, and their regeneration availability[91].

Figure 6.6 and Table 6.6 show that gas production increased significantly with the Ni-doped ZSM5[***], with total gas production increased with increasing nickel loadings. Interestingly, the concentrations of $H_2$ and CO remained relatively similar across no catalyst, ZSM5, 2Ni-ZSM5, and 4Ni-ZSM5 catalysts, while the $CO_2$ concentration increased with increasing nickel content. A one-way ANOVA indicated that the use of various ZSM5 catalysts had a statistically significant effect on both total gas production ($F_{3,6} = 5.25$, $p < 0.05$) and $CO_2$ concentration ($F_{3,6} = 5.08$, $p < 0.05$). However, the variations observed in $H_2$ ($F_{3,6} = 1.27$, $p = 0.37$) and CO concentrations ($F_{3,6} = 1.91$, $p = 0.23$) were not statistically significant. This suggests that nickel effectively breaks more C-bonds in molasses to form more carbon-based gas products. However, the cleaved carbon is over-oxidised, resulting in increasing $CO_2$ formation. Since $CO_2$ is an undesirable product in this study, this outcome reflects reduced selectivity toward syngas. Furthermore, the $H_2$/CO ratio did not change significantly with catalyst loading. This may indicate that the introduction of zeolite or Ni-doped zeolite did not significantly shift the equilibrium of steam reforming or dry reforming reactions. However, the observed increase in $CO_2$ yield with Ni incorporation suggests that Ni sites may promote further cracking of heavier hydrocarbons or oxygenated compounds in the biomass into smaller, more oxidised molecules such as $CO_2$, without altering the primary syngas-forming pathways. Alternatively, Ni may catalyse the oxidation of additional CO generated during sonochemical gasification to $CO_2$, thereby maintaining a relatively constant CO concentration and a stable $H_2$/CO ratio, despite an overall increase in total gas production.

It is also worth noting that in the series of Ni-doped ZSM5 experiments, ZSM5 alone increased gas production compared to the control with no catalyst. This effect was not observed in the earlier experiment with unmodified zeolites. This is likely because a 6x dilution was used here instead of 15x dilution in the series of experiments with unmodified zeolites. This finding agrees with earlier discussion that a minimum concentration of dissolved biomass-derived molecules may be required to initiate catalytic effects. Moreover, the results are consistent with the previous suggestion that metal-doped zeolites such as Ni-ZSM5 are more effective than unmodified zeolites in promoting sonochemical biomass gasification.

[***] The number of Ni-doped ZSM5 represents the nickel loading percentage by weight (wt %). For example, 2Ni-ZSM5 denotes 2% (w/t %) nickel-doped ZSM5.

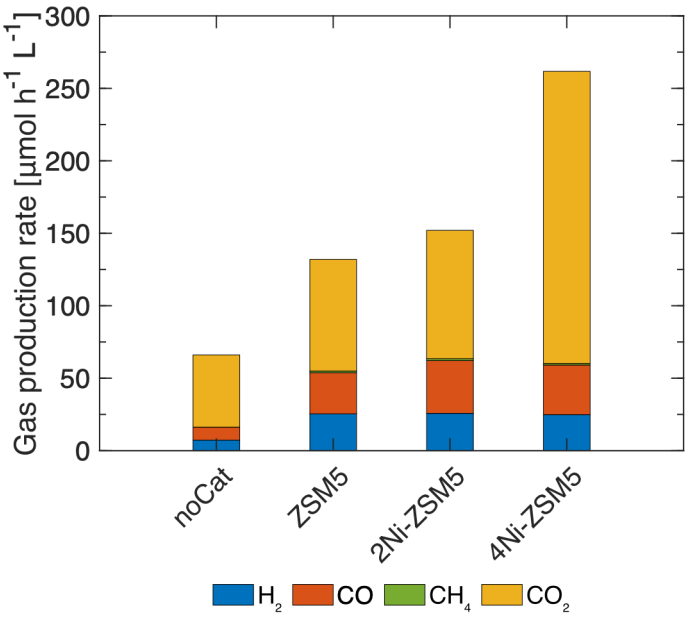



**Figure 6.6.** Gaseous products generated using various ZSM5 catalysts, including Ni-doped variants, during sonochemical biomass gasification. Acoustic parameters: 780 kHz, 100 cycles, 2.849 ms pulse duration, 4.5% duty cycle, 5.1 W power. Reaction time: 2 hours. Chemical parameters: 0.3 mg/mL catalyst concentration, 6x dilution molasses.

**Table 6.6.** Numerical data of gaseous products generated using various ZSM5 catalysts, including Ni-doped ZSM5 with different loadings, during sonochemical biomass gasification. The values represent the average of trials, with the errors indicating the standard deviation. Percentages represent the relative contribution of each gas to the total gas yield.

| | Gas production rate [µmol $h^{-1}$ $L^{-1}$] | | | | | |
|---|---|---|---|---|---|---|
| **ZSM5 type** | **$H_2$** | **CO** | **$CH_4$** | **$CO_2$** | **Total gas production** | **$H_2$/CO ratio** |
| No catalyst | 7.3 ± 6.8 (11%) | 9 ± 7.9 (13.6%) | Not detected | 49.8 ± 15 (75.4%) | 66 ± 29.7 (100%) | 0.78 |
| ZSM5 | 25.4 ± 7.3 (19.2%) | 28.3 ± 5.1 (21.5%) | 1.2 ± 0.2 (0.9%) | 77.1 ± 11.7 (58.4%) | 132 ± 0.9 (100%) | 0.89 |
| 2Ni-ZSM5 | 25.7 ± 12.2 (16.9%) | 36.4 ± 4 (24%) | 1.3 ± 0.5 (0.8%) | 88.6 ± 19.6 (58.3%) | 152 ± 8.8 (100%) | 0.69 |
| 4Ni-ZSM5 | 24.9 ± 14.5 (9.5%) | 34.2 ± 22.1 (13.1%) | 1.1 ± 0.5 (0.4%) | 201.6 ± 80.6 (77%) | 261.7 ± 95.2 (100%) | 0.77 |

### 6.2.5. Kinetic and cavitation study of sonochemical biomass gasification

The kinetics of the sonochemical reaction were investigated by monitoring hydrogen and carbon monoxide production over time. Figure 6.7 (a) and (b) show the $H_2$ and CO production rates as a function of reaction time, respectively. In general, both gases exhibit increasing production over time. However, as the reaction progresses, the data show significant variability despite identical

experimental conditions, particularly with the prolonged reaction time. This high degree of fluctuation suggests that reaction time alone is not a reliable parameter for understanding or monitoring sonochemical activity. The variability may be attributed to intermittent periods during which cavitation did not occur, referred as 'reaction downtime'. During these periods, the ultrasound might not initiate sufficient or any bubble cavitation or bubble implosion, resulting in minimal sonochemical activity.

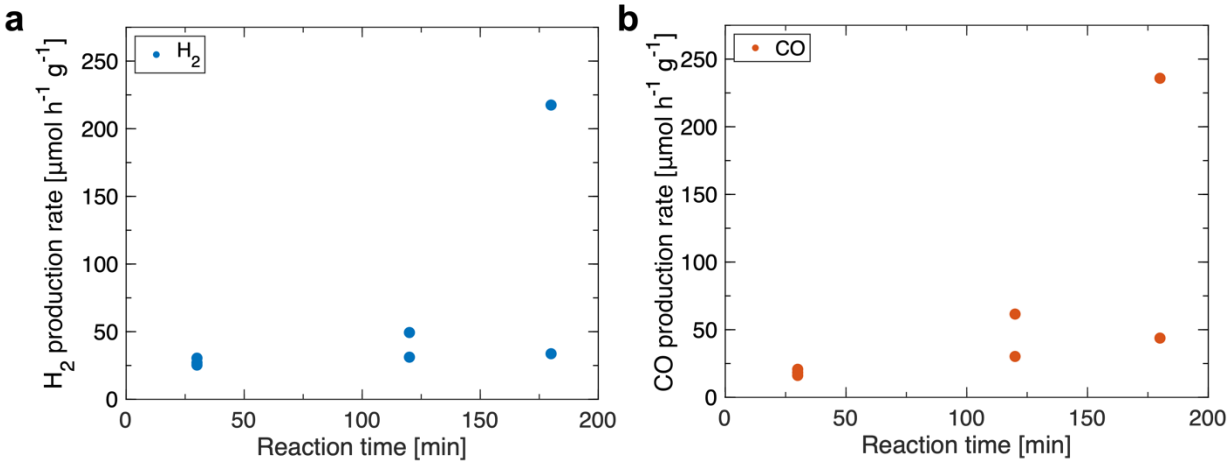



**Figure 6.7**. **(a)** $H_2$ and **(b)** CO production over time during sonochemical biomass gasification. Acoustic parameters: 780 kHz, 100 cycles, 2.849 ms pulse duration, 4.5% duty cycle, 5.1 W power. Reaction time: 30 minutes. Chemical conditions: no catalyst, 15x diluted molasses.

These findings indicate that time-based measurements alone do not provide a meaningful representation of reaction progress or efficiency. To better understand the reaction mechanism, cavitation activity was monitored directly over time using passive cavitation detection. The PCD signal was collected continuously at a frequency of three data points per minute. A FFT was applied to calculate the cavitation index at each time point, normalised using the baseline signal from degassed water.

Figure 6.8 presents the cavitation index trends over time for reaction durations of 30 minutes, 120 minutes, and 180 minutes. The data confirm findings from previous studies that inertial cavitation is inherently stochastic and dynamic. Cavitation involves repetitive nucleation and collapse of bubbles, driven by random nuclei distribution and flow turbulence of the liquid medium. These events are strongly influenced by local variations in acoustic pressure and the random distribution of nuclei in the medium. This leads to the cavitation index frequently exhibits sharp spikes and drops, reflecting the transient and intermittent nature of cavitation events. In some cases, cavitation activity may temporarily die out due to the absence of nuclei and reappear unpredictably when new nuclei emerge.

As a result, each experimental run produces a unique cavitation profile. Furthermore, there are notable differences in cavitation amplitude across different trials, even under seemingly identical experimental conditions. For example, in the 180-minute runs, Trial 1 shows significantly lower cavitation intensity compared to Trial 2. This further highlights the stochastic nature of cavitation activity in sonochemical systems.

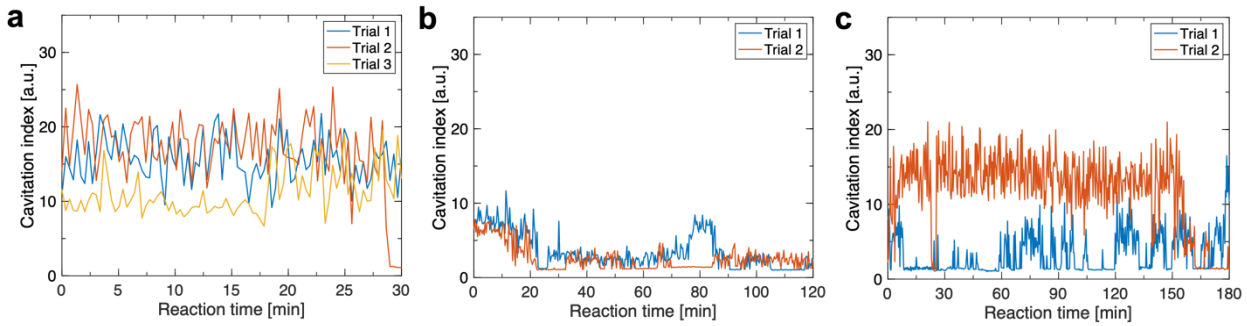



**Figure 6.8**. Cavitation index over time during sonochemical biomass gasification for reaction durations of **(a)** 30 minutes, **(b)** 120 minutes, and **(c)** 180 minutes. Acoustic parameters: 780 kHz, 100 cycles, 2.849 ms pulse duration, 4.5% duty cycle, 5.1 W power. Chemical conditions: no catalyst, 15x diluted molasses.

Cavitation activity varied considerably between trials, suggesting that although the reaction time was kept constant, the actual duration of sonochemically active conditions differed. To account for this, the cavitation index was integrated over time to yield the integrated cavitation index, which served as a proxy for the total cavitation activity during the reaction period. This index captured the total cumulative cavitation activity but did not resolve temporal variations at individual time points.

Figure 6.9 presents the gas production rates for $H_2$, CO, $CH_4$, and $CO_2$ as a function of the integrated cavitation index, covering all trials across different molasses dilutions, unmodified zeolite types, and reaction durations. Categorised data for different dilutions and catalyst types are provided in Appendix Section A.5 with different marker colours and marker shapes, respectively. Interestingly, $H_2$, CO, and $CH_4$ exhibited a rough linear relationship with the integrated cavitation index. This observation supports the hypothesis that these gases are primarily formed through cavitation-driven mechanisms, such as bubble implosion and reactions involving hydroxyl radicals. It also suggests that variations in dilution, unmodified zeolite type, or reaction time do not alter the underlying relationship between cavitation intensity and gas yield for these products, likely because the same reaction pathways dominate their formation.

In contrast, $CO_2$ production showed no clear trend with the integrated cavitation index. This might be due to the presence of multiple $CO_2$ formation pathways, including side reactions and the oxidation of CO, which were not directly governed by cavitation intensity alone. At present, the available data are insufficient to deconvolute the various sources of $CO_2$ generation. In addition, nearly all $CO_2$ data points exceeded 25 µmol $h^{-1}$ $L^{-1}$. This is attributed to background $CO_2$ present in atmospheric air (approximately 420 ppm), which corresponds to a similar value when converted to the same unit (µmol $h^{-1}$ $L^{-1}$). Despite extensive efforts to minimise air contamination during gas sampling, complete exclusion of atmospheric $CO_2$ from the gas chromatography analysis remained challenging. As a result, all measured $CO_2$ concentrations exceeded 25 µmol $h^{-1}$ $L^{-1}$.

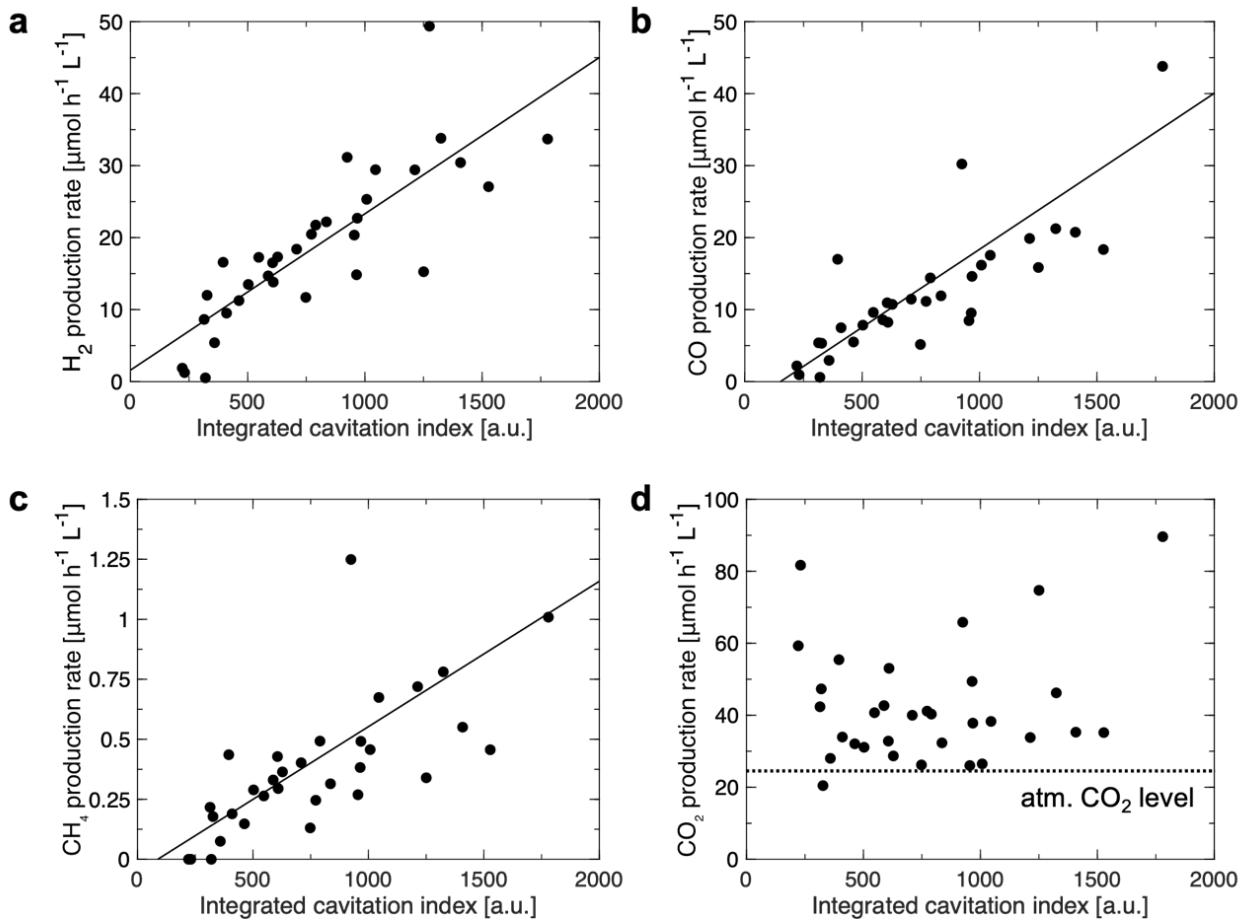



**Figure 6.9.** Gas production rate as a function of integrated cavitation index for **(a)** $H_2$, **(b)** CO, **(c)** $CH_4$, and **(d)** $CO_2$. Data points represent results from all experimental trials, including variations in molasses dilution, unmodified zeolite types, and reaction durations.

### 6.2.6. Selectivity for syngas production

From Table 6.4 and Table 6.5, the syngas ($H_2$/CO) production ratio consistently fell within the range of approximately 1 to 2. As discussed previously, the integrated cavitation index analysis suggested that $H_2$, CO, and $CH_4$ were likely formed through the same cavitation-driven mechanism. A single dominant mechanism typically results in a fixed product selectivity. To investigate this further, Figure 6.10 shows the $H_2$ and CO production rates against $CH_4$ production rates across all experimental trials, including variations in molasses dilution, unmodified zeolite types, and reaction durations. This approach enabled direct comparison of product ratios independent of both reaction time and integrated cavitation index, thereby normalising for batch-to-batch experimental variability.

The slope of the linear fit in the plots reflects the selectivity between the product gases: for every 1 unit of $CH_4$ produced, approximately 36 units of $H_2$ and 32 units of CO are generated, resulting in an estimated $H_2$/CO ratio of 1.125 in sonochemical molasses gasification.

Different chemical processes require specific $H_2$/CO ratios. A ratio of 1.125 aligns with the requirements for processes such as ethanol synthesis (with an ideal ratio ~1), dimethyl ether (DME) production (with an ideal ratio between 1 and 2), and hydrocarbon synthesis[254]. However, it is acknowledged that considering downstream applications at this research stage is premature, given the current low production rates in the micromole per litre per hour range. The immediate research priority is therefore to significantly improve the gas production rate through system scaling and optimisation of reaction parameters.

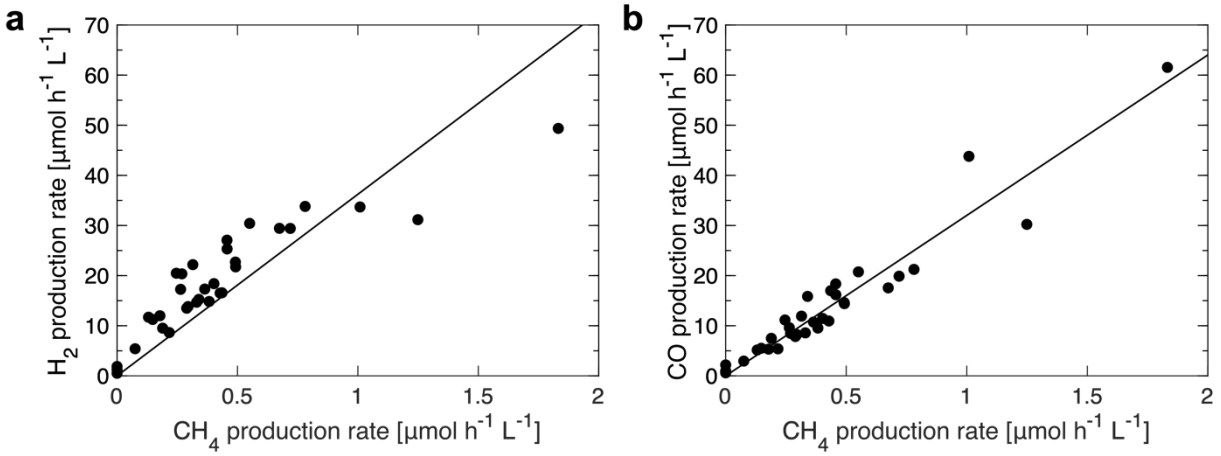



**Figure 6.10. (a)** $H_2$ and **(b)** CO production rates plotted against $CH_4$ production rate. The slope of the best-fit line represents the molar ratio of $H_2$:$CH_4$ and CO:$CH_4$. Data points represent results from all

experimental trials, including variations in molasses dilution, unmodified zeolite types, and reaction durations.

## 6.3. Conclusions

This research chapter investigated the feasibility of ultrasound-driven liquid-based biomass gasification for syngas production, using molasses as a representative unrefined liquid biomass feedstock. The effects of dissolved gas composition, sugar content, molasses dilution ratio, and catalyst incorporation on gas production were evaluated. The use of argon as the dissolved gas resulted in higher $H_2$ and CO yields compared with air, likely because the absence of oxygen reduces the over-oxidation of carbon-containing species in the molasses solution. In addition, argon has been reported to enhance bubble implosion temperatures due to its high isotropic ratio and low specific heat capacity. An optimal molasses dilution ratio of 15x was identified to produce the highest yields of $H_2$ and CO. This optimal ratio likely reflected a balance between organic content and favourable physical properties, such as viscosity and surface tension, which promote intense acoustic cavitation. The influence of catalyst incorporation was also examined using zeolite-based materials, including ZSM5, Y, and Beta. Under the conditions investigated, these catalysts did not significantly enhance gas production, possibly due to limited sonocatalytic activity or catalyst deactivation through coke formation. Ni-doped ZSM5 increased overall gas yields, particularly $CO_2$ production, suggesting that Ni enhanced decomposition of carbon-containing species in the molasses solution.

To provide further insight into the reaction mechanisms, kinetic and cavitation analyses were performed. A linear trend was observed between the time-integrated cavitation index and the production of $H_2$, CO, and $CH_4$, indicating that acoustic cavitation is the primary driving mechanism for the formation of these gases. In addition, the $H_2$/CO ratio remained at 1.125 for the sonochemical biomass gasification. The findings in this chapter present the first demonstration of syngas production from a liquid biomass feedstock using sonochemical processing and highlight the potential of ultrasound-driven biomass valorisation for syngas generation.

# 7. Conclusions and future work

## 7.1. Conclusions

As reviewed in the literature, sonochemistry holds great potential in advancing green chemistry. This thesis explores the development of a sonochemically efficient reactor and its application in two key areas of green chemistry. A novel sonochemical reactor was first designed and characterised, followed by its application in (1) hydrogen production via water and seawater splitting and (2) syngas production from molasses. The main findings and contributions are summarised below.

Chapter 3 introduces the design and characterisation of a novel sonochemical reactor, SonoCYL, which employs cylindrically converging acoustic waves to focus energy within a focal reaction volume of ~1.16 μL. The reactor was evaluated both acoustically and chemically. •OH generation was quantified using a sensitive and selective fluorescent probe, Res-DHB, and sonochemical efficiency was measured under various operating conditions. Sonochemical efficiency increased with acoustic pressure, with an optimum identified at 15.1 $MPa_{pkpk}$ and 100 acoustic cycles. Compared to conventional sonochemical reactors, including ultrasonic baths, immersed horns, and plate reactors, SonoCYL achieved at least two orders of magnitude higher •OH production and at least double the sonochemical efficiency. Similar trends were observed using the TA dosimetry method. These results highlight the importance of reactor geometry and acoustic conditions in enhancing sonochemical performance, and this design may inform future developments for industrial scale sonochemistry.

Chapter 4 focuses on sonochemical hydrogen production, using SonoCYL as the sonochemical reactor (780 kHz, 5.1 W) and $TiO_2$ as a sonocatalyst in both pure water and seawater. Acoustic and chemical parameters were optimised, with the optimal $TiO_2$ concentration determined to be 0.3 mg/mL and 100 acoustic cycles. Cavitation activity was validated via passive cavitation detection and acoustic signal processing. The negative effects of dissolved salts on hydrogen yield were investigated and attributed primarily to chemical scavenging effects, as confirmed by bubble dynamics simulations and EPR measurements. This study achieved the highest reported normalised sonochemical hydrogen production efficiencies in the literature for both pure water (7906 μmol $g^{-1}$ $L^{-1}$ $Whr^{-1}$) and seawater (4398 μmol $g^{-1}$ $L^{-1}$ $Whr^{-1}$), corresponding to production rates of 101.4 μmol $h^{-1}$ $g^{-1}$ and 56.4 μmol $h^{-1}$ $g^{-1}$, respectively. These findings demonstrate the viability of ultrasound-driven hydrogen production and suggest potential for this method to complement existing hydrogen generation technologies.

Chapter 5 explores less commonly studied metal oxides for sonochemical hydrogen production. Among the tested materials, $CeO_2$ exhibited the highest catalytic activity. The results suggest that hydrogen production performance is strongly influenced by the chemical composition of the sonocatalyst. Specifically, material-dependent properties may contribute significantly to the observed differences in catalytic activity. Furthermore, the effect of transition-metal doping of $CeO_2$ on sonochemical hydrogen production performance was investigated. Under the synthesis conditions employed in this study, doping $CeO_2$ with transition metals (Mn, Zn, Cu, Fe, Ni, and Co) resulted in reduced hydrogen production rates. This reduction may be attributed to disruption of the oxygen storage-release properties of $CeO_2$, reduced active site availability, or sub-optimised dopant synthesis method. Overall, these findings highlight the importance of further investigation into sonocatalyst design and reaction mechanisms to enable more effective optimisation of sonochemical processes.

Chapter 6 presents a feasibility study on ultrasound-driven biomass gasification for syngas production, with molasses used as a representative unrefined feedstock. The effects of dissolved gas composition, sugar content, molasses dilution ratio, and catalyst incorporation were investigated. Argon was shown to favour $H_2$ and CO generation compared to air. An optimal molasses dilution ratio of 15x was identified, likely due to the balance between organic content and favourable physical properties (such as viscosity and surface tension) for intense acoustic cavitation. The introduction of zeolite-based catalysts (ZSM5, Y, Beta) did not significantly improve gas yield, possibly due to their lack of sonocatalytic activity under the reaction conditions or coke formation. Ni-doped ZSM5 led to increased gas yields, particularly in $CO_2$, suggesting that Ni promotes additional breakdown of carbon-containing biomass compounds. A kinetic and cavitation analysis was also performed. The time-integrated cavitation index was found to correlate linearly with the production of $H_2$, CO, and $CH_4$, indicating that cavitation is the primary driving mechanism for the formation of these three gases. The $H_2$/CO ratio was maintained at 1.125 for the sonochemical biomass gasification. These findings present a first demonstration of sonochemical syngas production from a liquid-based biomass.

Overall, this research presents the development and characterisation of the SonoCYL reactor, a novel design that demonstrates improved sonochemical efficiency compared with conventional sonochemical reactors, as well as its potential application in green chemical processes.

While the reactor design represents an advancement in the application of sonochemistry, the transition from a laboratory-scale innovation to a practical viable technology remains a major challenge. To date, the experimental work has been conducted primarily in millilitre-scale batch systems, which are

suitable for fundamental research but insufficient for the larger processing volumes required for real-life implementation. Therefore, the most critical objective for future work is the scale-up to litre-scale volumes and continuous-flow operation. Without such progress, the unique acoustic environments created by the SonoCYL design will remain confined to specialised laboratory systems.

This thesis also successfully demonstrated ultrasound-driven hydrogen generation from water and seawater using catalysts such as $TiO_2$. However, comparison with established green hydrogen technologies highlights important limitations regarding its practical deployment. At present, green hydrogen is predominantly produced through water electrolysis, which typically achieves efficiencies exceeding 60% and operates at production scales of tonnes per year[255]. By contrast, the sonochemical hydrogen production observed throughout this study remained well below 1% efficiency. Since hydrogen is a global commodity, its market competitiveness depends on low production costs and high production volumes, sonochemical hydrogen generation currently faces a fundamental mismatch between its energy-intensive operation and the relatively low value of the resulting product. Consequently, unless a breakthrough in efficiency is achieved, sonochemical hydrogen production is unlikely to become a promising potential hydrogen production pathway. Currently, its greatest value lies as a research and development platform for advancing the fundamental understanding of sonochemistry, cavitation mechanisms, and catalyst-cavitation interactions, rather than as a realistic route toward sustainable hydrogen production.

The most promising future applications of sonochemical engineering may instead lie in the targeted treatment and upgrading of liquid-phase feedstocks and waste streams. The investigation into syngas generation from molasses demonstrated that sonochemical cavitation may effectively initiate the decomposition of water-soluble organic materials, upgrading a low-value by-product into more valuable products such as syngas. As ultrasound requires a liquid medium for efficient energy transfer, sonochemistry is particularly well suited to processing biomass-derived liquids and industrial waste streams that are difficult to treat or upgrade using conventional thermochemical gasification methods. This creates opportunities in sustainable applications such as wastewater treatment and waste valorisation, where sonochemistry may enable the recovery of valuable products from low- or near-zero-value materials that would otherwise be treated as waste.

Furthermore, the highly specialised chemical environment generated within acoustic cavitation hot spots provides unique reaction pathways that may be applied for the synthesis of high-value chemicals and advanced materials, such as pharmaceuticals and speciality chemicals. In such applications, production volumes are relatively low, while product value is exceptionally high. Under these

conditions, the high energy demands and low yields associated with sonochemistry may be justified by its ability to simplify synthesis routes, enhance selectivity, or produce molecular structures that are otherwise difficult to achieve using conventional methods. By focusing on low-volume, high-value chemical synthesis rather than large-scale commodity production, sonochemistry may become a valuable tool by utilising the unique chemical environments created by acoustic cavitation.

## 7.2. Future work

Based on insights gained through this thesis, future research in sonochemistry may be grouped into four aspects:

- **Scaling**: Increasing throughput and energy efficiency is essential for industrial viability.
- **Mechanism**: A more comprehensive mechanistic understanding in sonochemistry is important for selective reaction design and sonocatalyst development.
- **Applications**: Exploring emerging use cases for sonochemistry, particularly when it offers energy efficiency advantages, enables previously inaccessible reaction pathways, or facilitates decentralised production of chemical processes.
- **Techno-economic and environmental assessment (TEA and LCA)**: Comparative evaluation of sonochemical systems against conventional technologies will help to understand when and where sonochemistry offers a competitive advantage.

In the context of this research, several key areas remain open for further investigation to deepen understanding, improve system performance, and enable real-world implementation.

**Reactor design and standardisation**

Although the SonoCYL reactor showed substantial improvements in sonochemical efficiency compared to conventional sonochemical reactor designs, its current configuration is limited by its small active volume and batch operation mode. Future development efforts will need to prioritise reactor scale-up and the transition to a continuous flow design that is more compatible with industrial processes. Additionally, there remains a clear need to develop a standardised protocol for sonochemical efficiency benchmarking, as current practices vary widely in units, power measurements, and energy normalisation. Establishing consistent guidelines will benefit the broader sonochemistry community in comparing reactor systems and optimising acoustic parameters.

**Expanding sonochemical hydrogen production conditions and feedstocks**

This study demonstrated that salt composition significantly affected sonochemical hydrogen production, with yields that followed the trend of NaCl > KCl > $MgCl_2$ > $CaCl_2$ > $Na_2SO_4$. The observed differences suggested that factors such as the number of dissociated ions, cation size, and anion charge density might influence cavitation dynamics and radical-mediated $H_2$ generation. To

better understand these effects, future research will need to combine EPR spectroscopy, DFT calculations, and molecular dynamics simulations to investigate how specific ions affect radical stability and bubble collapse behaviour. Additionally, measuring solution properties, such as viscosity, surface tension, and gas solubility, under ultrasonic conditions will help distinguish physical from chemical contributions. These insights will be critical for understanding the influence of salt composition and advancing knowledge of how different feedwaters behave under sonochemical hydrogen production conditions.

Beyond seawater, other industrially relevant feedwaters, such as pharmaceutical effluents or PFAS-contaminated (per- and polyfluoroalkyl substances, also called 'forever chemicals') streams, may present opportunities for simultaneous pollutant degradation and $H_2$ generation, providing both environmental and energy benefits. Finally, the exploration of alternative sonocatalysts is crucial to further improve hydrogen yields under optimised conditions, as discussed in the following section.

**Sonocatalyst design and mechanistic understanding**

Among the metal oxides screened in this study, $CeO_2$ and talc exhibited notably high catalytic activity for sonochemical hydrogen production. However, the underlying reasons for their superior performance remain unclear. To uncover the sonocatalytic structure-activity relationships, future studies may isolate and examine key material properties, including oxygen storage-release capacity, particle size, surface area, surface roughness, defect chemistry, and redox-active metal centres. Pre- and post-reaction characterisation of the catalysts is essential for identifying which properties govern the sonocatalytic behaviour and for proposing plausible reaction mechanisms. Interestingly, although transition metal doping on metal oxides is widely reported to enhance catalytic performance, such doping in this study led to reduced hydrogen yields. This suggested either excessive or insufficient dopant incorporation, or disruption of key $CeO_2$ functionalities such as oxygen buffering capacity. Optimising the doping concentration and synthesis protocol will offer a promising pathway to engineer more efficient doped $CeO_2$ catalysts for sonochemical hydrogen production.

To further investigate sonocatalytic activity, DFT calculations will be essential for modelling the interaction between hydroxyl radicals and catalyst surfaces, enabling the identification of materials that most effectively promote $H_2$ formation. In parallel, bubble dynamics simulations may reveal how catalyst surfaces influence bubble nucleation, collapse intensity, and cavitation probability, all of which are factors that directly affect radical generation. The use of integrated cavitation index measurements, rather than instantaneous measurements, is also recommended to more accurately

represent the cumulative cavitation activity over the course of a reaction. These combined insights will be vital for developing a mechanistic understanding of sonocatalyst performance and guiding the rational design of effective sonocatalysts.

**Mechanistic study and product control in biomass gasification**

Ultrasound-assisted biomass gasification demonstrated potential for sustainable syngas production in Chapter 6, yet many fundamental aspects remain unknown. A priority for future work is a comprehensive mechanistic study to identify the primary reaction pathways for $H_2$, CO, $CO_2$, and $CH_4$ formation. This may be achieved through isotope labelling, time-resolved gas sampling, and computational modelling, which together may identify intermediate species and reaction pathways involved in the cavitation-driven chemistry. In parallel, greater effort is needed to improve product selectivity, particularly tuning the $H_2$/CO ratio through sonocatalyst selection and optimisation. The observed limited impact of zeolites and Ni-based catalysts suggests a need to screen broader catalyst classes, optimise loading and synthesis protocol, and explore alternative materials that suit the application of sonochemical biomass gasification. Another interesting avenue will be to explore why no liquid-phase products were observed, which may be linked to the temperature or intensity of cavitation implosions. Tailoring reaction conditions or catalyst design to favour molecular upgrading in the liquid phase, rather than full decomposition to gaseous products, may open new pathways for value-added biomass utilisation. These investigations will deepen the understanding of the chemistry in ultrasound-driven biomass gasification and guide the development of more efficient and tuneable sonochemical gasification systems.

# Appendix

## A.1. Calorimetry measurements and fitting

The acoustic power of the SonoCYL was estimated using a calorimetric method to enable comparison with sonochemical results reported in the literature. A heat transfer model was applied for the calculation. The calorimetric power measurements and estimations via heat transfer modelling were jointly conducted by Professor James Kwan and Cherie C.Y. Wong.

The calorimetric power is defined as

$$\mathbf{P_{calorimetry} = (H_v)\,(V)} \qquad \textbf{(Eq. A1.1)}$$

where $P_{calorimetry}$ is the acoustic power calculated by calorimetric method, $H_v$ ($W/m^3$) is the heat generation by volume, and V is the fixed sample volume. The heat transfer model is used to determine $H_v$ by fitting the experimental data.

The schematic of the sample vial used in the model is shown in Figure A1.1. R is the radius (i.e. the maximum radial length) of the cylindrical vial and r is the radial length of the cylindrical vial.

Several **assumptions** were defined for the heat transfer model.

1. $S_{shell} \gg S_{cap}$
   where $S_{shell}$ is the surface area of the cylindrical vial and $S_{cap}$ is the surface area of the bottom hemispheric of the sample vial.
2. $T(R) = \hat{T}$ (Eq. A1.2)
   where T is the temperature and $\hat{T}$ is the average temperature of the fluid in the sample vial.
3. The measured temperature is the spatial average temperature of the fluid in the sample vial.
4. The wall of the vial is free from heat transfer.

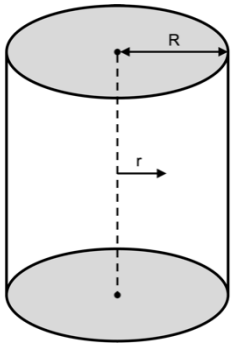



**Figure A1.1.** Schematics of the sample vial used in the heat transfer model.

The **boundary conditions** are defined.

1. At $t = 0$,

$$T = T_0$$

t is the reaction time;

$T_0$ is the initial temperature of the sample, which is the same as the water bath temperature.

2. At $r = R$, by applying the convective boundary condition

$$-k\frac{\partial T}{\partial R}\Big|_{r=R} = h(T(R) - T_0)$$

k is the thermal conductivity of the fluid;

h is the heat transfer coefficient; and

$$\frac{\partial T}{\partial R}\Big|_{r=R} = -\frac{h}{k}(T(R) - T_0)$$

Therefore, by Eq. A1.2

$$\frac{\partial T}{\partial R}\Big|_{r=R} = -\frac{h}{k}(\hat{T} - T_0) \qquad \text{(Eq. A1.3)}$$

The general **heat equation** is given in Eq. A1.4.

$$\mathbf{\frac{\partial T}{\partial t} = \alpha \nabla^2 T + \frac{H_v}{\rho C_p}} \qquad \textbf{(Eq. A1.4)}$$

$\frac{\partial T}{\partial t}$ represents the accumulation of heat;

$\alpha\nabla^2 T$ represents the diffusion of heat; and

$\frac{H_v}{\rho C_p}$ represents the heat generation from ultrasound attenuation.

$\alpha$ is the fluid's thermal diffusivity;

$\nabla^2$ is the Laplace operator;

$\rho$ is the density of the fluid; and

$C_p$ is the heat capacity of the fluid.

T is assumed to be a function of r and t,

$$T = f(r, t)$$

The Laplacian in cylindrical coordinates is used to describe heat diffusion.

$$\nabla^2 T = \frac{1}{r}\frac{\partial}{\partial r}\left(r\frac{\partial T}{\partial r}\right) + \frac{1}{r^2}\frac{\partial^2 T}{\partial \theta^2} + \frac{\partial^2 T}{\partial z^2} \qquad \text{(Eq. A1.5)}$$

$\frac{1}{r^2}\frac{\partial^2 T}{\partial \theta^2}$ represents the change of T with respect to the change in angle θ. As the cylindrical vial is symmetrical radially, therefore $\frac{1}{r^2}\frac{\partial^2 T}{\partial \theta^2} = 0$. Similarly, $\frac{\partial^2 T}{\partial z^2}$ represents the change of T with respect to the change in z-axis. As the temperature is assumed to be uniform across the z-axis here, therefore $\frac{\partial^2 T}{\partial z^2} = 0$.

Hence, the Laplacian is reduced to

$$\nabla^2 T = \frac{1}{r}\frac{\partial}{\partial r}\left(r\frac{\partial T}{\partial r}\right) \qquad \text{(Eq. A1.6)}$$

By substituting Eq. A1.6 back to the general heat equation (Eq. A1.4), it becomes

$$\frac{\partial T}{\partial t} = \alpha\frac{1}{r}\frac{\partial}{\partial r}\left(r\frac{\partial T}{\partial r}\right) + \frac{H_v}{\rho C_p} \qquad \text{(Eq. A1.7)}$$

$\widehat{T}$ is defined as

$$\widehat{T} = \frac{\int_0^{2\pi}\int_0^R T\, r\, dr\, d\theta}{\pi R^2} \qquad \text{(Eq. A1.8)}$$

where $\int_0^{2\pi}\int_0^R T\, r\, dr\, d\theta$ is the integral of the circle area multiplied by its temperature, and $\pi R^2$ is the circle area of the cylinder.

After integration,

$$\widehat{T} = \frac{2}{R^2}\int_0^R T\, r\, dr \qquad \text{(Eq. A1.9)}$$

Then, the temperature average for each term in the heat equation is calculated by multiplying $\frac{2}{R^2}$ and integrating $\int_0^R r\, dr$ to both side of the equation (Eq. A1.7).

$$\frac{\partial T}{\partial t} = \alpha\frac{1}{r}\frac{\partial}{\partial r}\left(r\frac{\partial T}{\partial r}\right) + \frac{H_v}{\rho C_p}$$

$$\frac{2}{R^2}\int_0^R \frac{\partial T}{\partial t}\, r\, dr = \frac{2\alpha}{R^2}\int_0^R \frac{1}{r}\frac{\partial}{\partial r}\left(r\frac{\partial T}{\partial r}\right)\, r\, dr + \frac{2}{R^2}\int_0^R \frac{H_v}{\rho C_p} r\, dr$$

$$\frac{\partial}{\partial t}\left(\frac{2}{R^2}\int_0^R T\, r\, dr\right) = \frac{2\alpha}{R^2}\int_0^R \partial\left(r\frac{\partial T}{\partial r}\right) + \frac{2}{R^2}\frac{H_v}{\rho C_p}\left[\frac{r^2}{2}\right]_0^R$$

By substituting Eq. A1.9,

$$\frac{\partial \widehat{T}}{\partial t} = \frac{2\alpha}{R^2}\left[r\frac{\partial T}{\partial r}\right]_0^R + \frac{H_v}{\rho C_p}$$

$$\frac{\partial \widehat{T}}{\partial t} = \frac{2\alpha}{R^2}\left(R\frac{\partial T}{\partial R}\Big|_{r=R} - (0)\frac{\partial T}{\partial R}\Big|_{r=R}\right) + \frac{H_v}{\rho C_p}$$

$$\frac{\partial \widehat{T}}{\partial t} = \frac{2\alpha}{R^2}\left(R\frac{\partial T}{\partial R}\Big|_{r=R}\right) + \frac{H_v}{\rho C_p}$$

By the boundary condition (Eq. A1.3), the heat equation becomes

$$\frac{\partial \widehat{T}}{\partial t} = \frac{2\alpha}{R}\left(-\frac{h}{k}(\widehat{T} - T_0)\right) + \frac{H_v}{\rho C_p} \qquad \text{(Eq. A1.10)}$$

Noted that the equation of thermal diffusivity is

$$\alpha = \frac{k}{\rho C_p} \qquad \text{(Eq. A1.11)}$$

By substituting Eq. A1.11 into the heat equation (Eq. A1.10),

$$\frac{\partial \hat{T}}{\partial t} = \frac{-2h}{R\rho C_p}\left(\hat{T} - T_0\right) + \frac{H_v}{\rho C_p} \qquad \text{(Eq. A1.12)}$$

The temperature is normalised and scaled to [0, 1] by defining θ.

$$\theta = \frac{\hat{T} - T_0}{T_B - T_0} \qquad \text{(Eq. A1.13)}$$

where $T_B$ is the boiling point of the sample fluid.

By differentiating both sides of the equation (Eq. A1.13) with respect to t,

$$\frac{\partial \theta}{\partial t} = \frac{1}{T_B - T_0}\frac{\partial(\hat{T} - T_0)}{\partial t}.$$

Note that $\frac{\partial(T_0)}{\partial t} = 0$ because $T_0$ is a constant. Therefore,

$$\frac{\partial \theta}{\partial t} = \frac{1}{T_B - T_0}\frac{\partial \hat{T}}{\partial t}$$

After rearranging,

$$\frac{\partial \hat{T}}{\partial t} = (T_B - T_0)\frac{\partial \theta}{\partial t} \qquad \text{(Eq. A1.14)}$$

By substituting Eq. A1.14, the heat equation (Eq. A1.12) becomes

$$(T_B - T_0)\frac{\partial \theta}{\partial t} = \frac{-2h}{R\rho C_p}\left(\hat{T} - T_0\right) + \frac{H_v}{\rho C_p}$$

$$\frac{\partial\theta}{\partial t} = \frac{-2h}{R\rho C_p}\frac{\left(\bar{T} - T_0\right)}{(T_B - T_0)} + \frac{H_v}{\rho C_p (T_B - T_0)}$$

$$\frac{R\rho C_p}{2h}\frac{\partial\theta}{\partial t} = -\theta + \frac{H_v R}{2h(T_B - T_0)} \qquad \text{(Eq. A1.15)}$$

By substitution,

$$A = \frac{H_v R}{2h(T_B - T_0)} \qquad \text{(Eq. A1.16)}$$

and

$$\tau = t\left(\frac{2h}{R\rho C_p}\right) \qquad \text{(Eq. A1.17)}$$

By differentiating both sides of the equation (Eq. A1.17) with respect to t,

$$\frac{\partial\tau}{\partial t} = \frac{\partial\left(t\left(\frac{2h}{R\rho C_p}\right)\right)}{dt}$$

$$\frac{\partial\tau}{\partial t} = \frac{2h}{R\rho C_p}$$

After reciprocal, this becomes

$$\frac{\partial t}{\partial\tau} = \frac{R\rho C_p}{2h} \qquad \text{(Eq. A1.18)}$$

By substituting A (Eq. A1.16) and $\frac{R\rho C_p}{2h}$ (Eq. A1.18) into the heat equation (Eq. A1.15)

$$\frac{\partial t}{\partial\tau}\frac{\partial\theta}{\partial t} = -\theta + A$$

$$\frac{\partial\theta}{\partial\tau} = A - \theta \qquad \text{(Eq. A1.19)}$$

To solve the equation (Eq. A1.9), the two components of $\theta$ are separated.

$$\theta(\tau) = \theta_{ss} + \theta_T \qquad \text{(Eq. A1.20)}$$

where $\theta_{ss}$ is the steady state component and $\theta_T$ is the transient component of $\theta$.

By definition,

$$\frac{\partial \theta_{ss}}{\partial \tau} = 0 \qquad \text{(Eq. A1.21)}$$

When $\tau = 0$,

$$\theta(0) = \theta_{ss}(0) + \theta_T(0) = 0$$

$$\theta_T(0) = -\theta_{ss}(0) \qquad \text{(Eq. A1.22)}$$

At steady state using Eq. A1.19 and Eq. A1.21,

$$\frac{\partial \theta_{ss}}{\partial \tau} = A - \theta_{ss} = 0$$

$$A = \theta_{ss} \qquad \text{(Eq. A1.23)}$$

By substituting $\theta = \theta_{ss} + \theta_T$ (Eq. A1.20) into the heat equation (Eq. A1.19),

$$\frac{\partial(\theta_{ss} + \theta_T)}{\partial \tau} = A - (\theta_{ss} + \theta_T)$$

$$\frac{\partial \theta_{ss}}{\partial \tau} + \frac{\partial \theta_T}{\partial \tau} = (A - \theta_{ss}) - \theta_T$$

Note that $\frac{\partial \theta_{ss}}{\partial \tau} = 0$ (Eq. A1.21) and $A = \theta_{ss}$ (Eq. A1.23), this becomes

$$\frac{\partial \theta_T}{\partial \tau} = -\theta_T$$

After integration,

$$\theta_T(\tau) = Ce^{-\tau} \qquad \text{(Eq. A1.24)}$$

where C is a constant.

When $\tau = 0$,

$$\theta_T(0) = Ce^{-0}$$

$$\theta_T(0) = C \qquad \text{(Eq. A1.25)}$$

Note that $\theta_T(0) = -\theta_{ss}(0)$ (Eq. A1.22) and $A = \theta_{ss}$ (Eq. A1.23), Eq. A1.25 becomes

$$\theta_T(0) = -\theta_{ss}(0) = C = -A \qquad \text{(Eq. A1.26)}$$

By replacing C by –A (Eq. A1.26), Eq. A1.24 becomes

$$\theta_T(\tau) = -Ae^{-\tau} \qquad \text{(Eq. A1.27)}$$

Now, θ is derived

$$\theta = \theta_{ss} + \theta_T$$

By substituting Eq. A1.23 and Eq. A1.27,

$$\theta = A - Ae^{-\tau}$$

$$\boldsymbol{\theta = A(1 - e^{-\tau})} \qquad \textbf{(Eq. A1.28)}$$

A is then used as the fitting parameters for the experimental data of temperature change over time.

To recap, $H_v$ is estimated to determine the acoustic power, $P_{calorimetry}$, of the SonoCYL.

$$\mathbf{A = \frac{H_v R}{2h(T_B - T_0)}} \qquad \textbf{(Eq. A1.16)}$$

At this system, R = 0.005 m and V = $3\times10^{-6}$ $m^3$. PBS has a similar thermal property as water, so the property of the fluid is assumed to be the same as water. For water, $T_B$ = 373K, ρ = 1000 kg $m^{-3}$, and $C_p$ = 4180 J $kg^{-1}$ $K^{-1}$. h is determined experimentally by inserting a sample vial with warm fluid into the water bath and measuring its temperature change over time.

A similar heat transfer model as above is used, but without the heat generation from the ultrasonic source, $\frac{H_v}{\rho C_p}$. After calculation, the heat equation becomes

$$\frac{\partial T}{\partial t} = \alpha \nabla^2 T \qquad \text{(Eq. A1.29)}$$

After some calculations

$$\boldsymbol{\phi = e^{-B\tau}} \qquad \textbf{(Eq. A1.30)}$$

$$\mathbf{h = B\left(\frac{R\rho C_p}{2}\right)} \qquad \textbf{(Eq. A1.31)}$$

where ϕ is the analogous version of θ, and B is the analogous version of A, under the case when there is no heat source.

ϕ was estimated from experimental temperature over time without heat source was estimated. By the fitting in Figure A1.2 with Eq. A1.30, this obtained

$$B = 0.0149$$

$$\phi = e^{-0.0149\tau}$$

And from Eq. A1.31,

$$h = 156.1$$

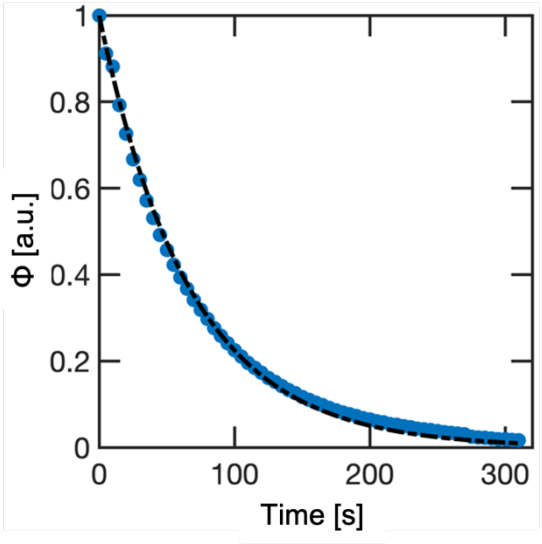



**Figure A1.2.** The estimation of ϕ with the average experimental temperature data (n = 3) over time without acoustic 'heat source'. The fitting is derived from the heat transfer equations above and the temperature data is used to fit into the model. The $R^2$ value of the fitting is 0.99.

Then, θ with experimental temperature over time with heat source was estimated by Eq. A1.28. The fitting is shown in Figure A1.3. With known A now, the $H_v$ (Eq. A1.16) was calculated for various acoustic pressures and the $P_{calorimetry}$ (Eq. A1.1). The fitting results are listed in Table A1.1.

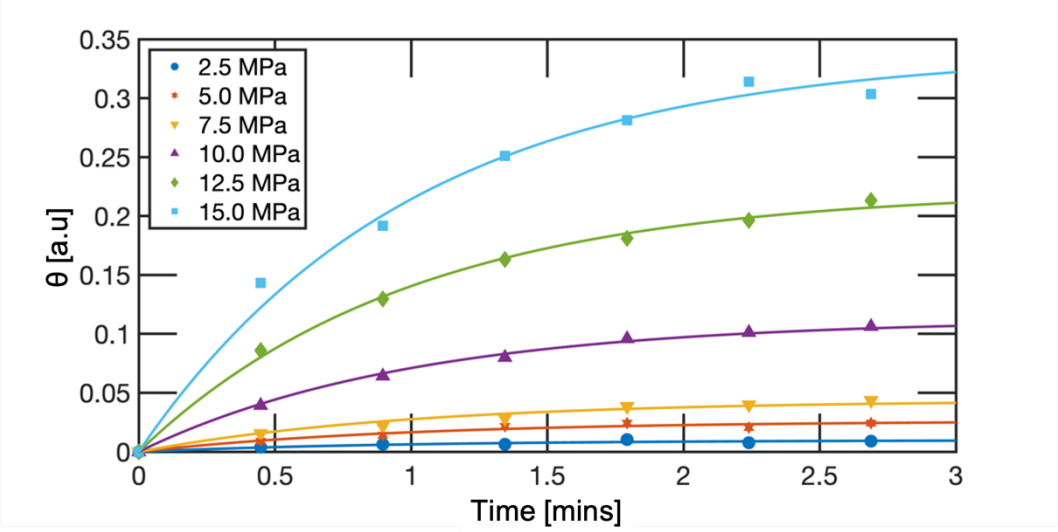



**Figure A1.3** The changes in θ overtime with SonoCYL (1 MHz) at different acoustic pressure. The fitting lines show the estimation of θ.

**Table A1.1.** The fitting results of the changes in θ overtime with SonoCYL (1 MHz) at different acoustic pressure in Figure A1.3.

| Acoustic Pressure [$MPa_{pkpk}$] | A | $R^2$ | $H_v$ [MW $m^{-3}$] | $P_{calorimetry}$ [W] |
|---|---|---|---|---|
| 2.5 | 0.0099 | 0.9061 | 0.0484 | 0.1453 |
| 5.0 | 0.0261 | 0.9545 | 0.1279 | 0.3838 |
| 7.5 | 0.0436 | 0.9683 | 0.2119 | 0.6358 |
| 10.1 | 0.1123 | 0.9974 | 0.5343 | 1.6030 |
| 12.6 | 0.2223 | 0.9971 | 1.0810 | 3.2429 |
| 15.1 | 0.3390 | 0.9895 | 1.6103 | 4.8310 |

$P_{calorimetry}$ against acoustic pressure is fitted with power law (with the form of $y = ax^b$). The fitted function and the fitting are shown in Eq. A1.31 and Figure A1.4, respectively.

$$\mathbf{P_{calorimetry} = (0.0043)(Acoustic\ pressure)^{2.6009}} \qquad \textbf{(Eq. A1.32)}$$

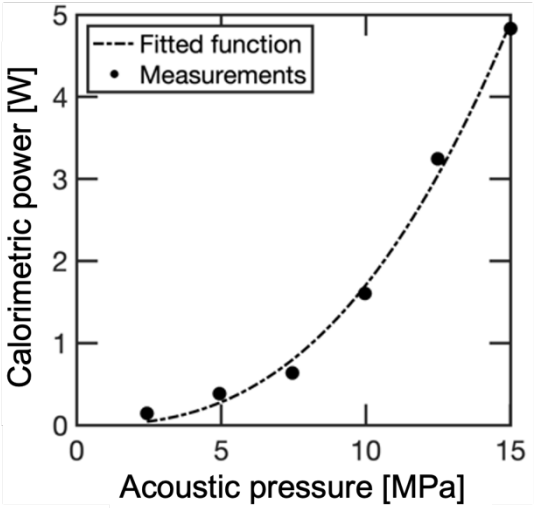



**Figure A1.4.** The estimation of the calorimetric power with different acoustic pressures. The fitting is based on power law, and the calorimetric power is obtained by the heat transfer model.
The average $R^2$ value of the fitting is 0.99.

## A.2. Fenton chemistry

The method for •OH production was adapted from a previous report on the Fenton reaction[256]. This reaction is used to calibrate the amount of hydroxyl radical produced. The concentration of •OH is equal to the Fe(II) concentration added. A fresh stock $Fe^{2+}$-EDTA solution was prepared for each experiment by dissolving $FeCl_2 \cdot 4H_2O$ (10 mM) and $Na_2EDTA$ (10 mM) into DI water. EDTA was used to avoid the precipitation of Fe(II) in PBS. To prepare the analyte, the $Fe^{2+}$-EDTA solutions were diluted into PBS (pH 7.4) containing $H_2O_2$ (10 mM) and Res-DHB (5 μM). The fluorescence measurements were taken at 60 minutes after the $Fe^{2+}$-EDTA solutions were added to the analyst solution. This is due to the slow kinetics of the Fenton reaction (> 60 mins)[130].

The Fenton reaction is presented in Eq. A2.1.

$$Fe^{2+} + H_2O_2 \rightarrow Fe^{3+} + \cdot OH + OH^- \qquad \text{(Eq. A2.1)}$$

Other side reactions in Fenton chemistry are presented in Eq. A2.2 and A2.3. The reaction kinetics of these reactions is much slower than Eq. A2.1 and are neglected in this study.

$$Fe^{3+} + H_2O_2 \rightarrow Fe^{2+} + HOO\cdot + H^+ \qquad \text{(Eq. A2.2)}$$

$$2H_2O_2 \rightarrow \cdot OH + HOO\cdot + H_2O \qquad \text{(Eq. A2.3)}$$

It is important to note that at micro-molar concentrations, the system is sensitive to trace contaminants such as organic compounds and solvents. This changes the Fenton reaction and the ability for the probes to scavenge available •OH. Therefore, rigorous cleaning and high purity reagents were critical for the Fenton reaction.

The calibration curve is presented in Figure A2.1 across a concentration range of 5 μM to 200 μM and was used to convert fluorescence intensity into Fenton-equivalent •OH concentrations. For measurements exceeding the calibration range, equivalent •OH concentrations were estimated by linear extrapolation of the calibration curve. While this approach assumes that the fluorescence response remains approximately linear beyond the calibrated region, it inherently introduces higher uncertainty beyond 200 μM. Therefore, these extrapolated values are used as semi-quantitative estimates of •OH activity rather than absolute concentrations, serving to illustrate an increase in activity. The scattered measurements were attributed to the kinetic sensitivity of the Fenton reaction, particularly its sensitivity to small variations in the concentration of the $Fe^{2+}$-EDTA solution prepared

in each trial, as discussed in more detail below. The calibration curve was conducted by Dr. Adam Sedgwick.

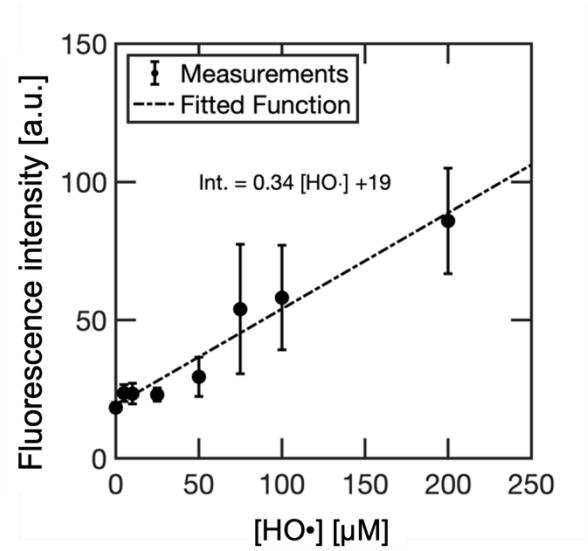



**Figure A2.1.** The calibration curve of resorufin (Res) in PBS (pH 7.4) . $\lambda_{excitation}$ = 500 nm, $\lambda_{emission}$ = 585 nm, slit widths: excitation = 10 nm and emission = 3.5 nm. The best fit line has an equation: y = 0.34x + 19, $R^2$ = 0.7784. Each value is the average of at least three trials and the error bars indicate the standard deviation.

The slow kinetic behaviour of the Fenton Chemistry reference system is illustrated in Figure A2.2, which shows the change in relative fluorescence emission intensity over a 3600 seconds (60 minutes) period. Even in the presence of a high hydrogen peroxide concentration (10 mM) relative to Res-DHB (5 μM), the fluorescence signal did not increase instantaneously or rapidly reach equilibrium. Instead, it exhibited a gradual rise throughout the measurement window, demonstrating that the reaction is kinetically controlled and strongly time dependent.

As the system did not reach equilibrium within the experimental timeframe, all calibration and experimental measurements were performed at a fixed reaction time of 60 minutes to ensure comparability across experiments. This standardised measurement timing is particularly important at higher hydrogen peroxide concentrations, where small variations in mixing efficiency, local reactant concentrations (such as the exact concentration of $Fe^{2+}$-EDTA solution prepared in each trial), or initial reaction rates may significantly influence the fluorescence response. Therefore, these factors may contribute to the relatively low coefficient of determination observed in the calibration curve ($R^2$ = 0.7784) in Figure A2.1.

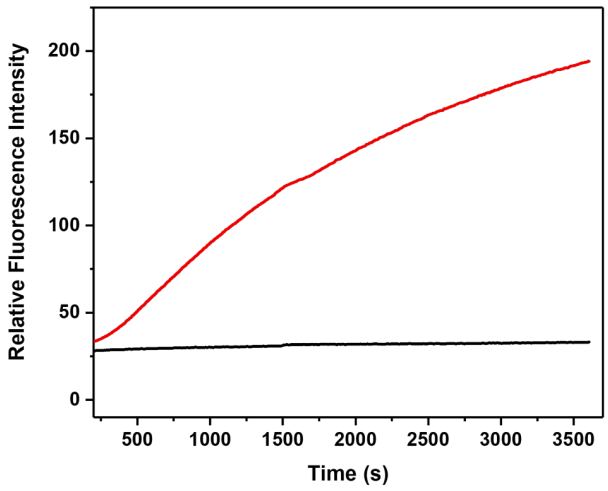



**Figure A2.2.** Change in relative fluorescence emission intensity of Res-DHB (5 μM) in PBS buffer and $H_2O_2$ (10 mM) (pH =7.40). $\lambda_{excitation}$ = 350 nm, $\lambda_{emission}$ = 585 nm, slit widths: excitation = 10 nm and emission = 3.5 nm. **Red**: Fe(II)-EDTA addition. **Black**: control.

## A.3. An example calculation of hydrogen production

The triplicate (n = 3) peak areas obtained from a sonochemical testing with 2.5 mL of natural seawater, 0.3 mg/mL $TiO_2$ catalysts for 180 minutes were 45694, 41272, and 56618.

The mean peak area of the triplicate data is

$$\text{Mean peak area} = \frac{45694 + 41272 + 56618}{3} = 47861.$$

Converting the mean peak area to the concentration of hydrogen in ppm:

$$\text{Hydrogen concentration (ppm)} = \frac{47861}{38.094} = 1256 \text{ ppm}$$

Applying Eq. 4.3, the volume of hydrogen gas produced is estimated:

$$V_{hydrogen} = (1256 \text{ ppm})(2.5 \text{ mL})\left(10^{-6}/\text{ppm}\right) = 0.003141 \text{ mL}$$

The number of moles of hydrogen is estimated by Eq. 4.4:

$$n_{hydrogen} = \frac{(101.325 \text{ kPa})\ (0.003141 \text{ mL})\left(\frac{10^{-6}\ \text{m}^3}{\text{mL}}\right)}{(8.314 \text{ J K}^{-1} \text{ mol}^{-1})(293.15 \text{ K})} = 0.1307 \text{ μmol}$$

The production rate of hydrogen is:

$$\text{Hydrogen production rate (μmol h}^{-1}) = \frac{0.1307 \text{ μmol}}{(180 \text{ mins})\left(\frac{\text{h}}{60 \text{ mins}}\right)} = 0.0432 \text{ μmol h}^{-1}$$

The amount of $TiO_2$ catalysts and seawater used is 0.3 mg/mL and 2.5 mL respectively. Therefore, the production rate of hydrogen per unit of catalyst is:

$$\text{Hydrogen production rate } \left(\text{μmol h}^{-1}\text{g}^{-1}\right) = \frac{0.0432 \text{ μmol h}^{-1}}{(0.3 \text{ mg/mL})(2.5 \text{ mL g}/1000\text{mg})} = 57.6 \text{ μmol h}^{-1}\text{g}^{-1}$$

## A.4. Sigmoid function fitting for cavitation noise index

The sigmoid fit follows the formula of Eq. A4.1 and the parameters for the fitting are shown in Table A4.1.

$$f(x) = (a–d)\left[\exp\left(–\exp\left(–b(x–c)\right)\right)\right] \qquad \text{(Eq. A4.1)}$$

**Table A4.1.** The parameters for the sigmoid function fitting for the normalised cavitation noise index.

| **$TiO_2$ concentration [mg/mL]** | **a** | **b** | **c** | **d** |
|---|---|---|---|---|
| 0.1 | 14.2591 | 1.6333 | 3.4224 | 8.6607 |
| 0.2 | 17.9349 | 2.2443 | 3.0413 | 6.9717 |
| 0.3 | 19.7778 | 1.7718 | 2.8495 | 4.4533 |
| 0.4 | 18.6965 | 1.4717 | 2.7990 | 6.1758 |
| 0.5 | 16.5533 | 1.7535 | 3.1730 | 6.7773 |

## A.5. Categorised gas production rate data for biomass gasification

Categorised gas production rate data for sonochemical biomass gasification are presented in Figure A5.1 and Figure A5.2. Different water-to-molasses dilution ratios and catalyst types are distinguished using different marker colours and marker shapes, respectively.

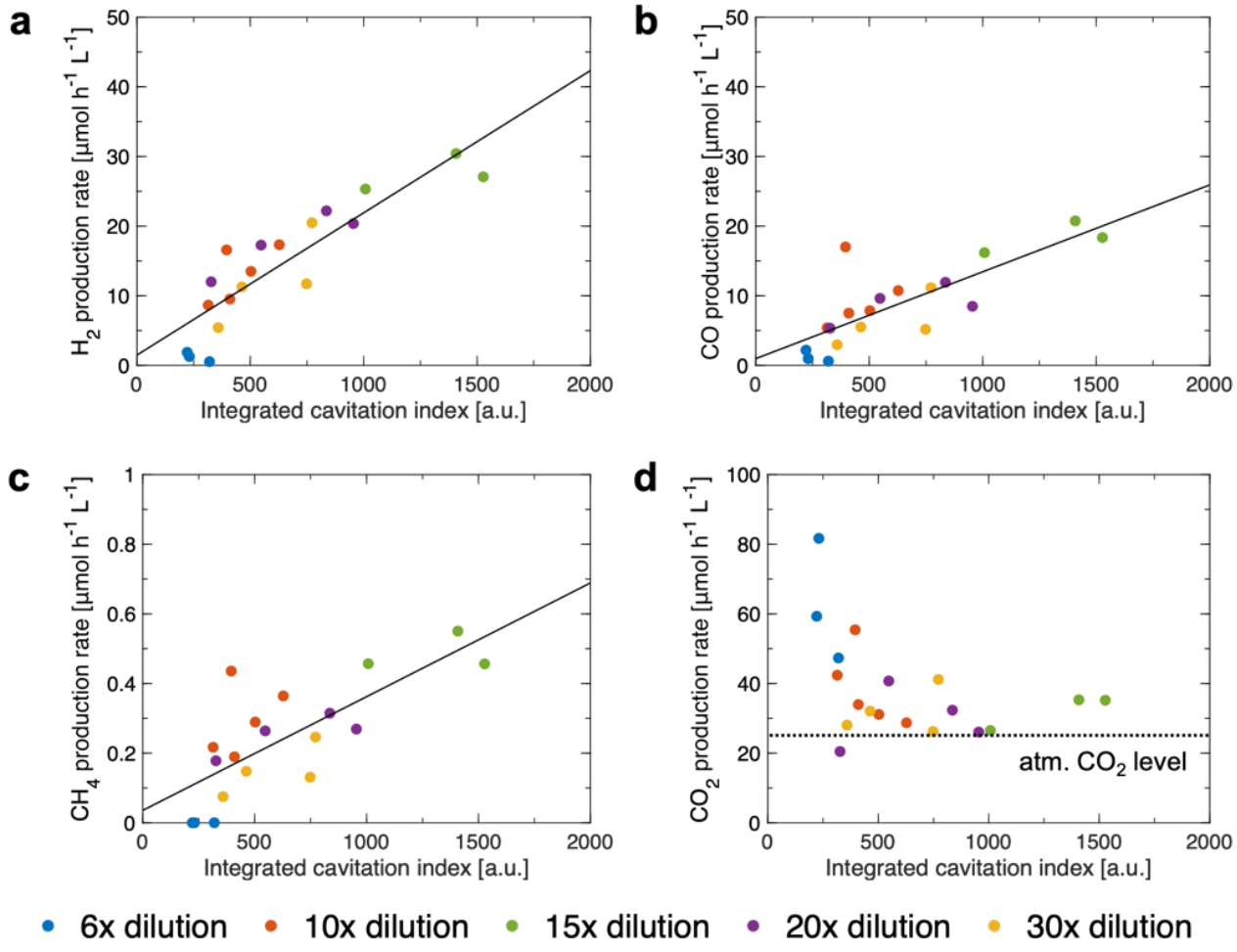



**Figure A5.1.** Gas production rates for different water-to-molasses dilution ratios used in sonochemical biomass gasification, represented using different marker colours. Acoustic parameters: 780 kHz, 100 cycles, 2.849 ms pulse duration, 4.5% duty cycle, 5.1 W power. Reaction time: 30 minutes. Chemical conditions: no catalyst, with varying water-to-molasses dilution ratios.

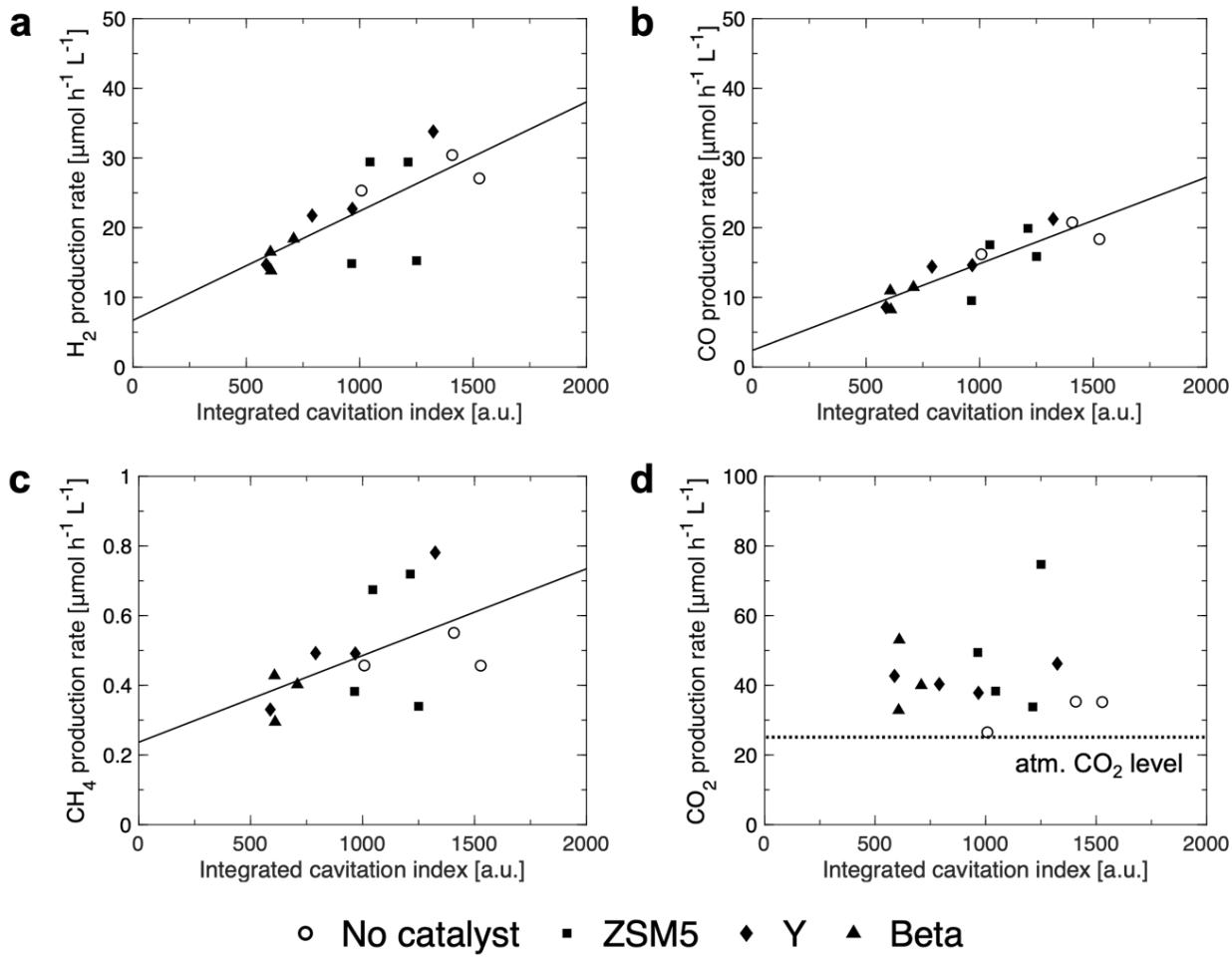



**Figure A5.2.** Gas production rates for different catalyst types used in sonochemical biomass gasification, represented using different marker shapes. Acoustic parameters: 780 kHz, 100 cycles, 2.849 ms pulse duration, 4.5% duty cycle, 5.1 W power. Reaction time: 30 minutes. Chemical conditions: 15x diluted molasses, with varying catalyst types.

## A.6. MATLAB code

### A.6.1. EPR data fitting

#### Loading and preparing EPR data

```
clear, clc, clf;

[OrgB,spc,par] = eprload('Ar_water_TiO2.DTA'); % load epr data
B = OrgB/10;                                   % convert G -> mT

% Baseline correction
[CorrSpec,BLine] = basecorr(spc,1,3);
figure(1);
plot(B, spc); hold on; plot(B, CorrSpec); plot(B, BLine);
legend('Exp spectrum','Corrected spectrum','Baseline');

% Experimental parameters
Exp.mwFreq = par.MWFQ / 1e9;  % GHz
Exp.Range  = [min(B) max(B)]; % mT
Exp.nPoints = numel(B);

% Spin system
% Spin system for OH radical
Sys0_OH.S = 1/2;
Sys0_OH.Nucs = '14N,1H';
Sys0_OH.n = [1 1];
g_offset = +0.00297;
Sys0_OH.g = 2.0023 + g_offset;
Sys0_OH.A = [14.9 14.9]*2.802; % MHz
Sys0_OH.lwpp = [0.05 0.05];    % mT
Sys0_OH.weight = 0.8;

% Spin system for H radical
Sys0_H.S = 1/2;
Sys0_H.Nucs = '14N,1H,1H';
Sys0_H.n = [1 1 1];
Sys0_H.g = 2.0023 + g_offset;
Sys0_H.A = [16.4 22.6 22.6] * 2.802; % MHz, [14N, 1H, 1H]
Sys0_H.lwpp = [0.05 0.05];           % mT
Sys0_H.weight = 1-Sys0_OH.weight;

% Margin of error
SysVary.g = 0.05; % search within +- of 0.01 to get the best spectrum
SysVary.A = [0.05 0.05];
SysVary.lwpp = [0.03 0.03];
SysVary.weight = 0.2;
```

#### EPR fitting

```
% Multi-component fitting
esfit(CorrSpec,@garlic,{{Sys0_H,Sys0_OH},Exp},{{SysVary,SysVary}})
```

Extract individual component (OH and H radicals) from esfit

```
fit_para_H = fitresult.argsfit{1,1}{1,1};

fit_para_OH = fitresult.argsfit{1,1}{1,2};

Exp = fitresult.argsfit{1,2};

fit_scale = fitresult.scale;



[Bsim_H,  spc_sim_H]  = garlic(fit_para_H,Exp);

[Bsim_OH, spc_sim_OH] = garlic(fit_para_OH,Exp);



% Plotting of EPR fitting for individual components

figure;
plot(B, CorrSpec); hold on;
plot(Bsim_H, spc_sim_H * fitresult.scale);
plot(Bsim_OH, spc_sim_OH * fitresult.scale);
legend('Exp Corrected spectrum', 'Sim component H', 'Sim component OH');
```

### A.6.2. PCD noise collection for cavitation threshold determination

The script was adopted from the work by Lillian Usadi. The script provides an example of collecting PCD noise signals under varying applied voltages. In this research, it is used to determine the cavitation threshold.

```
% [Created by Lillian Usadi, adapted by Cherie Wong]
% [Last updated: 08/08/2024]
% [Objective: Record the PCD noise data across voltage to determine the cavitation
threshold (fixed data points)]
```

Initialise instruments

```
% Initialize TiePie oscilloscope

clear all;
close all;

instrreset % resets instruments and clear everything

UI.Basename = 'Threshold_Test';
saveTitle = "001";
```

Make directory for each experiment

```
pn=sprintf('%s',cd,filesep,'data',filesep,datestr(now,'yyyymmdd'),filesep,UI.Basename);

if (~exist(pn))
    mkdir(pn);
end
```

Setting up TiePie Oscilloscope

```
NUMCHANNELS=1;

fprintf('[%s] Initializing TiePie oscilloscope ...\n',mfilename);
addpath(genpath('./matlab-libtiepie-master'));

if verLessThan('matlab', '8')
    error('Matlab 8.0 (R2012b) or higher is required.');
end

% Open LibTiePie and display library info if not yet opened:+
import LibTiePie.Const.*
import LibTiePie.Enum.*

if ~exist('LibTiePie', 'var')
    % Open LibTiePie:
    LibTiePie = LibTiePie.Library
end

% Enable network search:
LibTiePie.Network.AutoDetectEnabled = true;

% Search for devices:
LibTiePie.DeviceList.update();

% Try to open an oscilloscope with block measurement support:
clear scp;
for k = 0 : LibTiePie.DeviceList.Count - 1
```

```
    item = LibTiePie.DeviceList.getItemByIndex(k);
    if item.canOpen(DEVICETYPE.OSCILLOSCOPE)
        scp = item.openOscilloscope();
        if ismember(MM.BLOCK, scp.MeasureModes)
            break;
        else
            clear scp;
        end
    end
end
clear item;

if ~exist('scp', 'var')
    error('No oscilloscope available with block measurement support!');
end

%Initialize arbitrary waveform generator (AWG)
RS232INSTR.BOARD_ADDR=9;
RS232INSTR.AWG_ADDR=9;
SERIAL.PORT = 'COM3';

% Initialize instruments
fprintf('[%s] %s\n',mfilename,'Initializing ...');
% Close any open instruments, ignore errors
try fclose(instrfind); delete(instrfind); clear instrfind; end;

try
rs232_awg = serial(SERIAL.PORT); % creates serial object
rs232_awg.BaudRate = 9600;
rs232_awg.Terminator = 'LF';
fopen(rs232_awg); % opens rs port
flushinput(rs232_awg);
flushoutput(rs232_awg);
catch
error('Could not connect to awg. Check RS232 connection.');
end
```

## Connecting Keysight 33600A

```
InstrLoc = 'USB0::0x0957::0x4B07::MY59000119::0::INSTR';
KEYSIGHT33600A = visa('agilent', InstrLoc);
KEYSIGHT33600A.InputBufferSize = 8388608;
KEYSIGHT33600A.ByteOrder = 'littleEndian';
fopen(KEYSIGHT33600A);
disp("Done");
```

## Commands

```
% Switch off output 1
chnl = 1;
outputimpd = 50;
chnstr = 'CH1';
freq = 0.780e6;

voltagepp = 1;
offset = 0;
Ncyc = 100;
burstperiod = 2.849e-3; % 10 ms
startphase = 0;
output = 1;

fprintf(KEYSIGHT33600A, sprintf(':OUTPut%i %d',chnl, 0));
%Switch on the Sync
fprintf(KEYSIGHT33600A, sprintf(':OUTPut:SYNC %d', 1));
%Set the Sync output to synchronous on output
fprintf(KEYSIGHT33600A, sprintf(':OUTPut:SYNC:SOURce %s', chnstr));
% Set the output impedance % Default of 50 ohms
fprintf(KEYSIGHT33600A, sprintf(':OUTPut:LOAD %g', outputimpd));
```

```
% set up the sinusoid waveform on channel with frequency = Freq (Hz), Peak to
% Peak voltage = voltagepp (Volts) , Voltage offset = offset (Volts)
fprintf(KEYSIGHT33600A, sprintf(':SOURce%i:APPLy:SINusoid %g,%g VPP,%g V',chnl, freq,
voltagepp, offset));
% Set the channel to burst mode, internally triggered
fprintf(KEYSIGHT33600A, sprintf(':SOURce%i:BURSt:MODE %s',chnl, 'TRIGgered'));
% Set the channel to burst Ncyc cycles
fprintf(KEYSIGHT33600A, sprintf(':SOURce%i:BURSt:NCYCles %g',chnl, Ncyc));
% Set the Burst period to burstperiod (seconds)
fprintf(KEYSIGHT33600A, sprintf(':SOURce%i:BURSt:INTernal:PERiod %g',chnl, burstperiod));
% Set the initial starting phase of the burst at startphase degrees
fprintf(KEYSIGHT33600A, sprintf(':SOURce%i:BURSt:PHASe %g',chnl, startphase));
% Set the trigger to be internal
fprintf(KEYSIGHT33600A, sprintf(':TRIGger%i:SOURce %s', chnl,'IMMediate'));
% Switch on burst mode post setup
fprintf(KEYSIGHT33600A, sprintf(':SOURce%i:BURSt:STATe %d',chnl, 1));
% Switch on or off the output
fprintf(KEYSIGHT33600A, sprintf(':OUTPut%i %d',chnl, output));
```

## Setting up TiePie

```
% Set measure mode:
scp.MeasureMode = MM.BLOCK;
scp.Resolution = 14; % 16-bit 6.25 MS/s max; 14-bit 100 MS/s max; 12-bit 500 MS/s

% Sampling frequency
scp.SampleFrequency = 100e6; % 1 MHz/

% Window Size
scp.RecordLength = 20e3; % Samples for 100 cycles with 150 us delay, tested
experimentally

% TimeWindow
TimeWindow = scp.RecordLength/scp.SampleFrequency;
scp.PreSampleRatio = 0.0; % 0 % [JLR] NOT HANDLED YET

scp.Channels(1).Enabled = true;
scp.Channels(1).Range = 4;
scp.Channels(1).Coupling = CK.DCV; % DC Volt
scp.Channels(1).ProbeGain = 1; %

scp.Channels(2).Enabled = true;
scp.Channels(2).Range = 4;
scp.Channels(2).Coupling = CK.DCV; % DC Volt
scp.Channels(2).ProbeGain = 1; %

% Set trigger timeout:
scp.TriggerDelay = 130e-6; % 200 microseconds delay (PCD)

scp.TriggerTimeOut = -1; % How long to wait for a trigger, n.b. 0=immediate trigger
(don't wait at all)

% Disable all channel trigger source on each channel;
for ch = scp.Channels
    ch.Trigger.Enabled = false;
    clear ch;
end

% Setup external trigger for input channels:
scp.TriggerInputs(1,1).Enabled = 1;
scp.TriggerInputs(1,1).Kind = TK.RISINGEDGE; % Rising edge

scp.TriggerInputs(1,2).Enabled = 1;
scp.TriggerInputs(1,1).Kind = TK.RISINGEDGE; % Rising edge

% Print oscilloscope info:
display(scp);
```

## Data Acquisition

```
fprintf('\n[%s] Setting up function generator...',mfilename);
fprintf('\n[%s] Acquiring waveforms...\n',mfilename);

%Counting down
ampl_vpp = []; % Create an empty array for testing voltage
   for i = 40:-1:0
       ampl_vpp = [ampl_vpp i*0.1]; % Here, it is testing 4V to 0V, with a step of 0.1V.
   end

max_ampl_vpkpk = max(ampl_vpp);
min_ampl_vpkpk = min(ampl_vpp);

fprintf('Amp Voltage pkpk [Vpkpk]: %3.1f to %3.1f V\n',max_ampl_vpkpk,min_ampl_vpkpk);

% Reaction time
reaction_time = 0.025;                              % reaction time [min] - arbitrary time
for now
burst_number = reaction_time * 30.0867678 /burstperiod;    % burst length = reaction_time
/ burst period. The number of burst for the whole reaction time.
timepoints = 100;                                   % # data points saved.
k = floor(burst_number/timepoints);                         % k: the interval of
burst_number need to record 1 datapoint. Floor func for the nearest integer (round down)

fprintf('Reaction time : %d mins\n',reaction_time);
fprintf('Total # data points: %d\n',timepoints);

% Create empty array for recording data
matData_ch1=zeros(scp.RecordLength,timepoints); % Save channel 1 data only
matData_ch2=zeros(scp.RecordLength,timepoints); % Save channel 2 data only

% Read current time
RunStartTime = datetime('now','Format','yyyy-MM-dd HH:mm:ss.SSS'); % Get the exact time
when the sample collection starts
dataTime = zeros(timepoints,1); % Create empty array for the sample collection time

    for myidx=1:length(ampl_vpp) % Iterate through different voltage levels

            fprintf(KEYSIGHT33600A, sprintf(':VOLTage %g',ampl_vpp(myidx)));

        for myidy = 1:k*timepoints

            % Start measurement:
            scp.start();

            % Wait for measurement to complete:
            while ~scp.IsDataReady
                pause(1e-4) % 10 ms delay, to save CPU time.
            end

            % Get data:
            if mod(myidy,k)==0                      % Remainder after division of myidy
by k, if it's = 0, then perform the following

                dataReadTime = datetime('now','Format','yyyy-MM-dd HH:mm:ss.SSS'); % Get
exact time when the data is collected at every timepoints
                dataTime(myidy/k,1) = seconds(dataReadTime - RunStartTime); % The time
difference between the run start and the data collection time

                newData = scp.getData();            % only get data when if is fulfilled
                matData_ch1(:,myidy/k)=newData(:,1); % Save channel 1 data only
                matData_ch2(:,myidy/k)=newData(:,2); % Save channel 2 data only
            end

        end

        % MATLAB cannot load objects, so convert to struct for saving
        scp_verify.verifySampleFrequency =
scp.verifySampleFrequency(scp.SampleFrequency);
        scp_verify.verifyRecordLength = scp.verifyRecordLength(scp.RecordLength);
```

```
        scp_verify.verifyTriggerTimeOut = scp.verifyTriggerTimeOut(scp.TriggerTimeOut);
        scp_verify.verifyTriggerDelay = scp.verifyTriggerDelay(scp.TriggerDelay);
        warning('off','MATLAB:structOnObject')
        scp_struct=struct(scp);
        scp_channel1_struct=struct(scp.Channels(1));
        scp_channel2_struct=struct(scp.Channels(2));
        LibTiePie_struct=struct(LibTiePie);
        warning('on','all')

        % Saving file
        savename = UI.Basename + "_" + saveTitle + "_" + ampl_vpp(myidx) + "pkpk_" +
datestr(now,'HHMMSS');
        save (pn + "\" + savename + ".mat", "matData_ch1", "matData_ch2")

        % clear newData k myidx;
    end

fprintf(savename);

% Switch on or off the output
output = 0; % off
fprintf(KEYSIGHT33600A, sprintf(':OUTPut%i %d',chnl, output));
```

## Plot results

```
tvec = ((1:scp_struct.RecordLength) / scp_struct.SampleFrequency) +
scp_struct.TriggerDelay;


 figure();


plot(tvec/1e-6, matData_ch2(:,1));       % Choosing data 1 here, it can be anything
between 1 to the last datapoint.
 ylabel('Amplitude [V]');
 xlabel('Time [\mus]');
 title('Channel 2: PCD');
```

## Close-up

```
  % Close oscilloscope:
    clear scp;
  % Close generator:
    clear gen;
```

### A.6.3. Noise signal processing for cavitation index determination

The script was adopted from the work by Lillian Usadi and Lucia Millings. This script provides an example for determining the cavitation index under varying experimental conditions, here specifically on different NaCl concentrations and applied voltages.

```
clear all; close all; clc
```

Initialise parameters

```
sample_frequency = 100e6;  % 100MHz
no_bursts = 100;           % Number of burst periods measured
record_length = 12.5e3;    % Number of samples recorded per measured burst
trigger_delay = 130e-6;    % Delay to PCD measurement (s)
voltage_gain = 10^(35/20); % Voltage gain due to attenuator/amplifier
```

Insert sample type you want to analyse

```
trial = '1';
folderpath = ['/Users/Signal_In/trial',trial];
filelist = dir(folderpath);
name = {filelist.name};
name = name(~strncmp(name, '.', 1));   % No files starting with '.'

% Define the concentration and test voltage peak-to-peak ranges
NaClconc = [0.1, 0.25, 0.48, 0.75, 1];
test_vpp = 3:0.1:4;
```

Loop through all combinations of TiO2 concentration and test voltage peak-to-peak

```
% Initialise total intenisty for specific voltage vector
intensity_table_data = zeros(length(test_vpp),length(NaClconc));

for conc = NaClconc
    for vpp = test_vpp
        % Generate the filename pattern
        filenamePattern = sprintf('Signal_In_NaCl_%gM_%gpkpk_*.mat', conc, vpp);

        % Get a list of all files that match the pattern
        files = dir(fullfile(folderpath, filenamePattern));
        filePath = fullfile(folderpath, files.name);
        load(filePath); % Load file

        intensity_per_burst = zeros(1, no_bursts);

        for burst = 1 : no_bursts % Loop around each burst
            burst_data_ch2 = voltage_gain * matData_ch2(:, burst); % Separate channel 2
(PCD) data
            fourier_ch2 = abs(fft(burst_data_ch2));                % Obtain absolute FFT
of individual burst
            FFT_integrated = trapz(fourier_ch2);                   % Integrate to get
total PCD intensity over burst
            intensity_per_burst(burst) = FFT_integrated;           % Store integrated
value in vector
        end

    total_intensity = intensity_per_burst * ones(no_bursts, 1);    % Get total summed
intensity over 100 bursts

    vpp_idx = find(test_vpp == vpp);
```

```
    conc_idx = find(NaClconc == conc);

    intensity_table_data(vpp_idx,conc_idx) = total_intensity;

    end
end

% plot
figure;
heatmap(intensity_table_data);
```

## Degassed - Loop through all combinations of TiO2 concentration and test voltage peak-to-peak

```
% Initialise total intenisty for specific voltage vector
intensity_table_data_degassed = zeros(length(test_vpp),1);

for vpp = test_vpp
    % Generate the filename pattern
    filenamePattern = sprintf('Signal_In_degassedH2O_%gpkpk_*.mat', vpp);

    % Get a list of all files that match the pattern
    files = dir(fullfile(folderpath, filenamePattern));
    filePath = fullfile(folderpath, files.name);
    load(filePath); % Load file

    intensity_per_burst = zeros(1, no_bursts);

    for burst = 1 : no_bursts % Loop around each burst
        burst_data_ch2 = voltage_gain * matData_ch2(:, burst); % Separate channel 2 (PCD)
data
        fourier_ch2 = abs(fft(burst_data_ch2));                % Obtain absolute FFT of
individual burst
        FFT_integrated = trapz(fourier_ch2);                   % Integrate to get total
PCD intensity over burst
        intensity_per_burst(burst) = FFT_integrated;           % Store integrated value
in vector
    end

total_intensity = intensity_per_burst * ones(no_bursts, 1);    % Get total summed
intensity over 100 bursts
vpp_idx = find(test_vpp == vpp);
intensity_table_data_degassed(vpp_idx) = total_intensity;

end
```

## Post-processing of data

```
% Normalised against degassed water + log scale calculation
log_int_data = 20*log10(intensity_table_data./intensity_table_data_degassed);

% Plotting of heatmap for intensity vs salt concentration
figure;
heatmap(log_int_data);
```

### A.6.4. PCD noise collection over time

The script was adopted from the work by Lillian Usadi. The script is an example script to collect PCD noise signal over a fixed reaction time.

```
% [Created by Lillian Usadi, adapted by Cherie Wong]
% [Last updated: 08/08/2024]
% [Objective: Record the PCD noise data for a reaction time (fixed time interval) with a
fixed voltage]
```

Initialize instruments

```
% Initialize TiePie oscilloscope

clear all;
close all;
%clc

instrreset % resets instruments and clear everything

UI.Basename = 'Experiment';
saveTitle = "Biomass_001_Ar-molasses10x-30min-noCat-4VUS";
```

Make directory for each experiment

```
pn=sprintf('%s',cd,filesep,'data',filesep,datestr(now,'yyyymmdd'),filesep,UI.Basename);

if (~exist(pn))
    mkdir(pn);
end
```

Setting up TiePie Oscilloscope

```
NUMCHANNELS=1;


fprintf('[%s] Initializing TiePie oscilloscope ...\n',mfilename);
addpath(genpath('./matlab-libtiepie-master'));

if verLessThan('matlab', '8')
    error('Matlab 8.0 (R2012b) or higher is required.');
end

% Open LibTiePie and display library info if not yet opened:+
import LibTiePie.Const.*
import LibTiePie.Enum.*

if ~exist('LibTiePie', 'var')
    % Open LibTiePie:
    LibTiePie = LibTiePie.Library
end

% Enable network search:
LibTiePie.Network.AutoDetectEnabled = true;

% Search for devices:
LibTiePie.DeviceList.update();

% Try to open an oscilloscope with block measurement support:
clear scp;
for k = 0 : LibTiePie.DeviceList.Count - 1
    item = LibTiePie.DeviceList.getItemByIndex(k);
```

```
    if item.canOpen(DEVICETYPE.OSCILLOSCOPE)
        scp = item.openOscilloscope();
        if ismember(MM.BLOCK, scp.MeasureModes)
            break;
        else
            clear scp;
        end
    end
end
clear item;

if ~exist('scp', 'var')
    error('No oscilloscope available with block measurement support!');
end

%Initialize arbitrary waveform generator (AWG)
RS232INSTR.BOARD_ADDR=9;
RS232INSTR.AWG_ADDR=9;
SERIAL.PORT = 'COM3';

% Initialize instruments
fprintf('[%s] %s\n',mfilename,'Initializing ...');
% Close any open instruments, ignore errors
try fclose(instrfind); delete(instrfind); clear instrfind; end;

try
rs232_awg = serial(SERIAL.PORT); % creates serial object
rs232_awg.BaudRate = 9600;
rs232_awg.Terminator = 'LF';
fopen(rs232_awg); % opens rs port
flushinput(rs232_awg);
flushoutput(rs232_awg);
catch
error('Could not connect to awg. Check RS232 connection.');
end
```

## Connecting Keysight 33600A

```
InstrLoc = 'USB0::0x0957::0x4B07::MY59000119::0::INSTR';
KEYSIGHT33600A = visa('agilent', InstrLoc);
KEYSIGHT33600A.InputBufferSize = 8388608;
KEYSIGHT33600A.ByteOrder = 'littleEndian';
fopen(KEYSIGHT33600A);
disp("Done");
```

## Commands

```
% Switch off output 1
chnl = 1;
outputimpd = 50;
chnstr = 'CH1';
freq = 0.780e6;

voltagepp = 1;
offset = 0;
Ncyc = 100;
burstperiod = 2.8490e-3; % 10 ms
startphase = 0;
output = 1;

fprintf(KEYSIGHT33600A, sprintf(':OUTPut%i %d',chnl, 0));
%Switch on the Sync
fprintf(KEYSIGHT33600A, sprintf(':OUTPut:SYNC %d', 1));
%Set the Sync output to synchronous on output
fprintf(KEYSIGHT33600A, sprintf(':OUTPut:SYNC:SOURce %s', chnstr));
% Set the output impedance % Default of 50 ohms
fprintf(KEYSIGHT33600A, sprintf(':OUTPut:LOAD %g', outputimpd));
% set up the sinusoid waveform on channel with frequency = Freq (Hz), Peak to
```

```
% Peak voltage = voltagepp (Volts) , Voltage offset = offset (Volts)
fprintf(KEYSIGHT33600A, sprintf(':SOURce%i:APPLy:SINusoid %g,%g VPP,%g V',chnl, freq,
voltagepp, offset));
% Set the channel to burst mode, internally triggered
fprintf(KEYSIGHT33600A, sprintf(':SOURce%i:BURSt:MODE %s',chnl, 'TRIGgered'));
% Set the channel to burst Ncyc cycles
fprintf(KEYSIGHT33600A, sprintf(':SOURce%i:BURSt:NCYCles %g',chnl, Ncyc));
% Set the Burst period to burstperiod (seconds)
fprintf(KEYSIGHT33600A, sprintf(':SOURce%i:BURSt:INTernal:PERiod %g',chnl, burstperiod));
% Set the initial starting phase of the burst at startphase degrees
fprintf(KEYSIGHT33600A, sprintf(':SOURce%i:BURSt:PHASe %g',chnl, startphase));
% Set the trigger to be internal
fprintf(KEYSIGHT33600A, sprintf(':TRIGger%i:SOURce %s', chnl,'IMMediate'));
% Switch on burst mode post setup
fprintf(KEYSIGHT33600A, sprintf(':SOURce%i:BURSt:STATe %d',chnl, 1));
% Switch on or off the output
fprintf(KEYSIGHT33600A, sprintf(':OUTPut%i %d',chnl, output));
```

## Setting up TiePie

```
% Set measure mode:
scp.MeasureMode = MM.BLOCK;
scp.Resolution = 14; % 16-bit 6.25 MS/s max; 14-bit 100 MS/s max; 12-bit 500 MS/s

% Sampling frequency
scp.SampleFrequency = 100e6; % 1 MHz

% Window Size
scp.RecordLength = 20e3; % Samples for 100 cycles with 150 us delay

% TimeWindow
TimeWindow = scp.RecordLength/scp.SampleFrequency;
scp.PreSampleRatio = 0.0; % 0 % [JLR] NOT HANDLED YET

scp.Channels(1).Enabled = true;
scp.Channels(1).Range = 4;
scp.Channels(1).Coupling = CK.DCV; % DC Volt
scp.Channels(1).ProbeGain = 1; %

scp.Channels(2).Enabled = true;
scp.Channels(2).Range = 4;
scp.Channels(2).Coupling = CK.DCV; % DC Volt
scp.Channels(2).ProbeGain = 1; %

% Set trigger timeout:
scp.TriggerDelay = 130e-6; % 200 microseconds delay (PCD)

scp.TriggerTimeOut = -1; % How long to wait for a trigger, n.b. 0=immediate trigger
(don't wait at all)

% Disable all channel trigger source on each channel;
for ch = scp.Channels
    ch.Trigger.Enabled = false;
    clear ch;
end

% Setup external trigger for input channels:
scp.TriggerInputs(1,1).Enabled = 1;
scp.TriggerInputs(1,1).Kind = TK.RISINGEDGE; % Rising edge

scp.TriggerInputs(1,2).Enabled = 1;
scp.TriggerInputs(1,1).Kind = TK.RISINGEDGE; % Rising edge

% Print oscilloscope info:
display(scp);
```

## Data Acquisition

```
fprintf('\n[%s] Setting up function generator...',mfilename);
fprintf('\n[%s] Acquiring waveforms...\n',mfilename);

%Counting down
ampl_vpp = [4];
fprintf('Amp Voltage pkpk [Vpkpk]: %3.1f V\n',ampl_vpp);

% Reaction time
reaction_time = 30;                                 % reaction time [min]
bl = reaction_time * 30.0867678 / burstperiod;      % burst length = reaction_time / burst
period. The number of burst for the whole reaction time.
%timepoints = 100;                                  % # data points saved.
timepoints = 3 * reaction_time;                     % # data points saved. Set as 3
datapoints per min or 1 datapoint every 20 seconds. The number of timepoints scales with
time.
k = floor(bl/timepoints);                           % k: the interval of bl need to record
1 datapoint. Floor func for the nearest integer (round down)

fprintf('Reaction time : %d mins\n',reaction_time);
fprintf('Total # data points: %d\n',timepoints);

matData_ch1=zeros(scp.RecordLength,timepoints); % Save channel 1 data only
matData_ch2=zeros(scp.RecordLength,timepoints); % Save channel 2 data only

% Read current time
RunStartTime = datetime('now','Format','yyyy-MM-dd HH:mm:ss.SSS'); % Get the exact time
when the sample collection starts
dataTime = zeros(timepoints,1); % Create empty array for the sample collection time

    for myidx=1:length(ampl_vpp) % Iterate through different voltage levels

            fprintf(KEYSIGHT33600A, sprintf(':VOLTage %g',ampl_vpp(myidx)));

        for myidy = 1:k*timepoints

            % Start measurement:
            scp.start();

            %fprintf(rs232_awg,'*WAI;');% waiting for operation to complete

            % Wait for measurement to complete:
            while ~scp.IsDataReady
                pause(1e-4) % 10 ms delay, to save CPU time.
            end

            % Get data:

            if mod(myidy,k)==0                      % Remainder after division of myidy
by k, if it's = 0, then perform the following

                data_index = round(myidy/k);            % The index number for the data
across the total data points

                dataReadTime = datetime('now','Format','yyyy-MM-dd HH:mm:ss.SSS'); % Get
exact time when the data is collected at every timepoints
                dataTime(data_index,1) = seconds(dataReadTime - RunStartTime); % The time
difference between the run start and the data collection time

                remaining_time = (reaction_time * 60 - dataTime(data_index,1)) / 60; %
Remaining time for the reaction [min]. You can use N*round(X/N) to round X to nearest
number N.

                newData = scp.getData();            % only get data when if is fulfilled
                matData_ch1(:,data_index)=newData(:,1); % Save channel 1 data only
                matData_ch2(:,data_index)=newData(:,2); % Save channel 2 data only

                fprintf('Data number: %3.0f / %3.0f ; Remaining time:
%6.2f\n',data_index,timepoints,remaining_time)
            end
```

```
        end

        % MATLAB cannot load objects, so convert to struct for saving
        scp_verify.verifySampleFrequency =
scp.verifySampleFrequency(scp.SampleFrequency);
        scp_verify.verifyRecordLength = scp.verifyRecordLength(scp.RecordLength);
        scp_verify.verifyTriggerTimeOut = scp.verifyTriggerTimeOut(scp.TriggerTimeOut);
        scp_verify.verifyTriggerDelay = scp.verifyTriggerDelay(scp.TriggerDelay);
        warning('off','MATLAB:structOnObject')
        scp_struct=struct(scp);
        scp_channel1_struct=struct(scp.Channels(1));
        scp_channel2_struct=struct(scp.Channels(2));
        LibTiePie_struct=struct(LibTiePie);
        warning('on','all')

        % Saving file
        savename = UI.Basename + "_" + saveTitle + "_" + datestr(now,'HHMMSS');
        save (pn + "\" + savename + ".mat", "matData_ch1", "matData_ch2")

    end

fprintf(savename)

% Switch on or off the output
output = 0; % off
fprintf(KEYSIGHT33600A, sprintf(':OUTPut%i %d',chnl, output));
```

Plot results:

```
tvec = ((1:scp_struct.RecordLength) / scp_struct.SampleFrequency) +
scp_struct.TriggerDelay;


 figure();


plot(tvec/1e-6, matData_ch2(:,1));


 ylabel('Amplitude [V]');
 xlabel('Time [\mus]');
 title('Channel 2: PCD');
```

Close-up

```
  % Close oscilloscope:
    clear scp;
  % Close generator:
    clear gen;
```

### A.6.5. Noise signal processing for cavitation noise over time

This script provides an example for determining the cavitation index over the reaction time.

```
clear all; close all; clc;
```

Search for matching files

```
folderpath = '/BiomassExperiment/PCDnoiseData';
filelist = dir(folderpath);
allFileName = {filelist.name}; allFileName = allFileName(~strncmp(allFileName, '.', 1));
% No files starting with '.'

% Get a list of all .mat files in the folder
files = dir(fullfile(folderpath, '*.mat'));

% Initialize a cell array to hold matching file names
matchingFiles = {};
pattern = ['^Experiment_' '.*' '4VUS_\d{6}\.mat$'];
filePattern.maxTime          = 180;     % The reaction time of the experiment [min]
filePattern.num_dataPoint    = max(filePattern.maxTime) * 3;    % The number of
datapoints in the file (3 datapoints per min)

% Loop through files and match filenames
for k = 1:length(files)
    fileName = files(k).name;
    if ~isempty(regexp(fileName, pattern, 'once'))
        matchingFiles{end+1} = fileName;
    end
end
```

FFT for getting cavitation index (cav_index)

```
cav_index = zeros(length(matchingFiles),filePattern.num_dataPoint); % create an empty
array for storing output

% Loop all data for cavitation index

for file_idx = 1: length(matchingFiles)

    load(fullfile(folderpath,matchingFiles{file_idx}));

    % Intialise parameters (same as tested values)
    Par.exp_frequency    = 780e3;               % kHz
    Par.sample_frequency = 100e6;               % 100MHz
    Par.no_cyc           = 100;                 % Number of cycles
    Par.no_timepoint     = size(matData_ch2,2); % Number of timepoints
    Par.record_length    = 20e3;                % Number of samples recorded per measured
burst
    Par.trigger_delay    = 130e-6;              % Delay to PCD measurement (s)
    Par.voltage_gain     = 10^(35/20);          % Voltage gain due to
attenuator/amplifier

    % Data pretreatment
    num_data_per_burst = (1/Par.exp_frequency) * Par.no_cyc * Par.sample_frequency; %
number of data points per burst

    start_trim = 2800; % idx of datapoint starting the trim
    end_trim = round(start_trim + num_data_per_burst); % idx of datapoint ending the trim

    PCDsignal_trim = matData_ch2(start_trim:end_trim,:);
    PCDsignal_trim_realV = Par.voltage_gain * PCDsignal_trim;

    % FFT
```

```
    for timepoint = 1:Par.no_timepoint
        fourier_ch2 = abs(fft(PCDsignal_trim_realV(:,timepoint)));
        FFT_integrated = trapz(fourier_ch2);
        cav_index(file_idx,timepoint) = FFT_integrated;
    end
end
```

## Post FFT processing

```
int_cav_index = sum(cav_index,2);


% Normalised with degassed H2O
load('degassedH2O_burst_cav_index.mat'); % loading degassed H2O cavitation index for
cavitation index normalisation
log_norm_cav_index = 20 * log10(cav_index ./ avg_cav_index_degassedH2O_single);
```

## Plotting

```
% Plot for original integrated cavitation intensity per timepoint
figure;

time = linspace(0, max(filePattern.maxTime), filePattern.num_dataPoint);
for dataIdx = 1:size(cav_index,1)
    plot(time, cav_index(dataIdx,:));
    hold on
end

xlabel('Time')
ylabel('Cavitation index')
legend(matchingFiles,'Interpreter','none')

% Plot for normalised integrated cavitation intensity (with degassed water) per timepoint
figure;

for dataIdx = 1:size(cav_index,1)
    plot(time, log_norm_cav_index(dataIdx,:));
    hold on
end

xlabel('Time')
ylabel('Normalised cavitation index [dB]')
legend(matchingFiles,'Interpreter','none')
```

# References


1 Bouckaert, S., Pales, A. F., McGlade, C., Remme, U., Wanner, B., Varro, L., D'Ambrosio, D. & Spencer, T. Net zero by 2050: A roadmap for the global energy sector. (2021).

2 Suslick, K. S., Didenko, Y., Fang, M. M., Hyeon, T., Kolbeck, K. J., McNamara III, W. B., Mdleleni, M. M. & Wong, M. Acoustic cavitation and its chemical consequences. *Philosophical Transactions of the Royal Society of London. Series A: Mathematical, Physical and Engineering Sciences* **357**, 335-353, doi:https://doi.org/10.1098/rsta.1999.0330 (1999).

3 Wang, C., Tao, R., Wu, J., Jiang, H., Hu, Z., Wang, B. & Yang, Y. Sonochemistry: Materials science and engineering applications. *Coordination Chemistry Reviews* **526**, 216373, doi:https://doi.org/10.1016/j.ccr.2024.216373 (2025).

4 Machado, I. V., dos Santos, J. R. N., Januario, M. A. P. & Corrêa, A. G. Greener organic synthetic methods: Sonochemistry and heterogeneous catalysis promoted multicomponent reactions. *Ultrasonics Sonochemistry* **78**, 105704, doi:https://doi.org/10.1016/j.ultsonch.2021.105704 (2021).

5 Chatel, G. How sonochemistry contributes to green chemistry? *Ultrasonics Sonochemistry* **40**, 117-122, doi:https://doi.org/10.1016/j.ultsonch.2017.03.029 (2018).

6 Rajamma, D. B., Anandan, S., Yusof, N. S. M., Pollet, B. G. & Ashokkumar, M. Sonochemical dosimetry: A comparative study of Weissler, Fricke and terephthalic acid methods. *Ultrasonics Sonochemistry* **72**, 105413, doi:https://doi.org/10.1016/j.ultsonch.2020.105413 (2021).

7 Mishra, S. & Upadhyay, R. K. Review on biomass gasification: Gasifiers, gasifying mediums, and operational parameters. *Materials Science for Energy Technologies* **4**, 329-340, doi:https://doi.org/10.1016/j.mset.2021.08.009 (2021).

8 Richards, W. T. & Loomis, A. L. The chemical effects of high frequency sound waves I. A preliminary survey. *Journal of the American Chemical Society* **49**, 3086-3100, doi:https://doi.org/10.1021/ja01411a015 (1927).

9 Martínez, R. F., Cravotto, G. & Cintas, P. Organic Sonochemistry: A Chemist's Timely Perspective on Mechanisms and Reactivity. *The Journal of Organic Chemistry* **86**, 13833-13856, doi:https://doi.org/10.1021/acs.joc.1c00805 (2021).

10 Islam, M. H., Burheim, O. S. & Pollet, B. G. Sonochemical and sonoelectrochemical production of hydrogen. *Ultrasonics Sonochemistry* **51**, 533-555, doi:https://doi.org/10.1016/j.ultsonch.2018.08.024 (2019).

11 Serna-Galvis, E. A., Porras, J. & Torres-Palma, R. A. A critical review on the sonochemical degradation of organic pollutants in urine, seawater, and mineral water. *Ultrason Sonochem* **82**, 105861, doi:https://doi.org/10.1016/j.ultsonch.2021.105861 (2022).

12 Jing Kwan, J. & Bhatnagar, S. Ultrasound-Enhanced Transdermal Drug Delivery. *Imaging Technologies and Transdermal Delivery in Skin Disorders*, 271-289, doi:https://doi.org/10.1002/9783527814633.ch11 (2019).

13 Leighton, T. *The acoustic bubble*. (Academic press, 2012).

14 Ashokkumar, M. The characterization of acoustic cavitation bubbles – An overview. *Ultrasonics Sonochemistry* **18**, 864-872, doi:https://doi.org/10.1016/j.ultsonch.2010.11.016 (2011).

15 Li, Z., Dong, J., Zhang, H., Zhang, Y., Wang, H., Cui, X. & Wang, Z. Sonochemical catalysis as a unique strategy for the fabrication of nano-/micro-structured inorganics. *Nanoscale Adv* **3**, 41-72, doi:https://doi.org/10.1039/d0na00753f (2021).

16 Suslick, K. S. The Chemical Effects of Ultrasound. *Scientific American* **260**, 80-87, doi:https://www.jstor.org/stable/24987145 (1989).

17 Speirs, N. B., Langley, K. R., Pan, Z., Truscott, T. T. & Thoroddsen, S. T. Cavitation upon low-speed solid–liquid impact. *Nature Communications* **12**, 7250, doi:https://doi.org/10.1038/s41467-021-27383-5 (2021).

18 Yasui, K. Effect of volatile solutes on sonoluminescence. *The Journal of Chemical Physics* **116**, 2945-2954, doi:https://aip.scitation.org/doi/abs/10.1063/1.1436122 (2002).
19 Suslick, K. S. Sonochemistry. *Science* **247**, 1439-1445, doi:https://doi.org/10.1126/science.247.4949.1439 (1990).
20 Young, F. R. *Sonoluminescence*. (CRC press, 2004).
21 Kolasinski, K. W. in *Porous Silicon for Biomedical Applications* (ed Hélder A. Santos) 52-80 (Woodhead Publishing, 2014).
22 Asakura, Y. & Yasuda, K. Frequency and power dependence of the sonochemical reaction. *Ultrason Sonochem* **81**, 105858, doi:https://doi.org/10.1016/j.ultsonch.2021.105858 (2021).
23 d'Auzay, S. d. L. R., Blais, J.-F. & Naffrechoux, E. Comparison of characterization methods in high frequency sonochemical reactors of differing configurations. *Ultrasonics sonochemistry* **17**, 547-554, doi:https://doi.org/10.1016/j.ultsonch.2009.10.024 (2010).
24 Tuziuti, T., Yasui, K., Lee, J., Kozuka, T., Towata, A. & Iida, Y. Mechanism of Enhancement of Sonochemical-Reaction Efficiency by Pulsed Ultrasound. *The Journal of Physical Chemistry A* **112**, 4875-4878, doi:https://doi.org/10.1021/jp802640x (2008).
25 Iida, Y., Ashokkumar, M., Tuziuti, T., Kozuka, T., Yasui, K., Towata, A. & Lee, J. Bubble population phenomena in sonochemical reactor: II. Estimation of bubble size distribution and its number density by simple coalescence model calculation. *Ultrasonics Sonochemistry* **17**, 480-486, doi:https://doi.org/10.1016/j.ultsonch.2009.08.017 (2010).
26 Delacour, C., Lutz, C. & Kuhn, S. Pulsed ultrasound for temperature control and clogging prevention in micro-reactors. *Ultrasonics Sonochemistry* **55**, 67-74, doi:https://doi.org/10.1016/j.ultsonch.2019.03.012 (2019).
27 Yang, L., Rathman, J. F. & Weavers, L. K. Degradation of Alkylbenzene Sulfonate Surfactants by Pulsed Ultrasound. *The Journal of Physical Chemistry B* **109**, 16203-16209, doi:https://doi.org/10.1021/jp0523221 (2005).
28 Casadonte, D. J., Flores, M. & Petrier, C. Enhancing sonochemical activity in aqueous media using power-modulated pulsed ultrasound: an initial study. *Ultrasonics Sonochemistry* **12**, 147-152, doi:https://doi.org/10.1016/j.ultsonch.2003.12.004 (2005).
29 Didenko, Y. T., McNamara, W. B. & Suslick, K. S. Effect of Noble Gases on Sonoluminescence Temperatures during Multibubble Cavitation. *Physical Review Letters* **84**, 777-780, doi:https://link.aps.org/doi/10.1103/PhysRevLett.84.777 (2000).
30 Rooze, J., Rebrov, E. V., Schouten, J. C. & Keurentjes, J. T. F. Dissolved gas and ultrasonic cavitation – A review. *Ultrasonics Sonochemistry* **20**, 1-11, doi:https://doi.org/10.1016/j.ultsonch.2012.04.013 (2013).
31 Merouani, S., Ferkous, H., Hamdaoui, O., Rezgui, Y. & Guemini, M. New interpretation of the effects of argon-saturating gas toward sonochemical reactions. *Ultrasonics Sonochemistry* **23**, 37-45, doi:https://doi.org/10.1016/j.ultsonch.2014.09.009 (2015).
32 Amaniampong, P. N. & Jérôme, F. Catalysis under ultrasonic irradiation: a sound synergy. *Current Opinion in Green and Sustainable Chemistry* **22**, 7-12, doi:https://doi.org/10.1016/j.cogsc.2019.11.002 (2020).
33 Bizzi, C. A., Zanatta, R. C., Santos, D., Giacobe, K., Dallago, R. M., Mello, P. A. & Flores, E. M. Ultrasound-assisted extraction of chromium from residual tanned leather: An innovative strategy for the reuse of waste in tanning industry. *Ultrasonics Sonochemistry* **64**, 104682, doi:https://doi.org/10.1016/j.ultsonch.2019.104682 (2020).
34 Meroni, D., Djellabi, R., Ashokkumar, M., Bianchi, C. L. & Boffito, D. C. Sonoprocessing: From Concepts to Large-Scale Reactors. *Chemical Reviews*, doi:https://doi.org/10.1021/acs.chemrev.1c00438 (2021).
35 Adamou, P., Harkou, E., Villa, A., Constantinou, A. & Dimitratos, N. Ultrasonic reactor set-ups and applications: A review. *Ultrasonics Sonochemistry* **107**, 106925, doi:https://doi.org/10.1016/j.ultsonch.2024.106925 (2024).
36 De La Calle, I., Cabaleiro, N., Lavilla, I. & Bendicho, C. Analytical evaluation of a cup-horn sonoreactor used for ultrasound-assisted extraction of trace metals from troublesome

matrices. *Spectrochimica Acta Part B: Atomic Spectroscopy* **64**, 874-883, doi:https://doi.org/10.1016/j.sab.2009.07.004 (2009).
37 Saheban, H. & Kordrostami, Z. Hydrophones, fundamental features, design considerations, and various structures: A review. *Sensors and Actuators A: Physical* **329**, 112790, doi:https://doi.org/10.1016/j.sna.2021.112790 (2021).
38 Morris, P., Hurrell, A., Shaw, A., Zhang, E. & Beard, P. A Fabry–Pérot fiber-optic ultrasonic hydrophone for the simultaneous measurement of temperature and acoustic pressure. *The Journal of the Acoustical Society of America* **125**, 3611-3622, doi:https://doi.org/10.1121/1.3117437 (2009).
39 Harris, G. R., Howard, S. M., Hurrell, A. M., Lewin, P. A., Schafer, M. E., Wear, K. A., Wilkens, V. & Zeqiri, B. Hydrophone Measurements for Biomedical Ultrasound Applications: A Review. *IEEE Trans Ultrason Ferroelectr Freq Control* **70**, 85-100, doi:https://doi.org/10.1109/TUFFC.2022.3213185 (2023).
40 Mason, T. J., Lorimer, J. P. & Bates, D. M. Quantifying sonochemistry: Casting some light on a 'black art'. *Ultrasonics* **30**, 40-42, doi:https://doi.org/10.1016/0041-624X(92)90030-P (1992).
41 Toma, M., Fukutomi, S., Asakura, Y. & Koda, S. A calorimetric study of energy conversion efficiency of a sonochemical reactor at 500kHz for organic solvents. *Ultrasonics Sonochemistry* **18**, 197-208, doi:https://doi.org/10.1016/j.ultsonch.2010.05.005 (2011).
42 Mark, G., Tauber, A., Laupert, R., Schuchmann, H.-P., Schulz, D., Mues, A. & von Sonntag, C. OH-radical formation by ultrasound in aqueous solution – Part II: Terephthalate and Fricke dosimetry and the influence of various conditions on the sonolytic yield. *Ultrasonics Sonochemistry* **5**, 41-52, doi:https://doi.org/10.1016/S1350-4177(98)00012-1 (1998).
43 Weissler, A., Cooper, H. W. & Snyder, S. Chemical Effect of Ultrasonic Waves: Oxidation of Potassium Iodide Solution by Carbon Tetrachloride. *Journal of the American Chemical Society* **72**, 1769-1775, doi:https://doi.org/10.1021/ja01160a102 (1950).
44 Morison, K. R. & Hutchinson, C. A. Limitations of the Weissler reaction as a model reaction for measuring the efficiency of hydrodynamic cavitation. *Ultrasonics Sonochemistry* **16**, 176-183, doi:https://doi.org/10.1016/j.ultsonch.2008.07.001 (2009).
45 Merouani, S., Hamdaoui, O., Rezgui, Y. & Guemini, M. Sensitivity of free radicals production in acoustically driven bubble to the ultrasonic frequency and nature of dissolved gases. *Ultrasonics Sonochemistry* **22**, 41-50, doi:https://doi.org/10.1016/j.ultsonch.2014.07.011 (2015).
46 Matuszek, K., Pankalla, E., Grymel, A., Latos, P. & Chrobok, A. Studies on the Solubility of Terephthalic Acid in Ionic Liquids. *Molecules* **25**, doi:https://doi.org/10.3390/molecules25010080 (2019).
47 Koda, S., Kimura, T., Kondo, T. & Mitome, H. A standard method to calibrate sonochemical efficiency of an individual reaction system. *Ultrasonics Sonochemistry* **10**, 149-156, doi:https://doi.org/10.1016/S1350-4177(03)00084-1 (2003).
48 Kojima, Y., Asakura, Y., Sugiyama, G. & Koda, S. The effects of acoustic flow and mechanical flow on the sonochemical efficiency in a rectangular sonochemical reactor. *Ultrasonics Sonochemistry* **17**, 978-984, doi:https://doi.org/10.1016/j.ultsonch.2009.11.020 (2010).
49 Löning, J.-M., Horst, C. & Hoffmann, U. Investigations on the energy conversion in sonochemical processes. *Ultrasonics Sonochemistry* **9**, 169-179, doi:https://doi.org/10.1016/S1350-4177(01)00113-4 (2002).
50 Khaligh, V., Ghezelbash, A., Akhtar, M. S., Zarei, M., Liu, J. & Won, W. Optimal integration of a low-carbon energy system – A circular hydrogen economy perspective. *Energy Conversion and Management* **292**, 117354, doi:https://doi.org/10.1016/j.enconman.2023.117354 (2023).

51 Kabir, M. M., Akter, M. M., Huang, Z., Tijing, L. & Shon, H. K. Hydrogen production from water industries for a circular economy. *Desalination* **554**, 116448, doi:https://doi.org/10.1016/j.desal.2023.116448 (2023).
52 Jin, H., Xu, J., Liu, H., Shen, H., Yu, H., Jaroniec, M., Zheng, Y. & Qiao, S.-Z. Emerging materials and technologies for electrocatalytic seawater splitting. *Science Advances* **9**, eadi7755, doi:https://doi.org/10.1126/sciadv.adi7755 (2023).
53 Xu, S.-W., Li, J., Zhang, N., Shen, W., Zheng, Y. & Xi, P. Recent advances in direct seawater splitting for producing hydrogen. *Chemical Communications* **59**, 9792-9802, doi:https://doi.org/10.1039/D3CC02074F (2023).
54 Li, C. & Baek, J.-B. Recent Advances in Noble Metal (Pt, Ru, and Ir)-Based Electrocatalysts for Efficient Hydrogen Evolution Reaction. *ACS Omega* **5**, 31-40, doi:https://doi.org/10.1021/acsomega.9b03550 (2020).
55 Salonen, L. M., Petrovykh, D. Y. & Kolen'ko, Y. V. Sustainable catalysts for water electrolysis: Selected strategies for reduction and replacement of platinum-group metals. *Materials Today Sustainability* **11-12**, 100060, doi:https://doi.org/10.1016/j.mtsust.2021.100060 (2021).
56 Dresp, S., Dionigi, F., Klingenhof, M. & Strasser, P. Direct Electrolytic Splitting of Seawater: Opportunities and Challenges. *ACS Energy Letters* **4**, 933-942, doi:https://doi.org/10.1021/acsenergylett.9b00220 (2019).
57 Dang, V.-H., Nguyen, T.-A., Le, M.-V., Nguyen, D. Q., Wang, Y. H. & Wu, J. C. S. Photocatalytic hydrogen production from seawater splitting: Current status, challenges, strategies and prospective applications. *Chemical Engineering Journal* **484**, 149213, doi:https://doi.org/10.1016/j.cej.2024.149213 (2024).
58 Merouani, S., Hamdaoui, O., Rezgui, Y. & Guemini, M. Mechanism of the sonochemical production of hydrogen. *International Journal of Hydrogen Energy* **40**, 4056-4064, doi:https://doi.org/10.1016/j.ijhydene.2015.01.150 (2015).
59 Fischer, C. H., Hart, E. J. & Henglein, A. Ultrasonic irradiation of water in the presence of oxygen 18, 18O2: isotope exchange and isotopic distribution of hydrogen peroxide. *The Journal of Physical Chemistry* **90**, 1954-1956, doi:https://doi.org/10.1021/j100400a043 (1986).
60 Gutierrez, M., Henglein, A. & Dohrmann, J. K. Hydrogen atom reactions in the sonolysis of aqueous solutions. *Journal of Physical Chemistry* **91**, 6687-6690, doi:https://doi.org/10.1021/j100311a026 (1987).
61 Ziembowicz, S., Kida, M. & Koszelnik, P. Sonochemical Formation of Hydrogen Peroxide. *Proceedings* **2**, 188, doi:https://doi.org/10.3390/ecws-2-04957 (2018).
62 Ziembowicz, S., Kida, M. & Koszelnik, P. The impact of selected parameters on the formation of hydrogen peroxide by sonochemical process. *Separation and Purification Technology* **204**, 149-153, doi:https://doi.org/10.1016/j.seppur.2018.04.073 (2018).
63 Zhang, T., Guan, X., Zhu, B., Zhang, Z., Ye, X., Zeng, W., Gao, Z. & Guo, L. Boosting solar-driven thermal-assisted photocatalytic hydrogen production through device thermal management. *International Journal of Hydrogen Energy* **51**, 921-934, doi:https://doi.org/10.1016/j.ijhydene.2023.07.103 (2024).
64 Zhang, X., Xu, C., Zhang, L., Li, Z., Hong, J. & Zhang, Y. Photothermal Catalytic Water Splitting at Diverse Two-Phase Interfaces Based on Cu–TiO2. *ACS Applied Energy Materials* **5**, 4564-4576, doi:https://doi.org/10.1021/acsaem.2c00009 (2022).
65 Gentili, P. L., Penconi, M., Ortica, F., Cotana, F., Rossi, F. & Elisei, F. Synergistic effects in hydrogen production through water sonophotolysis catalyzed by new La2xGa2yIn2(1−x−y)O3 solid solutions. *International Journal of Hydrogen Energy* **34**, 9042-9049, doi:https://doi.org/10.1016/j.ijhydene.2009.09.027 (2009).
66 Penconi, M., Rossi, F., Ortica, F., Elisei, F. & Gentili, P. L. Hydrogen Production from Water by Photolysis, Sonolysis and Sonophotolysis with Solid Solutions of Rare Earth,

Gallium and Indium Oxides as Heterogeneous Catalysts. *Sustainability* **7**, 9310-9325, doi:https://doi.org/10.3390/su7079310 (2015).
67 Rashwan, S. S., Dincer, I., Mohany, A. & Pollet, B. G. The Sono-Hydro-Gen process (Ultrasound induced hydrogen production): Challenges and opportunities. *International Journal of Hydrogen Energy* **44**, 14500-14526, doi:https://doi.org/10.1016/j.ijhydene.2019.04.115 (2019).
68 Merouani, S. & Hamdaoui, O. *The Sonochemical Approach for Hydrogen Production*. (Springer International Publishing, 2020).
69 Sharifishourabi, M., Dincer, I. & Mohany, A. Experimental testing of a novel sonic method for clean hydrogen generation. *International Journal of Hydrogen Energy* **82**, 206-217, doi:https://doi.org/10.1016/j.ijhydene.2024.07.378 (2024).
70 Sharifishourabi, M., Dincer, I. & Mohany, A. Implementation of experimental techniques in ultrasound-driven hydrogen production: A comprehensive review. *International Journal of Hydrogen Energy* **62**, 1183-1204, doi:https://doi.org/10.1016/j.ijhydene.2024.03.013 (2024).
71 Wang, Y., Zhao, D., Ji, H., Liu, G., Chen, C., Ma, W., Zhu, H. & Zhao, J. Sonochemical Hydrogen Production Efficiently Catalyzed by Au/TiO2. *The Journal of Physical Chemistry C* **114**, 17728-17733, doi:https://doi.org/10.1021/jp105691v (2010).
72 Qi, W., Liu, J., Guo, X., Guo, H., Thomas, T., Zhu, Y., Liu, S. & Yang, M. Vacancy-Defective Cobalt Nitride Nanostructures for Sonocatalytic Hydrogen Production Using Various Water Resources. *ACS Applied Nano Materials* **6**, 2636-2645, doi:https://doi.org/10.1021/acsanm.2c05054 (2023).
73 Qiu, P., Park, B., Choi, J., Thokchom, B., Pandit, A. B. & Khim, J. A review on heterogeneous sonocatalyst for treatment of organic pollutants in aqueous phase based on catalytic mechanism. *Ultrasonics sonochemistry* **45**, 29-49, doi:https://doi.org/10.1016/j.ultsonch.2018.03.003 (2018).
74 Danish, M. S. S. Exploring metal oxides for the hydrogen evolution reaction (HER) in the field of nanotechnology. *RSC Sustainability* **1**, 2180-2196, doi:http://dx.doi.org/10.1039/D3SU00179B (2023).
75 El-Sawy, A. M., Salem, M. A., Salem, I. A., Hydara, M. M. & Zaki, A. B. Sonophotocatalytic degradation of malachite green in aqueous solution using six competitive metal oxides as a benchmark. *Photochemical & Photobiological Sciences* **22**, 579-594, doi:https://doi.org/10.1007/s43630-022-00336-7 (2023).
76 Mazlum, İ., Keyikoğlu, R., Seifi, A., Yoon, Y., Kobya, M. & Khataee, A. LaCuFe mixed metal oxide as catalyst for degradation of refractory pollutants from water by hybrid ultrasonic/peroxymonosulfate process. *Journal of Environmental Chemical Engineering* **14**, 121428, doi:https://doi.org/10.1016/j.jece.2026.121428 (2026).
77 Her, N., Park, J.-S. & Yoon, Y. Sonochemical enhancement of hydrogen peroxide production by inert glass beads and TiO2-coated glass beads in water. *Chemical engineering journal* **166**, 184-190, doi:https://doi.org/10.1016/j.cej.2010.10.059 (2011).
78 Morosini, V., Chave, T., Virot, M., Moisy, P. & Nikitenko, S. I. Sonochemical water splitting in the presence of powdered metal oxides. *Ultrasonics Sonochemistry* **29**, 512-516, doi:https://doi.org/10.1016/j.ultsonch.2015.11.006 (2016).
79 Pereira, E. G., da Silva, J. N., de Oliveira, J. L. & Machado, C. S. Sustainable energy: A review of gasification technologies. *Renewable and Sustainable Energy Reviews* **16**, 4753-4762, doi:https://doi.org/10.1016/j.rser.2012.04.023 (2012).
80 Shahbaz, M., AlNouss, A., Ghiat, I., McKay, G., Mackey, H., Elkhalifa, S. & Al-Ansari, T. A comprehensive review of biomass based thermochemical conversion technologies integrated with CO2 capture and utilisation within BECCS networks. *Resources, Conservation and Recycling* **173**, 105734, doi:https://doi.org/10.1016/j.resconrec.2021.105734 (2021).
81 Furusawa, Y., Taguchi, H., Ismail, S. N., Thangavel, S., Matsuoka, K. & Fushimi, C. Estimation of cold gas efficiency and reactor size of low-temperature gasifier for advanced-

integrated coal gasification combined cycle systems. *Fuel Processing Technology* **193**, 304-316, doi:https://doi.org/10.1016/j.fuproc.2019.05.023 (2019).
82 Kumar, S., Palange, R. & De Blasio, C. Advancements in gasification technologies: insights into modeling studies, power-to-X applications and sustainability assessments. *Sustainable Energy & Fuels* **9**, 4793-4831, doi:https://doi.org/10.1039/D5SE00504C (2025).
83 Glushkov, D., Nyashina, G., Shvets, A., Pereira, A. & Ramanathan, A. Current Status of the Pyrolysis and Gasification Mechanism of Biomass. *Energies* **14**, 7541, doi:https://doi.org/10.3390/en14227541 (2021).
84 Ma, C., Hu, J., Wang, H., Yu, Y. & Tan, C. Advances and challenges in biomass thermochemical conversion: From resource utilization to process optimization. *Renewable and Sustainable Energy Reviews* **226**, 116385, doi:https://doi.org/10.1016/j.rser.2025.116385 (2026).
85 Cortazar, M., Santamaria, L., Lopez, G., Alvarez, J., Zhang, L., Wang, R., Bi, X. & Olazar, M. A comprehensive review of primary strategies for tar removal in biomass gasification. *Energy Conversion and Management* **276**, 116496, doi:https://doi.org/10.1016/j.enconman.2022.116496 (2023).
86 Tezer, Ö., Karabağ, N., Öngen, A., Çolpan, C. Ö. & Ayol, A. Biomass gasification for sustainable energy production: A review. *International Journal of Hydrogen Energy* **47**, 15419-15433, doi:https://doi.org/10.1016/j.ijhydene.2022.02.158 (2022).
87 Pradana, Y. S. & Budiman, A. Bio-syngas derived from Indonesian oil palm empty fruit bunch (EFB) using middle-scale gasification. *Journal of Engineering Science and Technology* **10**, 1-8 (2015).
88 Gao, Y., Wang, M., Raheem, A., Wang, F., Wei, J., Xu, D., Song, X., Bao, W., Huang, A., Zhang, S. & Zhang, H. Syngas Production from Biomass Gasification: Influences of Feedstock Properties, Reactor Type, and Reaction Parameters. *ACS Omega* **8**, 31620-31631, doi:https://doi.org/10.1021/acsomega.3c03050 (2023).
89 Gomes, H. G. M. F., Matos, M. A. A. & Tarelho, L. A. C. Influence of Oxygen/Steam Addition on the Quality of Producer Gas during Direct (Air) Gasification of Residual Forest Biomass. *Energies* **16**, 2427, doi:https://doi.org/10.3390/en16052427 (2023).
90 Wang, Y., Yoshiie, R., Ueki, Y. & Naruse, I. Characteristics of biomass gasification by oxygen-enriched air in small-scale auto-thermal packed-bed gasifier for regional distribution. *Fuel* **342**, 127852, doi:https://doi.org/10.1016/j.fuel.2023.127852 (2023).
91 Gao, N., Salisu, J., Quan, C. & Williams, P. Modified nickel-based catalysts for improved steam reforming of biomass tar: A critical review. *Renewable and Sustainable Energy Reviews* **145**, 111023, doi:https://doi.org/10.1016/j.rser.2021.111023 (2021).
92 Papa, A. A., Bartolucci, L., Cordiner, S., Di Carlo, A., Mele, P., Mulone, V. & Vitale, A. The effect of pyrolysis temperature on the optimal conversion of residual biomass to clean syngas through fast-pyrolysis/steam gasification integration. *International Journal of Hydrogen Energy* **95**, 1316-1327, doi:https://doi.org/10.1016/j.ijhydene.2024.09.100 (2024).
93 Ajorloo, M., Ghodrat, M., Scott, J. & Strezov, V. Evaluating the role of feedstock composition and component interactions on biomass gasification. *Fuel* **381**, 133528, doi:https://doi.org/10.1016/j.fuel.2024.133528 (2025).
94 Ibitoye, S. E., Mahamood, R. M., Jen, T.-C., Loha, C. & Akinlabi, E. T. An overview of biomass solid fuels: Biomass sources, processing methods, and morphological and microstructural properties. *Journal of Bioresources and Bioproducts* **8**, 333-360, doi:https://doi.org/10.1016/j.jobab.2023.09.005 (2023).
95 Flores, E. M. M., Cravotto, G., Bizzi, C. A., Santos, D. & Iop, G. D. Ultrasound-assisted biomass valorization to industrial interesting products: state-of-the-art, perspectives and challenges. *Ultrasonics Sonochemistry* **72**, 105455, doi:https://doi.org/10.1016/j.ultsonch.2020.105455 (2021).
96 Momayez, F., Okoro, O. V., Shavandi, A., Martín, C., Denayer, J. F. M. & Karimi, K. A critical review of ultrasonication as a green technology for enhanced biomass valorization in

bioethanol and biogas production. *Process Safety and Environmental Protection* **200**, 107334, doi:https://doi.org/10.1016/j.psep.2025.107334 (2025).
97 Ong, V. Z. & Wu, T. Y. An application of ultrasonication in lignocellulosic biomass valorisation into bio-energy and bio-based products. *Renewable and Sustainable Energy Reviews* **132**, 109924, doi:https://doi.org/10.1016/j.rser.2020.109924 (2020).
98 Zhou, C., Zhang, L., Liang, J. & Ren, M. in *Sustainable Radiation Technologies in Waste-biomass Valorization: Greener Energy and High-Value Product Generation* (eds Pradeep Verma & Bikash Kumar) 215-237 (Springer Nature Switzerland, 2024).
99 Bundhoo, Z. M. A. & Mohee, R. Ultrasound-assisted biological conversion of biomass and waste materials to biofuels: A review. *Ultrasonics Sonochemistry* **40**, 298-313, doi:https://doi.org/10.1016/j.ultsonch.2017.07.025 (2018).
100 Nasir, J. A., Rehman, Z. u., Shah, S. N. A., Khan, A., Butler, I. S. & Catlow, C. R. A. Recent developments and perspectives in CdS-based photocatalysts for water splitting. *Journal of Materials Chemistry A* **8**, 20752-20780, doi:http://dx.doi.org/10.1039/D0TA05834C (2020).
101 Chen, L., Qin, Y., Coulthard, C. T., Turner, Z. R., Chen, C., Kwan, J. & O'Hare, D. Catalytic ultrasound-driven synthesis of syngas from CO2 saturated water. *Energy & Environmental Science*, doi:http://dx.doi.org/10.1039/D5EE01202C (2025).
102 De Vrieze, J., Plovie, K., Verstraete, W. & Boon, N. Co-digestion of molasses or kitchen waste with high-rate activated sludge results in a diverse microbial community with stable methane production. *Journal of Environmental Management* **152**, 75-82, doi:https://doi.org/10.1016/j.jenvman.2015.01.029 (2015).
103 Vilela, R. S., Fuess, L. T., Saia, F. T., Silveira, C. R. M., Oliveira, C. A., Andrade, P. A., Langenhoff, A., van der Zaan, B., Cop, F., Gregoracci, G. B. & Damianovic, M. H. R. Z. Biofuel production from sugarcane molasses in thermophilic anaerobic structured-bed reactors. *Renewable and Sustainable Energy Reviews* **144**, 110974, doi:https://doi.org/10.1016/j.rser.2021.110974 (2021).
104 Jamir, L., Vikas, K., Jasleen, K., Satish, K. & and Singh, H. Composition, valorization and therapeutical potential of molasses: a critical review. *Environmental Technology Reviews* **10**, 131-142, doi:https://doi.org/10.1080/21622515.2021.1892203 (2021).
105 Xie, Z., Mahendran, V., Jonnalagadda, U. S., Fan, Q., Su, X., Fischer, A. F., Tan, M., Tao, L., Jérôme, F., Kwan, J. J., Valange, S., Choksi, T. S., Amaniampong, P. N. & Liu, W. Boosting energy efficiency and selectivity of glucose oxidation toward glucuronic acid in high-frequency ultrasound using multicavity CuO catalytic cavitation agents. *Green Chemistry* **27**, 573-585, doi:http://dx.doi.org/10.1039/D4GC03775H (2025).
106 Cai, R., Pei, X., Pan, H., Wan, K., Chen, H., Zhang, Z. & Zhang, Y. Biomass catalytic pyrolysis over zeolite catalysts with an emphasis on porosity and acidity: a state-of-the-art review. *Energy & Fuels* **34**, 11771-11790, doi:https://doi.org/10.1021/acs.energyfuels.0c02147 (2020).
107 Qazi, U. Y., Javaid, R., Ikhlaq, A., Khoja, A. H. & Saleem, F. A Comprehensive Review on Zeolite Chemistry for Catalytic Conversion of Biomass/Waste into Green Fuels. *Molecules* **27**, 8578, doi:https://doi.org/10.3390/molecules27238578 (2022).
108 Buchireddy, P. R., Bricka, R. M., Rodriguez, J. & Holmes, W. Biomass gasification: catalytic removal of tars over zeolites and nickel supported zeolites. *Energy & Fuels* **24**, 2707-2715, doi:https://doi.org/10.1021/ef901529d (2010).
109 Lok, C. M., Van Doorn, J. & Aranda Almansa, G. Promoted ZSM-5 catalysts for the production of bio-aromatics, a review. *Renewable and Sustainable Energy Reviews* **113**, 109248, doi:https://doi.org/10.1016/j.rser.2019.109248 (2019).
110 Huo, R., Pei, M., Xue, N., Cheng, H., Chen, D., Zhu, H. & Yin, J. Synergistic stabilization of nickel nanoparticles on dealuminated β-zeolite for high-efficiency H2-rich syngas production from biomass gasification. *Journal of the Energy Institute* **126**, 102535, doi:https://doi.org/10.1016/j.joei.2026.102535 (2026).

111 Jentoft, F. C. & Gates, B. C. Solid-acid-catalyzed alkane cracking mechanisms: evidence from reactions of small probe molecules. *Topics in Catalysis* **4**, 1-13, doi:https://doi.org/10.1023/A:1019184004885 (1997).
112 Xu, B., Sievers, C., Hong, S. B., Prins, R. & van Bokhoven, J. A. Catalytic activity of Brønsted acid sites in zeolites: Intrinsic activity, rate-limiting step, and influence of the local structure of the acid sites. *Journal of Catalysis* **244**, 163-168, doi:https://doi.org/10.1016/j.jcat.2006.08.022 (2006).
113 Mahmood, J., Li, F., Jung, S.-M., Okyay, M. S., Ahmad, I., Kim, S.-J., Park, N., Jeong, H. Y. & Baek, J.-B. An efficient and pH-universal ruthenium-based catalyst for the hydrogen evolution reaction. *Nature Nanotechnology* **12**, 441-446, doi:https://doi.org/10.1038/nnano.2016.304 (2017).
114 Guisnet, M. & Perot, G. in *Zeolites: Science and Technology* (eds F. Ramôa Ribeiro, Alírio E. Rodrigues, L. Deane Rollmann, & Claude Naccache) 397-420 (Springer Netherlands, 1984).
115 Khowatimy, F. A., Priastomo, Y., Febriyanti, E., Riyantoko, H. & Trisunaryanti, W. Study of Waste Lubricant Hydrocracking into Fuel Fraction over the Combination of Y-Zeolite and ZnO Catalyst. *Procedia Environmental Sciences* **20**, 225-234, doi:https://doi.org/10.1016/j.proenv.2014.03.029 (2014).
116 Zsinka, V., Miskolczi, N., Juzsakova, T. & Jakab, M. Pyrolysis-gasification of biomass using nickel modified catalysts: The effect of the catalyst regeneration on the product properties. *Journal of the Energy Institute* **105**, 16-24, doi:https://doi.org/10.1016/j.joei.2022.08.003 (2022).
117 Niu, Y.-h., Chi, Z.-y., Li, M., Du, J.-z. & Han, F.-t. Advancements in biomass gasification and catalytic tar-cracking technologies. *Materials Reports: Energy* **4**, 100295, doi:https://doi.org/10.1016/j.matre.2024.100295 (2024).
118 Yung, M. M., Starace, A. K., Mukarakate, C., Crow, A. M., Leshnov, M. A. & Magrini, K. A. Biomass catalytic pyrolysis on Ni/ZSM-5: effects of nickel pretreatment and loading. *Energy & Fuels* **30**, 5259-5268, doi:https://doi.org/10.1021/acs.energyfuels.6b00239 (2016).
119 Limlamthong, M. & Yip, A. C. K. Recent advances in zeolite-encapsulated metal catalysts: A suitable catalyst design for catalytic biomass conversion. *Bioresource Technology* **297**, 122488, doi:https://doi.org/10.1016/j.biortech.2019.122488 (2020).
120 Suslick, K. S., Doktycz, S. J. & Flint, E. B. On the origin of sonoluminescence and sonochemistry. *Ultrasonics* **28**, 280-290, doi:https://doi.org/10.1016/0041-624X(90)90033-K (1990).
121 Leong, T. S. H., Manickam, S., Martin, G. J., Li, W. & Ashokkumar, M. *Ultrasonic production of nano-emulsions for bioactive delivery in drug and food applications*. (Springer, 2018).
122 Greillier, P., Bawiec, C., Bessière, F. & Lafon, C. Therapeutic Ultrasound for the Heart: State of the Art. *IRBM* **39**, 227-235, doi:https://doi.org/10.1016/j.irbm.2017.11.004 (2018).
123 Jajko-Liberka, G., Anagha, M. G., Chytrosz-Wróbel, P., Kubisiak, P., Kulig, W., Cwiklik, L. & Kotarba, A. Sonochemical synthesis of nanoparticles from bioactive compounds: advances, challenges, and future perspectives. *Ultrasonics Sonochemistry* **121**, 107559, doi:https://doi.org/10.1016/j.ultsonch.2025.107559 (2025).
124 Mitome, H. & Hatanaka, S.-i. Optimization of a sonochemical reactor using a pulsing operation. *Ultrasonics* **40**, 683-687, doi:https://doi.org/10.1016/S0041-624X(02)00258-5 (2002).
125 Prabhu, A. V., Gogate, P. R. & Pandit, A. B. Optimization of multiple-frequency sonochemical reactors. *Chemical Engineering Science* **59**, 4991-4998, doi:https://doi.org/10.1016/j.ces.2004.09.033 (2004).
126 Sutkar, V. S. & Gogate, P. R. Design aspects of sonochemical reactors: Techniques for understanding cavitational activity distribution and effect of operating parameters. *Chemical Engineering Journal* **155**, 26-36, doi:https://doi.org/10.1016/j.cej.2009.07.021 (2009).

127 Preso, D. B., Smirnov, I., Salimi, M. & Kwan, J. Broadening the sonochemistry horizon: hurdles and challenges to address in cavitation. *Current Opinion in Chemical Engineering* **48**, 101128, doi:https://doi.org/10.1016/j.coche.2025.101128 (2025).
128 Elhelf, I. A. S., Albahar, H., Shah, U., Oto, A., Cressman, E. & Almekkawy, M. High intensity focused ultrasound: The fundamentals, clinical applications and research trends. *Diagnostic and Interventional Imaging* **99**, 349-359, doi:https://doi.org/10.1016/j.diii.2018.03.001 (2018).
129 Cao, Z., Wu, Z., Faghri, M. & Sundén, B. in *Advances in Heat Transfer* Vol. 53 (eds John Patrick Abraham, John M. Gorman, & Wolodmyr Minkowycz) 97-158 (Elsevier, 2021).
130 Wong, C. C. Y., Sun, L.-L., Liu, M.-J., Stride, E., Raymond, J. L., Han, H.-H., Kwan, J. & Sedgwick, A. C. Fluorescence-based chemical tools for monitoring ultrasound-induced hydroxyl radical production in aqueous solution and in cells. *Chemical Communications* **59**, 4328-4331, doi:http://dx.doi.org/10.1039/D3CC00364G (2023).
131 Villeneuve, L., Alberti, L., Steghens, J. P., Lancelin, J. M. & Mestas, J. L. Assay of hydroxyl radicals generated by focused ultrasound. *Ultrasonics Sonochemistry* **16**, 339-344, doi:https://doi.org/10.1016/j.ultsonch.2008.09.007 (2009).
132 Chen, T.-W., Liu, C.-T., Chen, C.-Y., Wu, M.-C., Chien, P.-C., Cheng, Y.-C. & Wu, J.-S. Analysis of Hydroxyl Radical and Hydrogen Peroxide Generated in Helium-Based Atmospheric-Pressure Plasma Jet and in Different Solutions Treated by Plasma for Bioapplications. *ECS Journal of Solid State Science and Technology* **9**, 115002, doi:https://doi.org/10.1149/2162-8777/ab9c78 (2020).
133 Palmer, D. A., Ramette, R. & Mesmer, R. Triiodide ion formation equilibrium and activity coefficients in aqueous solution. *Journal of solution chemistry* **13**, 673-683, doi:https://doi.org/10.1007/BF00650374 (1984).
134 Toegel, R., Gompf, B., Pecha, R. & Lohse, D. Does Water Vapor Prevent Upscaling Sonoluminescence? *Physical Review Letters* **85**, 3165-3168, doi:https://link.aps.org/doi/10.1103/PhysRevLett.85.3165 (2000).
135 Weninger, K., Camara, C. & Putterman, S. Observation of bubble dynamics within luminescent cavitation clouds: Sonoluminescence at the nano-scale. *Physical Review E* **63**, 016310, doi:https://doi.org/10.1103/PhysRevE.63.016310 (2000).
136 Yasui, K., Tuziuti, T., Kozuka, T., Towata, A. & Iida, Y. Relationship between the bubble temperature and main oxidant created inside an air bubble under ultrasound. *The Journal of chemical physics* **127**, doi:https://doi.org/10.1063/1.2790420 (2007).
137 Yasui, K. Influence of ultrasonic frequency on multibubble sonoluminescence. *The Journal of the Acoustical Society of America* **112**, 1405-1413, doi:https://doi.org/10.1121/1.1502898 (2002).
138 Su, X., Jonnalagadda, U. S., Bharatula, L. D. & Kwan, J. J. Unsupported gold nanocones as sonocatalytic agents with enhanced catalytic properties. *Ultrasonics Sonochemistry* **79**, 105753, doi:https://doi.org/10.1016/j.ultsonch.2021.105753 (2021).
139 Lafon, C., Moore, D., Eames, M. D., Snell, J., Drainville, R. A. & Padilla, F. Evaluation of Pseudorandom sonications for reducing cavitation with a clinical neurosurgery HIFU device. *IEEE Transactions on Ultrasonics, Ferroelectrics, and Frequency Control* **68**, 1224-1233, doi:https://doi.org/10.1109/tuffc.2020.3036774 (2020).
140 Li, T., Chen, H., Khokhlova, T., Wang, Y.-N., Kreider, W., He, X. & Hwang, J. H. Passive cavitation detection during pulsed HIFU exposures of ex vivo tissues and in vivo mouse pancreatic tumors. *Ultrasound in medicine & biology* **40**, 1523-1534, doi:https://doi.org/10.1016/j.ultrasmedbio.2014.01.007 (2014).
141 Deojay, D. M., Sostaric, J. Z. & Weavers, L. K. Exploring the effects of pulsed ultrasound at 205 and 616kHz on the sonochemical degradation of octylbenzene sulfonate. *Ultrasonics Sonochemistry* **18**, 801-809, doi:https://doi.org/10.1016/j.ultsonch.2010.10.005 (2011).

142 Al-Juboori, R. A., Yusaf, T. & Bowtell, L. Energy Conversion Efficiency of Pulsed Ultrasound. *Energy Procedia* **75**, 1560-1568, doi:https://doi.org/10.1016/j.egypro.2015.07.340 (2015).
143 Pan, Z., Qu, W., Ma, H., Atungulu, G. G. & McHugh, T. H. Continuous and pulsed ultrasound-assisted extractions of antioxidants from pomegranate peel. *Ultrasonics Sonochemistry* **18**, 1249-1257, doi:https://doi.org/10.1016/j.ultsonch.2011.01.005 (2011).
144 Li, R., Ni, Q.-Q., Xia, H. & Natsuki, T. Analysis of individual attenuation components of ultrasonic waves in composite material considering frequency dependence. *Composites Part B: Engineering* **140**, 232-240, doi:https://doi.org/10.1016/j.compositesb.2016.03.045 (2018).
145 de La Rochebrochard, S., Suptil, J., Blais, J.-F. & Naffrechoux, E. Sonochemical efficiency dependence on liquid height and frequency in an improved sonochemical reactor. *Ultrasonics Sonochemistry* **19**, 280-285, doi:https://doi.org/10.1016/j.ultsonch.2011.07.009 (2012).
146 Asakura, Y., Nishida, T., Matsuoka, T. & Koda, S. Effects of ultrasonic frequency and liquid height on sonochemical efficiency of large-scale sonochemical reactors. *Ultrasonics Sonochemistry* **15**, 244-250, doi:https://doi.org/10.1016/j.ultsonch.2007.03.012 (2008).
147 Iida, Y., Yasui, K., Tuziuti, T. & Sivakumar, M. Sonochemistry and its dosimetry. *Microchemical Journal* **80**, 159-164, doi:https://doi.org/10.1016/j.microc.2004.07.016 (2005).
148 Merouani, S., Hamdaoui, O., Saoudi, F. & Chiha, M. Influence of experimental parameters on sonochemistry dosimetries: KI oxidation, Fricke reaction and H2O2 production. *Journal of Hazardous Materials* **178**, 1007-1014, doi:https://doi.org/10.1016/j.jhazmat.2010.02.039 (2010).
149 Hua, I. & Hoffmann, M. R. Optimization of Ultrasonic Irradiation as an Advanced Oxidation Technology. *Environmental Science & Technology* **31**, 2237-2243, doi:https://doi.org/10.1021/es960717f (1997).
150 Entezari, M. H. & Kruus, P. Effect of frequency on sonochemical reactions II. Temperature and intensity effects. *Ultrasonics Sonochemistry* **3**, 19-24, doi:https://doi.org/10.1016/1350-4177(95)00037-2 (1996).
151 Wu, T.-N. & Shi, M.-C. pH-affecting sonochemical formation of hydroxyl radicals under 20 kHz ultrasonic irradiation. *Journal of Environmental Engineering and Management* **20**, 245-250 (2010).
152 Hossain Bhuiyan, M. M. & Siddique, Z. Hydrogen as an alternative fuel: A comprehensive review of challenges and opportunities in production, storage, and transportation. *International Journal of Hydrogen Energy* **102**, 1026-1044, doi:https://doi.org/10.1016/j.ijhydene.2025.01.033 (2025).
153 Zhao, Y., Yu, Z., Ge, A., Liu, L., Faria, J. L., Xu, G. & Zhu, M. Direct seawater splitting for hydrogen production: Recent advances in materials synthesis and technological innovation. *Green Energy & Environment* **10**, 11-33, doi:https://doi.org/10.1016/j.gee.2024.02.001 (2025).
154 Bernt, M., Hartig-Weiß, A., Tovini, M. F., El-Sayed, H. A., Schramm, C., Schröter, J., Gebauer, C. & Gasteiger, H. A. Current Challenges in Catalyst Development for PEM Water Electrolyzers. *Chemie Ingenieur Technik* **92**, 31-39, doi:https://doi.org/10.1002/cite.201900101 (2020).
155 Honnappa, B., Ganesan, S., Kokulnathan, T., Palaniappan, A. & Sekar, K. Advances and challenges in photo/electrocatalytic seawater splitting for sustainable hydrogen production: A comprehensive review. *International Journal of Hydrogen Energy* **120**, 642-681, doi:https://doi.org/10.1016/j.ijhydene.2025.03.168 (2025).
156 Gupta, A., Likozar, B. & Jaidka, S. A review on photocatalytic seawater splitting with efficient and selective catalysts for hydrogen evolution reaction. *Renewable and Sustainable Energy Reviews* **208**, 115074, doi:https://doi.org/10.1016/j.rser.2024.115074 (2025).

157 Kerboua, K. & Hamdaoui, O. Numerical estimation of ultrasonic production of hydrogen: Effect of ideal and real gas based models. *Ultrasonics Sonochemistry* **40**, 194-200, doi:https://doi.org/10.1016/j.ultsonch.2017.07.005 (2018).
158 Mardare, L. & Benea, L. Effects of TiO2 nanoparticles on the corrosion protection ability of polymeric primer coating system. *Polymers* **13**, 614, doi:https://doi.org/10.3390/polym13040614 (2021).
159 Wong, C. C. Y., Raymond, J. L., Usadi, L. N., Zong, Z., Walton, S. C., Sedgwick, A. C. & Kwan, J. Enhancement of sonochemical production of hydroxyl radicals from pulsed cylindrically converging ultrasound waves. *Ultrasonics Sonochemistry* **99**, 106559, doi:https://doi.org/10.1016/j.ultsonch.2023.106559 (2023).
160 Gegenschatz, S. A., Chiappini, F. A., Teglia, C. M., Muñoz de la Peña, A. & Goicoechea, H. C. Binding the gap between experiments, statistics, and method comparison: A tutorial for computing limits of detection and quantification in univariate calibration for complex samples. *Analytica Chimica Acta* **1209**, 339342, doi:https://doi.org/10.1016/j.aca.2021.339342 (2022).
161 Kester, D. R., Duedall, I. W., Connors, D. N. & Pytkowicz, R. M. Preparation of artificial seawater. *Limnology and Oceanography* **12**, 176-179, doi:https://doi.org/10.4319/lo.1967.12.1.0176 (1967).
162 Kyriakou, Z., Corral-Baques, M. I., Amat, A. & Coussios, C.-C. HIFU-induced cavitation and heating in ex vivo porcine subcutaneous fat. *Ultrasound in medicine & biology* **37**, 568-579, doi:https://doi.org/10.1016/j.ultrasmedbio.2011.01.001 (2011).
163 Jonnalagadda, U. S., Su, X. & Kwan, J. J. Nanostructured TiO2 cavitation agents for dual-modal sonophotocatalysis with pulsed ultrasound. *Ultrasonics Sonochemistry*, 105530, doi:https://doi.org/10.1016/j.ultsonch.2021.105530 (2021).
164 Shimadzu Corporation. *Tracera (GC-BID) Solution*, <https://www.antteknik.com/Upload/ProductDoc/tr/28/Tracera_(GC-BID)-LAAN-B-GC004.pdf> (2013), Accessed: 20 May 2025.
165 Shimadzu Corporation. *Detector, 6.1. Type of Detector*, <https://www.shimadzu.co.uk/service-support/technical-support/analysis-basics/fundamentals/detector.html#6_3_3_BID> (2025), Accessed: 30 May 2025.
166 Keller, J. B. & Miksis, M. Bubble oscillations of large amplitude. *The Journal of the Acoustical Society of America* **68**, 628-633, doi:https://doi.org/10.1121/1.384720 (1980).
167 Preso, D. B., Fuster, D., Sieber, A. B., Obreschkow, D. & Farhat, M. Vapor compression and energy dissipation in a collapsing laser-induced bubble. *Physics of Fluids* **36**, doi:https://doi.org/10.1063/5.0200361 (2024).
168 Rowland, D. *Advanced Thermodynamics*, <https://advancedthermo.com> (2021), Accessed: 12 Feb 2025.
169 Kestin, J., Khalifa, H. E. & Correia, R. J. Tables of the dynamic and kinematic viscosity of aqueous NaCl solutions in the temperature range 20–150 °C and the pressure range 0.1–35 MPa. *Journal of Physical and Chemical Reference Data* **10**, 71-88, doi:https://doi.org/10.1063/1.555641 (1981).
170 Ozdemir, O., Karakashev, S. I., Nguyen, A. V. & Miller, J. D. Adsorption and surface tension analysis of concentrated alkali halide brine solutions. *Minerals Engineering* **22**, 263-271, doi:https://doi.org/10.1016/j.mineng.2008.08.001 (2009).
171 Taha, T. A., Elsayed, H. A. & Mehaney, A. One-dimensional symmetric phononic crystals sensor: towards salinity detection and water treatment. *Optical and Quantum Electronics* **54**, 313, doi:https://doi.org/10.1007/s11082-022-03716-6 (2022).
172 Han, Y., Zhang, J., Hao, W., Jiang, C., Nakabayashi, A., Ma, D., Xia, X. & Li, D. Review on the Application of Electron Paramagnetic Resonance in Surface Chemistry Research. *Langmuir*, doi:https://doi.org/10.1021/acs.langmuir.5c04744 (2026).

173 Roessler, M. M. & Salvadori, E. Principles and applications of EPR spectroscopy in the chemical sciences. *Chemical Society Reviews* **47**, 2534-2553, doi:http://dx.doi.org/10.1039/C6CS00565A (2018).
174 Mišík, V. r. & Riesz, P. EPR characterization of free radical intermediates formed during ultrasound exposure of cell culture media. *Free Radical Biology and Medicine* **26**, 936-943, doi:https://doi.org/10.1016/S0891-5849(98)00282-2 (1999).
175 Stoll, S. & Schweiger, A. EasySpin, a comprehensive software package for spectral simulation and analysis in EPR. *Journal of Magnetic Resonance* **178**, 42-55, doi:https://doi.org/10.1016/j.jmr.2005.08.013 (2006).
176 Mittag, J. J., Trutschel, M. L., Kruschwitz, H., Mäder, K., Buske, J. & Garidel, P. Characterization of radicals in polysorbate 80 using electron paramagnetic resonance (EPR) spectroscopy and spin trapping. *Int J Pharm X* **4**, 100123, doi:https://doi.org/10.1016/j.ijpx.2022.100123 (2022).
177 Atherton, N. M. *Principles of electron spin resonance*. (Ellis Horwood: PTR Prentice Hall, 1993).
178 Weil, J. A. The analysis of large hyperfine splitting in paramagnetic resonance spectroscopy. *Journal of Magnetic Resonance (1969)* **4**, 394-399, doi:https://doi.org/10.1016/0022-2364(71)90049-7 (1971).
179 Shchukin, D. G., Skorb, E., Belova, V. & Möhwald, H. Ultrasonic cavitation at solid surfaces. *Advanced Materials* **23**, 1922-1934, doi:https://doi.org/10.1002/adma.201004494 (2011).
180 Doktycz, S. J. & Suslick, K. S. Interparticle collisions driven by ultrasound. *Science* **247**, 1067-1069, doi:https://doi.org/10.1126/science.2309118 (1990).
181 Wang, G. & Cheng, H. Application of photocatalysis and sonocatalysis for treatment of organic dye wastewater and the synergistic effect of ultrasound and light. *Molecules* **28**, 3706, doi:https://doi.org/10.3390/molecules28093706 (2023).
182 Ogi, H., Hirao, M. & Shimoyama, M. Activation of TiO2 photocatalyst by single-bubble sonoluminescence for water treatment. *Ultrasonics* **40**, 649-650, doi:https://doi.org/10.1016/S0041-624X(02)00191-9 (2002).
183 Matsumoto, K., Sato, Y., Ebara, T. & Mizuguchi, J. Hydrogen production from methanol or methane by the use of thermally generated holes in TiO2. *Journal of Chemical Engineering of Japan* **41**, 57-61, doi:https://doi.org/10.1252/jcej.07we234 (2008).
184 Zong, Z., Gilbert, E., Wong, C. C. Y., Usadi, L., Qin, Y., Huang, Y., Raymond, J., Hankins, N. & Kwan, J. Efficient sonochemical catalytic degradation of tetracycline using TiO2 fractured nanoshells. *Ultrasonics Sonochemistry* **101**, 106669, doi:https://doi.org/10.1016/j.ultsonch.2023.106669 (2023).
185 Maxwell, A. D., Cain, C. A., Hall, T. L., Fowlkes, J. B. & Xu, Z. Probability of Cavitation for Single Ultrasound Pulses Applied to Tissues and Tissue-Mimicking Materials. *Ultrasound in Medicine & Biology* **39**, 449-465, doi:https://doi.org/10.1016/j.ultrasmedbio.2012.09.004 (2013).
186 Iersel, M. M. v., Benes, N. E. & Keurentjes, J. T. F. Importance of acoustic shielding in sonochemistry. *Ultrasonics Sonochemistry* **15**, 294-300, doi:https://doi.org/10.1016/j.ultsonch.2007.09.015 (2008).
187 Agarwal, K., Trivedi, M. & Nirmalkar, N. Does salting-out effect nucleate nanobubbles in water: Spontaneous nucleation? *Ultrasonics Sonochemistry* **82**, 105860, doi:https://doi.org/10.1016/j.ultsonch.2021.105860 (2022).
188 Yang, Y., Nie, G., Bi, J., Zhang, P. & Huo, P. Agitation-intensified sonochemistry for water disinfection. *Environmental Surfaces and Interfaces* **3**, 176-182, doi:https://doi.org/10.1016/j.esi.2025.05.003 (2025).
189 Schumpe, A. The estimation of gas solubilities in salt solutions. *Chemical Engineering Science* **48**, 153-158, doi:https://doi.org/10.1016/0009-2509(93)80291-W (1993).

190 Gonçalves, F. A. & Kestin, J. The Viscosity of NaCl and KCl Solutions in the Range 25–50°C. *Berichte der Bunsengesellschaft für physikalische Chemie* **81**, 1156-1161, doi:https://doi.org/10.1002/bbpc.19770811108 (1977).
191 Brotchie, A., Statham, T., Zhou, M., Dharmarathne, L., Grieser, F. & Ashokkumar, M. Acoustic Bubble Sizes, Coalescence, and Sonochemical Activity in Aqueous Electrolyte Solutions Saturated with Different Gases. *Langmuir* **26**, 12690-12695, doi:https://doi.org/10.1021/la1017104 (2010).
192 Pflieger, R., Nikitenko, S. I. & Ashokkumar, M. Effect of NaCl salt on sonochemistry and sonoluminescence in aqueous solutions. *Ultrasonics Sonochemistry* **59**, 104753, doi:https://doi.org/10.1016/j.ultsonch.2019.104753 (2019).
193 Lepoint-Mullie, F., Voglet, N., Lepoint, T. & Avni, R. Evidence for the emission of 'alkali-metal–noble-gas' van der Waals molecules from cavitation bubbles. *Ultrasonics Sonochemistry* **8**, 151-158, doi:https://doi.org/10.1016/S1350-4177(00)00030-4 (2001).
194 Didenko, Y. T., McNamara, W. B. & Suslick, K. S. Temperature of multibubble sonoluminescence in water. *The Journal of Physical Chemistry A* **103**, 10783-10788, doi:https://doi.org/10.1021/jp991524s (1999).
195 Didenko, Y. T., McNamara, W. B. & Suslick, K. S. Hot spot conditions during cavitation in water. *Journal of the American Chemical Society* **121**, 5817-5818, doi:https://doi.org/10.1021/ja9844635 (1999).
196 Suslick, K. S. & Flannigan, D. J. Inside a collapsing bubble: sonoluminescence and the conditions during cavitation. *Annu Rev Phys Chem* **59**, 659-683, doi:https://doi.org/10.1146/annurev.physchem.59.032607.093739 (2008).
197 Yusof, N. S. M., Anandan, S., Sivashanmugam, P., Flores, E. M. M. & Ashokkumar, M. A correlation between cavitation bubble temperature, sonoluminescence and interfacial chemistry – A minireview. *Ultrasonics Sonochemistry* **85**, 105988, doi:https://doi.org/10.1016/j.ultsonch.2022.105988 (2022).
198 Young, J. A. Sodium Chloride. *Journal of Chemical Education* **84**, 1758, doi:https://doi.org/10.1021/ed084p1758 (2007).
199 Kohno, M., Mokudai, T., Ozawa, T. & Niwano, Y. Free radical formation from sonolysis of water in the presence of different gases. *J Clin Biochem Nutr* **49**, 96-101, doi:https://doi.org/10.3164/jcbn.10-130 (2011).
200 John, S. G. & Adkins, J. F. Analysis of dissolved iron isotopes in seawater. *Marine Chemistry* **119**, 65-76, doi:https://doi.org/10.1016/j.marchem.2010.01.001 (2010).
201 Mahamuni, N. N. & Pandit, A. B. Effect of additives on ultrasonic degradation of phenol. *Ultrasonics Sonochemistry* **13**, 165-174, doi:https://doi.org/10.1016/j.ultsonch.2005.01.004 (2006).
202 Gole, V. L. & Gogate, P. R. Sonochemical degradation of chlorobenzene in the presence of additives. *Water Science and Technology* **69**, 882-888, doi:https://doi.org/10.2166/wst.2013.790 (2013).
203 Chen, Y.-C. & Smirniotis, P. Enhancement of photocatalytic degradation of phenol and chlorophenols by ultrasound. *Industrial & engineering chemistry research* **41**, 5958-5965, doi:https://pubs.acs.org/doi/10.1021/ie020415o (2002).
204 Rashwan, S. S., Dincer, I. & Mohany, A. An investigation of ultrasonic based hydrogen production. *Energy* **205**, 118006, doi:https://doi.org/10.1016/j.energy.2020.118006 (2020).
205 Hemmati-Sarapardeh, A., Larestani, A., Nait Amar, M. & Hajirezaie, S. in *Applications of Artificial Intelligence Techniques in the Petroleum Industry* 1-22 (Gulf Professional Publishing, 2020).
206 Do, D. D. & Weiland, R. H. Catalyst Deactivation in an Isothermal CSTR with First-Order Chemical Kinetics. *The Chemical Engineering Journal* **21**, 115-122, doi:https://doi.org/10.1016/0300-9467(81)80042-1 (1981).

207 Simonin, J.-P. On the comparison of pseudo-first order and pseudo-second order rate laws in the modeling of adsorption kinetics. *Chemical Engineering Journal* **300**, 254-263, doi:https://doi.org/10.1016/j.cej.2016.04.079 (2016).
208 Kumari, N., Mahata, A. & Chakraborty, B. Immobilization of Phosphamide on the TiO2 Surface for Heterogeneous Phase Catalytic Appel Reaction. *Inorganic Chemistry* **62**, 7728-7737, doi:https://doi.org/10.1021/acs.inorgchem.3c00304 (2023).
209 Fernández-Pérez, A. & Marbán, G. Titanium dioxide: A heterogeneous catalyst for dark peroxidation superior to iron oxide. *Journal of Environmental Chemical Engineering* **8**, 104254, doi:https://doi.org/10.1016/j.jece.2020.104254 (2020).
210 Vikulin, P. & Vikulina, V. in *IOP Conference Series: Materials Science and Engineering.* 042007 (IOP Publishing).
211 Sasikala, R., Jayakumar, O. D. & Kulshreshtha, S. K. Enhanced hydrogen generation by particles during sonochemical decomposition of water. *Ultrasonics Sonochemistry* **14**, 153-156, doi:https://doi.org/10.1016/j.ultsonch.2006.06.005 (2007).
212 Soleimani, F., Madaah Hosseini, H. R., Ordikhani, F. & Mokhtari-Dizaji, M. Enhancing sonocatalytic properties of TiO2 nanocatalysts by controlling the surface conditions: effect of particle size and PVA modification. *Desalination and Water Treatment* **57**, 28378-28385, doi:https://doi.org/10.1080/19443994.2016.1185746 (2016).
213 Li, Z., Zhuang, T., Dong, J., Wang, L., Xia, J., Wang, H., Cui, X. & Wang, Z. Sonochemical fabrication of inorganic nanoparticles for applications in catalysis. *Ultrasonics Sonochemistry* **71**, 105384, doi:https://doi.org/10.1016/j.ultsonch.2020.105384 (2021).
214 El-Shafie, M. Hydrogen production by water electrolysis technologies: A review. *Results in Engineering* **20**, 101426, doi:https://doi.org/10.1016/j.rineng.2023.101426 (2023).
215 Zhou, P., Navid, I. A., Ma, Y., Xiao, Y., Wang, P., Ye, Z., Zhou, B., Sun, K. & Mi, Z. Solar-to-hydrogen efficiency of more than 9% in photocatalytic water splitting. *Nature* **613**, 66-70, doi:https://doi.org/10.1038/s41586-022-05399-1 (2023).
216 Loomba, S., Khan, M. W., Haris, M., Mousavi, S. M., Zavabeti, A., Xu, K., Tadich, A., Thomsen, L., McConville, C. F., Li, Y., Walia, S. & Mahmood, N. Nitrogen-Doped Porous Nickel Molybdenum Phosphide Sheets for Efficient Seawater Splitting. *Small* **19**, 2207310, doi:https://doi.org/10.1002/smll.202207310 (2023).
217 Xie, H., Zhao, Z., Liu, T., Wu, Y., Lan, C., Jiang, W., Zhu, L., Wang, Y., Yang, D. & Shao, Z. A membrane-based seawater electrolyser for hydrogen generation. *Nature* **612**, 673-678, doi:https://doi.org/10.1038/s41586-022-05379-5 (2022).
218 Harada, H. Sonophotocatalytic decomposition of water using TiO2 photocatalyst. *Ultrasonics Sonochemistry* **8**, 55-58, doi:https://doi.org/10.1016/S1350-4177(99)00050-4 (2001).
219 Harada, H., Hosoki, C. & Ishikane, M. Sonophotocatalysis of water in a CO2–Ar atmosphere. *Journal of Photochemistry and Photobiology A: Chemistry* **160**, 11-17, doi:https://doi.org/10.1016/S1010-6030(03)00214-4 (2003).
220 Vovchok, D., Guild, C. J., Llorca, J., Palomino, R. M., Waluyo, I., Rodriguez, J. A., Suib, S. L. & Senanayake, S. D. Structural and chemical state of doped and impregnated mesoporous Ni/CeO2 catalysts for the water-gas shift. *Applied Catalysis A: General* **567**, 1-11, doi:https://doi.org/10.1016/j.apcata.2018.08.026 (2018).
221 Jomjaree, T., Sintuya, P., Srifa, A., Koo-amornpattana, W., Kiatphuengporn, S., Assabumrungrat, S., Sudoh, M., Watanabe, R., Fukuhara, C. & Ratchahat, S. Catalytic performance of Ni catalysts supported on CeO2 with different morphologies for low-temperature CO2 methanation. *Catalysis Today* **375**, 234-244, doi:https://doi.org/10.1016/j.cattod.2020.08.010 (2021).
222 Zhang, L., Belova, V., Wang, H., Dong, W. & Möhwald, H. Controlled cavitation at nano/microparticle surfaces. *Chemistry of Materials* **26**, 2244-2248, doi:https://doi.org/10.1021/cm404194n (2014).

223 Yan, H., Zhang, N. & Wang, D. Highly efficient CeO2-supported noble-metal catalysts: From single atoms to nanoclusters. *Chem Catalysis* **2**, 1594-1623, doi:https://doi.org/10.1016/j.checat.2022.05.001 (2022).
224 Savun-Hekimoğlu, B. A Review on Sonochemistry and Its Environmental Applications. *Acoustics* **2**, 766-775, doi:https://doi.org/10.3390/acoustics2040042 (2020).
225 Choi, Y., Lee, D., Hong, S., Khan, S., Darya, B., Lee, J.-Y., Chung, J. & Cho, S.-H. Investigation of the Synergistic Effect of Sonolysis and Photocatalysis of Titanium Dioxide for Organic Dye Degradation. *Catalysts* **10**, 500, doi:https://doi.org/10.3390/catal10050500 (2020).
226 Frohly, J., Labouret, S., Bruneel, C., Looten-Baquet, I. & Torguet, R. Ultrasonic cavitation monitoring by acoustic noise power measurement. *The Journal of the Acoustical Society of America* **108**, 2012-2020, doi:https://doi.org/10.1121/1.1312360 (2000).
227 Seeharaj, P., Saenman, T., Phiwhom, T., Muangsuwan, C., Srinives, S. & Kim-Lohsoontorn, P. Improvement of surface properties of metal doped-CeO2 nanospindle catalysts for direct synthesis of dimethyl carbonate from CO2 and methanol. *Journal of Environmental Chemical Engineering* **11**, 109813, doi:https://doi.org/10.1016/j.jece.2023.109813 (2023).
228 Suzuki, K., Kato, M., Sunaoshi, T., Uno, H., Carvajal-Nunez, U., Nelson, A. T. & McClellan, K. J. Thermal and mechanical properties of CeO2. *Journal of the American Ceramic Society* **102**, 1994-2008, doi:https://doi.org/10.1111/jace.16055 (2019).
229 Parizot, L., Chave, T., Galvez, M.-E., Dutilleul, H., Da Costa, P. & Nikitenko, S. I. Sonocatalytic oxidation of EDTA in aqueous solutions over noble metal-free Co3O4/TiO2 catalyst. *Applied Catalysis B: Environmental* **241**, 570-577, doi:https://doi.org/10.1016/j.apcatb.2018.09.001 (2019).
230 Khataee, A., Karimi, A., Arefi-Oskoui, S., Soltani, R. D. C., Hanifehpour, Y., Soltani, B. & Joo, S. W. Sonochemical synthesis of Pr-doped ZnO nanoparticles for sonocatalytic degradation of Acid Red 17. *Ultrasonics sonochemistry* **22**, 371-381, doi:https://doi.org/10.1016/j.ultsonch.2014.05.023 (2015).
231 Nishimura, T., Kodama, T., Genta, S. & Ishii, T. Transition metals doped effects for the crystal stabilization of the cerium oxides with the first principle calculation. *Scientific Reports* **12**, 10103, doi:https://doi.org/10.1038/s41598-022-14180-3 (2022).
232 Yu, Y., Xia, W., Yu, A., Simakov, D. S. & Ricardez-Sandoval, L. Transition-Metal-Doped CeO2 for the Reverse Water-Gas Shift Reaction: An Experimental and Theoretical Study on CO2 Adsorption and Surface Vacancy Effects. *ChemSusChem*, e202400681, doi:https://doi.org/10.1002/cssc.202400681 (2024).
233 Su, Y.-Q., Zhang, L., Muravev, V. & Hensen, E. J. Lattice oxygen activation in transition metal doped ceria. *Chinese Journal of Catalysis* **41**, 977-984, doi:https://doi.org/10.1016/S1872-2067(19)63468-6 (2020).
234 Yi, L., Yu, L., Chen, S., Huang, D., Yang, C., Deng, H., Hu, Y., Wang, H., Wen, Z. & Wang, Y. The regulatory mechanisms of cerium oxide nanoparticles in oxidative stress and emerging applications in refractory wound care. *Frontiers in Pharmacology* **15**, 1439960, doi:https://doi.org/10.3389/fphar.2024.1439960 (2024).
235 Humphrey, J. J. L., Kronberg, R., Cai, R., Laasonen, K., Palmer, R. E. & Wain, A. J. Active site manipulation in MoS2 cluster electrocatalysts by transition metal doping. *Nanoscale* **12**, 4459-4472, doi:https://doi.org/10.1039/C9NR10702A (2020).
236 Chakma, S. & Moholkar, V. S. Investigation in mechanistic issues of sonocatalysis and sonophotocatalysis using pure and doped photocatalysts. *Ultrasonics sonochemistry* **22**, 287-299, doi:https://doi.org/10.1016/j.ultsonch.2014.06.008 (2015).
237 Wang, L.-l. & Lu, C.-h. The effect of viscosity on the cavitation characteristics of high speed sleeve bearing. *Journal of Hydrodynamics, Ser. B* **27**, 367-372, doi:https://doi.org/10.1016/S1001-6058(15)60494-2 (2015).
238 National Oceanic and Atmospheric Administration (NOAA). (NOAA Global Monitoring Laboratory, 2024).

239 Bio-Rad Laboratories. *Guide to Aminex HPLC Columns: for Food and Beverage, Biotechnology, and Bio-Organic Analysis*, Accessed: 11 Sept 2024.
240 Hao, X. H., Guo, L. J., Mao, X., Zhang, X. M. & Chen, X. J. Hydrogen production from glucose used as a model compound of biomass gasified in supercritical water. *International Journal of Hydrogen Energy* **28**, 55-64, doi:https://doi.org/10.1016/S0360-3199(02)00056-3 (2003).
241 Fang, Z., Minowa, T., Fang, C., Smith, J. R. L., Inomata, H. & Kozinski, J. A. Catalytic hydrothermal gasification of cellulose and glucose. *International Journal of Hydrogen Energy* **33**, 981-990, doi:https://doi.org/10.1016/j.ijhydene.2007.11.023 (2008).
242 Majumdar, S., Kumar, P. S. & Pandit, A. B. Effect of liquid-phase properties on ultrasound intensity and cavitational activity. *Ultrasonics Sonochemistry* **5**, 113-118, doi:https://doi.org/10.1016/S1350-4177(98)00019-4 (1998).
243 Ban, Z. H., K., L. K. & and Shariff, A. M. Prediction of the bubble nucleation rate in a quasi-stable cavitating nozzle using 2D computational fluid dynamics and enhanced classical nucleation theory. *Engineering Applications of Computational Fluid Mechanics* **9**, 247-258, doi:https://doi.org/10.1080/19942060.2015.1005873 (2015).
244 Jideani, T., Chukwuchendo, E. & Khotseng, L. An Approach towards the Conversion of Biomass Feedstocks into Biofuel Using a Zeolite Socony Mobil-5-Based Catalysts via the Hydrothermal Liquefaction Process: A Review. *Catalysts* **13**, 1425, doi:https://doi.org/10.3390/catal13111425 (2023).
245 Chen, W.-H., Cheng, C.-L., Lee, K.-T., Lam, S. S., Ong, H. C., Ok, Y. S., Saeidi, S., Sharma, A. K. & Hsieh, T.-H. Catalytic level identification of ZSM-5 on biomass pyrolysis and aromatic hydrocarbon formation. *Chemosphere* **271**, 129510, doi:https://doi.org/10.1016/j.chemosphere.2020.129510 (2021).
246 Aho, A., Kumar, N., Eränen, K., Salmi, T., Hupa, M. & Murzin, D. Y. Catalytic Pyrolysis of Biomass in a Fluidized Bed Reactor: Influence of the Acidity of H-Beta Zeolite. *Process Safety and Environmental Protection* **85**, 473-480, doi:https://doi.org/10.1205/psep07012 (2007).
247 Hernando, H., Moreno, I., Fermoso, J., Ochoa-Hernández, C., Pizarro, P., Coronado, J. M., Čejka, J. & Serrano, D. P. Biomass catalytic fast pyrolysis over hierarchical ZSM-5 and Beta zeolites modified with Mg and Zn oxides. *Biomass Conversion and Biorefinery* **7**, 289-304, doi:https://doi.org/10.1007/s13399-017-0266-6 (2017).
248 Xu, J., Wen, Y., Li, D., Zhang, S., Han, Z., Hu, H. & Jin, L. Catalytic upgrading of biomass pyrolysis volatiles over Y zeolites modified with different metal oxides. *Fuel* **371**, 131936, doi:https://doi.org/10.1016/j.fuel.2024.131936 (2024).
249 Porawati, H., Kurniawan, A. & Yuliwati, E. Effect of Temperature on Gasification of Biomass Using Zeolit. *Journal of Physics: Conference Series* **1845**, 012040, doi:https://dx.doi.org/10.1088/1742-6596/1845/1/012040 (2021).
250 Sudalaimuthu, P., Ali, U. & Sathyamurthy, R. Optimization of process parameters of catalytic pyrolysis using natural zeolite and synthetic zeolites on yield of plastic oil through response surface methodology. *Scientific Reports* **14**, 28442, doi:https://doi.org/10.1038/s41598-024-78180-1 (2024).
251 Sun, W., Yan, Y., Wei, Y., Ma, J., Niu, Z. & Hu, G. Catalytic Pyrolysis of Biomass: A Review of Zeolite, Carbonaceous, and Metal Oxide Catalysts. *Nanomaterials (Basel)* **15**, doi:https://doi.org/10.3390/nano15070493 (2025).
252 Ryczkowski, R., Goscianska, J., Panek, R., Franus, W., Przybysz, K. & Grams, J. Sustainable nickel catalyst for the conversion of lignocellulosic biomass to H2-rich gas. *International Journal of Hydrogen Energy* **46**, 10708-10722, doi:https://doi.org/10.1016/j.ijhydene.2020.12.169 (2021).
253 Yesilova, N., Tezer, O., Ongen, A. & Ayol, A. Enhancing biomass gasification: A comparative study of catalyst applications in updraft and modifiable-downdraft fixed bed

reactors. *International Journal of Hydrogen Energy* **76**, 290-303, doi:https://doi.org/10.1016/j.ijhydene.2024.05.075 (2024).

254 Olazar, L., Saldarriaga, J. F., Lopez, G., Santamaria, L., Amutio, M., Olazar, M. & Artetxe, M. Insight into the joint valorization of CO2 and waste plastics by pyrolysis and in line dry reforming for syngas production. *Fuel Processing Technology* **253**, 108024, doi:https://doi.org/10.1016/j.fuproc.2023.108024 (2024).

255 Wei, X., Sharma, S., Waeber, A., Wen, D., Sampathkumar, S. N., Margni, M., Maréchal, F. & Van herle, J. Comparative life cycle analysis of electrolyzer technologies for hydrogen production: Manufacturing and operations. *Joule* **8**, 3347-3372, doi:https://doi.org/10.1016/j.joule.2024.09.007 (2024).

256 Fu, Q., Li, H., Duan, D., Wang, C., Shen, S., Ma, H. & Liu, Z. External-Radiation-Induced Local Hydroxylation Enables Remote Release of Functional Molecules in Tumors. *Angewandte Chemie International Edition* **59**, 21546-21552, doi:https://doi.org/10.1002/anie.202005612 (2020).